Since the original proposal from Cirac and Zoller in 1995 to use trapped ions as a quantum computer and couple a chain of ions through their collective quantize motion, most of the experimental efforts to couple trapped ions have been performed with the use of laser light. To achieve a high fidelity of the implemented quantum gates, the lasers' frequency, intensity, phase, beam quality, pointing stability and diffraction must be controlled. Additionally, spontaneous emission affects the gate operation. In 2001 a method was proposed to use long-wavelength radiation, such as microwaves or radio-waves, to implement the quantum gates. In practice, an additional inhomogeneous magnetic field is applied to the cooled chain of trapped ions and in this way the ions can be individually addressed in frequency space. Furthermore, the gradient induces a coupling between the ions' internal and motional states and the Ising-type spin-spin coupling (J-coupling) between the ions' internal states. We call this method Magnetic Gradient Induced Coupling, MAGIC. By employing MAGIC, it is possible to use microwave radiation instead of optical light, avoiding the fundamental technical limitations mentioned above.

In this thesis a new experimental setup to implement MAGIC is described. Initially, the setup was characterized and then different experiments have been performed that evidenced the spin-spin coupling. The coupling constants have been measured for a two and three ion chain. The measured values are in good agreement with the calculated dependence $J \approx b^2/\nu_z^2$, where b is the magnetic field gradient and ν_z is the axial trap frequency of the common mode. The measurements demonstrated that the coupling constants can be varied by adjusting the axial trapping potential.

Spin-spin coupling can be used to implement controlled-NOT (CNOT) gates. First, a CNOT gate between two neighboring ions has been performed to demonstrate that the MAGIC method can be used for conditional dynamics. Furthermore, the CNOT gate has been implemented between non-neighboring ions in a three-ion chain as a proof-of principle of a quantum bus employing the ion chain. This has been done here for the first time using the MAGIC method. The quantum nature of a conditional gate is verified via creation of a bipartite entangled Bell state with a fidelity that exceeds the Bell limit and thus proves the existence of entanglement.

Anastasiya Khromova

Awarded with a BSc in Physics in June 2001 and the Specialist degree in Physics in June 2003 at the National University 'Kyiv-Mohyla Academy'of Kiev (Ukraine).
Received the MSc in Physics in February 2005 from the International Master Program 'Imaging Physics' at the University of Siegen (Germany) within the exchange program DAAD. Granted with a PhD degree in Quantum Optics at the University of Siegen (Germany) in August 2012.

A.Khromova Quantum Gates with Trapped Ions using Magnetic Gradient Induced Coupling

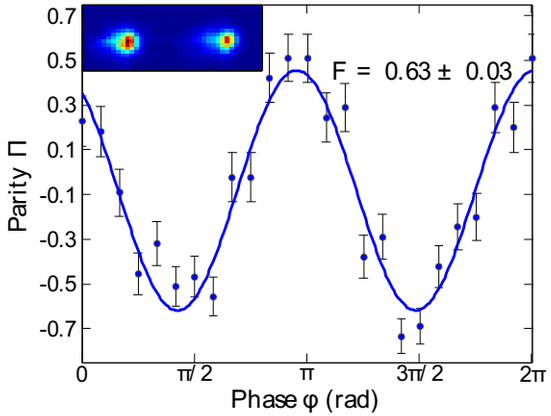

Quantum Gates with Trapped Ions using Magnetic Gradient Induced Coupling

Anastasiya Khromova

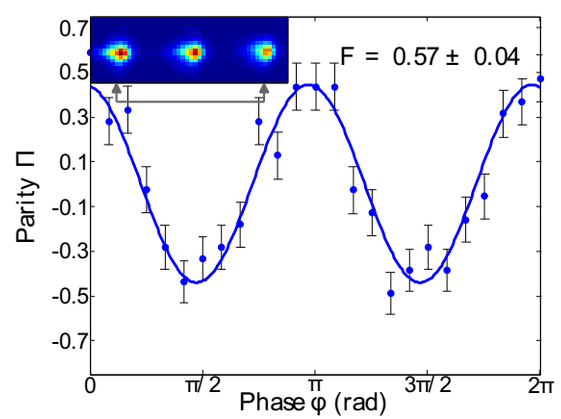

Quantum Gates with Trapped Ions using Magnetic Gradient Induced Coupling

Dissertation
zur Erlangung des Grades eines Doktors
der Naturwissenschaften

vorgelegt von

M.Sc. Anastasiya Khromova
aus Sankt Petersburg

eingereicht bei
der Naturwissenschaftlich-Technischen Fakultät
der Universität Siegen

Siegen 2012

Gutachter der Dissertation:	Prof. Dr. C. Wunderlich
	Prof. Dr. O. Gühne
Gutachter der Disputation:	Prof. Dr. C. Wunderlich
	Prof. Dr. O. Gühne
	Prof. Dr. C. Grupen
	Prof. Dr. T. Mannel
Datum der Disputation:	10.08.2012

Gedruckt auf alterungsbeständigem holz- und säurefreiem Papier

Zusammenfassung

Im Jahr 1995 machten Ignacio Cirac und Peter Zoller den Vorschlag, Ketten von gespeicherten Ionen für den Bau eines Quantencomputers zu nutzen [Cirac & Zoller, 1995]. Dieser Vorschlag wurde experimentell zumeist realisiert, indem die einzelnen Ionen einer Kette mit Hilfe von Laserlicht miteinander verschränkt wurden. Um mit dieser Methode eine hohe Fidelity der implementierten Quantengatter zu erreichen, müssen Frequenz, Intensität und Phase des benutzten Laserlichtes und außerdem das Strahlprofil und die Strahlbeugung sehr stabil und gut einstellbar sein. Zudem beeinflussen spontane Emissionen die Gatteroperationen. Eine Methode, diese fundamentalen technischen Einschränkungen zu umgehen, wurde im Jahr 2001 veröffentlicht [Mintert & Wunderlich, 2001]. Bei dieser Methode nutzt man langwellige Strahlung wie Mikrowellen oder Radiowellen statt des kurzwelligen Laserlichtes, um Quantengatter zu implementieren. Dafür wird ein zusätzliches inhomogenes Magnetfeld am Ort der Ionenkette angelegt. Dieser Magnetfeldgradient ermöglicht eine Adressierung der einzelnen Ionen der Kette im Frequenzraum. Zudem wird durch den Gradienten eine Kopplung zwischen den inneren und äußeren Zuständen der Ionen erzeugt, es entsteht eine Isingmodell-artige Spin-Spin Kopplung (J-Kopplung) zwischen den Ionen. Diese Methode wird als magnetfeldgradientinduzierte Kopplung, kurz MAGIC (Magnetic Gradient Induced Coupling), bezeichnet.

In der vorliegenden Arbeit wird ein neuartiger experimenteller Aufbau zur Umsetzung des MAGIC-Schemas beschrieben. Zunächst wurde der Aufbau charakterisiert und verschiedene Experimente für eine Evidenz der Spin-Spin Kopplung durchgeführt. An Ionenketten mit zwei bzw. drei Ionen wurden die Kopplungskonstanten vermessen. Die Ergebnisse aus diesen Messungen sind in guter Übereinstimmung mit dem berechneten Zusammenhang $J \propto \frac{b^2}{\nu_z^2}$ (b ist dabei der Magnetfeldgradient, ν_z die axiale Fallenfrequenz der Normalmode). Mit Hilfe dieser Messungen wurde demonstriert, dass die Kopplungskonstanten durch Variation des axialen Fallenpotentials eingestellt werden können.

Spin-Spin Kopplung kann dazu genutzt werden, Kontrollierte-Nicht- (CNOT-) Gatter umzusetzen. Im Rahmen dieser Arbeit wurde zunächst ein CNOT-Gatter zwischen zwei benachbarten Ionen ausgeführt und so gezeigt, dass die MAGIC-Methode für die bedingte Dynamik eingesetzt werden kann. Zudem wurde mit der MAGIC-Methode erstmalig ein CNOT-Gatter zwischen zwei nicht benachbarten Ionen einer drei-Ionen-Kette umgesetzt, was der Implementation eines Quantenbusses entspricht. Die Quantennatur der bedingten Gatter wurde gezeigt, indem ein verschränkter Bellzustand mit zwei Ionen erzeugt wurde. Dabei übersteigt die Fidelity das Bell-Limit, eine Verschränkung der Teilchen ist somit bewiesen.

Abstract

Since the original proposal from Cirac and Zoller in 1995 [Cirac & Zoller, 1995] to use trapped ions as a quantum computer and couple a chain of ions through their collective quantize motion, most of the experimental efforts to couple trapped ions have been performed with the use of laser light. To achieve a high fidelity of the implemented quantum gates, the lasers' frequency, intensity, phase, beam quality, pointing stability and diffraction must be controlled. Additionally, spontaneous emission affects the gate operation. In 2001 a method was proposed to use long-wavelength radiation, such as microwaves or radio-waves, to implement the quantum gates [Mintert & Wunderlich, 2001]. In practice, an additional inhomogeneous magnetic field is applied to the cooled chain of trapped ions and in this way the ions can be individually addressed in frequency space. Furthermore, the gradient induces a coupling between the ions' internal and motional states and the Ising-type spin-spin coupling (J-coupling) between the ions' internal states. We call this method Magnetic Gradient Induced Coupling, MAGIC. By employing MAGIC, it is possible to use microwave radiation instead of optical light, avoiding the fundamental technical limitations mentioned above.

In this thesis a new experimental setup to implement MAGIC is described. Initially, the setup was characterized and then different experiments have been performed that evidenced the spin-spin coupling. The coupling constants have been measured for a two and three ion chain. The measured values are in good agreement with the calculated dependence $J \propto \frac{b^2}{\nu_z^2}$, where b is the magnetic field gradient and ν_z is the axial trap frequency of the common mode. The measurements demonstrated that the coupling constants can be varied by adjusting the axial trapping potential.

Spin-spin coupling can be used to implement controlled-NOT (CNOT) gates. First, a CNOT gate between two neighboring ions has been performed to demonstrate that the MAGIC method can be used for conditional dynamics. Furthermore, the CNOT gate has been implemented between non-neighboring ions in a three-ion chain as a proof-of principle of a quantum bus employing the ion chain. This has been done here for the first time using the MAGIC method. The quantum nature of a conditional gate is verified via creation of a bipartite entangled Bell state with a fidelity that exceeds the Bell limit and thus proves the existence of entanglement.

Contents

Acknowledgements

1

Introduction

The term *quantum computer* was first introduced by Richard Feynman in 1982 [Feynman, 1982a,b] as a device that would use quantum-mechanical principles and quantum-mechanical phenomena for the efficient simulation of quantum mechanical many-body systems.

The main principles of quantum computation are based on two quantum-mechanical effects: *superposition* and *entanglement*. In quantum computing, a *qubit* (quantum bit) is a unit of quantum information, similar to the classical bit, and it is described by a quantum state in a two-state quantum-mechanical system. An example of a two-state system is a spin-1/2 particle such as an electron and projection of its spin to any axis can have values $\pm\frac{\hbar}{2}$. In a classical system, a bit would have to be in one state or the other, designated 0 or 1, but quantum mechanics allows the qubit to be in a coherent *superposition* of both states at the same time, a property that is fundamental to quantum computing. In general, a quantum computer with n qubits can be in an arbitrary superposition of up to 2^n different states simultaneously and performs a computation on all these possibilities at the same time (quantum parallelism), compared to a normal computer that can only be in any single of these 2^n state.

Any of these 2^n states describe the properties of all particles. The superposition of two such states might yield a strong correlation between a sub group of par-

ticles and is called entanglement. Entanglement is a purely quantum mechanical phenomenon that does not have analogies in the classical world. In an ordinary computer the bits represent independent subsystems of a big system (quantum register). In a quantum computer qubits can be strongly linked to each other even if they are separated by large distances and do not interact. As a result, a measurement on one qubit is correlated with the outcome of the measurement on the other qubit. Such states of a composite system are called *entangled states* and the simplest two-qubit entangled states known are Bell states [1] (or EPR pair[2]) [Nielsen & Chuang, 2000].

Superposition and entanglement make a quantum computer more suitable to solve certain problems that seem impossible for a classical computer. For example, in Shor's quantum algorithm [Shor, 1994] for factoring large numbers the time needed to find the prime factors of a number with N digits grows polynomially with N compared to a classical computer where the necessary time for finding prime factors grows exponentially with N. Another example where quantum computer is more powerful than a classical computer is the search algorithm for unsorted databases found by L. Grover [Grover, 1996]. Entanglement is also used in teleportation [Bennett *et al.*, 1993], as a quantum channel to exchange quantum information between two remote quantum systems. Teleportation was experimentally demonstrated with photons [Bouwmeester *et al.*, 1997; Ursin *et al.*, 2004] and with atoms [Barrett *et al.*, 2004; Olmschenk *et al.*, 2009; Riebe *et al.*, 2004]. Another important application of entanglement is in an error-correction algorithm, proposed by Shor in 1995 [Shor, 1995], that can compensate for gate infidelities during computation. A quantum computer can be also successfully implemented for simulation of other systems using the analog or digital approach. In the first case the time evolution of the simulator matches the dynamics of the simulated model. In the second case, the time dynamics is described by a sequence of quantum gates. Hence, a proof-of-principle experiment with two ions demonstrating an adiabatic evolution from paramagnetic to ferromagnetic order was performed in 2008 [Fridenauer *et al.*, 2008]. More recently, the experiment has been extended to up to 9 ions in a linear ion string [Islam *et al.*, 2011]. Among other possibilities are the simulation of the relativistic quantum particle [Gerritsma *et al.*, 2010], particle generation [Schützhold, 2007] or digital simulation of a two-spin Ising system [Lanyon *et al.*, n.d.].

In recent years considerable progress has been made in the theoretical and experimental development of a quantum computer and various physical systems were proposed for its realization. Any candidate for quantum computer must satisfy

[1] named after John Stewart Bell
[2] named after Einstein, Podolsky and Rosen

five criteria, formulated by David DiVincenzo in 2000 [DiVincenzo, 2000]:

1) The system must be scalable and the qubits must be well characterized

2) It must be possible to initialize the qubits to an intended state with high fidelity

3) The system must have long relevant decoherence times, much longer than the gate operation time

4) An universal set of quantum gates must exists

5) It must be possible to perform a qubit-specific measurement

In order to create quantum networks and establish quantum communication with quantum computers, two additional requirements need to be fulfilled:

6) The system must have the ability to interconvert stationary and flying qubits

7) It must be possible to faithfully transmit flying qubits between specified locations

Standard quantum computation (a *quantum circuit* model) is based on *sequences* of unitary *quantum logic gates*, elementary operations performed on a small amount of qubits, similar to classical logic gates in conventional computer, and they are responsible for creating entanglement needed for quantum information processing. A set of gates that is able to implement any unitary operation on a quantum computer is called a *universal quantum gates set*. It was proved [DiVincenzo, 1995] that quantum gates operating on just two qubits at a time are sufficient to construct a general quantum circuit. Additionally, Barenco showed that the set of one-qubit quantum gates and the two-qubit exclusive-or (XOR) gate is sufficient to describe all unitary operations on arbitrary many qubits, i.e this set is universal [Barenco *et al.*, 1995]. The equivalent of the classical XOR gate is the 2-qubit controlled-NOT (CNOT) gate. This is an important statement that will be considered in the current work. It is worth mentioning that not all models of quantum computers need to be made with gates. The one-way quantum computer, proposed by Raussendorf and Briegel [Raussendorf & Briegel, 2001], requires qubits to be initialized in a highly-entangled *cluster state*. Quantum computation proceeds by a sequence of single-qubit measurements depending on the previous outcome. The one-way quantum computation has been experimentally demonstrated for the first time by Zeilinger group on a four-qubit cluster states encoded into the polarization state of the four photons [Walther *et al.*, 2005]. Another example where quantum gates are not necessary for quantum computation is adiabatic quantum computation [Mizel *et al.*, 2007].

A quantum computer based on trapped ions is one of the promising candidates. Here, the ions are confined in linear radio-frequency traps. The information is encoded in the internal states of ions. Usually optical or hyperfine qubits are used. In the first case, the qubit is defined by a ground and an excited meta-stable states of ion separated by an optical frequency. Hyperfine levels in contrast are separated by a microwave of radio-frequency.

The original idea to use trapped ions as a quantum computer was conceived by Cirac and Zoller (CZ scheme) in 1995 [Cirac & Zoller, 1995]. Each ion is individually addressable by different lasers focussed on each ion. Hence, the single-qubit rotations (single-qubit gates) are performed by laser beams with controlled frequency, intensity and phase. The CNOT gate can be implemented by exciting the collective quantized motion of the ion string. As a prerequisite the ions are cooled into the motion ground state and the ground and first excited states of this mode are used as a 'bus' that couples different ions. The CZ gate was first experimentally demonstrated in a simplified form using motional and internal states of a single trapped $^{9}Be^{+}$ ion by [Monroe *et al.*, 1995]. The full implementation of the scheme using a $^{40}Ca^{+}$ ion string and the individual addressing was reported in [Schmidt-Kaler *et al.*, 2003].

Later alternative schemes for conditional gates have been proposed, that do not require cooling to motional ground state and individual optical addressing of the ions, by Milburn [Milburn *et al.*, 2000], Sørensen and Mølmer [Mølmer & Sørensen, 1999; Sørensen & Mølmer, 1999, 2000], Solano [Solano *et al.*, 1999]. These gates were experimentally realized by Sackett to entangle two and four $^{9}Be^{+}$ ions [Sackett *et al.*, 2000], by Leibfried and Haljan as a geometric phase shift gate [Haljan *et al.*, 2005; Leibfried *et al.*, 2003]. In these kind of gates a bichromatic laser field is used that interacts with two or more ions simultaneously. This bichromatic field can be a pair of co-propagating lasers (Raman beams) with frequencies tuned close to the upper and lower motional sideband of the qubit transition [3].

There exists at least two main difficulties in realizing a quantum computation: one is decoherence, that tends to destroy the phase information in a superposition of states, making long computations impossible, and the other is due to inaccuracies during the performance of operations on the qubits, rendering the computation unreliable. Therefore, quantum gates must be very precise and far faster than the possible coherence time (decay time of the coherence) in the physical system.

There are several sources of errors in both, CZ and Mølmer-Sørensen, kind of

[3]For optical qubits one bichromatic laser source is used for qubit manipulation, for hyperfine qubits a pair of bichromatic Raman laser beams is used.

gates that reduce the fidelity of the implemented quantum gates. First, there are technical problems such as laser intensity, frequency and phase fluctuations as well as the beam quality, pointing stability and diffraction. For example, in order to achieve a coherence time of about 1 s, the frequency error should not exceed 1 Hz. This means a frequency stability of about 10^{-15}! The value can be slightly more moderate: the frequency error should not exceed 1 Hz corresponding to a relative error below 10^{15}. The fundamental physical problems that affect the gates operation are spontaneous emission from the excited states [Ozeri *et al.*, 2007] and thermal excitation to the higher vibrational modes. The last contributes to the Rabi frequencies fluctuations and it is advisable to cool all modes that are parallel to the direction of motion to be coupled to the motional ground state [Wineland *et al.*, 1998b]. And, as a last contribution, everybody fights the decoherence from Zeeman shifts due to the magnetic field fluctuations.

Despite all the technical and physical problems, many experimental advances in quantum information processing using trapped ions have been so far achieved with these kind of gates. These includes:

1) The best measured entangling gate fidelity equal to 99.3 % was achieved using a Mølmer-Sørensen scheme on an optical transition of $^{40}Ca^{+}$ ions and manipulated by the laser light at 729 nm [Benhelm *et al.*, 2008].

2) Entanglement of up to 14 $^{40}Ca^{+}$ ion qubits was recently realized by the same Mølmer-Sørensen scheme [Monz *et al.*, 2011].

In 2001 a method was proposed to use long-wavelength radiation, such as microwaves or radio-waves, to implement the quantum gates [Mintert & Wunderlich, 2001]. In practice, an additional inhomogeneous magnetic field is applied to the cooled chain of trapped ions and in this way the ions can be individually addressed in frequency space. Furthermore, the gradient induces a coupling between the ions' internal and motional states due to the new supplementary coupling parameter, dependent on the gradient strength and not on the wavelength of the radiation used for qubit manipulation. In this way Ising-type spin-spin coupling (J-coupling) between the ions' internal states is created. We call this method MAgnetic Gradient Induced Coupling, MAGIC.

The coupling between the internal and motional states (one $^{172}Yb^{+}$ ion) as well as the individual addressing in the frequency space using the MAGIC-scheme (up to four $^{172}Yb^{+}$ ions) using the rf radiation has been already demonstrated in our group [Johanning *et al.*, 2009a]. In this thesis both experiments have been performed using microwave radiation and $^{171}Yb^{+}$ ions at 100 times higher magnetic field gradient. Individual microwave addressing of a particular ion has a substan-

tially smaller cross-talk error compared to laser light addressing. In this thesis an addressing error of less than 0.04 % is achieved with a magnetic field gradient of 19 T/m. Increasing the gradient or decreasing the Rabi frequency will further reduce this error. This is a considerable improvement since individual laser addressing has errors in the order of few percent [Häffner *et al.*, 2005; Monz *et al.*, 2009].

It is much easier and less costly to generate microwave radiation, compared to the complicated control of laser systems, since a huge industry knowledge in the field of microwave technology exists. There is no problem of spontaneous emission anymore and the main source of the errors that reduces the quantum gate fidelity in our experiments is due to magnetic field fluctuations. In this thesis several error-correcting multiple π-pulses sequences were used to compensate for dephasing errors due to the slow (on the timescale of the evolution time τ) magnetic field fluctuations. Besides, the suggestion to use *microwave-dressed states* was made that increases the coherence time by more than two orders of magnitude compared to the magnetic-field-sensitive states currently used in this work [Timoney *et al.*, 2011].

The main result of this thesis is the demonstration of conditional quantum gates using microwave radiation in a magnetic field gradient (MAGIC-scheme). CNOT-gates using this alternative scheme are demonstrated for the first time between two neighboring and two non-neighboring ions with fidelity equal to 0.63(3) and 0.57(4), respectively. Importantly, these gates were successfully demonstrated with thermally exited vibrational modes considerably above the ground state and that reduces the necessity for ground state cooling trapped ions in order to achieve high fidelity quantum gates. For the sake of completeness, we would like to mention that the microwave quantum gates were also performed using the alternative scheme of the oscillating magnetic field gradient in the near-field region [Ospelkaus *et al.*, 2011]. These scheme though does not allow a straight forward individual addressing of the ions and it will probably require extensive shuttling between different trapping regions for multi-qubit operations. The ability to directly entangle non-neighboring ions in long ion chain using the MAGIC-scheme reduces or eliminates the need for ion shuttling. A substantial part of this thesis is dedicated to the description of a new experimental setup that was constructed within this thesis in order to implement the MAGIC-scheme quantum operations with $^{171}Yb^{+}$ ions.

The thesis is structured as follows: chapter 2 discusses the main ideas of quantum information, introduces the concepts that will be used during the measurements and explains important principles of the MAGIC-scheme. Chapter 3 describes the new setup consisting of the linear Paul trap with the trap drive, laser and vacuum

systems, lambda-meter, static magnetic field Helmholtz coils, microwave system, magnetic gradient and detection system. Chapter 4 explains how the ions are loaded into the trap and how ions' micro-motion is compensated. In chapter 5 the suggestion for a new ion trap design is discussed which allows to increase the microwave magnetic field on the ions. In chapter 6 the fundamental experimental techniques and procedures are explained. Hence, the complete measurement sequence will be presented with short description of the main steps. The topics such as individual ion addressing with microwave radiation and microwave multiple π-pulse sequences to increase the coherence time in the experiment will be discussed in more detail. Chapter 7 gives the results of the coupling constants measurements which are essential prerequisites for quantum gates implementations using the MAGIC-scheme. In chapter 8 the realization of CNOT gates is presented. First, a CNOT gate between two neighboring ions has been carried out to demonstrate that the MAGIC method can be used for conditional dynamics. Furthermore, the CNOT gate has been implemented between non-neighboring ions in a three-ion chain as a proof-of principle of a quantum bus employing the ion chain. Additionally, the consecutive creation of Bell-state is discussed and verified by parity measurements. Finally, chapter 9 gives a summary of the thesis and an outlook to the next possible steps and possibilities.

2

Theory

This chapter reviews the most basic ideas of quantum computing, introduces the theoretical concepts that will be used during the measurements and explains the principle of the MAGIC-scheme. The theory presented in section 2.1 is based on [Nielsen & Chuang, 2000].

2.1 Quantum Logic with Trapped Ions

2.1.1 Control of a Single Qubit

Two possible basis states for a qubit are the states $|\downarrow\rangle$ and $|\uparrow\rangle$, often also labeled as $|0\rangle$ and $|1\rangle$, that correspond to the states 0 and 1 for a classical bit. The pure quantum state of a two-level system, representing qubit, can be written as a superposition of the basis states as:

$$|\psi\rangle = \alpha\,|\downarrow\rangle + \beta\,|\uparrow\rangle \quad . \tag{2.1}$$

The numbers α and β are complex numbers. When we measure a qubit we get

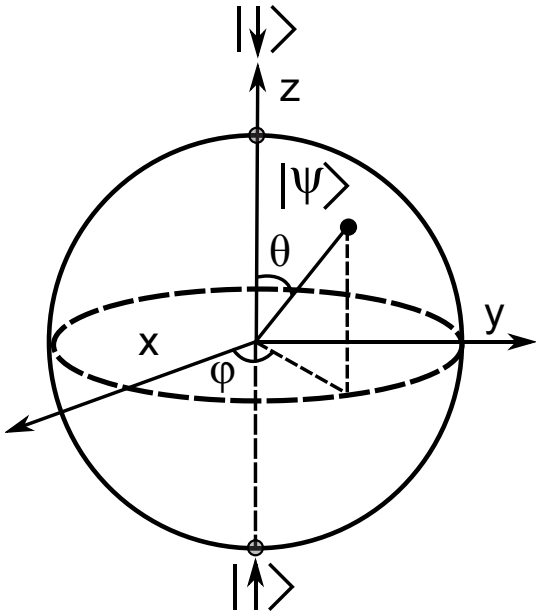

Figure 2.1: Bloch sphere representation of a two level system.

either the result $|\downarrow\rangle$, with probability $|\alpha^2|$, or the result $|\uparrow\rangle$, with probability $|\beta^2|$ and $|\alpha^2| + |\beta^2| = 1$.

The time evolution of a state $|\psi\rangle$ of a closed quantum system, that does not interact with any other system, is described by the Schrödinger equation

$$i\hbar\frac{d}{dt}|\psi(t)\rangle = H|\psi(t)\rangle \quad , \tag{2.2}$$

where H is the Hamiltonian describing the closed system. The general solution of equation 2.2 for time-independent H is

$$|\psi(t)\rangle = \exp\left[-\frac{iHt}{\hbar}\right]|\psi(0)\rangle \quad . \tag{2.3}$$

A practical way to visualize the state of a two-level system is to represent it as a point with spherical coordinates θ and φ on a unit sphere, as shown in Figure 2.1. This unit sphere is known as the *Bloch sphere* and the vector $\vec{\lambda} = (\cos\varphi\sin\theta, \sin\varphi\sin\theta, \cos\theta)$ is called the *Bloch vector*. Hence, the quantum state

$|\psi\rangle$ from equation 2.1 can be rewritten in the *Bloch sphere representation* as:

$$|\psi\rangle = \cos\frac{\theta}{2}|\downarrow\rangle + e^{i\varphi}\sin\frac{\theta}{2}|\uparrow\rangle \quad . \tag{2.4}$$

Any operations on a two level system (single qubit), represented by the Bloch vector $\vec{\lambda}$, can be expressed as a rotation about a certain axis $\widehat{n}$, defined by an angle φ in the $x-y$ plane of the Bloch sphere, and a polar angle θ. Such operations are called *single-qubit operations*, or *single-qubit gates*. The corresponding rotation operator can be written in general form as:

$$\begin{aligned} R_{\widehat{n}}(\theta,\varphi) &\equiv \exp(-i\frac{Ht}{\hbar}) = \exp(-i\frac{\theta}{2}\widehat{n}\cdot\vec{\sigma}) \\ &= \cos(\frac{\theta}{2})I - i\sin(\frac{\theta}{2})(n_x\sigma_x + n_y\sigma_y + n_z\sigma_z) \quad , \end{aligned} \tag{2.5}$$

where $\vec{\sigma}$ is the three component vector $(\sigma_x, \sigma_y, \sigma_z)$ of Pauli matrices and I is identity matrix. For definitions see Appendix A. The axis of rotation $\widehat{n}$ in general form is:

$$\widehat{n} \equiv (n_x, n_y, n_z) = \sin\theta\cos\varphi\vec{i} + \sin\theta\sin\varphi\vec{j} + \cos\theta\vec{k} \quad , \tag{2.6}$$

where $\vec{i}$, $\vec{j}$ and $\vec{k}$ are the unit vectors that denote the direction. If an arbitrary single-qubit operation is available for each individual qubit, we require only one universal two-qubit gate in order to construct all arbitrary operations including other multi-qubit gates.

2.1.2 Multiple Qubit Operations

For a system of N qubits the number of computational basis increases as 2^N and the state can be represented by the tensor product of the 2^N states as:

$$|\psi\rangle = |\psi_1\rangle \otimes |\psi_2\rangle \otimes ... \otimes |\psi_N\rangle \quad . \tag{2.7}$$

To give an example, for an uncorrelated two-qubit system, $N = 2$, with $|\psi_1\rangle = \alpha_1|\downarrow\rangle + \beta_1|\uparrow\rangle$ and $|\psi_2\rangle = \alpha_2|\downarrow\rangle + \beta_2|\uparrow\rangle$ the quantum state can be described as

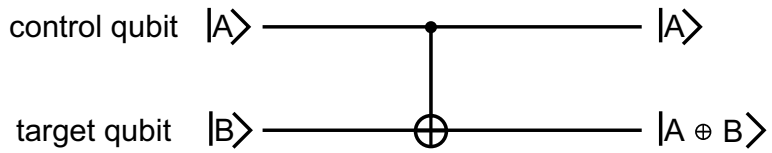

Figure 2.2: The circuit representation of the CNOT gate.

$$\begin{aligned} |\psi\rangle &= |\psi_1\rangle \otimes |\psi_2\rangle = |\psi_1\psi_2\rangle = \\ &= \alpha_1\alpha_2 |\downarrow\downarrow\rangle + \alpha_1\beta_2 |\downarrow\uparrow\rangle + \beta_1\alpha_2 |\uparrow\downarrow\rangle + \beta_1\beta_2 |\uparrow\uparrow\rangle \quad , \end{aligned} \tag{2.8}$$

where $|\alpha_1\alpha_2|^2 + |\alpha_1\beta_2|^2 + |\beta_1\alpha_2|^2 + |\beta_1\beta_2|^2 = 1$. As it is possible to see, there are four computational basis states for two qubits: $|\downarrow\downarrow\rangle$, $|\downarrow\uparrow\rangle$, $|\uparrow\downarrow\rangle$ and $|\uparrow\uparrow\rangle$.

With two qubits it is possible to perform the quantum controlled-NOT, or CNOT gate, a universal two-qubit gate. Controlled means that the state of one qubit is changed depending on the state of another qubit. The CNOT gate flips the state of Target qubit if and only if the Control qubit is in the excited state $|\uparrow\rangle$. The transformation of the two qubits C and T are as follows:

$$\begin{aligned} |\downarrow\rangle_C |\downarrow\rangle_T &\longrightarrow |\downarrow\rangle_C |\downarrow\rangle_T \\ |\downarrow\rangle_C |\uparrow\rangle_T &\longrightarrow |\downarrow\rangle_C |\uparrow\rangle_T \\ |\uparrow\rangle_C |\downarrow\rangle_T &\longrightarrow |\uparrow\rangle_C |\uparrow\rangle_T \\ |\uparrow\rangle_C |\uparrow\rangle_T &\longrightarrow |\uparrow\rangle_C |\downarrow\rangle_T \end{aligned}$$

$$|A, B\rangle \longrightarrow |A, A \oplus B\rangle \quad , \tag{2.9}$$

where $\oplus$ is addition mod 2 of basis states. The circuit representation of the CNOT is shown in Figure 2.2.

2.1.3 Entangled States

The states that cannot be written as a product of states are called *entangled* states. The simplest example of these kind of states are the Bell states, or EPR pair:

$$|\Phi^+\rangle \equiv |\beta_{\downarrow\downarrow}\rangle = \frac{|\downarrow\downarrow\rangle + |\uparrow\uparrow\rangle}{\sqrt{2}} \tag{2.10}$$

$$|\Phi^-\rangle \equiv |\beta_{\uparrow\downarrow}\rangle = \frac{|\downarrow\downarrow\rangle - |\uparrow\uparrow\rangle}{\sqrt{2}} \tag{2.11}$$

$$|\Psi^+\rangle \equiv |\beta_{\downarrow\uparrow}\rangle = \frac{|\downarrow\uparrow\rangle + |\uparrow\downarrow\rangle}{\sqrt{2}} \tag{2.12}$$

$$|\Psi^-\rangle \equiv |\beta_{\uparrow\uparrow}\rangle = \frac{|\downarrow\uparrow\rangle - |\uparrow\downarrow\rangle}{\sqrt{2}} \quad . \tag{2.13}$$

The $|\Phi^{\pm}\rangle$ wave-functions are for the case of perfect *positive correlation* and $|\Psi^{\pm}\rangle$ for the perfect *negative correlation*. Measuring the first qubit of the state $|\Phi^+\rangle$ results in two possible outcomes, $|\downarrow\rangle$ and $|\uparrow\rangle$, each with 1/2 probability and leaving the post measured state in $|\downarrow\downarrow\rangle$ or $|\uparrow\uparrow\rangle$, respectively. Measuring the second qubit results in the same output as the measurement of the first: $|\downarrow\rangle$ in case the first measured qubit is $|\downarrow\rangle$, and $|\uparrow\rangle$ in case the first measured qubit is $|\uparrow\rangle$. This is a positive correlation. In case of the $|\Psi^+\rangle$ state, for example, measuring the first qubit will also result in $|\downarrow\rangle$ or $|\uparrow\rangle$ in the half of the cases, but measuring the second qubit after the first will outcome in the opposite result — negative correlation.

The quantum gates, as a CNOT, have the property to produce entanglement out of a non-entangled state. It is possible to receive for example the Bell states in two steps: first, applying the Hadamard gate H_1 (experimentally equivalent to the application of a $\frac{\pi}{2}$-pulse), the superposition state for the first ion is created; then the CNOT operation is performed on the superposition state with the Bell states as final result:

$$|\downarrow\downarrow\rangle \xrightarrow{H_1} \frac{|\downarrow\downarrow\rangle + |\uparrow\downarrow\rangle}{\sqrt{2}} \xrightarrow{CNOT} \frac{|\downarrow\downarrow\rangle + |\uparrow\uparrow\rangle}{\sqrt{2}} \tag{2.14}$$

$$|\downarrow\uparrow\rangle \xrightarrow{H_1} \frac{|\downarrow\uparrow\rangle + |\uparrow\uparrow\rangle}{\sqrt{2}} \xrightarrow{CNOT} \frac{|\downarrow\uparrow\rangle + |\uparrow\downarrow\rangle}{\sqrt{2}} \tag{2.15}$$

$$|\uparrow\downarrow\rangle \xrightarrow{H_1} \frac{|\downarrow\downarrow\rangle - |\uparrow\downarrow\rangle}{\sqrt{2}} \xrightarrow{CNOT} \frac{|\downarrow\downarrow\rangle - |\uparrow\uparrow\rangle}{\sqrt{2}} \tag{2.16}$$

$$|\uparrow\uparrow\rangle \xrightarrow{H_1} \frac{|\downarrow\uparrow\rangle - |\uparrow\uparrow\rangle}{\sqrt{2}} \xrightarrow{CNOT} \frac{|\downarrow\uparrow\rangle + |\uparrow\downarrow\rangle}{\sqrt{2}} \quad . \tag{2.17}$$

2.1.4 Measurements

Projective measurements

Measurements are an important requirement for the quantum computer. The qubit state of the ions is detected by measuring resonance fluorescence from an additional state that is strongly coupled to one of the qubit states (excited qubit state $|\uparrow\rangle$ in our case) and decays back only to that same state. This is usually called *quantum non-demolition* (QND) detection since when the ion has been projected into a particular qubit state, it will remain in this stay throughout repeated excitation-emission cycles. Superpositions and the phase information encoded into a two level system, however, are destroyed by measuring fluorescence.

A quantum measurement is described by a set of operators M_m acting on the state of the system. The probability p of a measurement result m occurring when the state ψ is measured equals

$$p(m) = \langle\psi|M_m^\dagger M_m|\psi\rangle \tag{2.18}$$

and the state of the system after the measurement is

$$|\psi'\rangle = \frac{M_m|\psi\rangle}{\sqrt{p(m)}} \quad . \tag{2.19}$$

The sum over all measurement outcomes has to be unity (completeness condition):

$$1 = \sum_m p(m) = \sum_m \langle\psi|M_m^\dagger M_m|\psi\rangle \quad . \tag{2.20}$$

For example, for the projective measurement of a qubit in state $|\psi\rangle = \alpha\,|\downarrow\rangle + \beta\,|\uparrow\rangle$, computational basis of which is also a natural computation basis in our experiment, and with the measurement operators given by

$$|M_\downarrow\rangle = |\downarrow\rangle\langle\downarrow| = \begin{pmatrix} 1 & 0 \\ 0 & 0 \end{pmatrix} \tag{2.21}$$

$$|M_\uparrow\rangle = |\uparrow\rangle\langle\uparrow| = \begin{pmatrix} 0 & 0 \\ 0 & 1 \end{pmatrix} \quad , \tag{2.22}$$

the measurement probabilities are:

$$p(\downarrow) = \langle\psi|M_\downarrow^\dagger M_\downarrow|\psi\rangle = \alpha^*\alpha\langle\downarrow|\downarrow\rangle = \alpha^2 \quad (2.23)$$

$$p(\uparrow) = \langle\psi|M_\uparrow^\dagger M_\uparrow|\psi\rangle = \beta^*\beta\langle\uparrow|\uparrow\rangle = \beta^2 \quad . \quad (2.24)$$

and the states after the measurement are:

$$\frac{M_\downarrow|\psi\rangle}{\sqrt{p(\downarrow)}} = \frac{\alpha|\downarrow\rangle}{\sqrt{|\alpha|^2}} = \frac{\alpha}{|\alpha|}|\downarrow\rangle \quad (2.25)$$

$$\frac{M_\uparrow|\psi\rangle}{\sqrt{p(\uparrow)}} = \frac{\beta|\uparrow\rangle}{\sqrt{|\beta|^2}} = \frac{\beta}{|\beta|}|\uparrow\rangle \quad . \quad (2.26)$$

There is an infinite number of qubit states but a single measurement reveals only $|\downarrow\rangle$ or $|\uparrow\rangle$ with probabilities $|\alpha|^2$ or $|\beta|^2$. The measurement will collapse the state vector on the basis state. To determine α and β with perfect accuracy an infinite number of measurements has to be made.

Measurement in an entangled state

The Bell state basis is given by four Bell states, described in section 2.1.3. For example, if the qubits are in the entangled Bell state $|\psi\rangle = |\Phi^+\rangle$, the measurements of the first qubit result in the probability:

$$p_1(\downarrow) = \langle\psi|(M_\downarrow \otimes I)^\dagger(M_\downarrow \otimes I)|\psi\rangle = \frac{1}{\sqrt{2}}\langle\downarrow\downarrow|\frac{1}{\sqrt{2}}|\downarrow\downarrow\rangle = \frac{1}{2} \quad (2.27)$$

if the first ion was found in the $|\downarrow\rangle$ and the post measurement state is:

$$|\psi'\rangle = \frac{(M_\downarrow \otimes I)|\psi\rangle}{\sqrt{p_1(\downarrow)}} = \frac{\frac{1}{\sqrt{2}}|\downarrow\downarrow\rangle}{\frac{1}{\sqrt{2}}} = |\downarrow\downarrow\rangle \quad . \quad (2.28)$$

The measurement on the second qubit will then result with certainty in the same

result:

$$p_2(\downarrow) = \langle\psi'|(I \otimes M_\downarrow)^\dagger (I \otimes M_\downarrow)|\psi'\rangle = 1 \quad . \tag{2.29}$$

The two measurement results are *correlated* as it was highlighted also in section 2.1.3.

2.2 MAGIC Scheme

For the coupling between the internal states and the common vibrational mode (COM), the absorption of the light photon is accompanied by the impulse transfer, when the optical laser light is used for a qubit manipulation. This impulse transfer can be described by the Lamb-Dicke parameter η, the square root of the ratio between the change in kinetic energy of the ion due to the absorption or emission of a photon and harmonic oscillator energy for an angular trap frequency ν_z:

$$\eta = \sqrt{\frac{(\hbar k)^2}{2m}/(\hbar\nu_z)} = k\Delta z \quad , \tag{2.30}$$

where k is the wavevector of the light field and $\Delta z = \sqrt{\frac{\hbar}{2m\nu_z}}$ is the spread of the ground-state wave-function of a quantum harmonic oscillator with oscillation frequency ν_z and the mass of the ion m. This momentum transfer for microwave radiation, used for qubit manipulations on the hyperfine split levels, is three to four orders of magnitude smaller than for optical radiation. This make the coupling of the internal and motional states quite small. Besides, it is difficult to focus the microwave on an individual ion, since the wavelengths are in the order of cm and the distances between the ions are in μm region. These problems are resolved by adding a magnetic field gradient along the axis of the linear ion trap that on one hand makes the ion addressable in the frequency space and, on the other hand, induces the coupling between the internal and external dynamics of the ions, a so called MAgnetic Gradient Induced Coupling (MAGIC). More detailed explanations are presented below.

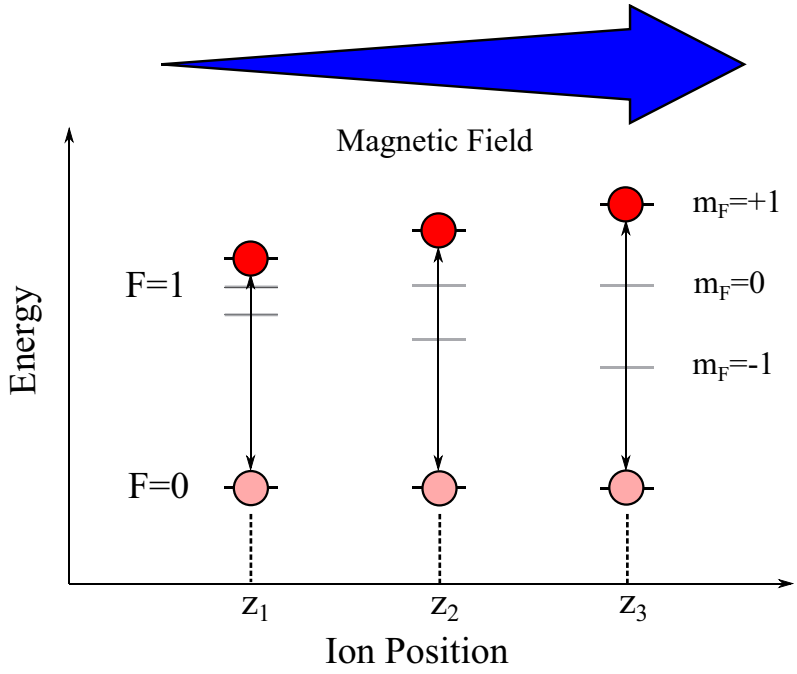

Figure 2.3: Schematic representation of the ions addressing in an inhomogeneous magnetic field, shown as a big arrow. The resonance frequencies along the linear trap axis are dependent on the position of the ion, designated by z_i, with $i = 1, 2, 3$ in the image to show three different ions.

2.2.1 Addressing of the Ions

The atom used in the experiments presented in this thesis is Ytterbium isotope $^{171}Yb^+$. The nuclear magnetic moment of this isotope is non zero at $I = 1/2$. This leads to the hyperfine structure in the atom.

The total inhomogeneous magnetic field along the linear trap axis in z-direction can be described as

$$\vec{B}(z) = \vec{B}_0 + b\hat{z}, \tag{2.31}$$

with the offset field $\vec{B}_0$, created by the Helmholtz coils, and the magnetic field gradient b, created by Samarium Cobalt (SmCo) permanent magnets in this experiment. This magnetic field lifts the degeneracy of the $^2S_{1/2}$ (F=1) ground state in $^{171}Yb^+$ ion. Due to the linear Zeeman effect, which is a valid approximation for field strength of a few Gauss typical for the experiments presented in this work, the

sublevels of the Zeeman manifold are shifted by an amount of $\Delta E = g_F \Delta m_F \mu_B B$, where m_F is the magnetic quantum number, Δm_F is the magnetic quantum number difference, g_F is the Landé factor, μ_B is the Bohr magneton and B is the magnitude of the inhomogeneous magnetic field. The frequency difference between the Zeeman split levels can be written as:

$$\omega(z) = \frac{\Delta E(z)}{\hbar} = \frac{g_F \mu_B \Delta m_F |B(z)|}{\hbar} \quad , \tag{2.32}$$

where $\hbar$ is the reduced Planck's constant. Substituting the magnetic field $|B(z)|$ from equation (2.31), the resonance frequencies of the ions are:

$$\omega(z) = \omega_0 + \frac{g_F \mu_B \Delta m_F |B_0|}{\hbar} + \frac{g_F \mu_B \Delta m_F |b|}{\hbar} \cdot z \quad . \tag{2.33}$$

Here, $\omega_0 = \frac{E_0}{\hbar}$ is the transition frequency without the external magnetic field and $\Delta m_F = 0, \pm 1$ is the magnetic quantum number difference. As it is possible to see from equation (2.33), due to the magnetic field gradient b the resonance frequency $\omega_i(z)$, where i is the ion's number, of the $|\downarrow\rangle_i \longleftrightarrow |\uparrow\rangle_i$ transition becomes dependent on the position of the ion. Here, $|\downarrow\rangle \equiv {}^2S_{1/2}$ (F=0) and $|\uparrow\rangle \equiv {}^2S_{1/2}$ (F=1), defining the qubit of ion i. The frequency separation of the resonances of two neighboring ions is given then by:

$$\Delta\omega(z_i, z_j) = \frac{g_F \mu_B \Delta m_F |b|}{\hbar} \delta z \quad , \tag{2.34}$$

where z_i and z_j are the positions of ion i and ion j and $\delta z = z_i - z_j$ is the ion separation. The schematic representation of the addressing is presented in Figure 2.3. Here the second order Zeeman shift is neglected since it is far smaller than the linear shift. The second order frequency shift lies in the range of $5 - 15\,\mathrm{kHz}$ (see Figure B.1 in Appendix B) for the magnetic fields used in our experiment of about $500 - 700\,\mu\mathrm{T}$. The fluctuations of the resonance frequencies due to the magnetic noise lie in the same range and the precision of the resonance frequency measurement is about 10 kHz. With the same external magnetic fields the linear effect term shifts the frequencies in the range of $15 - 20\,\mathrm{MHz}$, that is almost three orders of magnitude bigger.

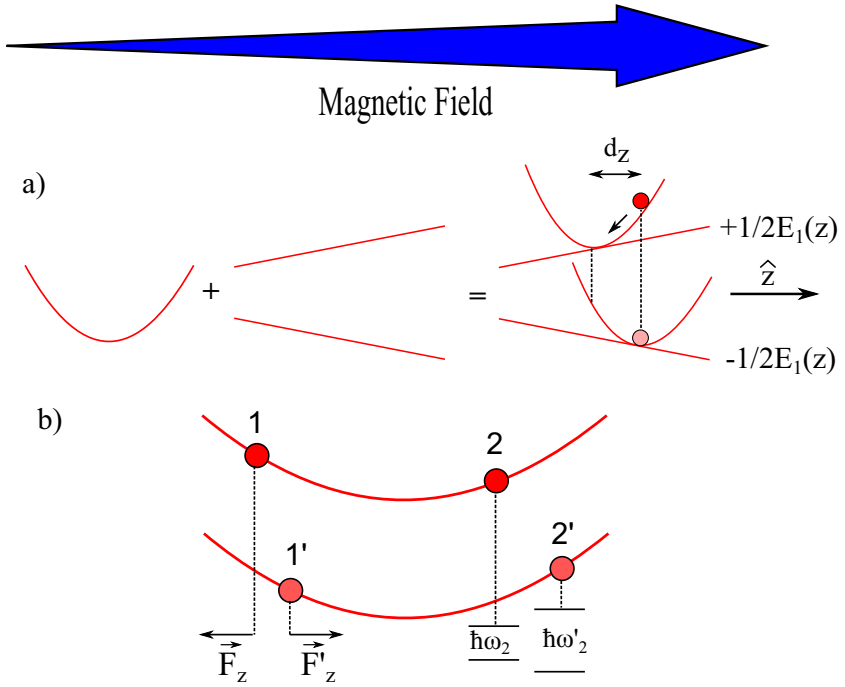

Figure 2.4: a) The superposition of the harmonic axial trapping potential and inhomogeneous Zeeman energies, giving rise to an ion's equilibrium position depending on the internal spin state. b) Schematic of the spin-spin coupling between two ions mediated by Coulomb repulsion. When the state of ion 1 is changed, the state dependent force acting on it will change sign, and thus its equilibrium position will change from 1 to 1 '. Through the Coulomb repulsion the second ion 2 will change its equilibrium position as well, from 2 to 2'. Since it moves in the magnetic field gradient, its internal energy will change from $\hbar\omega_2$ to $\hbar\omega_2'$.

2.2.2 Coupling between Internal and Motional States

The superposition of the axial harmonic trapping potential and the inhomogeneous Zeeman split levels give rise to an ion's equilibrium position depending on the internal spin state. The schematics that demonstrates the effect of this superposition is presented in Figure 2.4, a).

A magnetic moment in an external magnetic field has a potential energy U:

$$U = -\vec{\mu} \cdot \vec{B} \quad . \tag{2.35}$$

If the external field is inhomogeneous, there exists a force proportional to the

magnetic field gradient and acting on the magnetic momentum itself:

$$\vec{F} = \langle(\vec{\mu} \cdot \vec{\nabla})\vec{B}\rangle \quad . \tag{2.36}$$

Substituting the inhomogeneous magnetic field, described by equation (2.31), into equation (2.36) the absolute value of force acting on the dipole momentum in axial z-direction can be written as [Johanning *et al.*, 2009b]:

$$F_z = \gamma\frac{\hbar}{2}b\langle\sigma_z\rangle = \frac{\hbar}{2}\partial_z\omega\langle\sigma_z\rangle \quad , \tag{2.37}$$

with $\mu = \gamma\frac{\hbar}{2}\langle\sigma_z\rangle$, where γ is a gyromagnetic ratio and $\partial_z\omega$ is the resonance frequency separation given by equation (2.34). For an ion of mass m, trapped by the harmonic potential with angular frequency ν_z, the force described by equation (2.37) shifts the equilibrium position of the ion when its internal energy is changed. The amount of this shift equals to $d_z = \mp F_z/(m\nu_z^2)$ by analogy with the Hooke's law. As it is possible to see in Figure 2.4 a), when changing the internal state, the ion will oscillate around its new equilibrium position as if it had received a momentum kick, even if the microwave radiation causing the internal state change does not have enough momentum to excite the ion's motion. The coupling, therefore, is described by an effective Lamb-Dicke parameter

$$\eta_{\mathrm{eff}} \approx \kappa = \frac{\mathrm{d_z}}{\Delta\mathrm{z}} = \frac{\Delta\mathrm{z}\partial_\mathrm{z}\omega}{\nu_\mathrm{z}} \quad , \tag{2.38}$$

where Δz is the spatial extension of the ion's wave-function.

The change of the internal energy of the ion due to the shift of its equilibrium position can be written as:

$$\hbar J = -F_z d_z = -F_z^2/(m\nu_z^2) \propto (b/\nu_z)^2 \quad , \tag{2.39}$$

where J is the coupling constant. When one ion changes its equilibrium position, the position and the internal energy of the neighboring ion is also changed. This happens through Coulomb interaction and in this way an *indirect spin-spin coupling* (J-coupling) arises.

The ion trapped in a linear Paul trap with magnetic field gradient and interacting

with electro-magnetic field is described by the Hamiltonian [Nielsen & Chuang, 2000; Wineland *et al.*, 1998b; Wunderlich, 2002]:

$$\begin{aligned} H &= H_0 + H_{osc} + H_I && (2.40)\\ &= \frac{\hbar}{2}\omega(z)\sigma_z + \hbar\nu_z a^+ a + H_I \quad , && (2.41) \end{aligned}$$

where

$$H_I = \frac{\hbar}{2}\Omega(\sigma^+ + \sigma^-)(e^{i(kz - w_{mw}t + \varphi)} + e^{-i(kz - w_{mw}t + \varphi)}) \quad . \tag{2.42}$$

The part H_0 of the total Hamiltonian describes the internal state of the ion with the transition frequency ω. The second part is the quantum harmonic oscillator Hamiltonian written through the corresponding harmonic raising and lowering operators a^+ and a and the oscillation frequency ν_z: $H_{osc} = \frac{P^2}{2m} + \frac{1}{2}m\nu_z^2 X$, where $P = i\sqrt{\frac{m\hbar\nu_z}{2}}(a^+ - a)$ is the momentum operator and $X = \sqrt{\frac{\hbar}{2m\nu_z}}(a^+ + a)$ is the position operator of particle with mass m in the harmonic potential. The third part H_I describes the interaction of the ion with the electro-magnetic field of frequency w_{mw}, the wave-vector k and the phase φ, $\sigma^+ = (\sigma_x + i\sigma_y)/2$ and $\sigma^- = (\sigma_x - i\sigma_y)/2$ are raising and lowering operators of the ion's internal state, σ_x, σ_y and σ_z are the three standard Pauli matrices (for the definition see Appendix A). The Rabi frequency

$$\Omega = \frac{\vec{\mu}\cdot\vec{B}_{mw}}{\hbar} \quad , \tag{2.43}$$

where $\vec{\mu}$ is the magnetic dipole momentum and $\vec{B}_{mw}$ is the microwave magnetic field, is the measure of how strongly the internal state of the ion is coupled to the electro-magnetic radiation. In the case of the hyperfine splitting of $^{171}Yb^+$, used in the current experiment as a qubit, the Rabi frequency can be also given as:

$$\Omega = \frac{1}{\hbar}\langle S_{1/2}, F = 0, m_F|(\vec{\mu}\cdot\vec{B}_{mw})|S_{1/2}, F' = 1, m'_F\rangle \quad . \tag{2.44}$$

The position of the ion in the harmonic trapping potential can be defined as

$$z = \Delta z(a^+ + a) \quad , \tag{2.45}$$

where $\Delta z = \sqrt{\frac{\hbar}{2m\nu_z}}$ is the spread of the ground-state wave-function of a quantum harmonic oscillator with oscillation frequency ν_z and the mass of the ion m. Substituting the ion's position z in equation 2.42 with the one given in equation 2.45, performing the transformation into the interaction picture, defined by $U = e^{iH_0 t/\hbar}$, and using the rotating-wave approximation, the interaction Hamiltonian $\tilde{\mathrm{H}}_I = U^\dagger H_I U$ takes the form:

$$\widetilde{H}_I = \frac{1}{2}\hbar\Omega\left[\sigma^+ e^{i\eta(a(t)+a^+(t))}e^{-i(\Delta t-\varphi)} + \sigma^- e^{-i\eta(a(t)+a^+(t))}e^{i(\Delta t-\varphi)}\right] \quad , \tag{2.46}$$

where the Lamb-Dicke parameter (LDP) η, described by equation 2.30, shows how strongly the internal states of the ion are coupled to the COM mode of the ion string. Other notations in equation 2.46 are $a^+(t) = a^+ e^{i\nu_z t}$, $a(t) = ae^{-i\nu_z t}$ and $\Delta = \omega(z) - \omega_{mw}$.

The resulting Hamiltonian for the interaction of the ion with the microwave radiation in the magnetic field gradient is the same as in equation 2.46 with the standard LDP exchanged by an effective one [Mintert & Wunderlich, 2001; Wunderlich & Balzer, 2003]:

$$\widetilde{H}_I = \frac{1}{2}\hbar\Omega\left[\sigma^+ e^{i\eta_{eff}(a(t)+a^+(t))}e^{-i(\Delta t-\varphi)} + \sigma^- e^{-i\eta_{eff}(a(t)+a^+(t))}e^{i(\Delta t-\varphi)}\right] \quad . \tag{2.47}$$

When the coupling of equation 2.47 fulfills the resonance condition for a sideband, the system evolves between two quantum states $|n\rangle|\downarrow\rangle$ and $|n'\rangle|\uparrow\rangle$ with Rabi frequency [Wineland *et al.*, 1998b]

$$\begin{aligned}
\Omega_{n',n} &\equiv \frac{1}{\hbar}|\langle n'|\langle\uparrow|H_I|\downarrow\rangle|n\rangle| && (2.48)\\
&= \Omega|\langle n'|e^{\eta_{eff}(a(t)+a^+(t))}|n\rangle| && (2.49)\\
&= \Omega\eta_{eff}^{|n'-n|}e^{-\eta_{eff}^2/2}\sqrt{\frac{n_<!}{n_>!}}L_{n_<}^{|n'-n|}(\eta_{eff}^2) \quad , && (2.50)
\end{aligned}$$

where $n_<$ ($n_>$) is the greater (lesser) of n and n' and $L_n^\alpha(x)$ is a generalized Laguerre polynomial

$$L_n^\alpha(x) = \sum_{k=0}^{n}(-1)^k \left(\begin{array}{c} n+\alpha \\ n-k \end{array} \right) \frac{x^k}{k!} \quad , \tag{2.51}$$

where

$$\begin{aligned} L_0^\alpha(x) &= 1, L_1^\alpha(x) = \alpha + 1 - x & (2.52) \\ L_{n+1}^\alpha(x) &= \frac{1}{n+1}((2n+1+\alpha-x)L_n^\alpha - (n+\alpha)L_{n-1}^\alpha) & (2.53) \end{aligned}$$

Equation 2.53 is for n > 1.

In the *Lamb-Dicke regime* defined by the condition $\eta\sqrt{n} \ll 1$ [Wineland *et al.*, 1998b], when the ions's motion is confined to a region smaller than the wavelength of the radiation under consideration [Stenholm, 1986], the factor $e^{i\eta_{eff}(a(t)+a^+(t))}$ in equation 2.47 can be Taylor expanded as

$$e^{i\eta_{eff}(a(t)+a^+(t))} \approx 1 + i\eta_{eff}(a(t) + a^+(t)) + \mathcal{O}(\eta_{eff}^2) \quad . \tag{2.54}$$

Therefore, three distinct processes can be observed. When the resonance conditions are fulfilled and $\Delta = 0$ ($\omega(z) = \omega_{mw}$), the interaction Hamiltonian in equation 2.47 reduces to:

$$\begin{aligned} \widetilde{H}_I^C &= \frac{1}{2}\hbar\Omega_{n,n}\left[\sigma^+ e^{i\varphi} + \sigma^- e^{-i\varphi}\right] \\ &= \frac{1}{2}\hbar\Omega_{n,n}\left(\sigma_x \cos\varphi - \sigma_y \sin\varphi\right) & (2.55) \end{aligned}$$

and corresponds to excitation on the *carrier* qubit transition. The coupling strength on the *carrier* is well approximated by

$$\Omega_{n,n} = (1 - \eta_{eff}^2 n)\Omega \quad , \tag{2.56}$$

where Ω is the overall coupling strength.

If $\Delta = \nu_z$, the phonon number decreases by one for absorption and equation 2.47 can be approximated by a Hamiltonian of the Jaynes-Cummings type as:

$$\widetilde{H}_I^{JC} = \frac{1}{2}\hbar\Omega_{n-1,n}\eta_{eff}\left[\sigma^+ a e^{i\varphi} + \sigma^- a^+ e^{-i\varphi}\right] \quad , \tag{2.57}$$

where the coupling strength on the red sideband is:

$$\Omega_{n-1,n} = \eta_{eff}\sqrt{n}\Omega \quad . \tag{2.58}$$

If $\Delta = -\nu_z$, the phonon number increases by one for absorption and the corresponding interaction Hamiltonian 2.47 can be approximated by the *anti*-Jaynes-Cummings Hamiltonian:

$$\widetilde{H}_I^{AJC} = \frac{1}{2}\hbar\Omega_{n+1,n}\eta_{eff}\left[\sigma^+ a^+ e^{i\varphi} + \sigma^- a e^{-i\varphi}\right] \quad , \tag{2.59}$$

where the coupling strength on the blue sideband is:

$$\Omega_{n+1,n} = \eta_{eff}\sqrt{n+1}\Omega \quad . \tag{2.60}$$

In the current experiment the manipulations of the single qubit were performed on the ion's *carrier* transition. It is possible to prepare the qubit in any state by allowing it to interact with a field of particular direction and strength for a certain time t, i.e. by applying a pulse of duration t to a certain ion i. The action of such a *carrier* pulse is described by unitary operator, according to equation 2.5, as:

$$\begin{aligned} R_{\theta,\phi}^{(j)} &= \exp(-i\frac{\widetilde{H}_I^C t}{\hbar}) \\ &= \cos\left(\frac{\theta}{2}\right) I + i\sin\left(\frac{\theta}{2}\right)\left(\sigma_x^{(i)}\cos\varphi - \sigma_y^{(i)}\sin\varphi\right) \quad , \end{aligned} \tag{2.61}$$

where j is the number of the ion, $\widetilde{H}_I^C$ is the interaction Hamiltonian on the *carrier* transition (see equation 2.55) and $\theta = \Omega_{n,n}t$ is the rotation angle about rotation axis defined in the x-y plane by φ. In case of π-*pulse*, $\theta = \pi$ and the qubit state evolves through half a Rabi oscillation period. In case of $\pi/2$-*pulse*, $\theta = \pi/2$ and

the qubit state evolves through the quarter of a Rabi oscillation period. If the qubit is in its initial state $|\downarrow\rangle$ and we would like to prepare it in $|\uparrow\rangle$ state, the rotation around x-axis (y-axis) by $\theta = \pi$ will prepare the state in the $|\uparrow\rangle$ ($-i\,|\uparrow\rangle$). If the state is needed to be prepared in the superposition state, the spin rotation around x-axis (y-axis) by a $\theta = \frac{\pi}{2}$ angle is performed. Therefore, $\frac{|\downarrow\rangle+i|\uparrow\rangle}{\sqrt{2}}$ ($\frac{|\downarrow\rangle+|\uparrow\rangle}{\sqrt{2}}$) state is obtained. This is the same as to act on the $|\downarrow\rangle$ ($|\uparrow\rangle$) state with the Hadamard gate

$$H = \frac{1}{\sqrt{2}} \begin{pmatrix} 1 & 1 \\ 1 & -1 \end{pmatrix} \quad . \tag{2.62}$$

So far the Hamiltonian for a single trapped ion has been considered. For a string of N ions in a magnetic field gradient the Hamiltonian is [Wunderlich, 2002; Wunderlich & Balzer, 2003]:

$$\widetilde{H} = -\frac{\hbar}{2}\sum_{i=1}^{N}\omega_i(z_i)\sigma_z^{(i)} + \hbar\sum_{i=1}^{N}\nu_i a_i^{+}a_i - \frac{\hbar}{2}\sum_{i<j}^{N}J_{i,j}\sigma_z^{(i)}\sigma_z^{(j)} \quad , \tag{2.63}$$

where N is the number of ions in the chain and

$$J_{i,j} = \sum_{n=1}^{N}\nu_n\kappa_{ni}\kappa_{nj} \tag{2.64}$$

is the generalized expression for the spin-spin coupling constants between different ions i and j. The sum in equation 2.64 extends over all vibrational modes with angular frequency ν_n, and the coupling strength κ (see equation 2.38) for many ions takes the generalized form

$$\kappa_{nl} \equiv \frac{d_z^{nl}}{\Delta z_n}S_{nl} = \frac{\Delta z_n \partial_z \omega_l}{\nu_n}S_{nl} \quad , \tag{2.65}$$

indicating how strongly an ion l couples to the vibrational mode n, when the spin of the ion l is flipped. Here, $\Delta z_n = \sqrt{\frac{\hbar}{2m\nu_n}}$ is the spread of the ground-state wave-function of a quantum harmonic oscillator with oscillation frequency ν_n and the mass of the ion m. The dimensionless matrix elements S_{nl} gives the scaled deviation of ion l from its equilibrium position when a vibrational mode n is excited. The values of the matrix S_{nl} can be found in literature [James, 1998] and the values for two and three ions are given in Appendix L.

Considering that $\nu_n \propto \nu_z$, where ν_z is the frequency of the COM mode, for two ions we have

$$J_{12} = \frac{1}{3}\frac{g_F^2 \mu_B^2 b^2}{2m\hbar\nu_z^2} \tag{2.66}$$

$$= 1.21 \times 10^{10} \times (b/f_z)^2 Hz \quad , \tag{2.67}$$

where b is in T/m and $f_z = \nu_z/(2\pi)$ is in Hz.

3

Construction of the Experimental Setup

In this chapter a new experimental setup to implement the MAGIC-scheme is described. The ions are trapped in a linear Paul trap. The theory and operational characteristics of the trap are discussed in section 3.1 and the trap drive used to create the rf potential in the trap is in section 3.2. There are four different wavelengths that are used in the experiment and the corresponding laser system is explained in section 3.3. The laser wavelengths are measured by a Michelson-type lambda-meter that uses the transition of the ^{87}Rb as a reference. The details are explained in section 3.5. The vacuum chamber organization is presented in section 3.4. Furthermore, the static magnetic field, microwave and detection setups are discussed in sections 3.6, 3.8 and 3.10, respectively. How the magnetic field gradient was created is explained in section 3.9. Additionally, the polarizations of the laser beams, as it is used in the current experiment, is explained in section 3.7.

3.1 Linear Ion Trap

In order to trap charged particles it is needed to create a stable potential minimum in space. This is not possible using static electric fields alone, based on the Earnshaw's theorem, since there are no local minima or maxima of the field

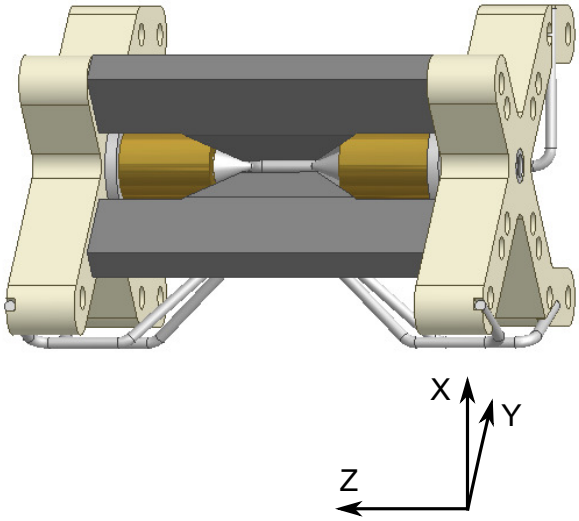

Figure 3.1: Linear Paul trap used in the current experiment. The original design is created by [Gulde, 2000]. Two permanent magnets on the end-cap electrodes are used to create the magnetic field gradient (section 3.9).

potential in free space, only saddle points. The Maxwell equation $\nabla E = 0$ for free space as well demonstrates that the electric field is divergence free. For a minimum potential all the electric field lines should point toward the equilibrium point (negative divergence). In case the divergence is zero, when the electric field in some direction points toward the equilibrium position, thus confining the particle into that position, it must point from the equilibrium position in some other direction. It is still possible to confine charged particles with electromagnetic fields by using either a combination of electric and magnetic fields (Penning trap) or dynamic electric fields (RF or Paul trap).

3.1.1 Theory

In our experiment the ions are confined in a linear Paul trap, as demonstrated in Figure 3.1, that is essentially a quadrupole mass filter [Ghosh, 1995; Paul, 1990], that as its name implies, has four electrodes. Two opposite electrodes of the trap are driven with an RF potential $U_0 - V_0 \cos(\Omega_{RF} t)$, while the other two electrodes are grounded. Near the axis of the trap, the potential in x and y direction due to

the RF electrodes is:

$$\phi(x,y) \equiv V(x,y,t) \approx \frac{U_0 - V_0 \cos(\Omega_{RF} t)}{2}(1 + \frac{x^2 - y^2}{R^2}) \quad , \tag{3.1}$$

where U_0 is a DC voltage (zero in our case), V_0 is an RF potential peak amplitude, Ω_{RF} is its driving frequency, R is the distance between the trap axis and the nearest electrode surface and x and y are the transverse coordinates. In order to trap the ions, we need an inhomogeneous field, like the quadrupole field, since only then the force that acts on the ions will not cancel out in the time average. The last term in equation 3.1 describes a hyperbola, the shape of the quadrupole equipotential surfaces.

The classical equations of motion for an ion of mass m and charge Q in the potential ϕ are

$$F = m\ddot{r} = QE(r,t) = -Q\nabla\phi \quad , \tag{3.2}$$

where r comprises both x and y coordinates (radial direction) and E(r,t) is the RF electric field that proportional to the gradient of the potential between the electrodes ϕ. These equations can be written in the following form:

$$\ddot{x} + \frac{Q}{mR^2}(U_0 - V_0 \cos(\Omega_{RF} t))x = 0 \tag{3.3}$$

$$\ddot{y} - \frac{Q}{mR^2}(U_0 - V_0 \cos(\Omega_{RF} t))y = 0 \tag{3.4}$$

$$\ddot{z} = 0. \tag{3.5}$$

Making the substitutions

$$a = \frac{4QU_0}{mR^2\Omega_{RF}^2} \tag{3.6}$$

$$q = \frac{2QV_0}{mR^2\Omega_{RF}^2} \tag{3.7}$$

$$\tau = \frac{\Omega_{RF} t}{2} \tag{3.8}$$

the Mathieu equations for the motion of the ions are:

$$\frac{d^2x}{d\tau^2} + (a - 2q\cos(2\tau))x = 0 \tag{3.9}$$

$$\frac{d^2y}{d\tau^2} - (a - 2q\cos(2\tau))y = 0 \tag{3.10}$$

$$\frac{d^2z}{d\tau^2} = 0. \tag{3.11}$$

These Mathieu equations have stable solutions for which the particle trajectory remains bounded (trapped). They depend only on the parameters a and q and for a=0, $U_0 = 0$, one has stability from $0 < q < 0.908$. In this parameter range the ions are trapped in radial (x and y) direction and move free along axial z direction. For the example of the stability diagram and for more detailed explanation see [Ghosh, 1995; Paul, 1990].

As it is possible to see from the analysis of the Mathieu equations in [Ghosh, 1995], particle motion x_{tot} can be separated into a large-amplitude slow **secular** motion X and a small-amplitude high-frequency **micromotion** δ in the way that $x_{tot} = X + \delta$. The secular motion occurs on a timescale longer than the period of the RF signal and it describes the motion of a particle trapped in a harmonic oscillator (pseudopotential) with trap frequencies ω_x, ω_y and ω_z. The micromotion is superimposed on this oscillation and it occurs on the same frequency as the RF drive signal Ω_{RF} and its amplitude is proportional to the instantaneous displacement of the particle from the RF null in the trap. For a,q $\ll 1$ the solution of the Mathieu equations for the motion in radial direction can be approximated by

$$x_{tot} \approx \cos(\omega_{x,y}t)\left[1 - \frac{q}{2}\cos(\Omega_{RF}t)\right] \tag{3.12}$$

with the frequency of the secular radial motion equal to

$$\omega_x = \frac{\Omega_{RF}}{2}\sqrt{\frac{q^2}{2} + a} \tag{3.13}$$

$$\omega_y = \frac{\Omega_{RF}}{2}\sqrt{\frac{q^2}{2} - a} \tag{3.14}$$

and for a=0

$$\omega_r = \omega_x = \omega_y = \frac{QV_0}{\sqrt{2}mR^2\Omega_{RF}} = \frac{q\Omega_{RF}}{2\sqrt{2}} \quad . \tag{3.15}$$

In order to stabilize the trap in the z-direction DC voltages are applied to the so called end-cap electrodes of the trap. Near the center of the trap an ion will experience a static saddle-point potential as from:

$$\phi_{end}(x,y,z) = \frac{4\alpha U_{cap}}{L^2}\left[z^2 - \frac{1}{2}(x^2+y^2)\right] \quad . \tag{3.16}$$

where U_{cap} is a DC voltage on the end-cap electrodes, L is the distance between the end-cap electrodes and $\alpha(<1)$ is a geometrical factor that depends on the trap geometry. From the equation of motion for a harmonic oscillator

$$\ddot{z} = \frac{8Q\alpha U_{cap}}{mL^2}z \tag{3.17}$$

and the axial frequency is

$$\omega_z = \sqrt{\frac{8Q\alpha U_{cap}}{mL^2}} \quad . \tag{3.18}$$

The new equations of motion near the trap center are given by

$$\frac{d^2x}{d\tau^2} + (a + a_z - 2q\cos(2\tau))x = 0 \tag{3.19}$$

$$\frac{d^2y}{d\tau^2} - (a - a_z - 2q\cos(2\tau))y = 0 \tag{3.20}$$

$$\frac{d^2z}{d\tau^2} + 2a_z z = 0 \tag{3.21}$$

where

$$a_z = \frac{16Q\alpha U_{cap}}{m\Omega_{RF}^2 L^2} = 2\frac{\omega_z^2}{\Omega_{RF}^2} \quad . \tag{3.22}$$

As equation 3.16 indicates, the radial potential $\phi(x,y)$ (equation 3.1) is weakened by the addition of static axial potential. Thus, the *effective* angular oscillation frequency is [Raizen *et al.*, 1992]

$$\omega_r' = \frac{\Omega_{RF}}{2}\sqrt{\frac{q^2}{2} - a_z} = \sqrt{\omega_r^2 - \frac{\omega_z^2}{2}} \quad . \tag{3.23}$$

Another important parameter that characterizes the trap and should be mentioned here is the depth of the pseudo-potential created by the ion trap. Coming back to the assumption, highlighted above, that the motion of the ion in the trap can be replaced by the sum of the secular motion and the micromotion $x_{tot} = X + \delta$ and with two additional assumption $\delta \ll X$ and $d\delta/dt \gg dX/dt$ [Ghosh, 1995], the final equation of motion averaged over a period of RF drive is:

$$\frac{d^2X}{dt^2} = -\frac{Q^2V_0^2}{2m^2R^4\Omega_{RF}^2}X \quad . \tag{3.24}$$

This equation can be rewritten as

$$m\frac{d^2X}{dt^2} = -Q\frac{d\psi_x}{dX} \tag{3.25}$$

where $\frac{d\psi_x}{dX} = \frac{QV_0^2}{2mR^4\Omega_{RF}^2}X$ is the electric field in x direction generated by a parabolic pseudo-potential ψ_x. Therefore,

$$\psi_x = \frac{QV_0^2}{4mR^4\Omega_{RF}^2}X^2 = \frac{m}{2Q}\omega_x^2X^2. \tag{3.26}$$

For $U_0 = 0$, where $\omega_r = \omega_x = \omega_y$ (see equation 3.15), the ion's motion in the x-y-plane of the trap can be approximated by a harmonic pseudo-potential of the form

$$\psi_r = \frac{m}{2Q}\left(\omega_x^2X^2 + \omega_y^2Y^2\right) = \frac{m}{2Q}\omega_r^2\left(X^2 + Y^2\right) \quad . \tag{3.27}$$

Integrating in the range of $\{0, R\}$ yields an expression for the potential depth in

the two directions

$$\psi_x = \psi_y = \frac{QV_0^2}{4mR^2\Omega_{RF}^2} = \frac{qV_0}{8} \tag{3.28}$$

and following equation 3.27

$$\psi_r = \frac{QV_0^2}{2mR^2\Omega_{RF}^2} = \frac{qV_0}{4} \quad . \tag{3.29}$$

In a similar way and considering equation 3.17 the potential depth in z-direction equals

$$\psi_z = \frac{m}{2Q}\omega_z^2 Z^2 \tag{3.30}$$

and integrating in the range of $\{0, L/2\}$ yields

$$\psi_z = \frac{m}{2Q}\omega_z^2 z_0^2 = \alpha U_{cap} \quad , \tag{3.31}$$

where $2z_0 = L$. This expression is for an ideal case when the static potential on both end-cap electrodes is equal.

Remembering that the radial frequency is reduced when the end-cap electrodes are connected to the DC voltage, an effective potential depth in radial direction results in

$$\psi_r' = \frac{m}{2Q}\omega_r' \left(X^2 + Y^2\right) = \psi_r - 4\alpha U_{cap}\frac{R^2}{L^2} \quad . \tag{3.32}$$

3.1.2 Experimental Trap Parameters

The trap frequencies were measured using the method of parametric heating. An additional sinusoidal signal was connected to one of the end-cap electrodes after the low-pass filter. Its frequency is in the range of the expected trap frequencies and the amplitude equals few mV, about $5 - 15\,\mathrm{mV}$, for axial trap frequencies

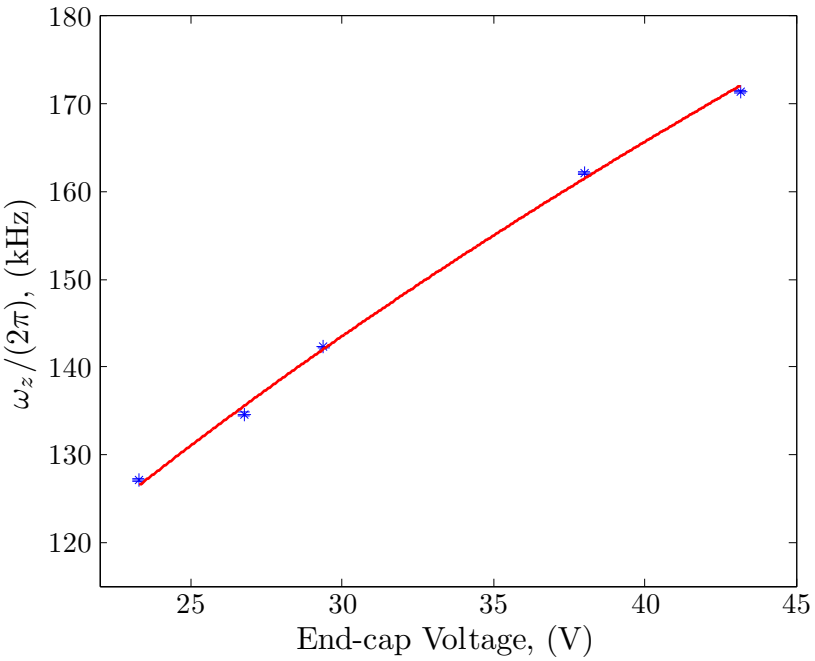

Figure 3.2: Measurement of ω_z vs. U_{cap}. The solid line is a fit to the data points yielding $\frac{\omega_z}{2\pi} = \sqrt{const \cdot \alpha \cdot U_{cap}}$, where $const = \frac{8Q}{mL^2}$. From the fit follows that the geometrical factor for the trap is $\alpha = 0.15$.

measurements and about $100 - 300\,\mathrm{mV}$ for radial trap frequencies measurements [1]. After the chain of ions was trapped, the frequency was scanned with a step of $0.1\,\mathrm{kHz}$ until the crystal of the ions melted. The frequency at which the crystal melts is the trap frequency.

The axial trap frequencies were measured for different end-cap voltages and the result is plotted in Figure 3.2. The geometrical factor α results from the fit and equals 0.15.

Typical operating parameters for our trap are a driving frequency $\Omega_{RF} = 2\pi \cdot 18.8\,\mathrm{MHz}$ and $R = 0.8\,\mathrm{mm}$. The radial trapping frequencies were measured for different RF source powers and the result is presented in Figure 3.3 (a). The measurements were performed at the axial trap frequency $\omega_z = 2\pi \cdot 53\,\mathrm{kHz}$ and the power was changed in the range of $5 - 25\,\mathrm{W}$.

The stability parameter q depends on both ω_r and ω_z secular trap frequencies as

[1] Depending on the mass of the ion chain different voltages are required.

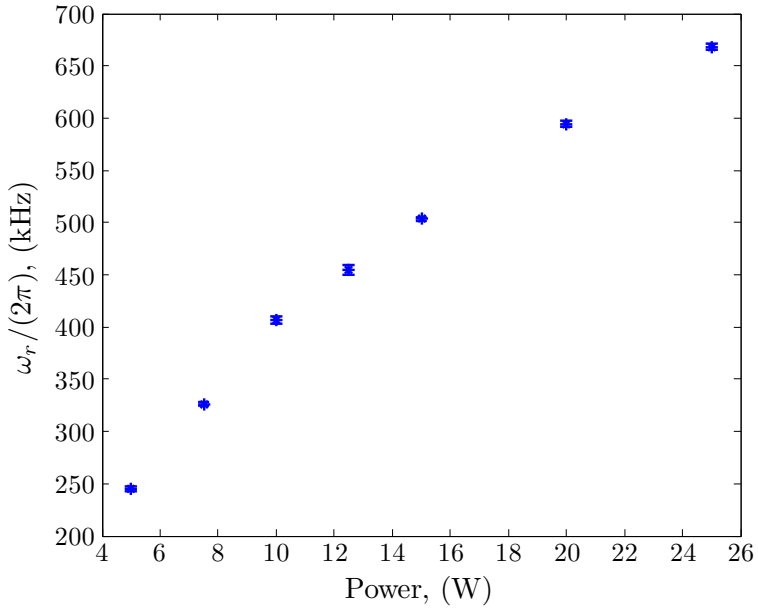

(a)

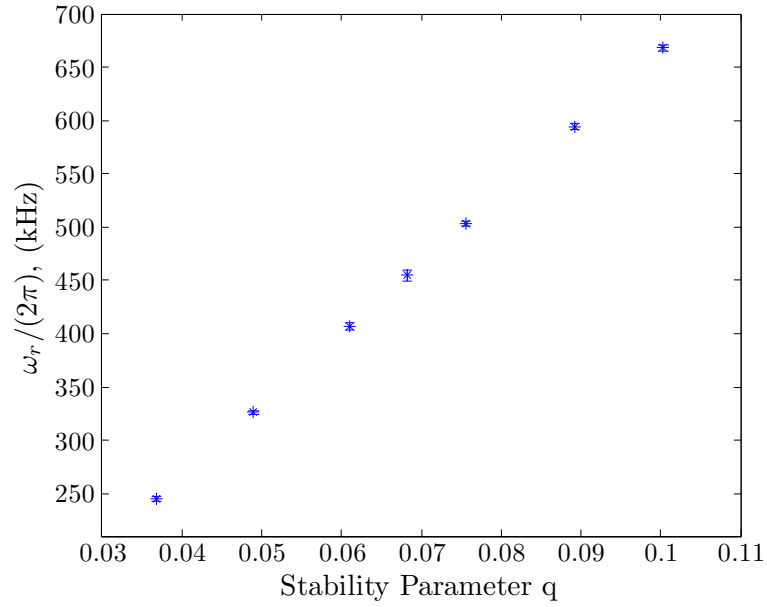

(b)

Figure 3.3: (a) Measured radial trap frequency vs. RF source power. (b) Measured radial trap frequency vs. stability parameter q. The q values are derived from the measured radial secular frequencies according to equation 3.33. The measurements were performed at the axial frequency $\omega_z = 2\pi \cdot 53\,\mathrm{kHz}$. The errors of the radial trapping frequencies are on the order of few kHz. Hence, the error bars are smaller than the data symbols.

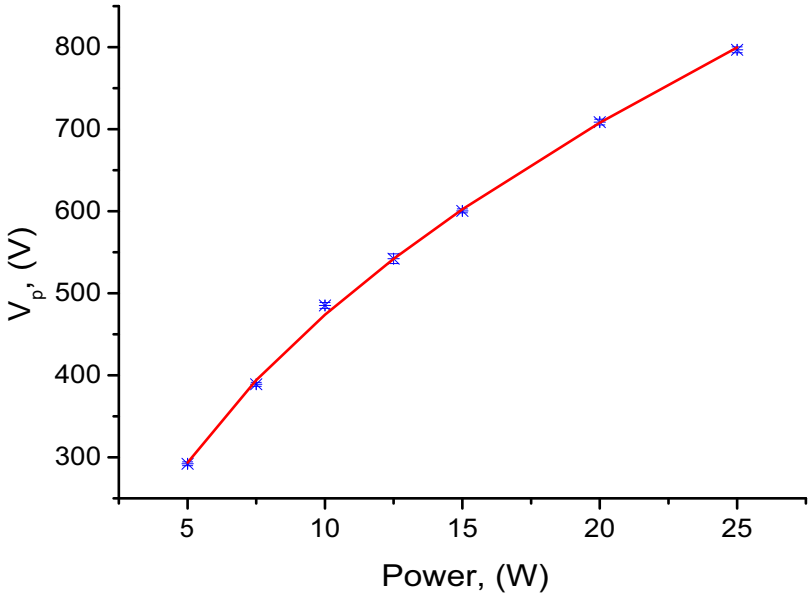

Figure 3.4: RF source peak voltage vs. RF source power. The solid line is a fit yielding $V_p = \xi \cdot \sqrt{Q' \cdot Power - \delta}$*, where* ξ *is the RF resonator geometric factor,* Q' *is the quality factor of the RF resonator and* δ *is the offset due to the trap geometry.* $Q' = 114$ *was measured and fixed during the fit. From the fit follows that* $\xi = 15.6(1)$ *and* $\delta = 215(15)$*.*

it is possible to see from equation 3.22 and equation 3.23 and, therefore,

$$q = \frac{2}{\Omega_{RF}} \sqrt{2\omega_r^2 + \omega_z^2}. \tag{3.33}$$

Figure 3.3 (b) shows the measured secular frequencies versus stability parameter q calculated by equation 3.33. The q lies in the range of $0.04 - 0.1$. We run the experiment at 15 W for which $q = 0.08$ and the radial trap frequency is $\omega_r \approx 2\pi \cdot 500\,\text{kHz}$. The depth of the trap in the radial directions at RF power of 15 W, that corresponds to $V_0 \approx 600\,\text{V}$ (see Figure 3.4), is 6 eV. The well depth along the z-direction is in the range of $3.5 - 6.5\,\text{eV}$ depending on the U_{cap} voltage used (see also Figure 3.2).

The RF voltage $V_0 \equiv V_p$ [2] applied to the RF electrodes can be found from equation 3.15. It was plotted in dependence of RF power and the results are shown in Figure

[2] V_p is a peak voltage

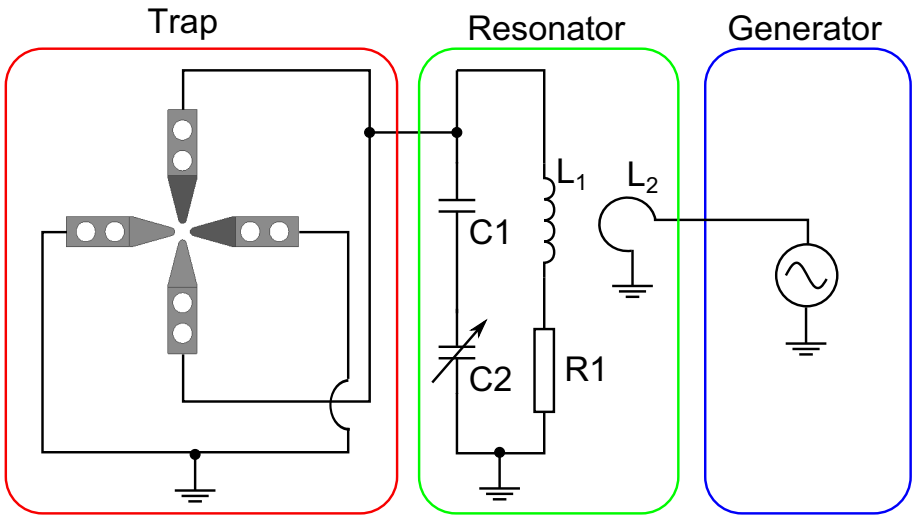

Figure 3.5: Schematic diagram of the RF circuit.

3.4. The solid line is a fit yielding $V_p = \xi \cdot \sqrt{Q' \cdot P - \delta}$, where Q' is the quality factor of the RF resonator ($Q' = 114$, see section 3.2), $\xi = 15.6(1)$ is the resonator geometric factor and $\delta = 215(15)$ is an offset influenced by the trap geometry.

If only a few ions are confined in the trap, they will align themselves linearly along the trap axis. Increasing the amount of the ions or increasing the DC voltage on the trap end-caps electrodes, the distance between the ions is decreasing and the Coulomb repulsion between the neighboring ions becomes stronger than the radial confinement. Therefore, the ions organize into the zigzag, or helix, pattern and some of the ions away from the center start to experience higher micromotion resulting in ions heating. We would like to avoid this situation. The condition for linear organized ions is [Steane, 1997]:

$$\frac{\omega_r}{\omega_z} > 0.73 N^{0.86} \quad , \tag{3.34}$$

where ω_r, ω_z are the radial and axial trap frequencies and N the number of the ions. For $\omega_r = 2\pi \cdot 502\,\mathrm{kHz}$ and $\omega_z = 2\pi \cdot 123.5\,\mathrm{kHz}$ in the current experiment, an ion chain of up to seven ions is linear.

3.2 Trap Drives

The high voltage amplitude RF signal needed to create the trapping potential is generated using a synthesized function generator, amplified and sent to a helical resonator. The last is attached to a power feedthrough (in our case a standard high-voltage SHV-feedthrough, see section 3.4). The amplifier works in the range of 20-1000 MHz with a maximum power output of 25 W.

Figure 3.5 depicts the schematic diagram of the RF circuit. The helical resonator is a parallel resonant LC-circuit. A helical copper coil, having inductance L_1, made of 12 windings and is placed inside a copper cylinder with capacitance C_1. The amplified RF signal from the generator is inductively connected to the helical resonator by a single-winded coil with inductance L_2. Figure C.1 shows the photos of the RF resonator, inside and outside views. The RF resonator used in the current experiment was designed and constructed by Dr. Ivo Polak of Prague University. More details can be also found in [Braun, 2007]. The resonator circuit contains as well a variable capacitor, C_2 in Figure 3.5, to match the impedance of the LC-circuit to the trap-chamber system load [3]. An additional resistor of low resistance $R_1 \approx 1\,\Omega$ was added in series to the coil with inductance L_1 to reduce the *quality factor* Q [4] of the resonator in order to decrease in this way its sensitivity to frequency fluctuations. The quality factor is the ratio of the resonator resonance frequency and its bandwidth $Q = \Omega_{RF}/\Delta\Omega_{RF}$. The higher the quality factor Q, the less power losses and, correspondingly, the less RF-power is required to reach the same voltage amplitude on the resonator output. At the same time, the resonator bandwidth is reduced what makes it less robust to small changes of the resonance frequency, the situation we would like to avoid in the current experiment.

The operating frequency of the current RF resonator is adjustable in the range of $\Omega_{RF} = 2\pi \cdot (18 - 23)\,\mathrm{MHz}$. During its construction the RF resonator was optimized for $\Omega_{RF} = 2\pi \cdot 21\,\mathrm{MHz}$ at the measured capacitance of the pre-built trap-vacuum system of around 15 pF (measured between the inner pin and the outer shield of the SHV-feedthrough connector). The current setup has a slightly higher capacitance that decreased the resonance frequency of the RF-resonator to $\Omega_{RF} = 2\pi \cdot 18.8\,\mathrm{MHz}$.

The impedance mismatches between the RF resonator and the trap-chamber system reflect the wave back toward the power source creating standing wave. Hence,

[3] The trap is connected to the vacuum chamber through the SHV-feedthrough shield.

[4] $Q = \frac{\Omega_{RF}}{\Delta\Omega_{RF}} = \frac{1}{R_1}\sqrt{\frac{L_1}{C}}$, where $C = \frac{C_1 C_2}{C_1 + C_2}$, Ω_{RF} is the resonator resonance frequency and $\Delta\Omega_{RF}$ is the resonator bandwidth.

only some power or, in the worse case, no power at all reaches the trap RF electrodes. The VSWR (Voltage Standing Wave Ratio), or, shortly, SWR, is defined as the ratio of the maximum amplitude of the standing wave to its minimum amplitude. The SWR is also related to the magnitude of reflection coefficient $\rho = \frac{V_r}{V_f}$, where V_f and V_r are the forward and reflected wave amplitudes, respectively. Therefore,

$$VSWR = \frac{V_{max}}{V_{min}} = \frac{1+\rho}{1-\rho}, \tag{3.35}$$

where $V_{max} = V_f + V_r$ and $V_{min} = V_f - V_r$. In the ideal transmission the SWR equals 1:1 (the first number is a maximum standing wave amplitude V_{max}, the second number - the minimum V_{min}) [5], or just one (1.0). The reflection coefficient $\rho = 0$ in this case. If the SWR is a big or infinite number, some or all of the initial power is reflected back. An SWR less then 1.5:1 is considered good.

The SWR, as well as the resistance R and the reactance X of the complete resonator, where measured by means of an antenna analyzer connected instead of the generator (see Figure 3.5). An example of the results is presented in Figure 3.6. Here, the measurements were performed when the RF power back reflection was still quite big and SWR > 2.0. The quality factor Q for the RF resonator from Figure 3.6 (blue curve) for these measurements was found to be 114. Here, the grounds of the vacuum chamber and the RF resonator were separated: the trap ground electrodes and the vacuum chamber were grounded through the getter pump. The SHV-feedthrough with a floating shield, used to bring the RF-signal to the trap electrodes, stops the current flow through the chamber back to the resonator. Several different connections combinations were tried in order to reduce the RF back reflection and the RF pick-up noise. The detailed explanation can be found in [Scharfenberger, 2012]. The best result was achieved when connecting the grounds of both, the RF resonator and the vacuum chamber, with a copper braid. The SWR = 1.0 was achieved at $\Omega_{RF} = 2\pi \cdot 18.8\,\mathrm{MHz}$ with resistance of $R = 50\,\mathrm{Ohm}$ and reactance of $X = 4\,\mathrm{Ohm}$. The RF noise was reduced since the impedance of the current path through the RF resonator is smaller than through the getter pump [Scharfenberger, 2012].

The maximum voltage amplitude obtained with the current amplifier is about $1600\,\mathrm{V_{pp}}$ at $25\,\mathrm{W}$ (see Figure 3.4). It turned out that the ion chain is not stable at this power (ion chain melts) and the experiment was performed at $15\,\mathrm{W}$. The parameters of the trap for this power are given in section 3.1.2.

[5] When SWR is expressed as a ratio, the denominator of the ratio is always 1.

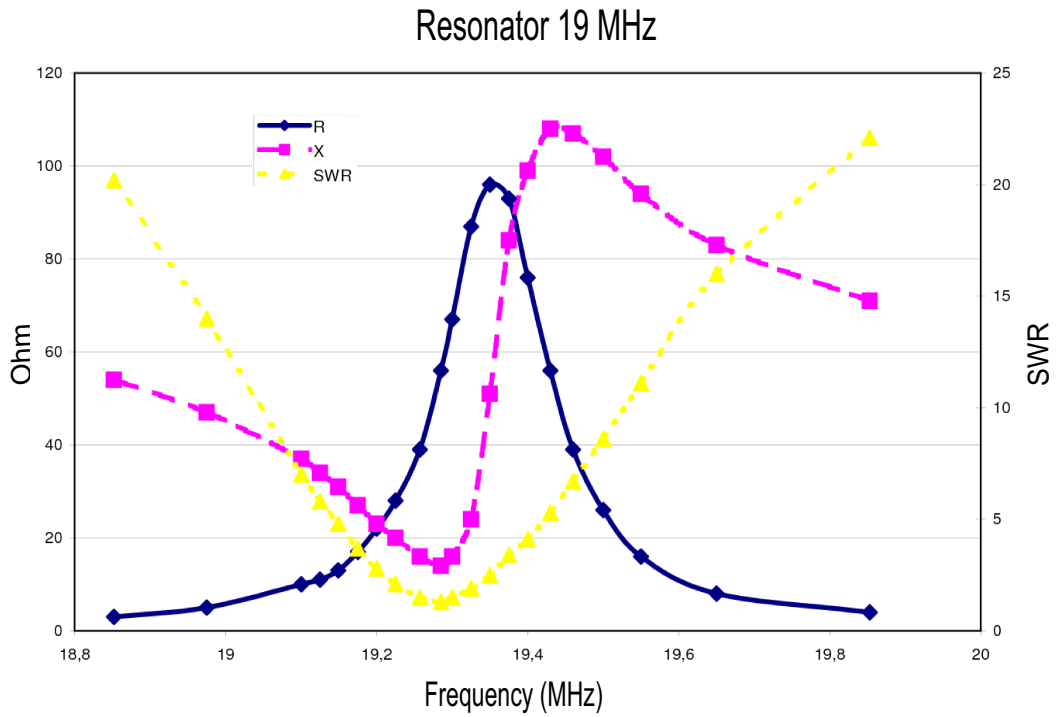

Figure 3.6: Characteristics of the 19 MHz resonator. Measured resistance (blue), reactance (magenta) and SWR (yellow) plotted versus resonator frequency. The resonance frequency Ω_{RF} is around 19.3 MHz and with the bandwidth $\Delta\Omega_{RF}$ of 170 kHz the quality factor equals 114.

The RF resonator was shielded in order to protect the electric devices (i.e. the electronics of the diode laser controllers, temperature controller of the cavities) sensitive to the RF noise. It is placed inside an aluminium shielding box that consists of two main parts: an 8 mm thick main box, where the body of the RF resonator lies, and a 2 mm thick external shield to cover the signal output conducting wire (see Figure C.2). The main box body was black anodized in order to reduce laser light reflections from the shiny surfaces.

The shielding box alone was not sufficient to minimize the RF pick-up noise. Hence, low-pass filters with cut-off frequencies below 1 MHz were added on the inputs of the lock-in amplifier, cavity temperature controllers, measurement electronics of the lambda-meter [Scharfenberger, 2012]. The cables of the photodiodes were shielded with metallic braid and additional ferrite rings. It is important to suppress the RF signal picked up by the cables that bring the DC signal from the power supplies to the end-cap and compensation electrodes as well as vice versa the RF signal picked up by the same electrodes should not propagate toward the DC

sources. For the compensation electrodes the low-pass filters of second order with the cut-off frequency about 100 Hz or smaller were used. The end-cap electrodes are connected to the two batteries in series through the circuit that is combination of a voltage divider and a single pole low-pass filter. The capacitor next to the end-cap electrode short circuit the high-frequency RF signal to the ground not allowing it to propagate on the DC cable.

3.3 Laser Systems for Ytterbium

Four different laser wavelengths are used in the current experiment with $^{171}Yb^{+}$ ions: 369.5 nm, 398.9 nm, 638.2 nm and 935.2 nm. The energy level scheme for the $^{171}Yb^{+}$ ion is shown in Figure 3.7. All the wavelengths are produced by diode laser systems in Littrow configuration that are frequency stabilized with an external optical resonators [Piltz, 2010; Reuner, 2007]. The hyperfine levels of the $^2S_{1/2}$ ground state serve as a qubit, with $|\downarrow\rangle \equiv {}^2S_{1/2}$ ($F = 0$, $m_F = 0$) and $|\uparrow\rangle \equiv {}^2S_{1/2}$ ($F = 1$, $m_F = +1$). These states are coherently controlled by microwave radiation near 12.65 GHz in resonance with the $|\downarrow\rangle \leftrightarrow |\uparrow\rangle$ transition.

The 398.9 nm laser light together with the 369.5 nm are used for the two-color photo-ionization process in order to create the Yb^{+} ions in the trap as will be explained in section 4.1.

$^{171}Yb^{+}$ ions are Doppler cooled by applying both 369.5 nm laser light and microwave radiation. The 369.5 nm light is red-detuned to the $^2S_{1/2}$ ($F = 1$) $\leftrightarrow$ $^2P_{1/2}$ ($F = 0$) resonance, *cooling transition*, and the microwave radiation is in resonance with the $|\downarrow\rangle \leftrightarrow {}^2S_{1/2}$ ($F = 1$, $m_F = 0$) transition at 12.642828 GHz (π-transition) to prevent optical pumping into state $|\downarrow\rangle$ (see Figure 3.7). To produce the 369.5 nm light a commercial UV laser diode was used. At room temperature it emits light at 371.0 nm but it is possible to cool the laser to achieve a smaller wavelength [Kielpinski *et al.*, 2006]. The 369.5 nm is obtained at -7 °C and it is placed inside a specially designed laser box, well isolated with silicon and vacuum grease, that is filled with chemicals which reduce the humidity inside the box. More details about the construction of the 369.5 nm source can be found in [Piltz, 2010]. A double-pass acousto-optical modulator setup, with a modulation frequency of 65 MHz, is used to tune the UV light to the red.

The $^2P_{1/2}$ state also decays to the meta-stable state $^2D_{3/2}$ (the natural lifetime $\tau = 53$ ms [Yu & Maleki, 2000]) with the probability of about 0.005 [Olmschenk *et al.*, 2007], and $^2D_{3/2}$ state itself, due to collisions of the ion with background gas

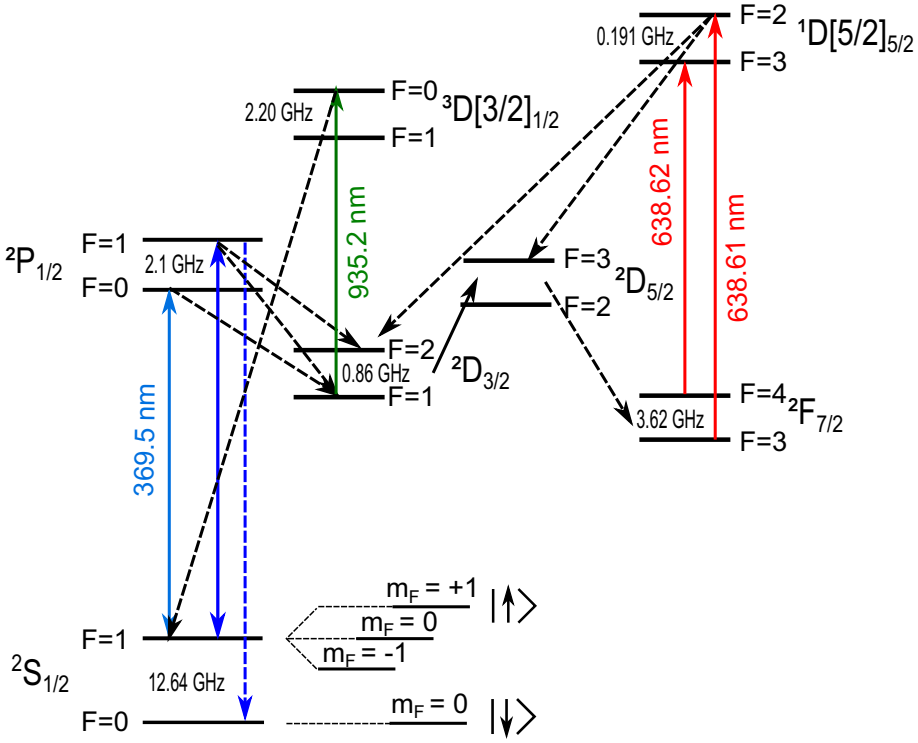

Figure 3.7: Partial energy level scheme for the $^{171}Yb^{+}$ ion. The ground state hyperfine levels $^2S_{1/2}$ $(F = 0, m_F = 0)$ and $^2S_{1/2}$ $(F = 1, m_F = +1)$ represents the qubit state $|\downarrow\rangle$ and $|\uparrow\rangle$, respectively. The $^2S_{1/2}$ $(F = 1) \leftrightarrow {}^2P_{1/2}$ $(F = 0)$ transition is used for Doppler cooling and fluorescence detection and is driven by 369.5 nm laser light. Microwave radiation at 12.6 GHz is used to prevent optical pumping into state $|\downarrow\rangle$ during the cooling and for qubit manipulation. The ion can decay from the $^2P_{1/2}$ to the metastable $^2D_{3/2}$ state and it is returned to the ground state through the $^2D_{3/2} \leftrightarrow {}^3D[3/2]_{1/2}$ transition using 935.2 nm laser light. Due to inelastic collisions with background gas in the vacuum chamber the ion can change the state from the $^2D_{3/2}$ to the $^2D_{5/2}$, which decays into the $^2F_{7/2}$ state. Laser light at 638.610 nm and 638.616 nm excites the transitions to the $^1D[5/2]_{5/2}$ state which decays back to the $^3D_{3/2}$ state.

[Bauch *et al.*, 1992], populates $^2F_{7/2}$ state ($\tau = 6$ (10) years according to [Hosaka *et al.*, 2005] ([Roberts *et al.*, 1997])) through the $^2D_{5/2}$ state with the probability of 0.83 [Taylor *et al.*, 1997]. In order to maintain cooling and detection, two additional laser wavelengths, at 935.2 nm and 638.6 nm, are used. The 935.2 nm light drives the ion from the $^2D_{3/2}$ to the $^3D[3/2]_{1/2}$ state ($\tau = 37.7$ ns [Yu & Maleki, 2000]), from which it immediately decays into the ground state $^2S_{1/2}$ with the probability of 0.98 [Roberts, 1996]. The laser light near 638.6 nm depopulates the $^2F_{7/2}$ state ($\tau \approx 6$ years [Hosaka *et al.*, 2005]) and brings the ion back into the four-level cooling cycle through the $^1D[5/2]_{5/2}$ state ($\tau < 50$ ms [Roberts, 1996]). Both laser lights, at 935.2 nm and 638.6 nm, are continuously turned on during the whole experiment.

In order to prepare the ions in the initial state $|\downarrow\rangle$, a direct resonance excitation $^2S_{1/2}$ $(F = 1) \leftrightarrow {}^2P_{1/2}$ $(F = 1)$, *preparation transition*, is used. The 2.1 GHz blue-shift of the 369.5 nm laser is also achieved with a double-pass acousto-optical modulator setup, with a modulation frequency at 985 MHz [Piltz, 2010]. The schematic of the 369.5 nm laser light system with the two AOMs using a double-pass configuration is demonstrated in Appendix D, Figure D.1.

The state selective detection was accomplished by tuning the 369.5 nm laser light close to the resonance of the *cooling transition* $^2S_{1/2}$ $(F = 1) \leftrightarrow {}^2P_{1/2}$ $(F = 0)$. For an ion in $|\uparrow\rangle$ state, the photon count rate approaches an average of 3000 - 4200 Hz. If the ions is in $|\downarrow\rangle$ state, only few photons are scattered and the photon count rate is in the range of 200 Hz.

The wavelength of a diode laser depends on the current applied to the laser chip, the temperature of the laser diode and the position of the Littrow grating, controlled by the piezo-actuator. Changing the voltage on the piezo-actuator changes the distance of the grating from the laser diode. Therefore, the length of the external resonator is changed and, together with it, the frequency of the laser beam. The settings used for the laser diodes in the current experiment are summarized in Appendix Q, Table Q.1.

3.4 Vacuum System

The vacuum chamber used in our experiment is a cylinder with two CF100 flanges and eight radially placed equidistant tubes with CF40 flanges at the end. It is possible to see the mechanical sketch of the vacuum chamber in Appendix Q.1. It is made of non-magnetic 316L-grade stainless steel. One of the CF100 flange is

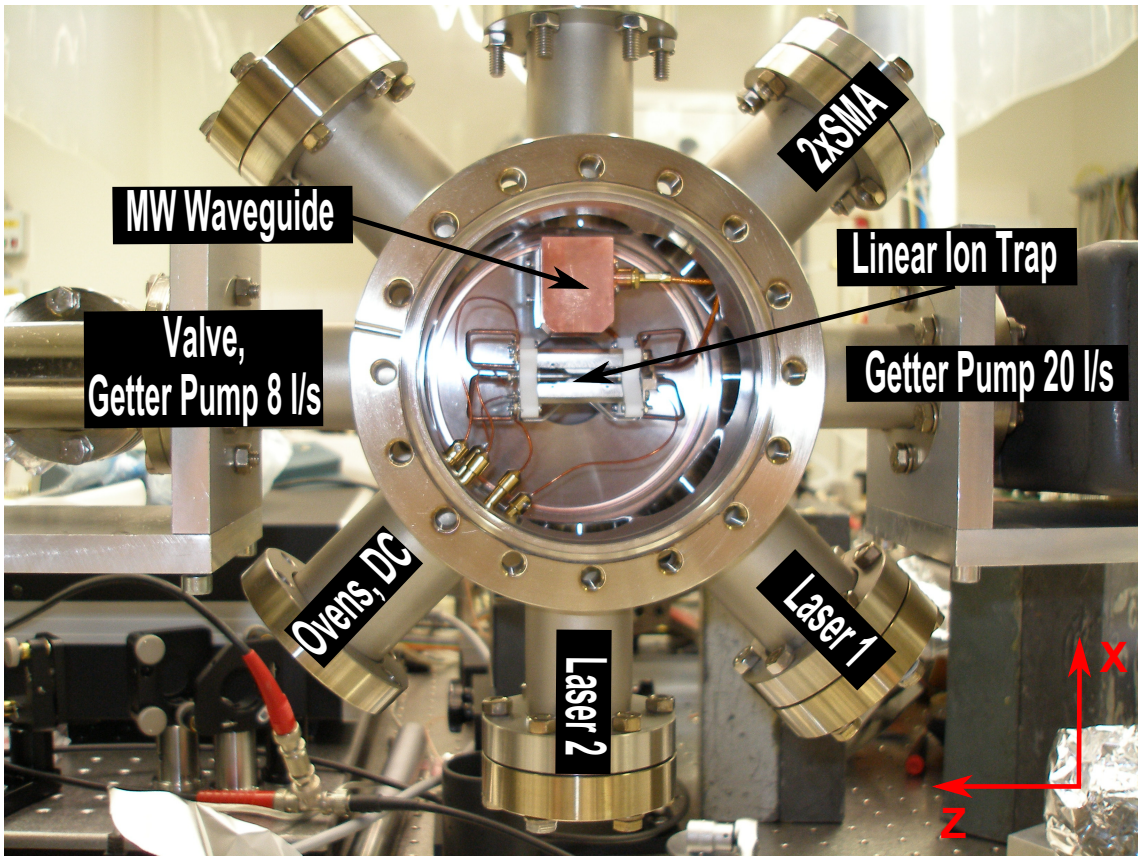

Figure 3.8: Vacuum Chamber. Laser1 and Laser2 flanges are used for the laser beams. Laser1 is used in the current experiments with the $^{171}Yb^{+}$ ions. Here, all four laser beams (369 nm, 399 nm, 935 nm and 638 nm) are at 45° to the trap axis. Laser2 flange is used in case only the π-polarization of the laser beam is required, for example for the 935.2 nm laser beam in the experiments involving the $^{2}D_{3/2}$ state. Ovens and linear ion trap compensation, DC and end-cap electrodes are connected to the flange that carries the current-feedthorugh and is perpendicular to the Laser1 flange. Two flanges in the plane of the trap axis are used to connect the getter pump and the valve. The last left flange contains the SMA-feedthrough with two SMA connectors to bring the microwave signal to the two antennas in the microwave waveguide.

rotating as well as four CF40 flanges (in alternating order rotating-nonrotating). The fixed CF100 flange is used for the viewport, in order to collect the fluorescence light, and the other, rotatating CF100 flange - for the RF feedthrough.

In Figure 3.8 the vacuum chamber organization is depicted. The linear trap is at the center of the vacuum chamber and the center of the trap should coincide with the center of the chamber (at least theoretically). The coordinates convention is the following: z-axis lies along the trap axis; x-axis is perpendicular to the trap axis, lies in the plane of the CF100 flange and points up through the microwave waveguide; y-axis points toward the SHV-feedthrough that will be discussed later in this section. Laser1 and Laser2 in Figure 3.8 label the paths for the lasers through the vacuum chamber. Laser1 path is used in the experiments with $^{171}Yb^{+}$ ions, where 45° angle with respect to the external magnetic field is preferred (see section 3.7). Laser2 path is used in case only the π-polarization of the laser beam is required, for example for the 935.2 nm laser beam in the experiments involving the $^2D_{3/2}$ state (see section 3.7).

The ovens are perpendicular to the 398.9 nm laser beam (see also section 4.1) passing through the flange Laser1 and they are connected to the same flange as the trap compensation, DC and end-cap electrodes through a current feedthrough (see Figure 3.8 **Ovens, DC** flange).

Two flanges in the vacuum chamber were used to connect a 20 l/s getter pump and a valve. The last flange contains a SMA-feedthrough with two SMA connectors in order to bring the microwave signal to the two antennas in the microwave waveguide (see section 3.8).

Fluorescence Viewport. The viewport was specially manufactured by UKAEA (United Kingdom Atomic Energy Authority). The viewport window is a fused silica [6], 8 mm thick, with both surfaces flatness of $\lambda/10$ and the wedge angle of 30 arc-seconds (high flatness, high parallelism glass). Fused silica is used because of its very high ultraviolet light transmission, $> 90\%$. The window is anti-reflection coated on both sides for 369 nm. More information can be found in Appendix E.

Laser Viewports. Four viewports on the CF40 flanges (see Appendix E, Figure E.2), used for the laser beams, have the windows from fused silica with a clear view of 25.4 mm and thickness of 3 mm. Their flatness is $\lambda/4$ at 633 nm and the scratch-dig number equals 40-20. The windows of these viewports were anti-reflection

[6] Spectrosil: synthetic silica

coated for four wavelengths: 369 nm, 399 nm, 935 nm and 638 nm, on both sides.

RF In-Vacuum Connection. A separate feedthrough is used to connect the RF generator to the trap. The idea is to minimize the pick-up of the RF voltage by the DC electrodes. For high RF voltages the SHV-feedthrough (see Appendix E, Figure E.3) is used with specified maximum acceptable voltage of 5 kV DC and current of 5 A. This feedthrough is mounted on the CF40 flange made of 304-grade stainless steel and its maximum bake-out temperature is 450 °C. This feedthrough does not have a constant impedance, so we characterized it after connecting to the RF resonator (see section 3.2). The CF40 base of the SHV-feedthrough is connected to a rotating zero-length CF100 to CF40 adapter.

The inner connector of the SHV-feedthrough, made from Nickel, is 2.4 mm long and it is connected to the two opposite RF-electrodes of the ion trap using two Oxygen-Free High thermal Conductivity (OFHC) copper wires with diameter of 2 mm. Initially, we used four wires, two for each RF-electrode side, to make the current flow more uniform in the stainless steel, since it conducts the current far worse than the copper. We took out one connector of the two for each electrode since too much power was reflected back. Figure 3.9 demonstrates how the RF connection was performed. The trap itself is connected to the CF100 to CF40 adapter by four stainless steel rods. A holder for the microwave waveguide is also visible and it is fixed to the adapter by two rods. The SHV-feedthrough has a floating shield, since initially we wanted to separate the grounds of the vacuum chamber and the RF resonator. However, the lowest RF noise and back reflection was achieved in case RF resonator and the vacuum chamber have the same ground [Scharfenberger, 2012]. Two ground electrodes of the trap are connected together through a stainless steel ground connection (see Figure 3.9) and to the SHV-feedthrough shield. At the beginning a Kapton coaxial cable was used for this connection in order to reduce the RF pick-up on the ground. Later, this cable was exchanged with the simple Kapton cable which had a thicker inner conductor and was less prone to be damaged.

Ovens and Trap Electrodes In-Vacuum Connection. The DC electrodes (two end-cap electrodes and three compensation electrodes) and two ovens (for isotopes $^{171}Yb^{+}$ and $^{172}Yb^{+}$) are connected to the current (power) feedthrough that has 12 copper pins and can withstand a maximum of 5 kV and 30 A on each pin. Three middle pins are used for the ovens and the grounds of the ovens (see Figure 3.10). The DC connections are again made via Kapton cables. CuBe connectors are used to make connection between the current feedthrough copper

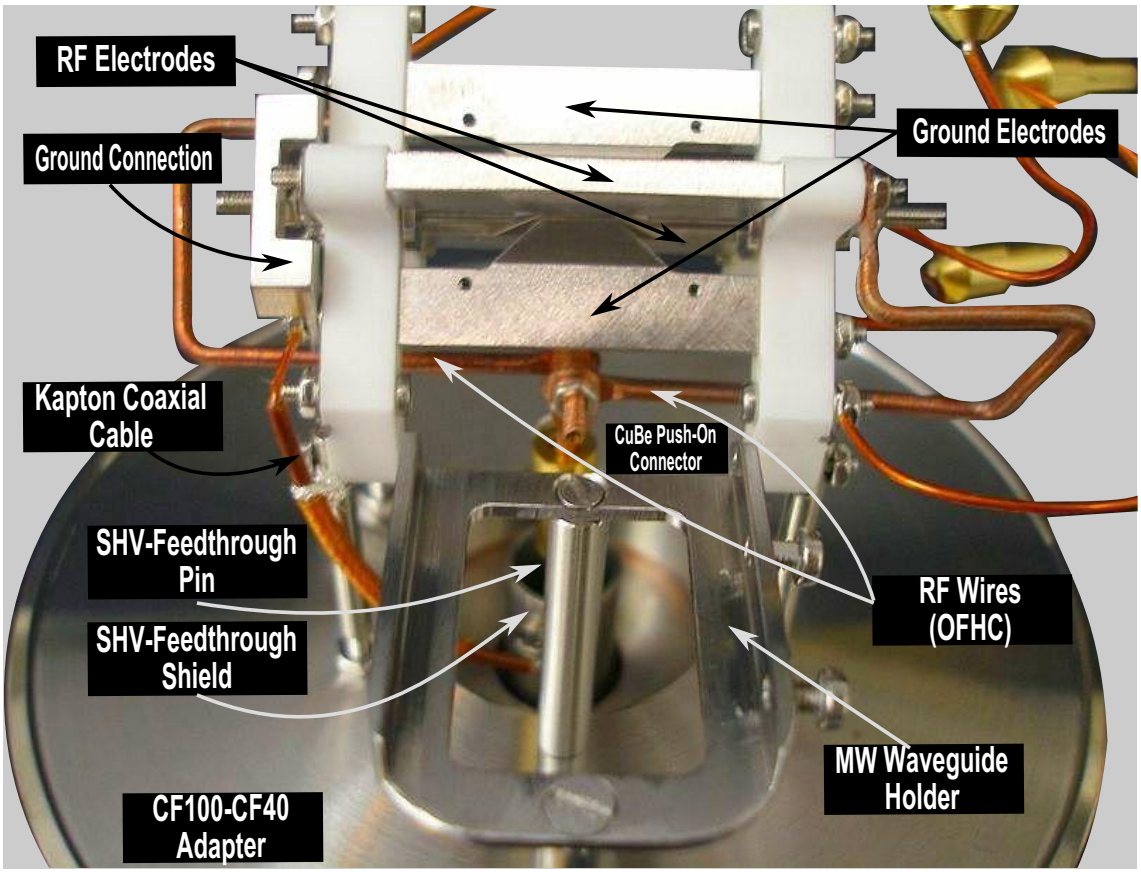

*Figure 3.9: In-vauum RF connections of the linear ion trap. Two opposite trap electrodes (**RF Electrodes**) are connected to the RF resonator through the OFHC **RF Wires** and the **SHV-feedthrough Pin**. Another two opposite trap electrodes (**Ground Electrodes**) are connected to the RF resonator ground through the **Ground Connection** and the **SHV-feedthrough Shield**. The SVH-feedthrough is connected to the vaccum chamber CF100 rotating flange through the **CF100-CF40 Adapter**. In the front plane one can also see the stainless steel holder for the microwave waveguide.*

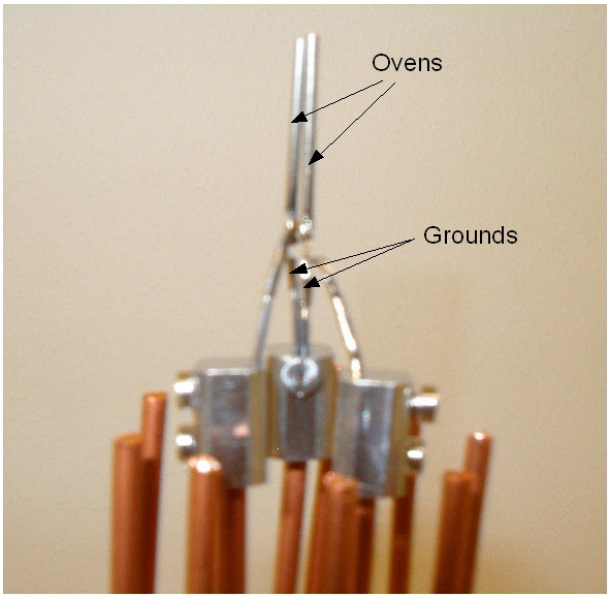

Figure 3.10: Ovens connection. Middle stainless steel connector is used for ovens' ground. Two other connectors are used to bring the current to the ovens.

wires and Kapton cables.

Microwave In-Vacuum Connection. The microwave waveguide is connected to the source through the SMA-feedthrough on the CF40 flange. The SMA connectors of this feedthrough are optimized for 50 Ω, can withstand up to 1000 V and have low power losses at 12.6 GHz (see Appendix Q, Figure Q.2). The final vacuum setup is shown in Figure 3.11.

3.5 Lambda-meter

A wavelength-meter, or lambda-meter, is used for precise wavelength measurements on laser lights. In our lab we have built a Michelson based wavelength-meter which uses an atomic ^{87}Rb (Rubidium) transition as a reference and works in the range of 350 nm-1 μm (range of the optical components). Locking to a narrow cross-over signal peak ($\Gamma = 2\pi \times 6.1$ MHz) gives us the possibility to reduce the reference laser frequency uncertainty down to about 1 MHz. Additional use of phase-lock loops (PLLs) increases the precision of the lambda-meter since the

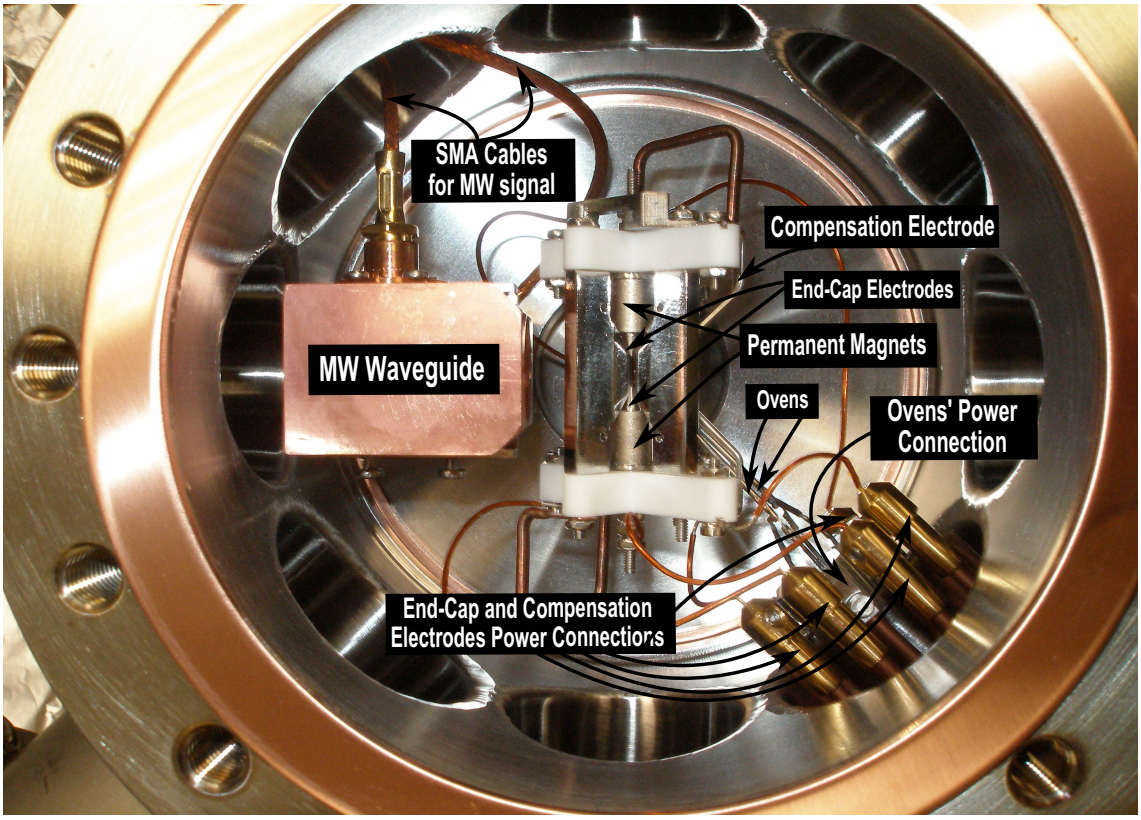

Figure 3.11: In-vacuum connections of the ovens, ion trap end-cap and compensation electrodes as well as the microwave waveguide connection. Ovens and trap electrodes are connected to the power supplies via the current (power) feedthrough with 12 pins. Microwave waveguide is connected to the microwave source through two SMA cables and SMA-feedthrough with two SMA connectors. Two permanent magnets, mounted on the end-cap electrodes, are also visible.

PLLs reduce the error in counting the interference fringes. Therefore, in our lab we are able to achieve a relative uncertainty on the unknown wavelength in the range of $1 - 2 \times 10^{-7}$.

3.5.1 Lambda-meter Optical Setup

The scanning Michelson interferometer consists of a beam-splitter (BS3), two end mirrors (M7 and M8) and two retro-reflectors (RR) mounted on a movable air-cushion wagon (Figure 3.12). Both the reference laser, with the wavelength that corresponds to a well defined atomic transition (λ_{ref}), and the unknown laser (λ_u)

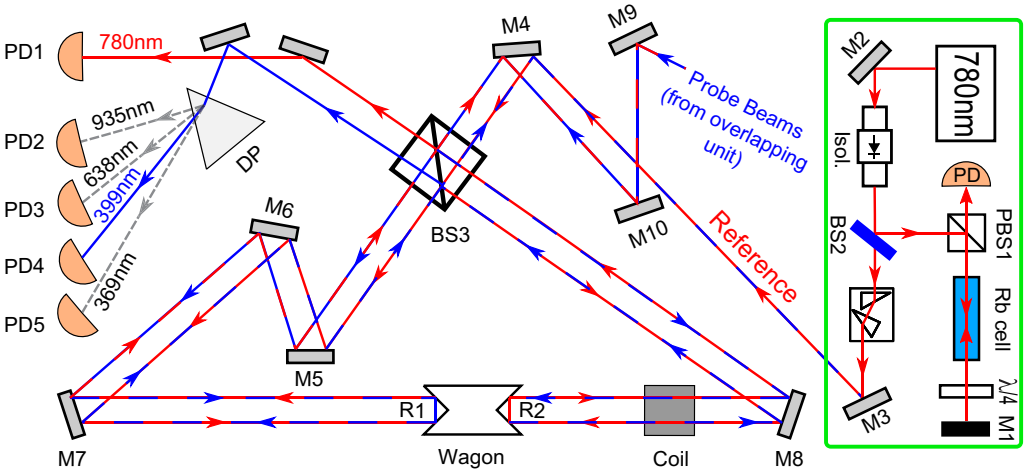

Figure 3.12: Sketch of the Michelson wavelength-meter. Here, PBS1 is a polarization beam splitter, BS2 is a beam sampler, BS3 is a 50 : 50 beam splitter, M_i - silver plated mirrors, Isol. - optical isolator, DP - dispersion prism, PD_i - photodiodes and R_i - retro-reflectors. The photo of the overlapping unit is presented in Figure 3.13

are split in two with the BS3. Two beams from each laser travel two different paths of lengths x_1 and x_2, correspondingly, in opposite directions. One of the partial beams travel the path BS3-M8-R2-M8-BS3 and the second the path BS3-M5-M6-M7-R1-M7-M6-M5-BS3. The two partial beams for the reference laser interfere at the detector PD1, and the two beams from the unknown lasers interfere at the detectors PD2-PD5. The time-averaged interference pattern on the photodiodes is [Burgarth, 1998]:

$$\overline{I} = I_0 \cdot [1 + |\zeta| \cdot cos(k\Delta x + \phi)]. \tag{3.36}$$

The intensity in equation 3.36 is proportional to the square of the sum of the electric fields of the two parts of the laser beam, E_1 and $E2$, that are splitted by the BS3. These electric fields can be described as $E_1 = E_0 e^{i(kx-\omega t)}$ and $E_2 = \zeta E_0 e^{i(k(x+\Delta x)-\omega t)}$, with $k = \frac{2\pi}{\lambda}$ and $\zeta = |\zeta| e^{i\phi}$. Since these beams come from the same source, the frequency is equal, but the amplitude and the phase can differ. The factor ζ includes the amplitude $|\zeta|$ and the relative phase ϕ. Considering further the ideal case $\zeta = 1$ ($\phi = 0$), the corresponding phase difference is simply the product of the propagation number k and the path length difference Δx: $\delta = 2\pi/\lambda \cdot \Delta x$. Basis of all measurements with the Michelson interferometer is the occurrence of minima and maxima as a function of wavelength λ, the path

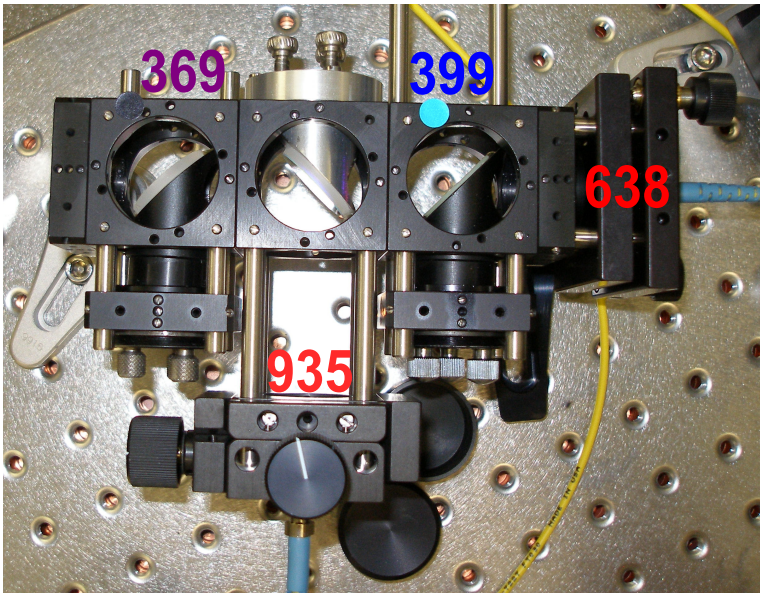

Figure 3.13: Wavemeter overlapping unit: collects different laser beams the wavelength of which has to be measured and overlaps these beams on the common mirror M9 (see Figure 3.12).

difference between the interfering partial beams Δx and the number of interference fringes N measured pro path difference Δx. The maximum and minimum of the interference pattern occurs at

$$\delta = 2\pi/\lambda \cdot \Delta x = 2\pi N \tag{3.37}$$

and

$$\delta = 2\pi/\lambda \cdot \Delta x = \pi(2N + 1), \tag{3.38}$$

respectively. In the experiment the phase δ is changed by means of moving the wagon with two retro-reflectors, as it is shown in Figure 3.12. The length of the track, where the wagon moves, is 70 cm. Two light barriers define two points on this track, **a** and **b**, between which the interference fringes will be counted. The distance between these light barriers, Δx_{ab}, is 35 cm [7] and the maximum possible optical path difference is, therefore, 4×35 cm. Considering equation 3.37, the path difference $4 \cdot \Delta x_{ab}$ can be given in terms of the number of interference fringes N, when the wagon travels down the track x_{ab}, and the wavelength λ, $4 \cdot \Delta x_{ab} = N\lambda$. Therefore, we have for the reference laser beam, with the known wavelength λ_{ref}, $4 \cdot \Delta x_{ab} = N_{ref}\lambda_{ref}$ and for the measured laser beam, with the unknown wavelength λ_u, $4 \cdot \Delta x_{ab} = (N_u + \epsilon)\lambda_u$, respectively. The counter is set to stop counting the

[7] In this region the wagon has more uniform speed, what reduces the counting error ϵ.

fringes after the preset number of N_{ref} is reached. Hence, ϵ is an error in counting the interference fringes of the unknown wavelength laser beam N_u. Since the lambda-meter is not in vacuum, the dispersion correction should be made and the resulting unknown vacuum wavelength λ_u^0 is [Demtröder, 2008]:

$$\lambda_u^0 = \frac{M_{ref} \cdot N_{ref}}{M_u \cdot N_u + \epsilon} \lambda_{ref}^0 \frac{n_u(\lambda_u, P, T)}{n_{ref}(\lambda_{ref}, P, T)}, \tag{3.39}$$

where n_u and n_{ref} are the refractive indices of air as the function of the light wavelength, pressure and temperature and M_{ref} (M_u) is a PLL's multiplication factor for the number of interference fringes of the reference (unknown) wavelength. The counter usually records information as number of counts N per ms, or counting rate: $f = \frac{N_u + \epsilon}{\Delta t} = 4\upsilon \cdot n_u(\lambda_u)/\lambda_u$, where υ is the speed of the wagon and Δt is the time window when the counting is performed. Some counters can directly calculate the ratio $\frac{N_{ref}}{N_u + \epsilon}$, as it is in our case.

There is a small coil with 1223 windings in the wave-meter setup which creates the magnetic field (about 0.5 Gauss at 1.44 mA) to which the wagon (via its iron rod) is attracted. A third light barrier sends a signal to the circuit that supplies the current to this coil. When the wagon passes this barrier, attracted by the coil's magnetic field, the current in the coil is switched off. The coil has also a spring that pushes the wagon toward the other side of the track, where it bounces from the second spring and come back again to the coil on the initial side of the track, activated this time by a timer circuit.

3.5.2 ^{87}Rb Reference

The reference laser is a frequency-stabilized diode laser at about 780 nm, that corresponds to the D2 line in the ^{87}Rb isotope (Figure 3.14, Left), with a line width of $\sim$ 500 kHz. It is locked to the cross-over 2,3 transition at a frequency of 384.2279819 THz [Kraft *et al.*, 2005; Steck, 2010] with a natural line width of $2\pi \cdot 6.1$ MHz. The cross-over 2, 3 frequency is the half of the sum of the $5^2S_{1/2}$ $(F = 2) \leftrightarrow 5^2P_{3/2}$ $(F' = 2)$ and $5^2S_{1/2}$ $(F = 2) \leftrightarrow 5^2P_{3/2}$ $(F' = 3)$ transitions. The expected wavelength in vacuum is, therefore, 780.24629 nm. At lab condition in air, when pressure is 983 $\pm$ 14 hPa, temperature is 20 $\pm$ 0.75 $^\circ C$, $CO_2 \simeq 0.040$ $\pm$ 0.005 % and humidity is 56 $\pm$ 4.5 %, the reference wavelength was estimated to be 780.041998 nm.

The Rubidium gas cell, used as an inexpensive frequency reference in the experi-

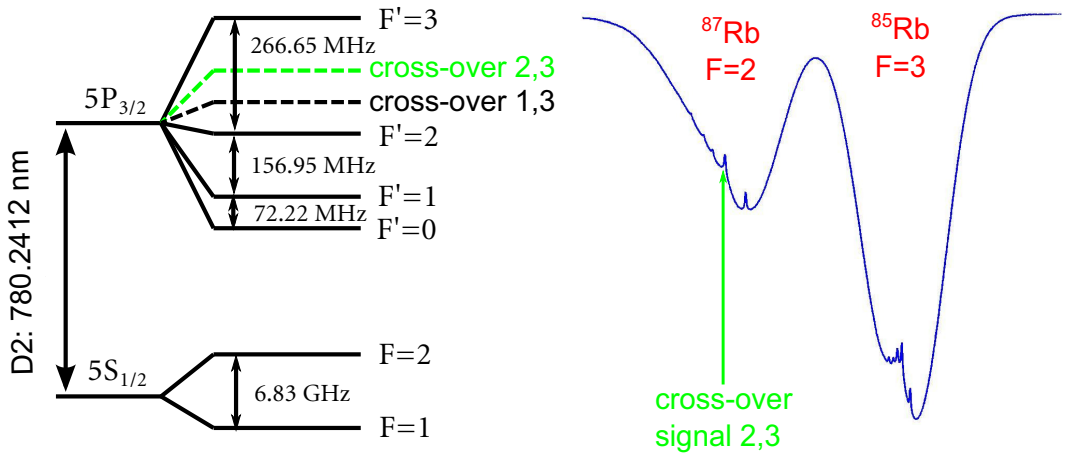

Figure 3.14: Left: Energy diagram of ^{87}Rb (I=3/2). Cross-over 1, 3 and cross-over 2, 3 are the cross-over transitions with frequencies equal to the half of the sum of the $5^2S_{1/2}$ ($F = 2$) $\leftrightarrow$ $5^2P_{3/2}$ ($F' = 1$ and 3) transitions and $5^2S_{1/2}$ ($F = 2$) $\leftrightarrow$ $5^2P_{3/2}$ ($F' = 2$ and 3) transitions, respectively. Right: Measured Doppler-broadened spectral line with the hyperfine structure for a Rb atom.

ment, contains two different isotopes, ^{85}Rb and ^{87}Rb, in a ratio of about 72 : 28. At room temperature, the spectral lines of the Rb are Doppler broadened. There are two ground-state hyperfine levels for each isotope ($F = 1, 2$ for ^{87}Rb and $F = 2, 3$ for ^{85}Rb) and, therefore, there are four Doppler-broadened peaks that are resolved in the absorption spectrum (hyperfine ground states split is in the GHz range), when the frequency of the 780 nm laser beam is changed [Steck, 2010]. Each of the isotopes has six allowed transitions, three for each hyperfine ground state (the hyperfine excited states split is in the MHz range). They are not visible in the standard absorbtion spectrum due to the Doppler broadening in the range of ~ 600 MHz. In order to resolve these hyperfine features of the Rubidium atom, a saturated absorption spectroscopy technique has been used and the schematic of the setup is presented in Figure 3.12 (Right part framed in green).

Saturation spectroscopy eliminates Doppler broadening by directing the pump beam (in our setup *forward* beam) and the probe beam (in our setup *reflected* from the mirror M1 beam) through the gas cell in opposite directions [Demtröder, 2008]. The two laser beams interact with the atoms of completely different velocity groups. Only when the frequency of the laser beam is very close to the resonance frequency of the allowed transition in the atom, both, probe and pump, laser beams begin to interact with the same atoms, those whose velocity component along the direction of propagation of the light is almost zero. If the pump beam intensity is high enough, the atom's ground state is strongly depleted (this

saturating beam equalizes the populations of the ground and excited states) and, therefore, the absorbance of the probe beam is significantly reduced. Hence, the Lamb dips are observed in the transmission spectrum. Their line widths are typically about $2\pi \cdot 10\,\mathrm{MHz}$ [Weel & Kumarakrishnan, 2002] (mainly due to power broadening), which is close to the natural line width of $2\pi \cdot 6.1\,\mathrm{MHz}$.

Only the atoms that have zero velocity component in the direction of propagation of the beams will be in resonance with both beams. The corresponding Lamb dips represent the hyperfine allowed transitions. For the rest of the atoms with different velocities along the beams, the frequencies of the probe and pump beams are shifted in different directions. Hence, the atoms can be in resonance with only one of the two beams. There are the resonances in the atom, the frequencies of which are equal to half the sum of any two allowed atomic transitions. They are called cross-over signals and they are characteristic for the atoms with non-zero velocities. The cross-over resonances are stronger because two velocity classes are addressed: velocity classes corresponding to atoms moving along the direction of the pump beam and those, moving along the direction of the probe beam.

The measured Doppler-broadened spectral line with resolved hyperfine structure is shown in Figure 3.14 (Right). The two Doppler-broadened peaks in the figure represent the ^{85}Rb and ^{87}Rb isotopes with $F = 3$ and $F = 2$ hyperfine ground state transitions, respectively. The energy diagram of the ^{87}Rb isotope is shown in Figure 3.14 (Left). There are three allowed transitions from the $F = 2$ ground state of the ^{87}Rb isotope, $F = 2 \leftrightarrow F' = 1,2,3$ ($\Delta F = 0, \pm 1$), and there are three cross-over signals (in Figure 3.14 (Left) only two cross-over signals are depicted). The corresponding narrow spectral features are clearly visible in Figure 3.14 (Right). The biggest Lamb dip corresponds to the cross-over 2, 3 and this is the peak we want to use as a reference in the wavelengths measurements.

3.5.3 Reference Frequency Stabilization

A lock-in amplifier in a feedback loop has been used in order to lock the laser to the peak (Dither Lock) of the chosen transition in ^{87}Rb atom. The reference laser lock-in setup is demonstrated in Appendix F.1, Figure F.1.

In the current experiment we use a Digital dual Lock-In amplifier with two PSD's (see Appendix F.1). The input to the lock-in amplifier is a signal from a photodiode. The last device detects the intensity of the laser beam that passes through the Rb cell and converts it into a voltage. The signal of the photodiode is the Doppler-broadened spectral line with resolved hyperfine structure (Figure 3.15,

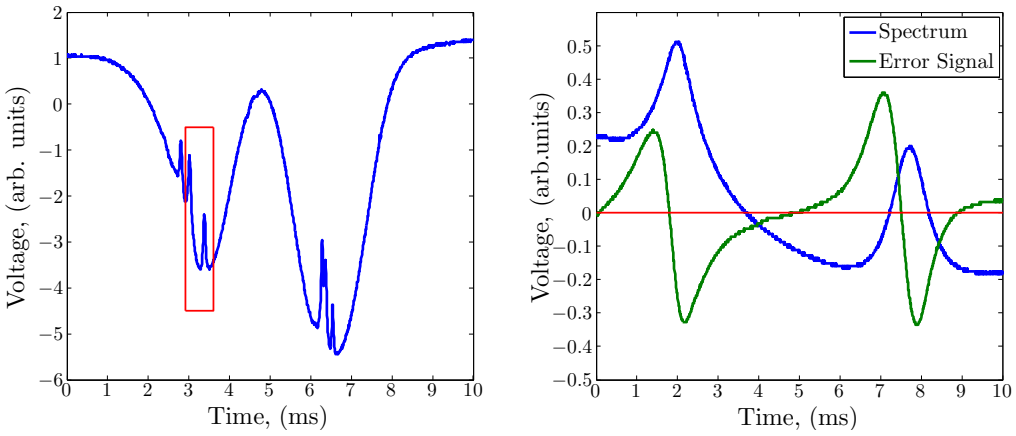

(a) (b)

Figure 3.15: (a) Spectrum of the ^{87}Rb. Red square shows the region of interest on the spectrum that is plotted in (b) together with the corresponding error signal.

(a)). Each Lamb dip has a Lorentzian form. A small modulation at 20 kHz (lock-in reference signal) is added to the laser current that results in laser frequency modulation. When the laser frequency is close to resonance, this frequency modulation produces an amplitude modulation of the photodiode signal. The lock-in amplifier transforms this photodiode signal into a derivative signal. One needs to adjust phase control of the lock-in amplifier, gain and bandpass filters after what the error signal can be seen. The measured error signal is depicted in Figure 3.15, (b) (in green). Why the error signal looks that way see in Appendix F.2. The error signal is the input of the locking feedback circuit (see Cavity Lock, Signal In in Figure F.1 [8]).

The spectra in Figure 3.15 were acquired by scanning the voltage of the piezoelectric transducer (PZT) and, hence, the frequency of the 780 nm diode laser. The triangular (ramp) signal, used to periodically change the voltage on the PZT, has a frequency of 40 Hz and it was generated by the H-Tronic function generator FG200. This triangular signal is connected to the Dither In on the Lock box (Cavity Lock in Figure F.1) front panel. The Dither 'Amplitude' sets the scanning range of the piezo and the Dither 'Offset' sets the voltage at which the 780 nm diode laser is in

[8] It is just called the 'Cavity Lock' here, it has nothing to do with the optical cavities used to lock the frequencies of the other lasers in the experiment to the side of the cavity Airy peaks. This is just the same lock-box device.

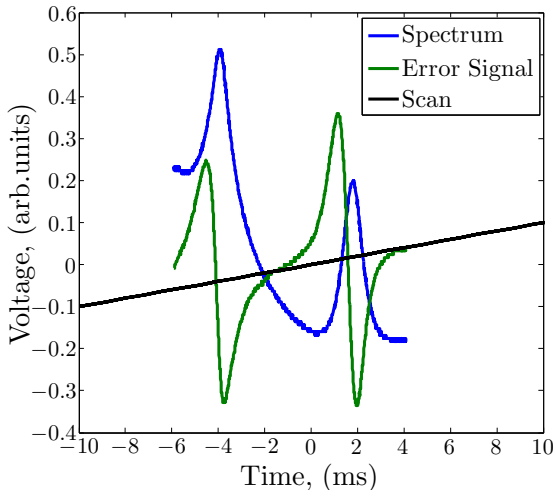

Figure 3.16: Error signals and voltage scanning slope (in black).

resonance with the Rubidium transitions so that the spectrum as in Figure 3.15 (a) is visible. This Dither 'Offset' has the same effect as the control knob on the laser diode Piezo Controller (Set Point) in Figure F.1 to find the laser resonance frequency when the Cavity Lock 'Piezo Out' is connected to the Piezo Controller Input, as it is depicted in Figure F.1. The Signal In 'Offset', than, sets the center of the error signal, as in Figure 3.15 (b), at 0 V of the ramp. The photodiode signal and the feedback circuit output signal (Cavity Lock Error Out) are connected to the oscilloscope. The oscilloscope is triggered with the same 40 Hz ramp signal from the function generator FG200.

To lock the laser frequency to the Rubidium atomic resonance, the scan Dither 'Amplitude' on the Cavity Lock is reduced slowly to zero and at the same time the voltage on the piezo is adjusted by the potentiometer of the Dither 'Offset' (or potentiometer of the Piezo Controller) so that the error signal zero corresponds to the center of the cross-over 2, 3 transition peak. When the 'Amplitude' is zeroed, the position of the 'lock/dither' knob on the Cavity Lock is set to 'lock'. In this way the feedback loop is closed. Moving up and down on the error signal slope (see Figure 3.16), the voltage goes down or up the derivative and this defines if the voltage on the PZT should increase or decrease, preventing the laser frequency from fluctuating [9].

[9]The output signal from the 'Piezo Out' lies in the range of -10 V and +10 V. The Piezo Controller amplifies this signal up to 150 V that is necessary to control the PZT of the diode laser.

3.5.4 Lambda-meter Precision

The maximum relative uncertainty of the absolute wavelength λ_u with the abbreviation $r = \frac{n_u}{n_{ref}}$ for the ratio of the refractive indices equals (from 3.39):

$$\left|\frac{\Delta\lambda_u}{\lambda_u}\right| \leq \left|\frac{\epsilon}{M_u \cdot N_u}\right| + \left|\frac{\Delta\lambda_{ref}}{\lambda_{ref}}\right| + \left|\frac{\Delta r}{r}\right| + \left|\frac{\delta x}{\Delta x}\right| + \left|\frac{\delta\phi}{2\pi \cdot N_u}\right| \tag{3.40}$$

In equation 3.40 the first term represents the counting error due to the uncertainty of the exact number of interference maxima for the unknown wavelength ϵ. There are two light barriers, as was already mentioned above, that define the region on the track where the interference fringes are counted. The TTL pulses from these light barriers are sent to a flip-flop circuit that generates another TTL signal changing the state from a logical **0** to a logical **1** [10] and vice versa with each pulse arrived from the barrier. This signal is connected to the ARMING channel of the counter.

The counter is set to start the counting rising edges of the reference signal's TTL pulses (Channel A Input) after the rising edge of the ARMING signal, defining the start time t'_0, and it stops after the ARMING signal goes down, defining the stop time t'_1. The signal sequences in the counter INPUT channels are demonstrated in Figure 3.17. Hence, $\Delta t = t'_1 - t'_0$ is the time period when the counter performs counting of the interference fringes and there are N_{ref} fringes for the reference laser and $N_u + \epsilon$ fringes for the unknown wavelength (Channel B Input). The unknown fraction ϵ, with $\epsilon < 2$, takes into account the fact that the rising edges of the TTL pulses for the unknown wavelength laser beam (Channel B Input) do not necessary coincide with the start t'_0 and stop t'_1 time of the counting period.

The uncertainty ϵ can be reduced using a phase-locked loop (PLL) that multiplies the frequency of the incoming signal by a factor of M. In our case the signals from the reference signal photodiode and from the measured signal photodiodes are multiplied by a PLLs by a factor of $M_{ref} = 12$ and $M_u = 6$, respectively. The signals from the photodiodes initially pass a Schmitt-trigger which converts the sinus oscillations into TTL pulses.

The wavelengths, measured with our wave-meter, are given in Table 3.1. First column contains the isotopes the transitions of which were used in the current experiment. Second column contains the measured wavelengths in the lab conditions in air. These values were received when the reference wavelength was set

[10] In the TTL pulse from the flip-flop circuit 0 V represents a logical **0**, 5 V - a logical **1**.

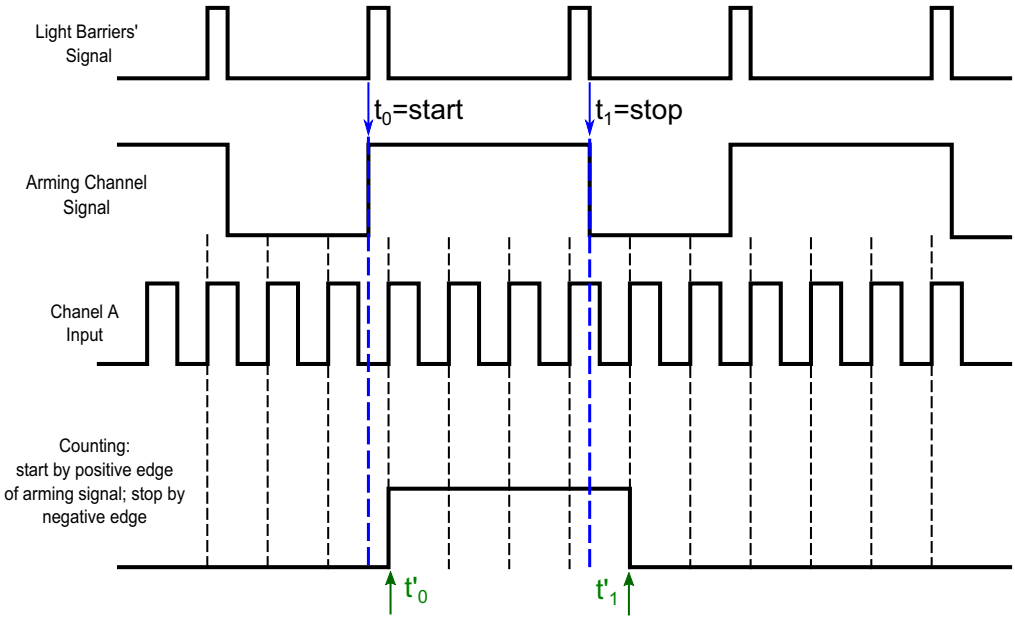

Figure 3.17: Signal sequences in the counter HP5334B INPUT channels.

to 780.0327 nm, as was measured in the already running experiment in another lab. The lambda-meter in this experiment uses He-Ne laser as a reference. In this way it was easier to find the correct wavelengths for our experiment. The vacuum wavelength of our reference is known and it is straightforward to estimate the reference wavelength at the lab conditions (see also section 3.5.2). It equals 780.041998 nm. Knowing the ratio between the measured and the reference wavelengths from the second column, it is easy to calibrate the measured wavelengths values to the correct reference wavelength. The corresponding values are given in the third column. The fourth column gives the wavelengths in vacuum and the last, fifth, column contains the literature values for comparison.

With average $\epsilon = 1$, $M_u = 6$ and $N_u = 1.5 \times 10^6$ (for $\Delta x = 4 * 35\,\text{cm}$ and $\lambda_u = 934.94437\,\text{nm}$), the first term in equation 3.40 is about 1.11×10^{-7} for a given infrared wavelength. In the similar way the first term was calculated for other wavelengths and the results are given in the second column of Table 3.2.

The second term gives an uncertainty of the reference wavelength λ_{ref} equal to 2.6×10^{-9}.

The third term gives the error in the measured vacuum wavelength due to the uncertainty of the ratio $r = \frac{n_u}{n_{ref}}$ of the refractive indices of air at two wavelengths λ_u

Isotope	Measured in lab λ #	Measured in lab λ	Vacuum λ	Vacuum λ measured lit.
$^{171}Yb^{+}$	369.42138(8) nm	369.42578(8) nm	369.52587(8) nm	369.52604(6) nm *
	398.79874(7) nm	398.80349(7) nm	398.91085(7) nm	398.91070(6) nm *
	638.44045 nm	638.448806 nm	638.61680 nm	638.616 nm ◇
	638.43941 nm	638.44702 nm	638.61501 nm	638.610 nm ◇
	934.93323(16) nm	934.94437(16) nm	935.18853(16) nm	935.18768(19) nm *
^{87}Rb (D_2)				780.24121 nm †
(cross-over 2,3)	780.0327 nm	780.041998 nm		780.24629 nm †

Table 3.1: $^{171}Yb^{+}$ transitions measured by our wave-meter. Vacuum wavelengths were calculated for the following conditions in the lab: pressure 983 ± 14 hPa, temperature 20 ± 0.75°C, $CO_2 \simeq 0.040 \pm 0.005\%$, humidity 56 ± 4.5%.
** [McLoughlin et al., 2011]; ◇ [Roberts et al., 1999]; † [Steck, 2010]*

Isotope	Measured in lab λ	$\frac{\epsilon}{M_u \cdot N_u}$	$\frac{\Delta r}{r}$	$\frac{\Delta \lambda_u}{\lambda_u}$
$^{171}Yb^{+}$	369.42578(8) nm	0.44×10^{-7}	1.52×10^{-7}	1.99×10^{-7}
	398.80349(7) nm	0.48×10^{-7}	1.24×10^{-7}	1.75×10^{-7}
	638.448806 nm	0.76×10^{-7}	2.08×10^{-8}	0.99×10^{-7}
	934.94437(16) nm	1.11×10^{-7}	1.76×10^{-8}	1.31×10^{-7}

Table 3.2: Calculated uncertainties for different wavelengths measured with our wave-meter were calculated for the following conditions in the lab: pressure 983 ± 14 hPa, temperature 20 ± 0.75 °C, $CO_2 \simeq 0.040 \pm 0.005\%$, humidity 56 ± 4.5%. Here, $\frac{\epsilon}{M_u \cdot N_u}$ represents the counting error, $\frac{\Delta r}{r}$ is the error in the measured wavelength due to the uncertainty of the ratio $r = \frac{n_u}{n_{ref}}$ of the refractive indices and $\frac{\Delta \lambda_u}{\lambda_u}$ is the total uncertainty of the wavelength.

and λ_{ref}. There are several different methods used to calculate the refractive index of air. Here, the Ciddor equation and a modified version of the Edlén equation were used. One can find the useful information about these equations in [Stone & Zemmerman, 2010]. Note that it is straightforward to go from vacuum to standard

Measured in lab λ	LSD
369.42578 nm	0.88×10^{-7}
398.80349 nm	0.95×10^{-7}
638.448806 nm	1.52×10^{-7}
934.94437 nm	2.22×10^{-7}

Table 3.3: Counter resolution for different measured wavelengths. Here, LSD is the Least Significant Digit and resolution is ±LSD.

air wavelengths with those equations. The inverse process, as in the current work, requires iterations, since the refractive index **n** is a function of *vacuum* wavelength. Three iterations are usually sufficient [Kaufmann, 2012] to find out the value of **n**. Further discussions about the air refractive index can be also found in [Owens, 1967] and [Castell *et al.*, 1985]. Additional information about the air relative humidity can be found in [Pulinets *et al.*, 2006]. The uncertainty of the third term was investigated for changes in temperature, humidity, concentration of CO2 and dry air partial pressure. The conditions in the lab were mentioned above in section 3.5.2. Pressure is the most crucial parameter. Reducing the pressure error from the current 14 hPa to 1 hPa will decrease the error of the ratio of the refractive indices $\frac{\Delta r}{r}$ by one order of magnitude (from 10^{-7} to 10^{-8}). The uncertainties of the third term for different measured wavelengths are given in the third column of Table 3.2.

The fourth term takes into account the systematic errors due to the misalignments of the two laser beams within the interferometer. As a result, the two path lengths for λ_{ref} and λ_u differ by $\delta x \approx (\alpha^2/2) \cdot \Delta x_{ref}$, where α is an inclination angle between the beams of the reference and the measured signals [Demtröder, 2008]. This error was not estimated in our experiment.

The last term $\delta\phi$ is the phase variation in the detector plane, where the phase is averaged over the cross-section of the beam. If the modulation of the interference intensity, described by equation 3.36, exceeds 90%, this term may be neglected [Demtröder, 2008].

The wave-meter built in our lab gives estimated relative errors in the range of $0.99 - 1.99 \times 10^{-7}$ depending on the measured wavelength in the last column of Table 3.2. The errors that are given in the round brackets together with the measured wavelengths are the errors observed in the experiment. They match the estimated errors in case the pressure error is in the range of 14-16 hPa.

Each counter is characterized by its own resolution that is limited by its electronics. For the HP5334B counter used in the current experiment the Least Significant Digit (LSD) equals $4 \times ratio/(M_{ref} \cdot N_{ref})$, where $ratio = \lambda_u/\lambda_{ref}$, and resolution is $\pm$ LSD, according to the manual. LSD values for different wavelengths used in the current experiment are given in Table 3.3. As it is possible to see the counter limits the precision of the 638.448806 nm and 934.94437 nm wavelengths. Hence, the observed errors for these wavelengths are higher than the estimated one.

3.6 Static Magnetic Fields

The static magnetic fields are necessary in the experiment for three reasons: i) to lift the degeneracy of the $^2S_{1/2}$ $(F = 1)$ $^{171}Yb^+$ hyperfine ion state; ii) to define the quantization axis of the transitions in the trapped ions and iii) to compensate for the disturbing magnetic fields of the Earth, of the vacuum pump etc. For the quantization axis the direction of the static magnetic field is important and we would like to set it parallel to the trap axis defined by the end-cap electrodes of the linear trap. Here, the coordinates convention is the one used during the simulation: the x-axis lies along the end-cap electrodes, y-axis is perpendicular and in the plane with the x-axis and the z-axis is perpendicular to the xy-plane. Hence, the magnetic field in the x-direction has to be stronger than in the other two directions. Besides, this field has to be homogeneous in a 5 mm wide region of the trap, corresponding to the distance between the end-cap electrodes. It is known that Helmholtz coils can be used to generate a very homogeneous magnetic field. In order to be able to control the quantization axis along arbitrary directions, three pairs of Helmholtz coils are required. The complete system of these three pairs of coils should be easily removable, since at the beginning of the experiment the chamber has very often to be baked out to achieve the necessary ultra-high vacuum conditions.

3.6.1 Simulation

Simulations have been done by Simon Viel using the BiotSavart program [11] that runs in Java within Mathematica. The initial idea was to generate a magnetic field of about 50 Gauss in the center of the trap in the x-direction (main coils) and about 5 Gauss in the y- and z- directions. The magnetic field in the x-direction is supposed to be larger (about 10 times should suffice) than in the other two directions since we wanted a strongly defined quantization axis along the linear trap axis. The simulation started with circular-shaped coils, as a perfect Helmholtz configuration requires. The maximum possible amount of loops in the coils as well as the radius and the distance between the coils were limited by the size of the chamber itself. For the main coils the magnetic field in the center of the trap resulted in just 30 Gauss and they consist of 360 loops in 9 rows with a circular shape of 38 mm radius, thickness of 40 mm, minimal possible distance between the coils of 196 mm and a current of 4.5 A. The magnetic field changes by 0.32 Gauss over 5 mm in both directions from the center of the trap.

[11] The programm has been written by M.Johanning.

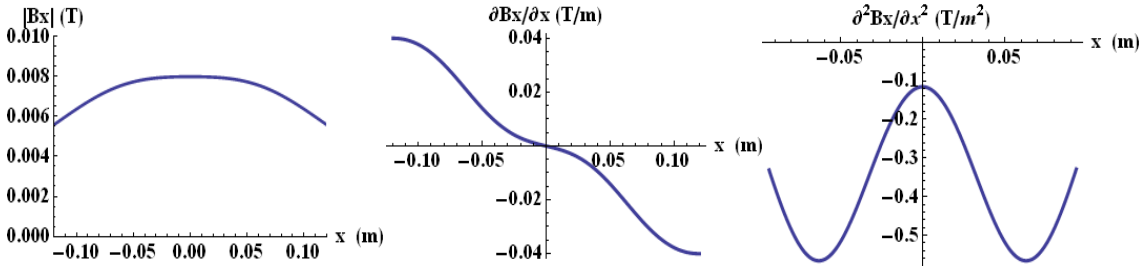

Figure 3.18: Simulation results for the pair of main rectangular coils for the x*-direction. Left: magnetic field in* x*-direction; Center: gradient of the magnetic field; Right: second derivative of the magnetic field. All the values are plotted versus the distance in* x*-direction in the range of* -120 *mm to* 120 *mm. The zero point corresponds to half a distance between the corresponding coils.*

To increase the strength of the magnetic field a configuration with a pair of rectangular coils was considered. In this case it is possible to make smaller the width of the coil in the horizontal direction and, therefore, to bring both coils closer to each other. The main rectangular coils, named shortly Big1 and Big2 coils, consist of 290 loops divided in 10 columns (number of wires in horizontal direction, total number gives a depth of the coil) and 29 rows (number of wires in vertical direction). The diameter of the copper wire is 1 mm. The same wire was used for the windings of all the coils. The inner width and the height of the main coils equals 200 mm and 420 mm, correspondingly. With a separation between the coils of 125 mm and the current of 4.5 A the magnetic field in the trap center equals 79.8 Gauss. As it is possible to see also in Figure 3.18, the magnetic field is quite homogeneous over 5 mm distance between the end-cap electrodes: at 5 mm from the trap center the field is changed by just 0.015 Gauss, in each direction. In the perpendicular y-direction the field changes by 0.008 Gauss over 5 mm. Three graphs are presented in Figure 3.18: the absolute value of the magnetic field between the two coils in the range of -120 mm to 120 mm, the gradient and the second derivative of the magnetic field in the same range. The minimum of the second derivative (its absolute value) indicates where the gradient is the smallest. As it is possible to see, the minimum lies in the region of the trap center.

The other smaller rectangular coils, designated SmallUp and SmallDown, aimed to compensate the magnetic field in the y-direction, consist of 100 loops in 10 columns and 10 rows. The inner width and height are 90 mm and 240 mm, respectively. The distance between them is 230 mm. For a current of 1.5 A the predicted magnetic field in the center of the trap produced by these coils equals 4.2 Gauss. The minimum gradient, as its possible to see in Figure 3.19, in the range of -100 mm to 100 mm is in the center of the trap. The magnetic field changes over the distance

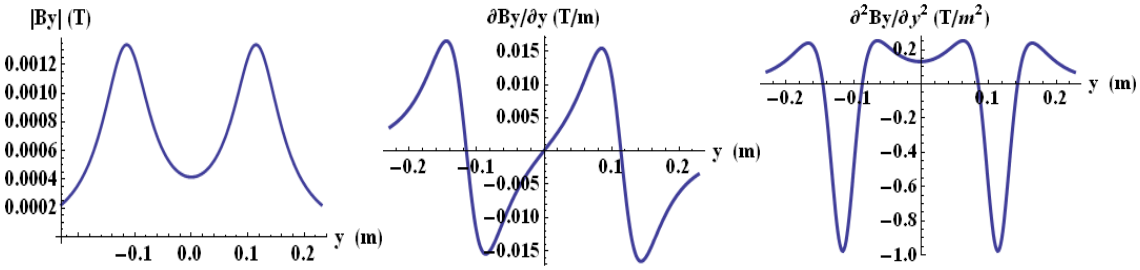

Figure 3.19: Simulation results for the pair of rectangular coils for the y*-direction. Left: magnetic field in* y*-direction; Center: gradient of this magnetic field; Right: second derivative of the magnetic field. All the values are plotted versus the distance in* y*-direction in the range of* $-230\,$*mm to* $230\,$*mm. The zero point corresponds to half a distance between the corresponding coils.*

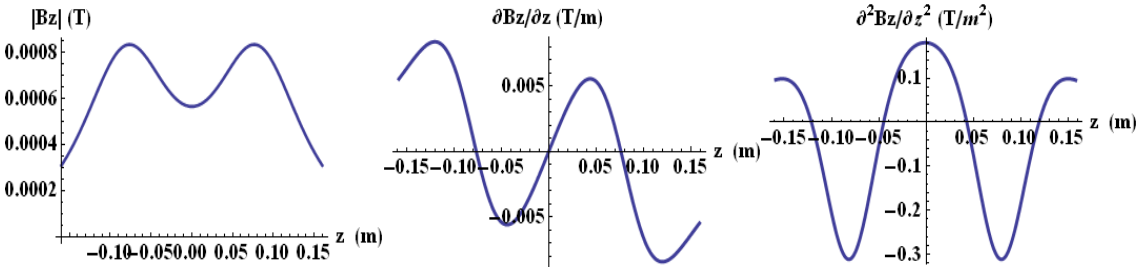

Figure 3.20: Simulation results for the pair of circular coils for the z*-direction. Left: magnetic field in* z*-direction; Center: gradient of this magnetic field; Right: second derivative of the magnetic field. All the values are plotted versus the distance in* z*-direction in the range of* $-160\,$*mm to* $160\,$*mm. The zero point corresponds to half a distance between the corresponding coils.*

of 5 mm in both y-directions from the center of the coils by 0.016 Gauss. In x-direction the change of the magnetic field over 5 mm in both directions from the center is 0.014 Gauss and it is comparable to the gradient produced in the center of the trap by the main coils.

Two circular coils, named RoundC and RoundW, for the magnetic field in z-direction consist of 100 loops of wire arranged in 10 rows and 10 columns. The inner radius of each coil is 78 mm. The simulation was performed for the distance between the coils of 160 mm and the current in the coils of 1 A. The calculated magnetic field is 5.7 Gauss. The magnetic field changes by 0.022 Gauss over 5 mm in z-direction and by 0.011 Gauss over 5 mm in x-direction. The simulation results for these coils are presented in Figure 3.20.

The magnetic field at different distances from the trap center can be found using

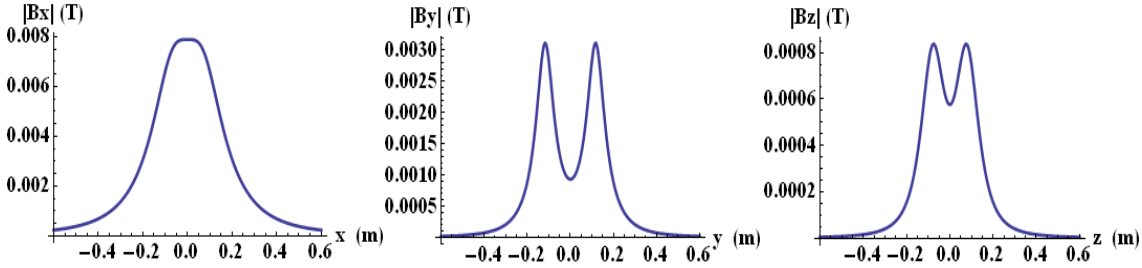

Figure 3.21: Simulation results of the magnetic field for the three different pairs of coils. Left: for the main rectangular coils producing the magnetic field in x*-direction; Center: for the small rectangular coils in* y*-direction; Right: for the circular coils in z-direction. The zero point corresponds to half a distance between the corresponding coils.*

the Taylor expansion:

$$B(x) = B_0 + \frac{\partial B}{\partial x} \cdot x + \frac{1}{2} \cdot \frac{\partial^2 B}{\partial x^2} \cdot x^2 + ..., \tag{3.41}$$

where the first term B_0 is the magnetic field in the center between two coils, the second term is the gradient of the magnetic field at a distance x from the center multiplied by this distance and the last term is the curvature of the magnetic field at distance x multiplied by the square of this distance and divided by the factorial of two. The second derivative demonstrates how fast the gradient changes at different points between the coils. In our case it proves that the fields in the region of the trap between the end-cap electrodes are quite homogeneous. The magnetic field simulation results for the three different pairs of coils are presented in Figure 3.21.

3.6.2 Construction and first tests of the static field coils

The ready assembly of the three pairs of static field coils is presented in Figure 3.22. Prior to the construction of the coils the amount of resistive dissipation during the coils' operation has been considered. The calculations are presented in Appendix G together with the discussion about the coils' frame material choice and measurements of the frames' temperature changes over the long operational times.

The measurements of the ready coils have been performed using a Hall sensor [Toyo Corporation, August 2010] and a Gauss/Teslameter (see Appendix P). The

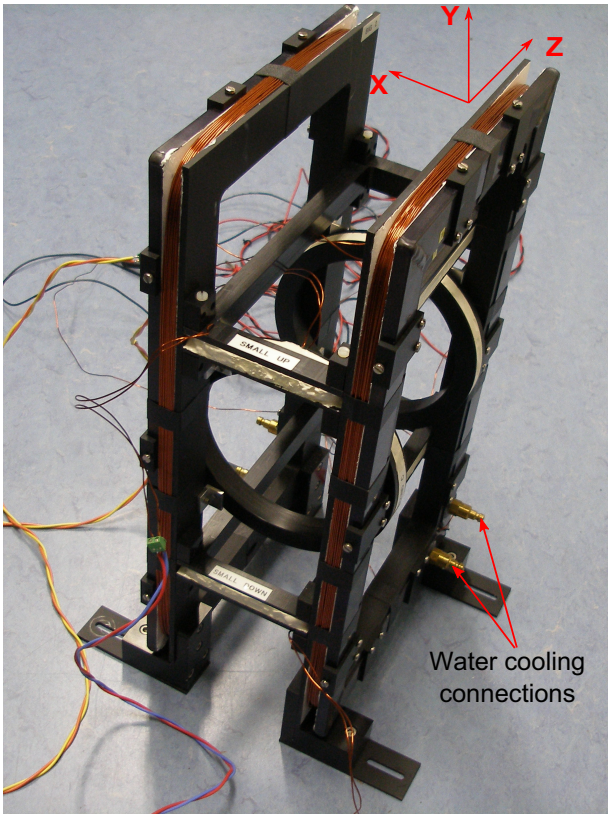

Figure 3.22: Ready three-pair static field coil configuration.

results of the simulations and measurements are summarized in Table 3.4, Table 3.5 and Table 3.6. B_x is the magnetic field created by the main rectangular coils, B_y is created by the small rectangular coils and B_z is created by the circular coils. In Table 3.4 the values of the magnetic field produced at half the distance between the coils pair (zero point) is compared to the corresponding simulations results. The measurements and the simulation were performed in two directions: in the direction between the coils pair (x-, y- and z-directions) and in the direction between the main coils (x-direction) that defines the quantization axis. In Table 3.5 the measured and simulated magnetic gradient values over the 5 mm in both directions around the zero point are compared. In Table 3.6 together with the simulated and the measured magnetic fields at half the distance between the coils' pair the dimensions of the coils and the corresponding settings are given.

The measured values of the magnetic field agree very well with the simulation prediction. Slight differences can be caused by the fact that the real coils construction is not ideal, the distances between the coils are not exactly as in simulation. Slightly different currents on two coils of the pair can be used to achieve the same

Magnetic Field (Gauss)	Zero Point		
	x-dir.	y-dir.	z-dir.
B_z^{sim}	5.7		5.7
B_z^{meas}	4.9		5.0
B_y^{sim}	4.2	4.2	
B_y^{meas}	3.9	3.9	
B_x^{sim}	79.8	79.8	
B_x^{meas}	76.1	77.7	

Table 3.4: Simulated and measured magnetic field values for the three pairs of coils. The zero point corresponds to half a distance between the corresponding coils.

Magnetic Field Change (Gauss)	−5 mm			5 mm		
	x-dir.	y-dir.	z-dir.	x-dir.	y-dir.	z-dir.
B_z^{sim}	0.011		0.022	0.011		0.022
B_z^{meas}	0.007		0.017	0.011		0.014
B_y^{sim}	0.014	0.016	0.014	0.016		
B_y^{meas}	0.012	0.012		0.013	0.02	
B_x^{sim}	0.015	0.008		0.015	0.008	
B_x^{meas}	0.03	0.01		0.03	0.01	

Table 3.5: Simulated and measured magnetic field changes for the three pairs of coils. The changes were considered over the 5 mm distance from the zero point in both directions. The zero point corresponds to half a distance between the corresponding coils.

magnetic field as in simulations.

The main rectangular coils magnetic field B_x was measured to be 76.1 Gauss at the center and between the coils. The gradient was definitely smaller than in case of another pair of coils. Hence, the Hall sensor resolution was not sufficient to distinguish the tiny differences in the magnetic field away from the coils' center. The measurements gave a magnetic field change of 0.03 Gauss over 5 mm distance around the center, but it can not be trusted since the field changes lie far beyond the resolution of the Gauss/Teslameter. In the perpendicular direction the magnetic field B_x in the center resulted in 77.7 Gauss, closer to the simulation results. The field changes in this direction over 5 mm are 0.01 Gauss, not reliable as well.

Type	Dim (mm)	# Loops	h (mm)	I (A)	B_{sim} (Gauss)	B_{meas} (Gauss)
RECTANGULAR (Big1 & Big2, x-direction)	420×200×10	290 29 rows × 10 columns	125	4.5	79.8	76.1
RECTANGULAR (SmallUp & SmallDown, y-direction)	240×90×10	100 10 rows × 10 columns	230	1.5	4.2	3.9
Circular (RoundC & RoundW, z-direction)	78×10	100 10 rows × 10 columns	160	1.0	5.7	5.0

Table 3.6: Magnetic fields at half the distance between the corresponding pair of coils. Here, Dim(mm) for rectangular coils is the internal height × width × length, for circular coils is internal radius × length; # Loops is the loops of wire arranged in n rows and n columns; h(mm) is the distance between the coils; I is the current; B_{sim} is the magnetic field obtained in the simulation; B_{meas} is the measured magnetic field.

The currents used for the Helmholtz coils in the current experiment are summarized in Appendix Q.4, Table Q.2. They were chosen during the experiment to achieve a direction of the static magnetic field parallel to the trap axis. Additionally, the relations for the components of the magnetic field in dependence on the applied current are also given in Appendix Q.4. The relations are valid for the coils when they are connected in series.

3.7 Polarization in the Experiment

The polarizations of the laser beams plays an important role in the experiment. The orientation of the respective polarizations are determined by the orientation of the magnetic field $\vec{B}_0$ causing the Zeeman splitting and defining the quantization axis. This static field is created by the three pairs of Helmholtz coils as it was described in section 3.6. In the experiment we work with electric (i.e. $^2S_{1/2} \leftrightarrow {}^2P_{1/2}$, $^2D_{3/2} \leftrightarrow {}^3D[3/2]_{1/2}$) and magnetic ($^2S_{1/2}$, $F = 0 \leftrightarrow {}^2S_{1/2}$, $F = 1$) dipole transitions. A linearly polarized transition, denoted as π-transition, is a transition without a change of angular momentum ($\triangle m_j$ or $\triangle m_F = 0$). The transitions with $\triangle m_j$ or $\triangle m_F = \pm 1$ are called circular polarized transitions and they are denoted as $\sigma^{\pm}$-transitions. All the transitions of the different polarizations for the $^2S_{1/2} \leftrightarrow {}^2P_{1/2}$ levels in the $^{171}Yb^+$ ion are demonstrated in Figure 3.23.

To drive the π-polarization in an electric dipole transition the electric component $\vec{E}$ of the *linear* polarized laser beam should be parallel to the coils magnetic field ($\vec{E} \| \vec{B}_0$). In case that $\vec{E}$ of the *linear* polarized laser beam is perpendicular to the static magnetic field ($\vec{E} \perp \vec{B}_0$), both σ^+- and σ^--transition are driven at the same

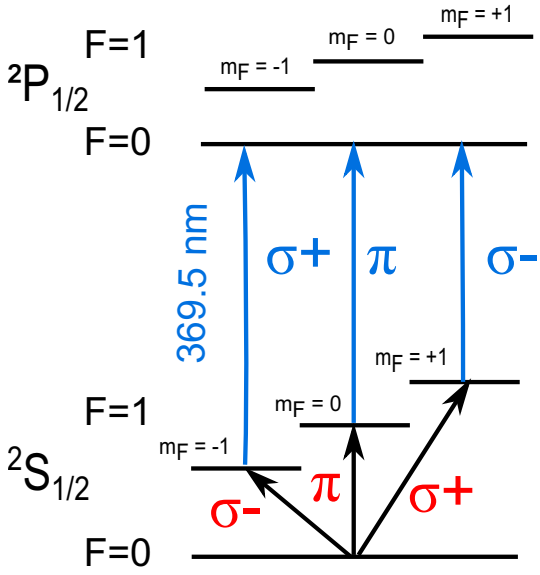

*Figure 3.23: Qubit (*magnetic dipole*) and cooling (*electric dipole*) transitions of the* $^{171}Yb^+$ *ion showing different types of the atomic polarizations.*

time.

The $^{171}Yb^+$ ion qubit manipulations are realized on the hyperfine levels $^2S_{1/2}$, $F = 0 \leftrightarrow {}^2S_{1/2}$, $F = 1$ driven by the microwave radiation at about 12.65 GHz. For the magnetic dipole transition of the hyperfine splitting the π-transition is excited when the electric component $\vec{E}$ of the microwave field is perpendicular to the coils magnetic field ($\vec{E} \perp \vec{B}_0$) and $\sigma^{\pm}$-transitions are excited when the electric component $\vec{E}$ of the microwave field is parallel to the coils magnetic field ($\vec{E} \| \vec{B}_0$). This is a standard convention. In this work different convention is used for the magnetic dipole, where the magnetic, and not electric, component of the microwave field defines the notation of the transition. Therefore, the π-transition of the hyperfine splitting is driven when the microwave magnetic field is parallel to the static magnetic field ($\vec{B}_{mw} \| \vec{B}_0$) and $\sigma^{\pm}$-transitions are driven simultaneously when the microwave magnetic field is perpendicular to the static magnetic field ($\vec{B}_{mw} \perp \vec{B}_0$). The same convention is shown in Figure 3.23 for the hyperfine split levels.

If one wants to drive the π- and $\sigma^{\pm}$-transitions simultaneously, the electric ($\vec{E}$) or/and magnetic ($\vec{B}_{mw}$) fields of the driving radiation should be at 45° with the static magnetic field $\vec{B}_0$.

In our experiment the static magnetic field $\vec{B}_0$ is along the trap axis (section

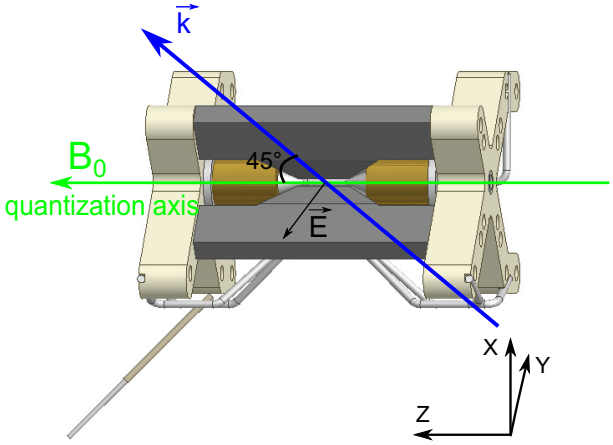

Figure 3.24: Relative directions of the propagation vector $\vec{k}$ and electric field $\vec{E}$ of the laser beams with respect to the static magnetic field $\vec{B}_0$ that defines the quantization axis (green) and is created by the three pairs of the Helmholtz coils.

3.6) and the propagation vectors $\vec{k}$ of all four lasers mentioned in section 3.3 are at 45° with respect to this axis. The coordinates convention used in the current experiment is shown in Figure 3.24. The lasers electric fields $\vec{E}$ are as well at 45° to the $\vec{B}_0$ driving π- and $\sigma^{\pm}$-transitions simultaneously, for all the laser wavelengths. The advantage of this is a more efficient repumping and cooling of the $^{171}Yb^{+}$ ions due to the minimized optical pumping into the sublevels of the $^2S_{1/2}$ ($F = 1$), $^2D_{3/2}$ ($F = 1$) and $^2F_{7/2}$ ($F = 3$ and $F = 4$) levels. The direction of the static magnetic field and propagation vector of the laser with respect to the trap axis are depicted in the same Figure 3.24. Another advantage is that directing the 369 nm laser at 45° to the trap axis two velocity components of the ion are cooled simultaneously.

Additionally, in the experiments that involve the $^2D_{3/2}$ state the polarization plays also an important role. For example, in the even isotope $^{172}Yb^{+}$ the Zeeman splitting lifts the degeneracy of four states: $^2D_{3/2}$ ($m_j = \pm 3/2$) and $^2D_{3/2}$ ($m_j = \pm 1/2$). It is possible to populate any of these states by choice using the different polarizations of the 935 nm laser beam. If the ion decays from the $P_{1/2}$ level into the $D_{3/2}, m_j = \pm 1/2$ states, the π-polarized light at 935 nm transfers the ion into the $[3/2]_{1/2}$ state, from where it rapidly decays into the $S_{1/2}$ ground-state. But if the ion decays into the $D_{3/2}, m_j = \pm 3/2$ states, a photon with σ-polarization of the 935 nm laser light is needed to bring the ion into the $[3/2]_{1/2}$ level. Choosing only the π-polarization assures that the ion remains in the $D_{3/2}, m_j = \pm 3/2$ states.

3.8 Microwave

Microwave radiation in resonance with the $^2S_{1/2}$ (F=0, $m_F = 0$) $\leftrightarrow$ $^2S_{1/2}$ (F=1, $m_F = 0$) transition of the $^{171}Yb^+$ ion at about 12.642828 GHz (π-transition) is necessary to prevent interruption of the cooling and detection cycles due to the optical pumping into the $^2S_{1/2}$ (F=0, $m_F = 0$) state. Additionally, microwave radiation is used for qubit manipulations i.e. one qubit rotations and, in the presence of magnetic field gradient, conditional quantum dynamics.

3.8.1 Microwave setup

Microwave radiation is obtained by mixing a phase coherent and controllable radio-frequency signal of 1 - 150 MHz from a versatile frequency generator (VFG150) with a high frequency oscillator at 12.568 GHz using a double-balanced mixer. Both devices are locked to a 10 MHz reference signal (Rubidium atomic clock). The resulting signal is amplified up to $\sim$ 2.5 W using a chain of amplifiers and is passed to a microwave circular waveguide situated in the vacuum chamber in close proximity to the trap center. The microwave setup overview is presented in Figure 3.25. The measurements in this thesis were performed only with one antenna of the waveguide. Therefore, power splitter and digital phase shifter were not included in the current setup but they will be certainly used in the future experiments.

3.8.2 Microwave circular waveguide

It is important to increase the microwave field at the location of the ions and, respectively, to achieve high Rabi frequencies (see equation 2.43). The stronger the magnetic momentum of the ion is coupled to the external field, the faster is the quantum gate operations and that can help to overcome some dephasing errors due to, for example, the ambient magnetic field fluctuations that cause the Zeeman shift of the qubit levels. To resolve individual ionic resonances with small cross-talks, the Rabi frequency of the hyperfine transition has to be, nevertheless, smaller than the frequency separation of the Zeeman resonances of neighboring ions. In the current experiment with the gradient of 19 T/m, a typical separation of the ions in the frequency space equals $\approx$ 3 MHz (see section 6.4). This value sets the limit for the highest possible Rabi frequency in the experiment, that is, indeed, not so easy to obtain. In the previous experiments [Timoney, 2010], a commercial horn antenna was used. It was situated outside the vacuum chamber at around

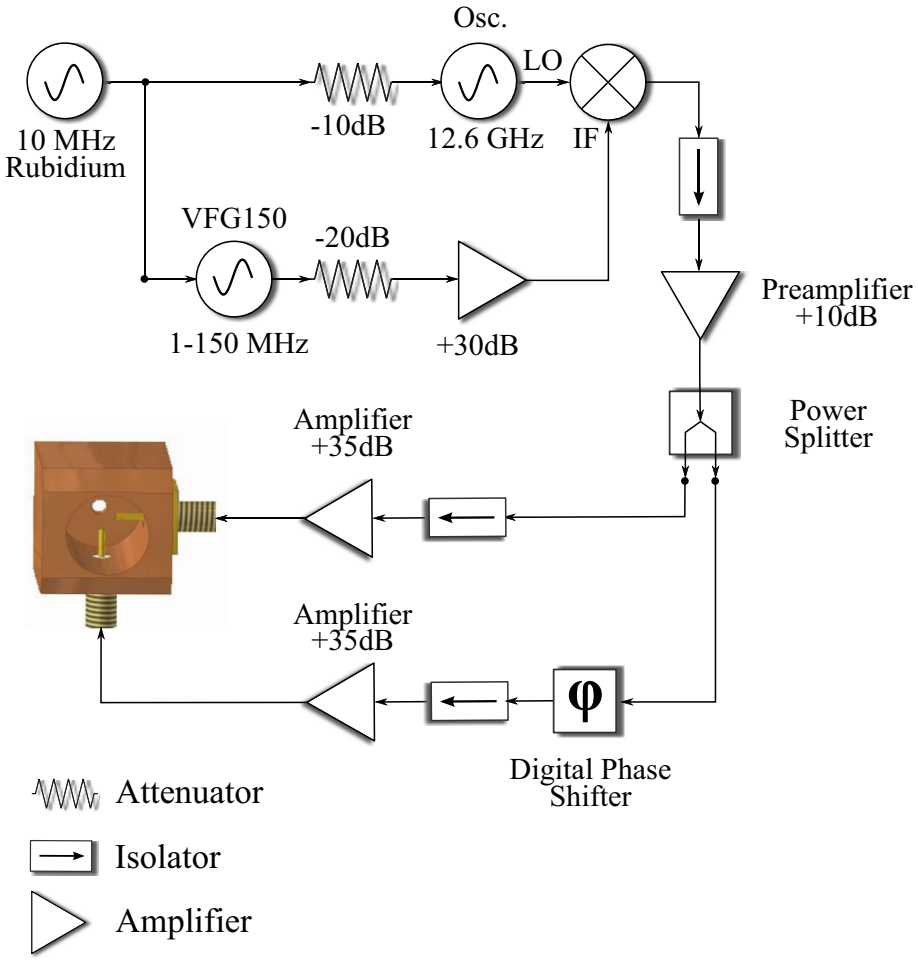

Figure 3.25: Microwave setup diagram. The RF signal of 1 - 150 MHz from VFG150 is mixed using a double-balanced mixer with a HF oscillator at 12.568 GHz. Both devices are locked to 10 MHz Rubidium atomic clock. The signal is then passed to the microwave waveguide antenna through the preamplifier of +10 dB and amplifier of +35 dB. Power splitter divides the power between two antennas and digital phase shifter sets the phase between the two antennas. In the current setup both these devices are not included in the current setup since only one antenna was used.

3.5-4 cm distance from the ions. With $\sim$ 4 W power fed into the antenna, the maximum Rabi frequency is in the range of 30 kHz. Since the power transmitted via the antenna is inversely proportional to the square of the distance from the antenna, we decided to put our antenna directly into the vacuum, closer to the ions. In this way, choosing the waveguide, we try to minimize the power losses and to guide the microwave power at 12.6 GHz directly in the proximity of the ions. The maximum Rabi frequency at 2.5 W is about 60 kHz, approximately 2.5 times higher than the Rabi frequency obtained at the same power using the commercial horn antenna in the previous experiments. Besides, we would like to control the different transitions of the hyperfine levels of the $^{171}Yb^+$ ions: π and σ^+/σ^-. It is easy to provide two probes (monopole antennas) in the waveguide that will be perpendicular to each other and will excite the waves with different polarization directions, as it is required. We choose the circular waveguide because it is suited better to carry electromagnetic waves with a circular polarization.

Theory

In order to find the optimal parameters for the circular waveguide at 12.64 GHz, measurements already made by Paul Walde for the 10 GHz circular waveguide were taken as a reference [Walde, 2001]. A suitable circular waveguide inner diameter for 12.64 GHz was estimated to be $\frac{10\,\mathrm{GHz}}{12.64\,\mathrm{GHz}} \times 20.6\,\mathrm{mm} = 16.3\,\mathrm{mm}$, where $20.6\,\mathrm{mm} = 0.81$ inches was the inner diameter of the tube used in [Walde, 2001] for the 10 GHz circular waveguide.

The inner diameter of the circular waveguide has to be chosen properly in order to allow for dominant modes propagation. The dominant mode is the mode with a lowest cutoff frequency f_c below which the wave will not propagate anymore. In a circular waveguide the dominant mode by definition is TE_{11}. The next mode is TM_{01}. Modes are shown in Figure 3.26.

The general formula for the cutoff wavelengths $\lambda_c = c/f_c$, with c - speed of light, of the TE_{nm} modes is ([Silver, 1997])

$$\lambda_{c,nm} = \frac{2\pi \cdot r}{p'_{nm}} \tag{3.42}$$

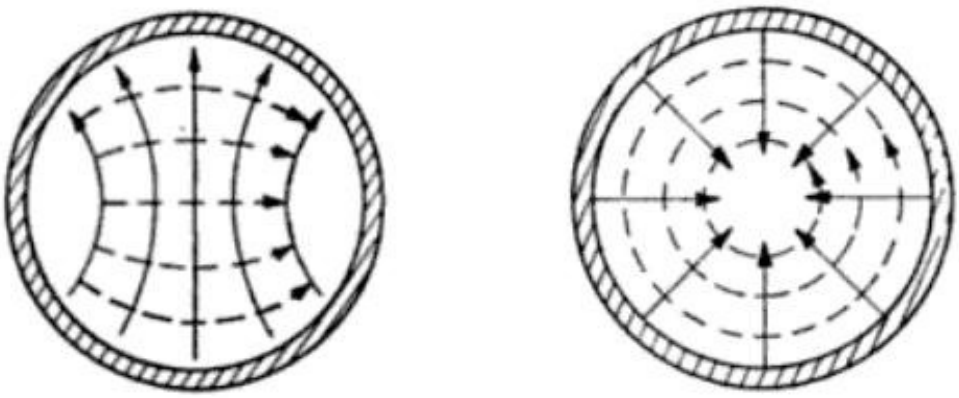

(a) (b)

Figure 3.26: (a) TE_{11}-mode and (b) TM_{01}-mode of the circular waveguide, from [Silver, 1997]. Solid line - electric field; dashed line - magnetic field.

n	p_{n1}	p_{n2}	p_{n3}
0	2.405	5.520	8.654
1	3.832	7.016	10.174
2	5.135	8.417	11.620

(a)

n	p'_{n1}	p'_{n2}	p'_{n3}
0	3.832	7.016	10.174
1	1.841	5.331	8.536
2	3.054	6.706	9.970

(b)

Table 3.7: (a) Values of p_{nm} for TM Modes; (b) Values of p'_{nm} for TE Modes

and for the TM_{nm} modes

$$\lambda_{c,nm} = \frac{2\pi \cdot r}{p_{nm}}. \tag{3.43}$$

Here, r is the inner radius of the waveguide, p_{nm} and p'_{nm} define the m^{th} zero of the n^{th}-order Bessel function and Bessel function derivative, respectively. The values of these zeros for TE (TM) modes are shown in Table 3.7.

Therefore, the cutoff wavelengths for the TE_{11} and TM_{01} modes of the circular waveguide are

$$\lambda_{c,TE_{11}} = 1.706 \times D \tag{3.44}$$

and

$$\lambda_{c,TM_{01}} = 1.306 \times D, \tag{3.45}$$

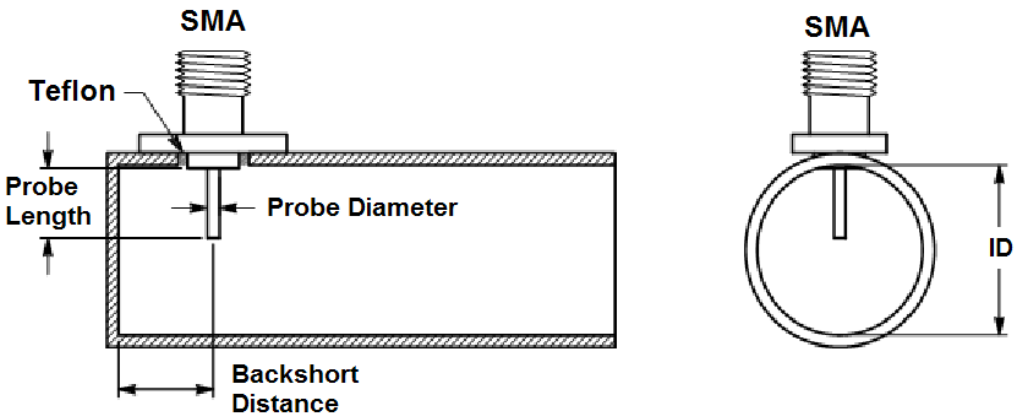

Figure 3.27: Schematics of the circular waveguide, from [Walde, 2001].

correspondingly. Here, $D = 2 \cdot r$ is the circular waveguide inner diameter. The minimum waveguide diameter is, therefore, $0.59\lambda_{c,TE_{11}}$. The next mode needs the minimum inner diameter of $0.76\lambda_{c,TM_{01}}$ to propagate.

The waveguide with the inner diameter of $\sim 16\,\text{mm}$ has the cutoff frequency for the TE_{11} mode equal to 11 GHz, sufficient to allow the propagation of the wave at 12.64 GHz. The next mode, TM_{01}, sets the maximum operating frequency for the 16 mm inner diameter circular waveguide equal to 14.25 GHz, defining the maximum limit for a single mode propagation.

Our waveguide is connected through coaxial cables to the microwave source and the impedances of the waveguide and the source need to be well-matched in order to reduce power loss of the traveling wave. There are three further circular waveguide parameters that help to transform the waveguide impedance to a desired impedance of usually $50\,\Omega$: probe diameter, probe length and distance to the backshort (see Figure 3.27). The last refers to the short circuit at the end of the waveguide behind the probe. The probe is used to feed the microwave radiation into the waveguide.

Several measurements have been performed by [Walde, 2001] to find an optimum probe length and backshort distance for a given probe diameter in order to reduce the SWR and the results were plotted on Smith charts. Although the measurements in [Walde, 2001] were made for the 10 GHz circular waveguide, it was also claimed in the article that it is possible to scale directly the dimensions of the

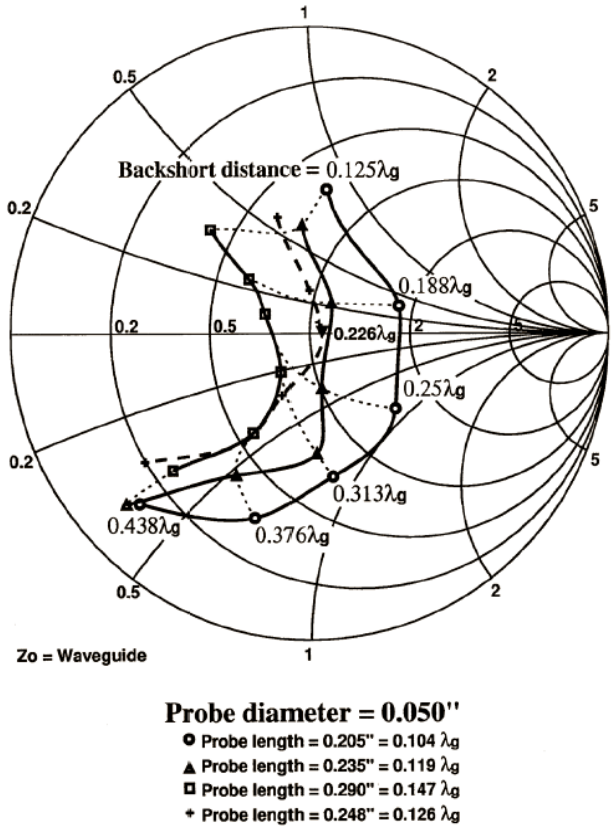

Figure 3.28: SWR curves for a 3/4 inch circular waveguide-to-coax transition. Probe diameter = 0.050 inches, from [Walde, 2001].

probe diameter, the probe length and the distance to the backshort for the frequency we are interested in to the ratio of the waveguide diameters, one of which is the fixed diameter of the 10 GHz circular waveguide. One need just to start with a convenient probe diameter and to take the rest of the parameter from Figure 3.29.

In our case the diameter ratio has the value of $\frac{16.3\,\mathrm{mm}}{20.6\,\mathrm{mm}} \sim 0.8$. The probe diameter for our waveguide was chosen to be **0.127 cm** or 0.05 inch. This is a standard diameter for the 50 Ω SMA connector center pin. The measured SWR curves for the probe diameter of 0.05 inch and a circular waveguide inner diameter of 0.81 inches, plotted on a Smith chart, are depicted in Figure 3.28. Here, the solid lines (three on the graph) represent the data for the same probe length but with the backshort

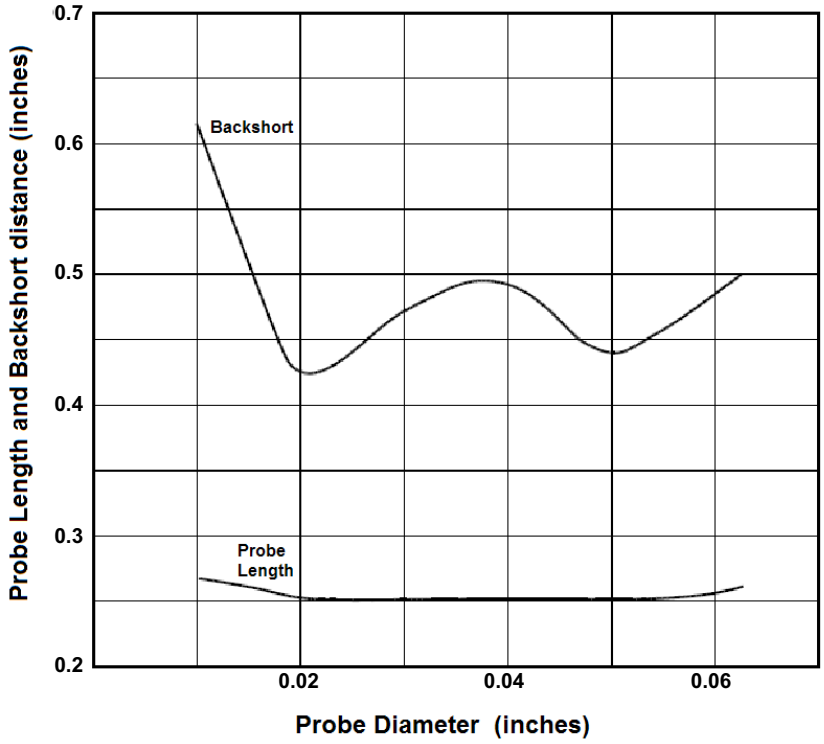

Figure 3.29: The 10 GHz circular waveguide best dimensions summary, from [Walde, 2001].

distance varying. The dashed curves, intersecting these lines, are plots for constant backshort distance with varying probe length. An additional dashed line, parallel to the solid lines, is an estimated optimal probe length. There is a point on this line that corresponds to the probe length of $0.126 \cdot \lambda_g = 0.248$ inches and backshort distance of $0.226 \cdot \lambda_g$, where λ_g is the wavelength inside the waveguide. It equals

$$\lambda_g = \frac{1}{\sqrt{(\frac{1}{\lambda_0})^2 - (\frac{1}{\lambda_c})^2}}, \tag{3.46}$$

where λ_0 is the wavelength in free space and λ_c is the cutoff wavelength. For a 10 GHz circular waveguide $\lambda_g = 1.97$ inches (5 cm). This point is close to the center of the Smith Chart, where the SWR is close to one.

We can now rescale these parameters for our circular waveguide at 12.64 GHz. Hence, the probe length will be 0.248 inches $\times$ 0.8 $\sim$ 0.20 inches (**0.51 cm**) and the backshort distance will be 0.226 inches $\times$ 0.8 $\times$ $\lambda_{g,10GHz} \sim$ 0.36 inches (**0.91 cm**).

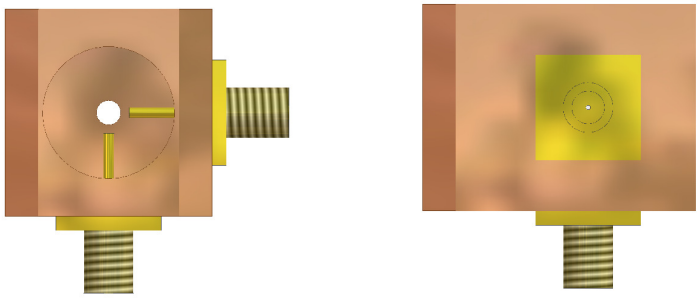

(a) (b)

Figure 3.30: (a) Front and (b) Side view of the designed 12.6 GHz circular waveguide used in our experiment.

Construction

The waveguide body is constructed from vacuum compatible OFHC copper and has a length of **33 mm**. The distance between the trap center and the waveguide front face is currently about **20 mm**, i.e. the center of the trap is in the near-field region of the microwave antenna, but it could be adjusted in the future experiments to maximize the magnetic field at the position of the ions. The edges of the waveguide are chamfered: the cut-off part is a right-angled triangle with equal sides of 4 mm and the right-angle top lying on the waveguide edge (see Figure 3.30). The edge chamfering was necessary in order to prevent blocking of the laser beams. The position of the waveguide in the vacuum chamber with respect to the ion trap can be seen in Figure 3.8 and in Figure 3.11 in section 3.4.

As it is possible to see in Figure 3.30, there are two probes, or monopole antennas, incorporated into the circular waveguide. They are perpendicular to each other and for both antennas the electric field vector is parallel to the antenna length direction and the magnetic field vector is perpendicular to both electric field vector and wave propagation vector.

If only one antenna is connected to the microwave source, the direction of electric and magnetic field does not change as the electromagnetic wave propagates inside the waveguide (the wave is linearly polarized). The antenna, directed parallel to the trap axis and, also, to the direction of the quantization axis (see chapter **??**

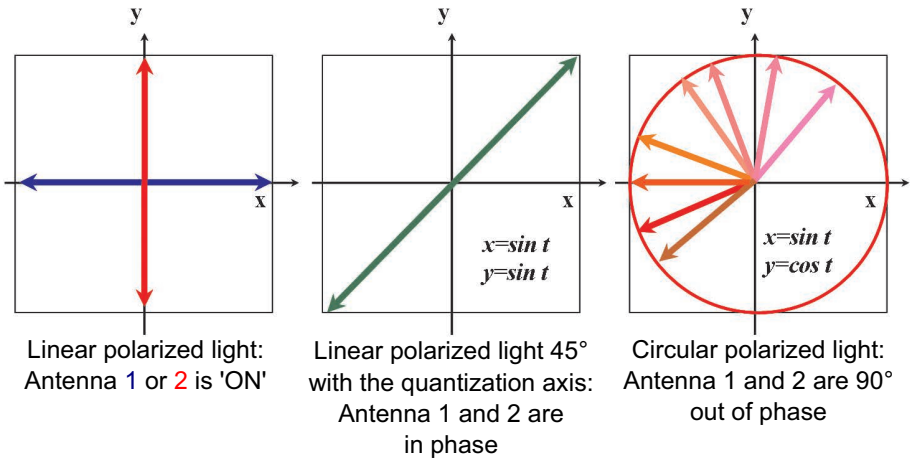

Figure 3.31: Polarization direction for the circular waveguide magnetic field.

and Figure 3.24), produces a magnetic field perpendicular to the quantization axis. Hence, the σ^+- and the σ^--transitions are driven. The antenna that is directed perpendicular to the trap axis, on the contrary, produces a magnetic field parallel to the quantization axis and the π-transition is driven.

There exists also the possibility to connect both antennas to the same microwave source. In this case two plane waves, having orthogonal electric fields, are superimposed. The resulting wave will have electric (and magnetic) field vector at 45 ° with the trap axis, exciting both the π- and the σ-transitions simultaneously.

If there is an additional $\pm$ 90 ° phase shift on one of the antenna, the resulting electric (magnetic) field vector rotates as the wave advances (the wave is circularly polarized): the electric field vector rotating clockwise produces right-handed circular polarization σ^+; the electric field vector rotating anti-clockwise produces left-handed circular polarized wave σ^-. Therefore, choosing an appropriate phase shift between the two antennas, one can drive either the σ^+- or σ^--transition. The different polarization directions for the magnetic field inside the circular waveguide are shown in Figure 3.31.

We provided a 3 mm hole in the back of the waveguide as it is possible to see Figure 3.30 (a). In the current setup for the $^{171}Yb^+$ ions experiments all the laser beams are directed at 45 ° to the trap axis. But, if $^{172}Yb^+$ ions experiments will be performed, the 935 nm laser beam will be perpendicular to the trap axis, as it was explained in section 3.4, and it will need to pass through this hole.

Considering that the microwave waveguide is placed inside the vacuum chamber,

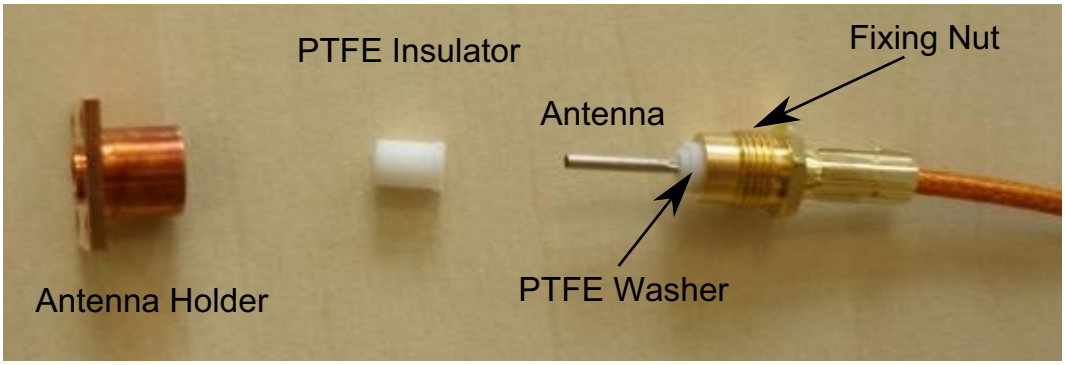

Figure 3.32: Specially designed vacuum compatible SMA connector for the circular waveguide: building blocks.

the antennas need to be suited for UHV. This means that the standard SMA connectors, as in Figure 3.27, are not advisable. Another problem is that there are no such UHV connectors on the market and we had to build them ourselves. For this reason, commercially existing SMA female connectors for UHV from ALLECTRA have been modified. The details are described in Appendix H.1. The building blocks of the home-made SMA connector are demonstrated in Figure 3.32.

Since the SMA connectors are not perfect, the consequences should be considered. On the Smith chart, as it is shown in Figure 3.28, the points on the horizontal central line are purely resistive and the wave impedance for TE modes in circular waveguide is:

$$Z_0 = Z_{fs} \cdot \frac{\lambda_g}{\lambda_0}, \tag{3.47}$$

where $Z_{fs} = 377\,\Omega$ is the impedance of free space. Impedances larger than Z_0 are to the right of the Smith chart center point and smaller impedances are to the left. The points on the median horizontal line of the Smith chart have only a resistive part with no reactive components and we are interested in the central point where the SWR is minimum and equal to one. Above the median horizontal line the points have inductive reactive components and below it they are capacitive. Any impedance mismatch moves us away from the center and the SWR increases. Longer probes produces lower resistances, while longer backshort distances turns the reactance from inductive to capacitive (see Figure 3.28). In our case, the backshort distance was chosen and fixed for the estimated optimum probe length and probe diameter. In case that the probe length is slightly smaller or larger than the theoretical value, the SWR will be slightly increased. If the diameter of the probe is smaller than the theoretical value, the bandwidth of the microwave waveguide will be reduced. This is exactly what happened, as it will be demonstrated below.

The ready vacuum SMA connector was fixed inside a new OFHC housing (Antenna Holder in Figure 3.32) and the ready microwave waveguide antenna is shown in Figure H.1. On the same Figure H.1 (top right) it is possible to see the small hole of 1 mm in the antenna holder body to let out the air from inside of the holder when it is placed in the vacuum chamber. For the same reason the antenna holder does not lie very tight on the waveguide body but there is a 0.5 mm protrusion, as it is possible to see in Figure H.2.

3.8.3 Characteristics

The first test we performed on the circular waveguide was to measure its radiated output. For this purpose a Wiltron Swept Frequency Synthesizer and a Narda Crystal (Schottky) Detector were used. The crystal detector operates in the range of 0.01-18 GHz and the input power is limited to 100 mW. The frequency on the synthesizer is swept in the range of 8-18 GHz and the power of the output radiation is put to the highest possible, i.e. 13 dBm (20 mW). To visualize a graph on the scope we used a special output on the rear panel of the frequency synthesizer called 'Horiz Output' that provides a ramp, between 0 V to 10 V, during the sweep modes that is proportional to frequency for all CW modes and is terminated on a 50 Ω impedance. In order to measure the transmittance output graph two circular waveguides were used: the first waveguide was connected to the frequency synthesizer working as emitter; the second waveguide was the receiver. The voltage readout at the receiver was done by a Narda crystal detector connected to channel one of an oscilloscope. The oscilloscope was operated in XY mode, i.e. the voltage on two channels was controlling both axis separately. The signal from the 'Horiz Output' was fed in channel two of the oscilloscope. Doing this, on the oscilloscope screen it is shown in the horizontal direction a voltages from 0 V to 10 V that is equivalent to frequencies from 8 GHz to 18 GHz. On the vertical axis were plotted the receiver output voltages. The highest voltage would correspond to the highest power detected, occurring at the resonant frequency of the circular waveguide.

The resulting microwave circular waveguide transmittances measured at 6 cm and 2 cm distances between the transmitter and the receiver waveguide front faces are shown in Figure 3.33. It is possible to see that the power bandwidth of the waveguide lies in the range of 11-15 GHz, as it was predicted. The peak at ~ 12.4 GHz that is visible in the pictures is due to a Frequency Synthesizer SYNC output malfunction, so it is to discard. These measurements were performed using standard SMA connectors and standard, not UHV, microwave cables. The transmittance output graph for the circular waveguide with the vacuum compatible cable, the

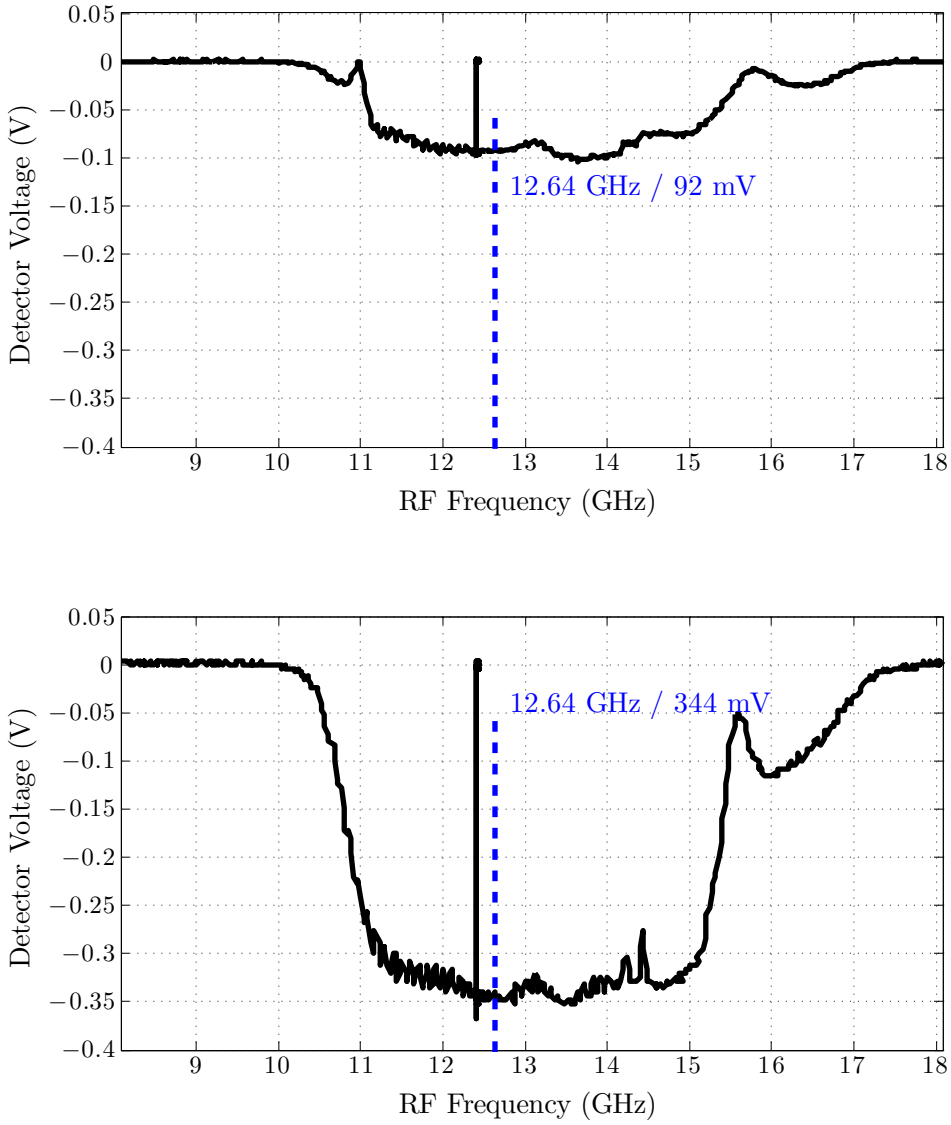

*Figure 3.33: The transmittance graph of the microwave circular waveguide with standard SMA connectors, plotted as a function of frequency for a 6 cm (**Top**) and 2 cm (**Bottom**) distance between transmitter and receiver.*

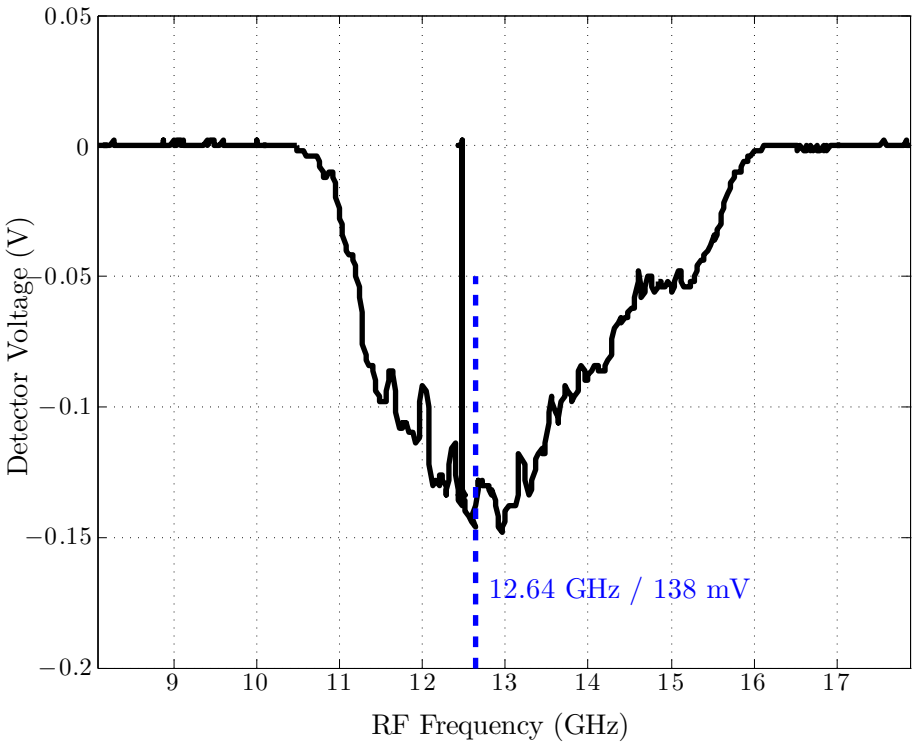

Figure 3.34: The transmittance graph of the microwave circular waveguide with vacuum SMA connectors, plotted as a function of frequency for a 2 cm distance between transmitter and receiver, as it is used in the current setup inside the vacuum chamber.

home-made SMA connectors fitted and 2 cm distances between the transmitter and the receiver waveguide front faces is depicted in Figure 3.34. The power loss in the first case, for the waveguide with the standard SMA connector and the receiver at distance of 2 cm, is 9 dB. For the waveguide with the vacuum components the power loss equals 17 dB, i.e. 8 dB more than with standard microwave cables and SMA connectors. As it is also possible to see in Figure 3.34, the bandwidth of the circular waveguide is reduced, but the maximum still lies around the desired frequency. It was discussed above that a reduced bandwidth is expected since the probe diameter was smaller than initially planned. Additionally, the detected voltage plotted versus distances from the commercial and the home-made waveguides is shown in Figure 3.35. Here, *WC* is a commercial rectangular waveguide and *WH* is our home-made circular waveguide. The home-made circular waveguide output with the standard SMA connectors used as antennas has a similar output

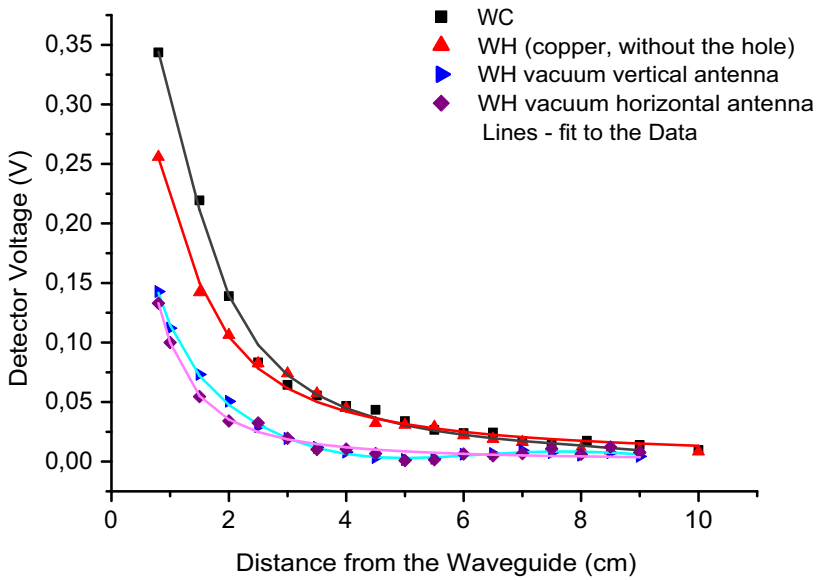

Figure 3.35: Detector voltage plotted versus distance from the emitting waveguide. WC *is for a commercial rectangular waveguide and* WH *for our home-made circular waveguide. Red symbols are data for the test waveguide made from copper with standard SMA connectors used as antennas and without hole for the laser beams in the back short surface. Blue and Viola symbols are data for two different vacuum compatible antennas used in the vacuum ready waveguide. Solid lines are the fits to the data. All measured voltages are taken at 12.6 GHz frequency.*

to the commercial waveguide. It is possible to see that the vacuum waveguide has an output power loss of about 8 dB for both antennas compared to the similar waveguide with the standard SMA connectors. The waveguides were emitting the radiation at 12.6 GHz, slightly smaller than for the data in Figure 3.33 and Figure 3.34 and this resulted in slightly smaller voltages for the data in Figure 3.35.

The SWR was additionally measured for both antennas to evaluate the return losses. For this measurement a directional coupler was used: from the coupling port -16 dB of the input power is sampled, from the isolated port the antenna reflected power is measured. The SWR for the first waveguide probe is 1.04 (return loss of -34.151 dB) and for the second equals 1.03 (return loss of -36.607 dB). This is a good match that brings us to the conclusion that the main power losses are due to the attenuation in the microwave cables, both the vacuum one and the external run, home-made SMA connectors and attenuation through the air when measured

outside the vacuum chamber.

3.9 Magnetic Gradient

3.9.1 Samarium Cobalt Permanent Magnets

The magnetic field gradient along the trap axis is created by two hollow cylindrical Samarium Cobalt (S2869, Magnetic Components Engineering) permanent magnets. They are mounted at each end-cap electrode of the trap with identical poles facing each other. The S2869-type magnets are produced by sintering, i.e. they are made by pressing magnetic powder baked by intense heat until its particle adhere to each other. Sintered Samarium Cobalt magnets are very brittle and, as all the materials produced by sintering, they have imperfections such as small cracks, voids and porosity in its structure. Nevertheless, these magnets were preferred to the bonded Samarium Cobalt. The last are manufactured by mixing magnetic powders with a base material, such as epoxy resin or plastic, and molding the mixture into a shape through a pressing or extrusion process. Such magnets have a weaker magnetic force than sintered magnets, since the amount of magnetic substance per unit volume is smaller. Besides, resins and plastic are bad for the vacuum due to their high outgassing rates. The permanent magnets used in our experiment are plated with Nickel. This was done in order to reduce the outgassing of the porous samarium cobalt magnet structure and to facilitate the cleaning prior to mounting into the vacuum. The S2869-type magnets are the magnets of the Series 2-17 (Sm2Co17, http://www.mceproducts.com) with a composition of two atoms of rare earth samarium and 13-17 atoms of transition metals (TM). The TM content is a cobalt rich combination of cobalt, iron and copper. Small amounts of zirconium, hafnium or other elements are added to enhance the heat treatment response. The rare earth content (samarium) is around $23 - 28\%$. This type of magnets have the advantage of high magnetic strength and the best reversible temperature coefficient of all rare earth alloys, typically of $-0.03\%/^{\circ}C$. The last means a good stability during the temperature changes. Hence, the magnets can be used up to $250 - 350^{\circ}C$, depending upon the permeance coefficient. Additionally, the magnets' high coercivity make them very resistant against external demagnetizing fields. The details about the physical and magnetic properties of the S2869-type magnets are given in Appendix J.

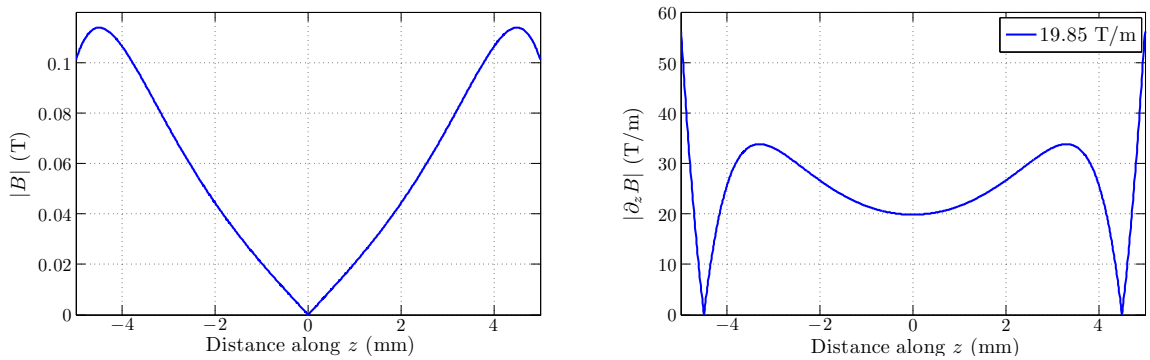

(a) (b)

Figure 3.36: (a) Magnetic flux density produced on the trap axis by the two hollow cylindrical permanent magnets; (b) The correspondent magnetic gradient.

3.9.2 Theoretical Magnetic Gradient

Each of the two hollow permanent magnets has the following dimensions: outer diameter $D_o = 6\,\text{mm}$, inner diameter $D_i = 3\,\text{mm}$ and length $L = 8\,\text{mm}$. The total magnetic field created by two permanent magnets along the trap axis z is $B_z(z) = B_1(z_0 + z) - B_2(z_0 - z)$, where z_0 is the distance from the trap center to each magnet and B_k, with $k = 1{,}2$, is the magnetic field produced by each magnet at distance z along the trap axis. The last equals $B_k = \frac{B_r}{2} \cdot [B_{out} - B_{in}]$, where B_{out} is a magnetic field for the solid rod magnet, B_{in} is the magnetic field for a magnet with the shape and dimensions of the hole and B_r is the residual magnetic flux density. Here,

$$B_{out,in}(z_0 \pm z) = \frac{z_0 \pm z + L}{((D_{o,i}/2)^2 + (z_0 \pm z + L)^2)^{1/2}} - \frac{z_0 \pm z}{((D_{o,i}/2)^2 + (z_0 \pm z)^2)^{1/2}}. \quad (3.48)$$

The theoretically predicted gradient, produced by the two permanent magnets of the given above dimensions, equals 19.85 T/m at the center of the trap. The results for the absolute value of the magnetic flux density and the magnetic field gradient along the trap axis is depicted in Figure 3.36.

If one looks at the magnetic flux density produced by a single hollow cylindrical permanent magnet, and not at its absolute value, one can see that close to the magnet the flux density has negative value, indicating a flux reversal in this region on the axis (see Figure 3.37). Approaching the magnet's pole the gradient start

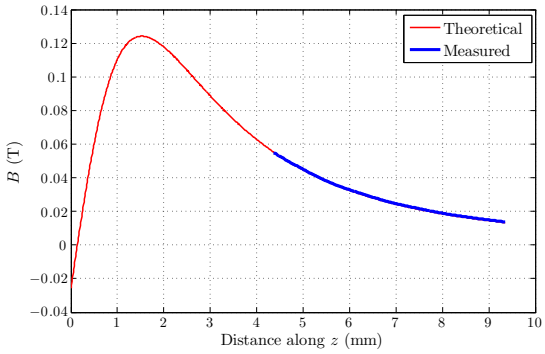

Figure 3.37: Red line: Theoretically predicted flux density for one hollow cylindrical magnet. Blue line: measured flux density from one magnet.

drastically to increase from $\approx 57\,\mathrm{T/m}$ at 1 mm from the pole to $\approx 188\,\mathrm{T/m}$ just next to the pole. In Figure 3.37 the theoretical values of the magnetic flux density B (red line) are compared to the measured values (blue line), demonstrating a good agreement.

3.10 Detection System

The fluorescence light of the trapped ions at 369 nm is detected using both a photo-multiplier and an image intensified CCD-camera. All the lasers in the experiment are collimated and shaped with optical fibers and collimators before they enter the vacuum chamber. Only the 369 nm laser beam was not coupled through the fiber. The reason was the demand for a high intensity to perform the laser cooling and the power losses of more than 75 % at this wavelength in the fiber. The laser beams are overlapped by means of the overlay unit and focused on the ions using an achromatic lens. The fluorescence light due to the spontaneous emission in the ions has a random direction in the full solid angle, forming the surface of a sphere. Part of this light is caught by a special objective designed in our group [Schneider, 2007]. Some of the objective parameters and properties will be mentioned in this work. The details can be found in [Schneider, 2007]. The objective focuses the light through the scattered-light reducing blades and pinholes onto the photo-multiplier or/and ICCD. By choice all the light can be directed exclusively toward the photo-multiplier to to the CCD.

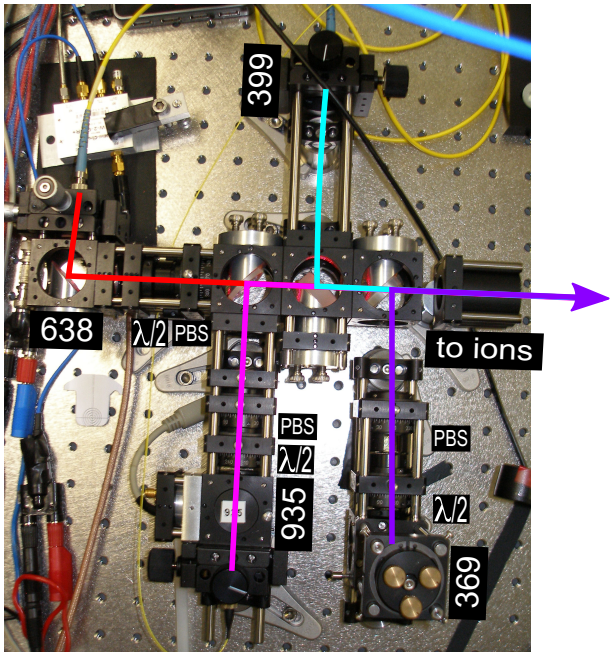

Figure 3.38: Photo of the overlay unit.

3.10.1 Overlay Unit

The overlay unit overlaps four laser beams, three of which (399 nm, 935 nm and 638 nm) pass through the fiber. The fiber couplers are fixed by an adapter ring in the opto-mechanical holder. All but the 399 nm beam pass through the $\lambda/2$-plates and polarized beam splitter (PBS). The PBS defines the polarization of the beams in the experiment and the $\lambda/2$-plate changes the polarization of the beam exiting the fiber in order to maximize the transmission through the PBS. The picture of the overlay unit is demonstrated in Figure 3.38. Further, the beams are focused onto the ions by means of the achromatic lens with a focal length of 200 mm. That limits the effects of chromatic aberrations and helps, therefore, to bring the focal points of the different laser wavelengths closer to each other. Our achromat is the achromatic doublet consisting of a convex and a concave-plane lens. The planar side of the achromatic doublet is directed toward the vacuum chamber and it brings the red and the blue light to the same focus (UV and IR focuses, nevertheless, are slightly shifted away). This part of the focusing setup is depicted in Figure 3.39.

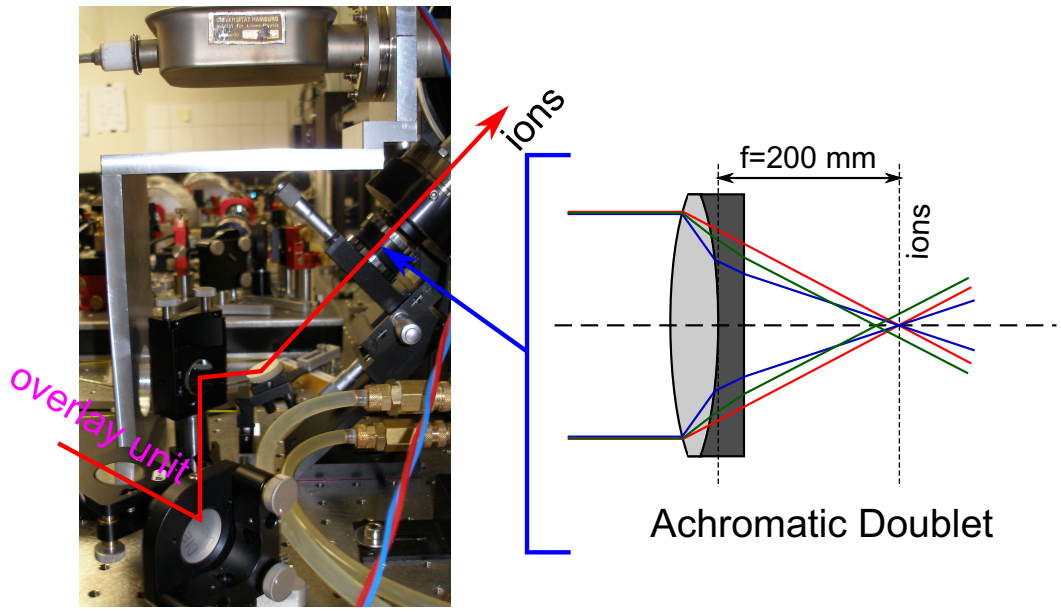

Figure 3.39: Focusing of the laser beams on the ions in the linear trap by the achromatic doublet consisting of a convex and a concave-plane lens. The planar side of the achromatic doublet is directed toward the vacuum chamber and it brings the red and the blue light to the same focus.

3.10.2 Detection Optical Setup

The overall final optical detection setup is demonstrated in Figure 3.40. The fluorescence from the Ytterbium ions trapped in the linear ion trap **(1)** is collected by the objective **(2)**. The objective used in the current experiment was designed to resolve the single Ytterbium ions using the small amount of the detected photons. It has a high numerical aperture (NA) of:

$$NA = n \cdot sin\theta_{max} \approx n \cdot \frac{r_{obj}}{f_{obj}} = 0.4, \tag{3.49}$$

where n is the index of refraction of the medium in which the optical system is working, θ_{max} is the half-angle of the maximum cone of light that can enter or exit the lens, $r_{obj} = 16\,\text{mm}$ is the radius of the objective's entrance pupil and $f_{obj} = 40\,\text{mm}$ is the effective focal length of the objective [12]. The NA describes the objective light-gathering ability, so the acceptance cone. The solid angle Ω,

[12] In air NA is always smaller than 1.

allowed by the objective is, therefore:

$$\frac{\Omega}{4\pi} = \frac{\pi \cdot (r_{obj})^2}{4\pi \cdot f_{obj}^2} = \frac{NA^2}{4 \cdot n^2} = 4\,\% \tag{3.50}$$

of the total solid angle.

The higher the NA, the better is the spatial resolution R of the objective and the lower is the depth of field (DOF). The spatial resolution is the ability to distinguish between small objects, i.e the smallest distance between two points on a specimen that can still be distinguished as two separate entities. Our objective reaches the resolution of $< 1\,\mu$m [13]. The DOF lies in the range of $< \pm 1\,\mu$m and it defines the distance between the nearest and farthest objects in the scene that appear acceptably sharp in the image. A small DOF is more effective in our case since in this way the image of the ions is emphasized while the foreground and background is neglected. The objective has an iris diaphragm with adjustable diameter that can decrease the NA and, therefore, increase the DOF [14].

The objective is suited for imaging of up to $500\,\mu$m long ion in a chain. Considering the distance between the ions in the range of 5-10 μm, up to 100 ions chain can be visible in the ion trap. In the current experiment the amount of trapped ions will be limited. The reason is the fact that for the successful experiments with the trapped ions the last have to be individually addressable in the frequency space with a negligible cross-talks between the neighboring ions. An estimate of the magnetic field gradient that minimizes the unwanted excitation of the neighboring resonances (carrier and motional sidebands) is described by equation [Mintert & Wunderlich, 2001]

$$b \geq \frac{\hbar}{2\mu_B} \left(\frac{4\pi\varepsilon_0 m}{Q^2}\right)^{\frac{1}{3}} \nu_z^{\frac{5}{3}} \left(4.7N^{0.56} + 0.5N^{1.56}\right) \quad . \tag{3.51}$$

With the current magnetic gradient in the experiment of $b = 19\,\mathrm{T/m}$ and an axial frequency of 123.5 kHz the equation 3.51 can be solved for number of distinguishable in the frequency space ions N that equals a maximum of 13 $^{171}\mathrm{Yb}^+$ ions.

During the development of the objective both the thickness of the vacuum chamber viewport (of 8 mm) and the possible distance between the ions and the objective (of 25 mm) were considered. The objective is as close to the viewport as it is possible in order to reduce the imaging errors. The picture of our objective is

[13] $R \sim \frac{\lambda}{2 \cdot NA} = 0.46\,\mu$m, where λ is the wavelength of the light

[14] $DOF = \frac{2 \cdot \lambda \cdot n}{NA^2}$, where n is refractive index of medium and λ is the wavelength of the light.

given in Figure I.1. It is mounted on a translation stage with a piezo-actuator that helps to fine-adjust the focus of the objective in the sub-micrometer range. Two additional stages with micrometer-screws help to align the objective along the horizontal and vertical directions.

The objective is optimized to infinity: the rays leave the lens parallel to each other. Therefore, an additional focusing lens is necessary for imaging onto the camera or the photo-multiplier. In the linear trap experiment a plane-convex lens of 55 mm diameter is used with the plane surface directed toward the imaging device (see **(3)** in Figure 3.40). The focal length f_{det} is 1000 mm that results in a magnification of [15]:

$$M = -\frac{f_{det}}{f_{obj}} = -\frac{1000\,\mathrm{mm}}{40\,\mathrm{mm}} = -25. \tag{3.52}$$

The pixels on the CCD detector must be matched to the existing spatial resolution R of the objective. Adequate resolution of an object can only be achieved if at least two samples are made for each resolvable unit, based on the Nyquist criterion [Piston, 1998]. Many prefer three samples per resolvable unit to ensure sufficient sampling [Rieder, 1999], [Inoué & Spring, 1997]. This means that in order to preserve the spatial resolution of the original image the pixel size of the CCD camera should not be greater than one-half the size of the smallest resolvable feature of the optical image. Considering the magnification M, the pixel size have to be a maximum of $P = M \cdot \frac{R}{2}$, where R is the spatial resolution of the objective given above. The pixel size is fixed and for our camera equals 24 μm. For the final detection setup (see Figure 3.40) one pixel corresponds to about 0.67 μm as will be explained later in section 3.10.3. That tells us that the magnification equals $M = \frac{24\,\mu\mathrm{m}}{0.67\,\mu\mathrm{m}} = 36$, not $M = 25$. There are two additional lenses in the detection setup, **(7)** and **(9)** in Figure 3.40, as will be explained below. The object and the image distances S_1 and S_2 of the second **(7)** and the third **(9)** converging lenses are chosen to keep the image magnification equal to one ($M = -\frac{S_2}{S_1} = 1$) and to fulfill the thin lens equation:

$$\frac{1}{S_1} + \frac{1}{S_2} = \frac{1}{f}. \tag{3.53}$$

For a lens with focal length of 100 mm the object and the image distances for $M = 1$ result to be 200 mm. It is possible, though, that the S_1 and S_2 distances of the

[15] Note the sign convention: negative magnification indicates an inverted image with respect to the object.

lenses are not exactly 200 mm, resulting in the additional small magnification from both lenses. Besides, there is also an image intensifier before the CCD camera, that has its own magnification factor. According to manual [PCO Computer Optics Manual, October 1993] it is possible to have magnifications of 0.95, 1.18 and 2. This could explain the bigger, than expected, magnification factor of $M = 36$. There is an odd number of lenses in the setup, each producing a reverse real image of the object. Therefore, there will be a reversed, real, 36 times magnified image on the ICCD.

Parts **(4)** through **(10)** in the detection setup are used for scattered-light reduction. The box **(4)** has one couple of blades and one iris diaphragm inside it. The blades cut the area around the ions from the top and the bottom. The distance between the blades is adjusted until the best *signal-to-noise ratio*, *SNR*, is achieved. The SNR is a measure that compares the level of a desired signal to the level of background noise. Here, the signal is the count rate at resonance and the noise is the background count rate. The SNR is then the ratio between the two values. One needs to achieve as high SNR as possible minimizing at the same time the noise level. The count rate of the bright ions, the signal, is compared to the count rate when the ions are dark (background noise). To make the ions dark it is sufficient to close for a couple of seconds the 935 nm laser light. The count rates are observed using the photo-multiplier. The iris diaphragm **(6)** is placed in the focus of the convex-plane lens **(3)**. It cuts the area around the ions from the sides. The diameter is adjusted to optimize the SNR, as explained above. The second convex lens **(7)** focuses the light onto the second iris diaphragm and the third convex lens focuses the light onto the iCCD and photo-multiplier. The second iris and the third lens were added solely for the purpose of gaining space further from the scattered-light box in order to place the robust photo-multiplier box. The photo-multiplier box contains beam-splitter, mirror and the hollow structure mounted on a rotatable holder and the rotation is performed from outside the box [Scharfenberger, 2012]. One can set the beam-splitter and then the light is divided 50/50 between the ICCD and photo-multiplier. A mirror will direct the light only toward the photomultiplier and the hollow structure will allow the light to reach the ICCD. A bandpass optical filter **(10)** rejects all the wavelengths of the light that do not lie in the narrow range of 367-373 nm [16]. The transmission in this range is larger than 90 % and the center wavelength is at 370 nm. Hence, only the 369 nm light is allowed to reach the detection devices.

[16] Semrock BrightLine®FF01-370/6-25

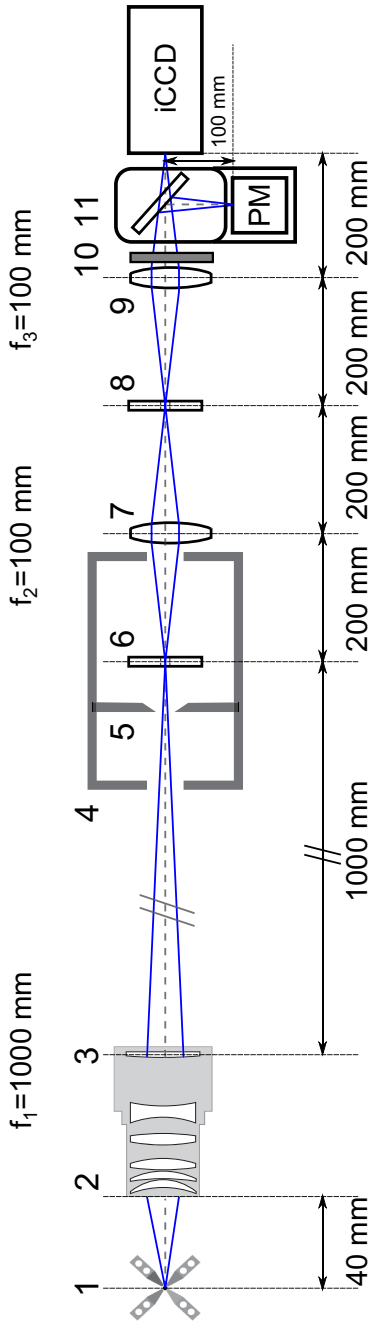

Figure 3.40: Final optical detection setup of the linear trap experiment.
On the picture: ***(1)*** *linear ion trap;* ***(2)*** *objective;* ***(3)*** *convex-plane focusing lens with the focal length* $f_1 = 1000\,\mathrm{mm}$*, screwed directly to the back of the objective;* ***(4)*** *scattered-light reducing box with two blades* ***(5)*** *and iris diaphragm* ***(6)****. Further, the light proceeds toward the second focusing lens* ***(7)*** *with the focal length* $f_2 = 100\,\mathrm{mm}$*, the the second iris diaphragm* ***(8)*** *and the third focusing lens* ***(9)*** *with the focal length* $f_3 = 100\,\mathrm{mm}$*. Passing through the bandpass optical filter* ***(10)****, the light falls onto the beam splitter/mirror inside the photo-multiplier box* ***(11)*** *designed to select the focusing of the light into the* ***ICCD*** *and/or into the photomultiplier (****PM****).*

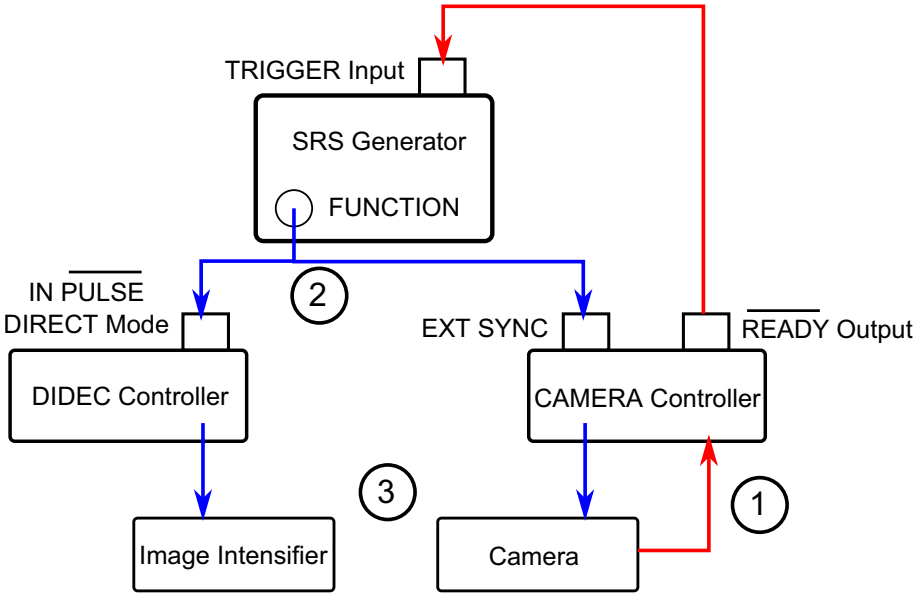

*Figure 3.41: Diagram of the detection devices connection. Circled **1**, **2** and **3** on the image demonstrate the different stages of the devices operation that are explained in the text.*

3.10.3 ICCD Camera

The ICCD (Intensified Charged Coupled Device) imaging system consists of an image-intensifier, a CCD detector, a CCD camera controller and a computer. Details can be found in Appendix I.2.

The camera is equipped with a 512×512 pixels array with the pixel size of $24 \times 24\,\mu$m, leading to a chip size of 12.3×12.3 mm. In order to reduce the dark current, the camera is thermoelectrically cooled using a four-stage peltier device. The CCD chip sits on a cold finger mounted on this peltier device. An internal fan cools the heat exchanger just behind the last peltier element and expel the hot air through the openings in the detector housing. The minimum possible cooling temperature is $-40°$, but in the current experiment we cooled down to $-30°$.

Connection of the Camera

The controller of the CCD camera was programmed to start each exposure in the acquisition sequence immediately after receiving the correspondent trigger signal. This exposure mode of the camera is called STROBED_MODE and it is set using

the PVCAM C library of camera control and data acquisition functions. The home-made program in Labview capable to access the PVCAM library has been written (see Appendix O for more details). This program initiates the PVCAM library and the camera software; sets important parameter as the camera temperature, shutter mode, camera gain, camera mode, binning, region-of-interest (ROI) and the exposure time; performs the acquisition sequence and close the camera and uninitiates the library at the end of the acquisition. For the present experiment the gain on the camera was set to the recommended Medium setting (gain 1×) and the shutter (mechanical shutter) was chosen to open before the sequence begins with a consequent closing after the sequence ends [17]. The binning of one (no binning) in both directions has been always used is our experiment. Besides the mechanical shutter controlled by the software there is also the image intensifier that acts as a shutter to the CCD camera. The intensifier photocathode has to be opened at the same period of time the CCD camera exposes. This can be done using common external trigger for the camera and for the intensifier which in its turn is externally triggered by a pulse indicating the readiness of the camera to take the next image.

The common trigger signal was generated by the synthesized function generator. The connection of the devices, used for the detection, is demonstrated in Figure 3.41. In the **DIRECT** mode, of the the **DIDEC** image intensifier control unit, the built in pulse generator is ignored and the exposure time is controlled by a trigger signal fed at the **IN $\overline{\textbf{PULSE}}$**. The TTL-low signal makes the photocathode to open and the TTL-high signal closes it (see also the operating manual [PCO Computer Optics Manual, October 1993], p. 11, port 11). The **EXT SYNC** connector of the camera controller is a TTL input that allows the data acquisition to be synchronized with external events. More details about different functions of the SRS generator, the CCD detector and the CCD camera controller can be found in the manuals: [MODEL DS345 Synthesized Function Generator, March 2005], [NTE/CCD Detector Manual, September 2001] and [ST-133 5 MHz Controller Manual, April 1999], respectively. In order to obtain a required TTL-pulse at the SRS FUNCTION output, to trigger both the photocathode (**IN $\overline{\textbf{PULSE}}$** input) and the camera (**EXT SYNC** input), a 50 Ω resistance has been added to the SRS **Function** output itself. The summarize of the detection timings is presented in Figure 3.42. The details can be found in Appendix I.2. In order to see the fluorescence of the single $^{171}Yb^{+}$ ions, having far less intensity than the $^{172}Yb^{+}$ isotope, the **DIDEC** gain was set to 8.0 and an exposure time of 400 ms was usually used.

[17] OPEN_PRE_SEQUENCE shutter mode (see Appendix O)

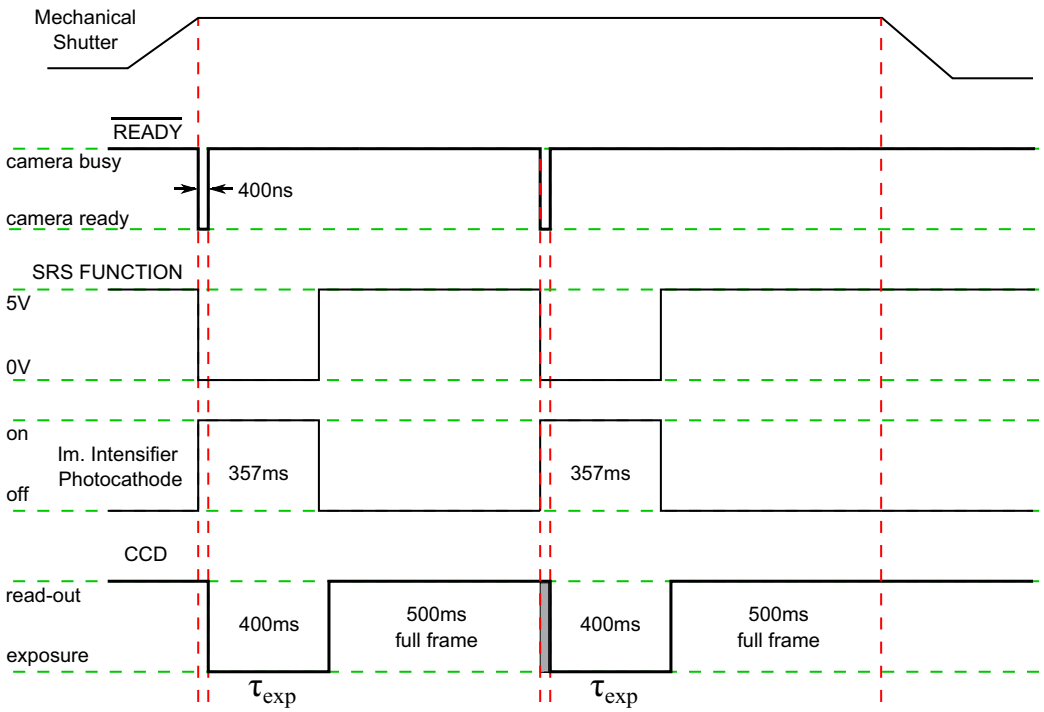

*Figure 3.42: Fluorescence detection timing diagram. After the mechanical shutter is opened and the ICCD camera is ready to take the image, the camera controller sends a short trigger pulse (**$\overline{\textbf{READY}}$**-pulse) to the SRS generator. In response to the received external trigger the SRS generator changes its output from 5 V to 0 V for a period of 357 ms. During this period of time the photocathode of the image intensifier stays opened. At the same time, when the photocathode opens, the camera starts to expose. The exposure time is set via software to 400 ms. After 357 ms the photocathode closes. The CCD camera continues the exposure for a bit longer and then starts to read-out the information from the CCD chip. The photocathode is closed during this time. When the camera finished the read-out it is ready to take a new image. Hence, a new **$\overline{\textbf{READY}}$**-pulse is sent to the SRS and the detection cycle repeats itself. In order to obtain the required 5 V amplitude at the **SRS FUNCTION** output, to trigger both the photocathode and the camera, a 50 Ω resistance is additionally attached to the output itself. The mechanical shutter is programmed via software to open before the exposure sequence starts and to close after it ends. The **$\overline{\textbf{READY}}$**-pulse always goes down when the camera is ready to take an image and goes up when the camera starts an exposure. The SRS is programmed to generate a burst when the negative slope of the external trigger is detected. The photocathode is opened at 0 V and is closed at 5 V.*

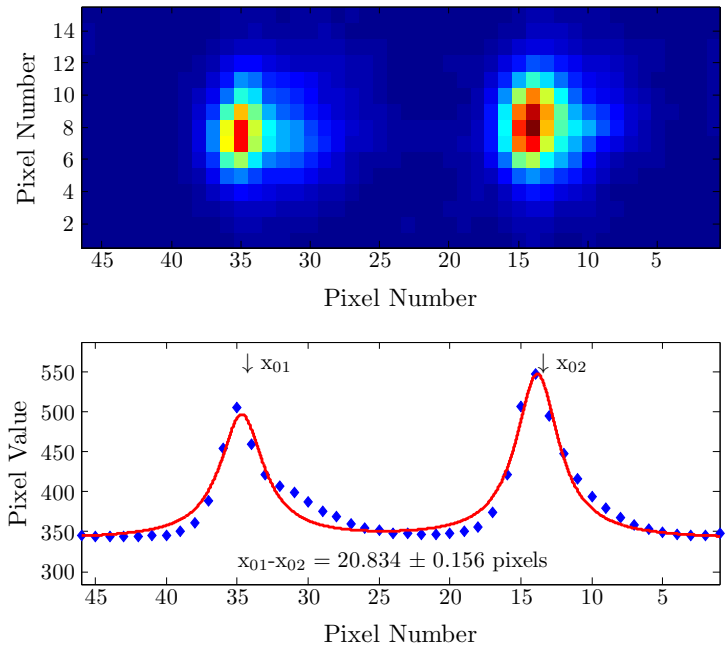

Figure 3.43: Image of two ions, taken with the ICCD at 123.5 kHz axial trap frequency, and the corresponding ion position graph, where the pixel values are plotted versus the pixel numbers. Here, the solid line is the Lorentzian fit. It is used to find the position of the ion resonance peak and, respectively, the inter-ion separation in pixels.

Imaging Scale

It is important to know the scaling factor between the real inter-ion distance and the distance of the imaged ions in pixels. This parameter was changed during the experiment since the detection setup was periodically updated to improve the suppression of the scattered light. To attempt a calibration, a direct imaging of the ions allows to find out the distance between them in pixels as it is possible to see in Figure 3.43. In order to find the distance in micrometers, the axial trap frequency ν_z has to be measured, since the distance δz between the ions depends on it. The inter-ion distance between two ions is (see equation 6.12)

$$\delta z = \left(\frac{Q^2}{2\pi\varepsilon_0 m \nu_z^2} \right)^{1/3} \quad , \tag{3.54}$$

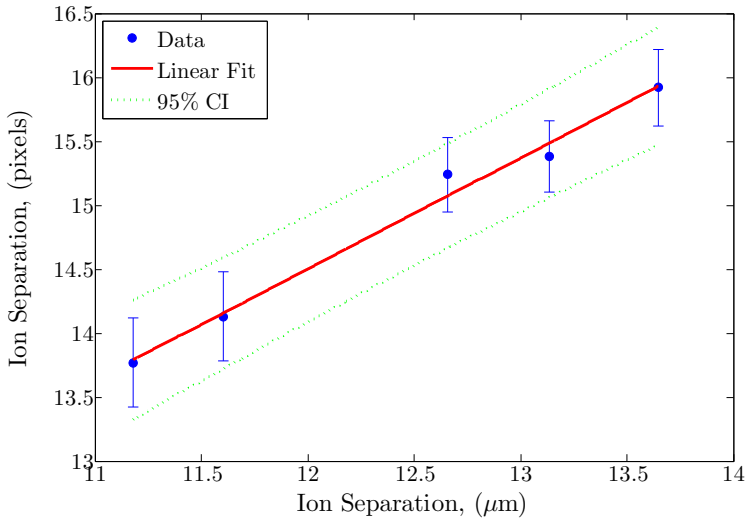

Figure 3.44: Calibration graph transferring ion separation in pixels into the meters. The solid line is a linear fit from which the scaling parameter is found. It equals $0.87 \pm 0.06\ \frac{\mu\text{m}}{\text{pixel}}$.

where Q is the charge, ε_0 is the dielectric constant and m is the ion mass. In order to find the scaling factor, the images of two ions at different axial potentials were taken: $2\pi\cdot 127.1\,\text{kHz}$, $2\pi\cdot 134.6\,\text{kHz}$, $2\pi\cdot 142.3\,\text{kHz}$, $2\pi\cdot 162.1\,\text{kHz}$ and $2\pi\cdot 171.4\,\text{kHz}$. An example of such an image, taken with the ICCD, is shown in Figure 3.43. Below the ions image there is a plot of pixel values versus the pixel number. Two ion's resonances are visible. The Lorentzian fit was used to estimate the position of the peaks and, respectively, to find the inter-ion separation in pixels. Figure 3.44 shows the plot of the ion separation in pixels versus the ions separation in micrometers for different axial trapping potentials. The slope of the resulting linear dependence gives the scaling factor. The data in Figure 3.44 were taken before the elements **(6)-(10)** in the detections setup of Figure 3.40 were added. The scaling factor then was around $0.87 \pm 0.06\ \frac{\mu\text{m}}{\text{pixel}}$. The image in Figure 3.43 was taken after the final version of the detection setup was constructed. Here, the axial frequency was fixed at 123.5 kHz. The distance between two ions at this frequency is $13.92\,\mu\text{m}$ that results in the scaling factor of around $\frac{13.92\,\mu\text{m}}{20.83\,\text{pixels}} = 0.67 \pm 0.01\ \frac{\mu\text{m}}{\text{pixel}}$.

3.10.4 Photo-multiplier

Two photomultiplier tubes (PMT) were used during the experiments. On the early stages of the experiment, an Hamamatsu R5600P for single photon counting was

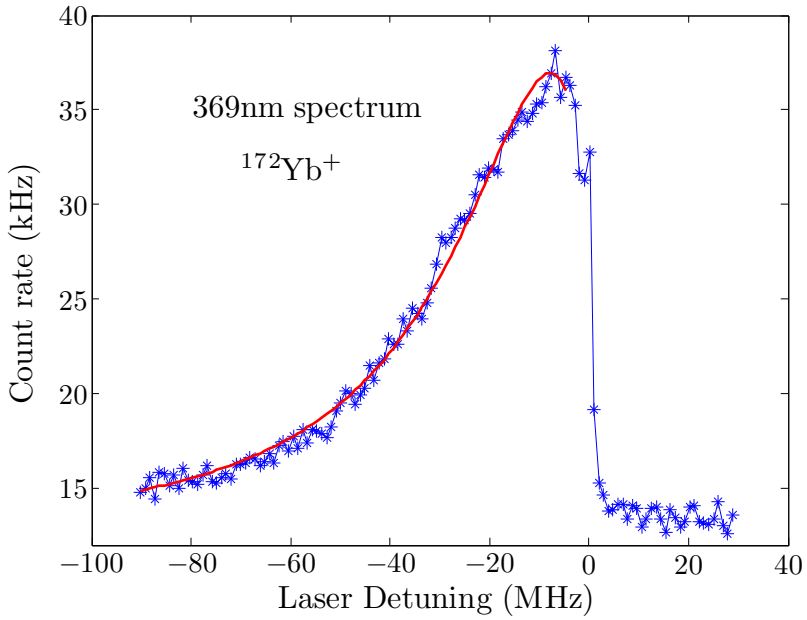

Figure 3.45: Fluorescence photon-count signal of a single trapped $^{172}Yb^{+}$ ion as a function of the 369 nm laser detuning $\Delta\omega$. The sharp decrease in signal at $\Delta\omega \leq 0$ indicates the transition from laser cooling to heating. Solid line is a Lorentzian fit (see explanation in text). The Lorentzian line-width is $2\pi \times 58$ MHz. The laser beam waist is 72 μm measured at 150 μW laser power.

used. It has 20 % quantum efficiency at 369 nm. Only approximately 4 % of the emitted photons are collected by the objective (see section 3.10.2). The total detection efficiency for one given event is the product of independent efficiencies. Hence, the detection efficiency varies between the 0.4 % in case the 50/50 beam-splitter is used and 0.8 % in case the mirror directs the light only to the photomultiplier. The dark count rate of this PMT is 80 Hz. Since a higher level of detected photons was necessary, the old PMT was exchanged with a new Hamamatsu, model R7518P, that has a higher quantum efficiency of around 28.5 % at 369 nm and a dark count rate in the range of 10-50 Hz. The detection efficiency for this PMT is 0.57 % in case the 50/50 beam-splitter is used or 1.14 % is case the light is directed only to the photomultiplier.

The spectrum in Figure 3.45 was taken with the detection system without the scattered-light reducing elements **(6)-(10)**. The noise level was very high. For the given image it equals around 13 kHz with the corresponding very small SNR

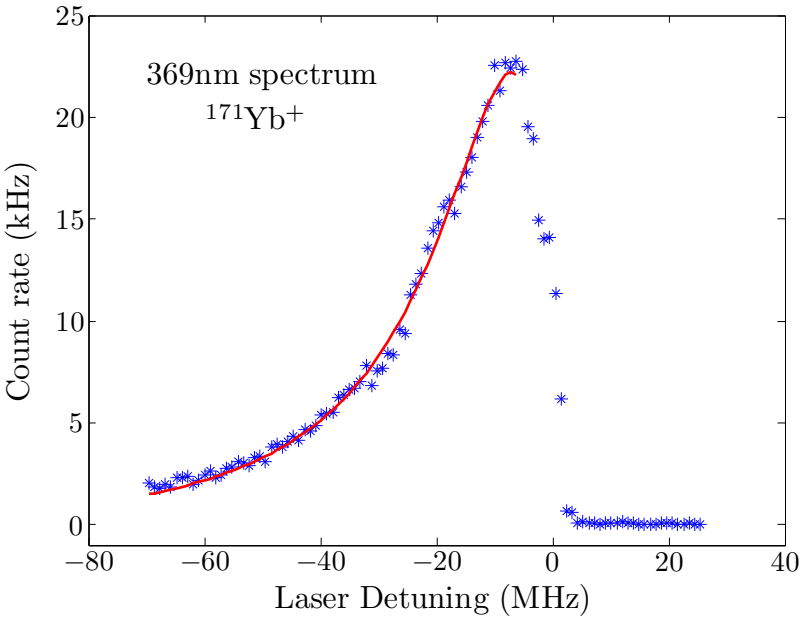

Figure 3.46: Fluorescence photon-count signal of two trapped $^{171}Yb^{+}$ ions as a function of the 369 nm laser detuning $\Delta\omega$. Average noise level is about 32 Hz, count rate at resonance is about 22.7 kHz. Corresponding SNR for 1 ion is about 350. Solid line is a Lorentzian fit (see explanation in text). The Lorentzian linewidth is $2\pi \times 38.6$ MHz. The laser beam waist is 72 μm measured at 150 μW laser power.

= 3. During the coupling constants measurements experiment the smallest noise achieved was in the range of 650-700 Hz and the best SNR was around 5. We did not manage to reach the limit of 80 Hz for the old PMT: the scattered light had to be further reduced. This detection was sufficient for the J-coupling measurements but not for the CNOT-gates. After the new PMT was installed the first iris diaphragm **(6)** was added to the detection setup. The noise level decreased drastically. Two scans of the ^{172}Yb^{+} ion fluorescence were made: with the beam splitter (BP) and the mirror. In the first case 50 % of the light is directed toward the ICCD hence less photons are detected by the PMT. The count rate here reaches 15 kHz with the noise level equal to 330 Hz and SNR of around 50. With the mirror in place, all the photons are directed toward the PMT, the count rate at resonance is up to 34 kHz with the noise level of 660 Hz and SNR of around 50. As one can see, with only one diaphragm the SNR improved approximately 10 times. The addition of the second iris diaphragm **(8)** reduces the noise level

even more: down to 30-50 Hz. Hence, the SNR of 350 is achieved, 70 times higher than without the diaphragms (see the spectrum in Figure 3.46). The solid line in Figure 3.45 and Figure 3.46 is a Lorentzian fit. It suits better to the data since the transition is power broadened and the Voigt fit does not give good results. The step function does not fit the count rate drop either, since only a small part of the emitted photons reaches the photo-multiplier.

The current burst for a single photon event is discriminated and translated into a voltage TTL pulse by a photon counting unit. The TTL pulses are collected and counted by the digital signal processor (DSP) system.

4

Operating the Trap

The ions are loaded into the trap using the photo-ionization process described in the beginning of this chapter. Furthermore, the loading procedure is explained in detail. Before to start any experiment the ions' micromotion must be compensated: the method used in our experiment is presented at the end of this chapter.

4.1 Photo-ionization

The ytterbium ions are loaded into the trap by an isotope selective two-color photo-ionization process using both the 398.9 nm and 369.5 nm laser lights.

There are two steps in the ionization process. First, the photo-ionization laser at 398.9 nm excites the transition $^1S_0 \longrightarrow {}^1P_1$ in the ytterbium. After this a second photon at $\lambda < 394$ nm is needed to excite the electron further to the continuum and ionize the atom. For this purpose the 369.5 nm laser light, already present in the experiment and used for ion cooling, can be used. This process is called two-color photo-ionization and it is depicted in Figure 4.1.

It was demonstrated experimentally that it is sufficient to use only the laser light at 398.9 nm as a second light field since the potential of the ion trap lowers the

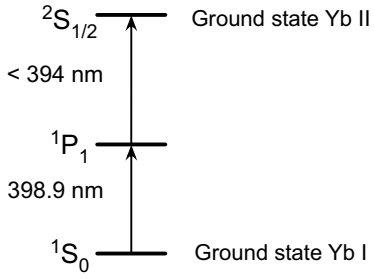

Figure 4.1: Two-photon ionization of YbI via the $^1P_1$ state. The image is taken from [Johanning et al.*, 2011]*

ionization threshold so that a second photon at 398.9 nm reaches the continuum [Braun, 2007; Eiteneuer, 2009; Johanning *et al.*, 2011]. But the trap loading rate in this case is lower compared to the two-color process. Hence, the 369.5 nm light was preferred in the current experiment.

Ovens

There are two ovens in the vacuum chamber as it is possible to see in Figure 3.10. They are molybdenum tubes with an inner diameter of 0.78 mm and a wall thickness of 0.2 mm, spot welded to a tantalum wire. Two ovens contain YbI that is enriched with isotopes $^{171}Yb^+$ and $^{172}Yb^+$, respectively. The ytterbium evaporates during the resistive heating of the ovens. The detailed description of the ovens used in the current experiment can be found in [Eiteneuer, 2009]. The atomic beam has a divergence angle of 30 ° [Eiteneuer, 2009] and the atoms are spread over the big region in the trap. The images of the atomic resonance fluorescence of YbI, containing $^{172}Yb^+$ isotopes, taken with the CCD camera at different currents of the oven are shown in Figure 4.2. The exposure time for the images taken equals 100 ms and each image has a size of around $500 \times 500\,\mu$m. The atomic beam comes from the down left, and the 399 nm laser beam from the down right. The atoms in the place of intersection are excited by the laser and become visible due to the emitted fluorescence, as it is possible to see in Figure 4.2. From the image taken at 1.75 A results that the width of the 399 nm laser beam is equal to about $50\,\mu$m.

The ovens are connected perpendicular to the 398.9 nm laser beam (see Figure 3.8 **Ovens, DC** flange) in order to reduce the line width broadening due to the Doppler effect. In case the oven would contain more isotopes, the perpendicular position would facilitate isotope selectivity [Johanning *et al.*, 2011]. There is still

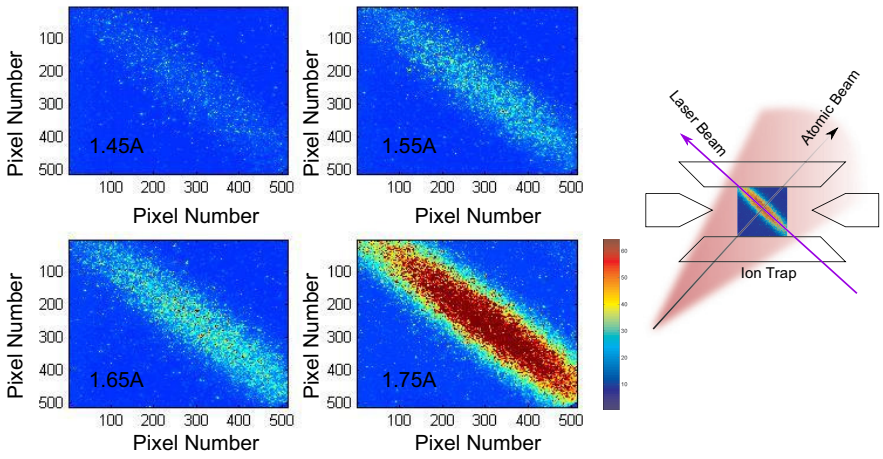

Figure 4.2: The atomic resonance fluorescence of the $^{172}Yb^{+}$ ions at around 399 nm taken with the CCD camera at different currents of the ovens. The exposure time equals 100 ms and each image has a size of around 500×500 μm.

the remaining Doppler effect due to the divergence of the atomic beam plus power broadening. Figure 4.3 shows the atomic resonance spectrum of the $^1S_0 \longrightarrow {}^1P_1$ transition for the oven enriched with $^{171}Yb^{+}$ isotopes. The solid line is a Voigt fit. The Lorentzian and Gaussian linewidths are, respectively, $\Gamma_{171} = 2\pi \times 62\,\text{MHz}$ and $2\pi \times 23.5\,\text{MHz}$. The natural linewidth of the $^1S_0 \longrightarrow {}^1P_1$ transition equals $2\pi \times 28\,\text{MHz}$ [Johanning *et al.*, 2011] and that is approximately two times smaller than the value obtained in the current setup. Three different peaks are visible in Figure 4.3. Extreme left peak contains three unresolved resonances: $^{173}Yb^{+}$ ($F = 3/2$), $^{172}Yb^{+}$ and $^{173}Yb^{+}$ ($F = 7/2$); extreme right peak has two unresolved resonances: $^{171}Yb^{+}$ ($F = 1/2$) and $^{170}Yb^{+}$, and the middle peak corresponds to the $^{171}Yb^{+}$ ($F = 3/2$) isotope. It is possible to see that the Voigt fit is a bit asymmetric. This means that the oven used was not exactly at 90° with the 398.9 nm laser beam.

Reducing the Doppler effect, most of the atoms in the atomic beam will have a zero velocity. The more such an atoms in the beam, the more $^1S_0 \longrightarrow {}^1P_1$ excitations happens, the more efficient is the ionization by the 369.5 nm laser beam and, consequently, the higher is the loading rate. But there are also atoms that will always have a rest velocity in the direction of the 398.9 nm laser beam. This is the reason why the measured line width of the $^1S_0 \longrightarrow {}^1P_1$ transition will be always larger than its natural one and the smaller is the measured line width, the higher is the loading rate.

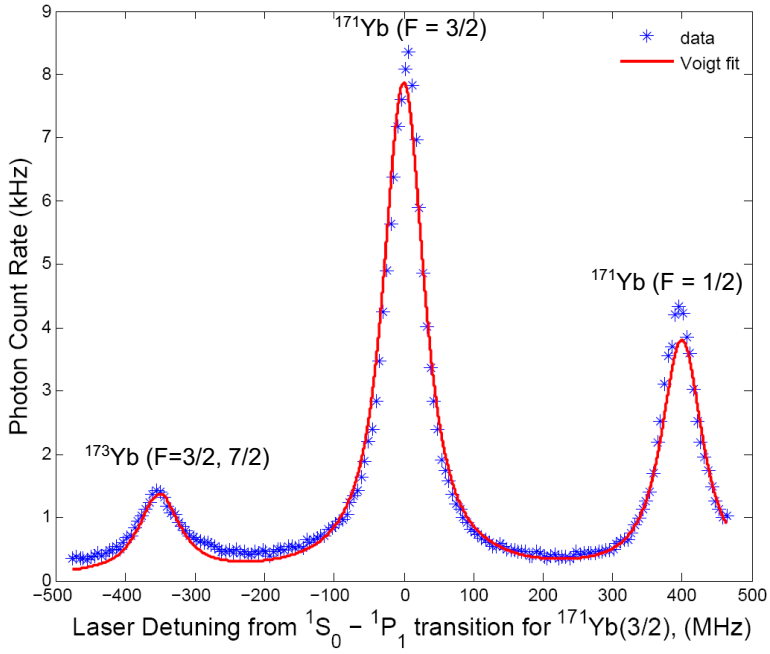

Figure 4.3: Atomic resonance fluorescence spectrum measured with the $^{171}Yb^{+}$ isotopes enriched oven. The oven is perpendicular to the 398.9 nm laser beam, therefore the Doppler broadening is reduced and the resonances for different isotopes are clearly resolved. The solid line is a Voigt fit. The Lorentzian and Gaussian line-widths are $2\pi \times 62$ MHz and $2\pi \times 23.5$ MHz, respectively.

4.2 Loading the Ions

In order to trap a low number of ions the current we use for the $^{171}Yb^{+}$ and $^{172}Yb^{+}$ ovens are about 1.60 A and 1.45 A, respectively. After the ionization laser at 398.9 nm, the repumping lasers at 935.2 nm and 638.2 nm are brought to resonance, the cooling laser at 369.5 nm is slightly red-detuned from resonance to facilitate cooling. The heating current is applied to the cold ovens. It takes usually about 5-10 minutes until the first ion is ionized. The 369.5 nm light wavelength is shifted toward resonance until a stable crystal forms. The 398.9 nm is blocked when the ion loading is finished. In Figure 4.4 the first images of the ion cloud crystallization are shown. On the upper image the 369.5 nm laser light was strongly red-detuned. In the following images the laser wavelength was moved closer and closer to resonance, the ions are gradually cooled and a crystal as in Figure 4.4 (b) appears.

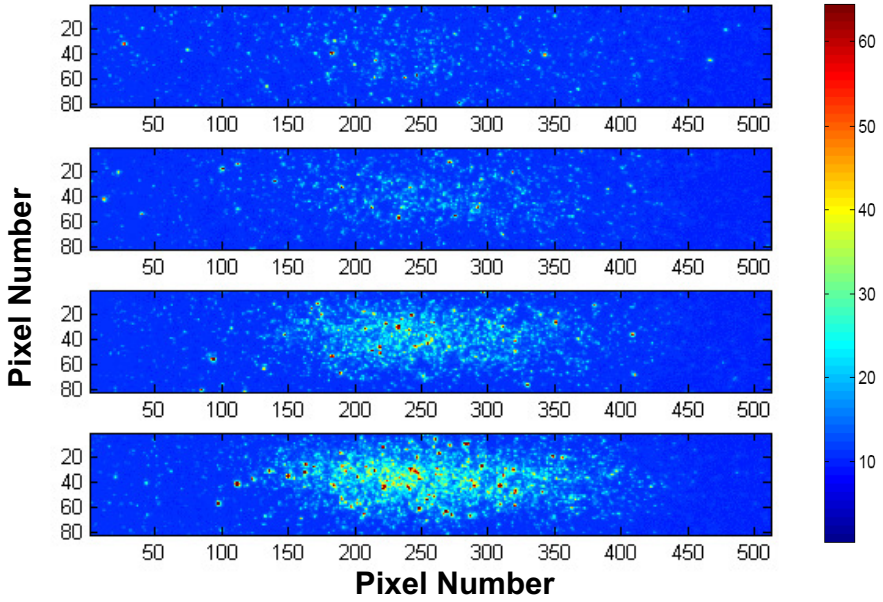

(a)

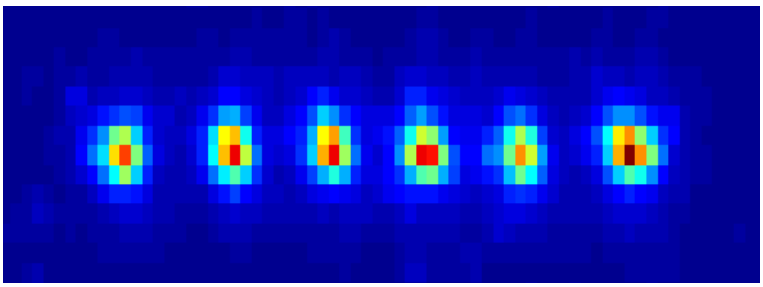

(b)

Figure 4.4: (a) First images of the ion cloud crystallization. On the upper image the 369.5 nm laser light was detuned far to the red side. Moving its wavelength closer to the resonance the ions are cooled and the crystal is formed. (b) $^{172}Yb+$ ion chain.

4.3 Micro-motion Compensation

As was mentioned in section 3.1.1, the motion of the ion in the electromagnetic trap could be described as a superposition of the slow secular motion in the trap pseudo-potential and the fast micro-motion at frequency Ω of the trapping RF

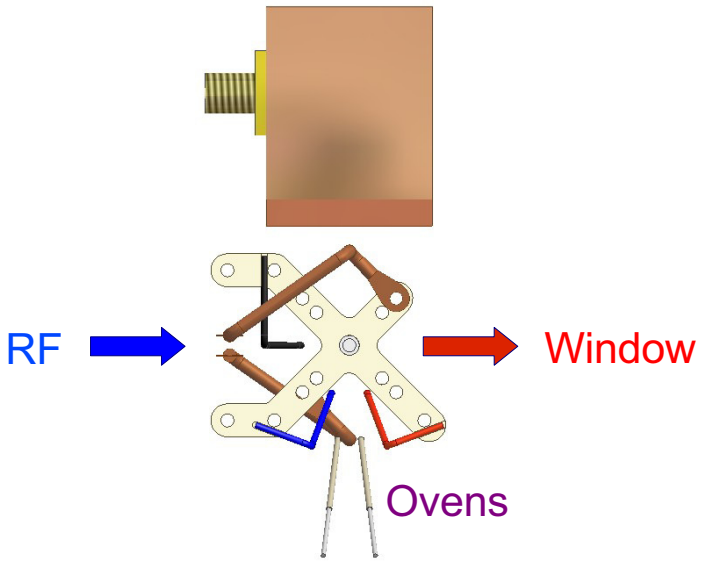

Figure 4.5: Three compensation electrodes are shown in different colors. Black: 'RF Side' electrode; Red: 'Down Window' electrode; Blue: 'RF Side Down' electrode.

signal. The farther the ion from the trap center, the larger is the amplitude of the micro-motion. An additional force, responsible for the displacement of the ion from the trap center, arises in cases of, for example, geometric imperfections due to the trap construction (misalignment of the end-cap electrodes with the trap axis defined by the RF-electrodes) or residual stray electric fields (metallic ytterbium deposited on the electrodes during the heating of the ovens). High micro-motion level complicates Doppler cooling (increased cooling temperature limit) and the side-band cooling becomes impossible. Besides, the ions disappear faster from the trap with enhanced micro-motion.

The RF-photon correlation method has been used in the current experiment to measure the extent of the micro-motion. It provides a measure of the fluorescence against the phase of the RF drive voltage. The idea is similar to the frequency modulation absorption spectroscopy. The ions's velocity is converted into the modulation of the fluorescence level via the emission Lorentzian line shape. Most effectively the micro-motion compensation occurs when the cooling laser is tuned to the middle of the red side of the line shape. As the ions perform their movements in the trap, the Doppler effect ensures that they oscillate alternately closer or farther

from the resonance with the cooling laser. The level of fluorescence is therefore modulated at the oscillation frequency. The closer to resonance the absorbed light is the greater the fluorescence. If the ion is at end points of its trajectory, the fluorescence will be at its average level. Closer to the center of the ion's trajectory the absorbed light will be closer or farther from the resonance that results in maximum or minimum levels of fluorescence.

The measurement procedure can be described as follows. The TTL pulse from the photon counting unit (discriminator) starts the record of the arrival times of the photons on the photo-multiplier by a time-to-digital converter (TDC) [1]. This trigger pulse from the photo-multiplier will be called a START trigger event. A second trigger TTL pulse, the STOP trigger, from the RF drive is generated by the DS345 synthesized function generator (SYNC OUTPUT) [2] that stops the TDC. The SRS is continuously ON generating TTL pulses at the frequency of the RF drive. The TDC measures the time delay between the arrival of the photons on the photo-multiplier and the arrival of the STOP pulses. The number of repetitions in the current experiment is about 20000 and it can be set via the TDC software. The information is sent to the computer via the MCA (multi-channel analyser) and the computer displays the number of photon counts versus the time delay. In case the ion is far from the trap center, this sinusoidal signal has large amplitude and the ion is in resonance only for some part of the RF cycle. The trap has three extra 'compensation electrodes', shown in Figure 4.5. Adjusting the DC voltages on these electrodes and on the end-cap electrodes, the sinusoidal signal amplitude can be decreased and, correspondingly, the micro-motion amplitude is reduced.

The data collected by the TDC where plotted as histograms (see Figure K.2 in Appendix K.1, right image). First, the summation over all the times was performed after which the histogram with the bins representing the photon counts was performed. In case of negligible micro-motion this histogram is described by a purely Poissonian distribution where the standard deviation $\sigma = \sqrt{\lambda}$, with λ the mean number of occurrences. With increased micro-motion the distribution deviates from the Poissonian, the standard deviation increases and it will be notated as σ_μ. A good compensation is achieved when the ratio between these two standard deviations, $\frac{\sigma_\mu}{\sigma}$, is close to one. See also Appendix K.1 for an example of the taken data.

[1] Fast Com Tec GmbH P7888 PCI TDC unit
[2] SRS, Stanford Research Systems

5

Design of a new Linear Resonator Trap

As it was already explained in section 3.8, it is important to increase the microwave field at the location of the ions. In the linear trap experiment we used for this purpose a cylindrical waveguide situated close to the trap itself. Why not to put the ions directly inside such a waveguide? In fact, in the fields of electron spin resonance (ESR) and nuclear magnetic resonance (NMR) such a waveguide is used already for decades for sample analysis. It is called loop-gap resonator (LGR) and it comprises inductive and capacitive elements called *loops* and *gaps*, respectively. An additional use of gaps together with the variation of gap dimensions and dielectric constants allows us to adjust the resonance frequency of the cylindrical waveguide for any radius. There is a lot of information on the subject, e.g. [Froncisz & Hyde, 1982; Hardy & Whitehead, 1981; Mehdizadeh *et al.*, 1983; Wood *et al.*, 1984] etc. Here only the most important equations will be presented.

The resonance frequency of the LGR is equal approximately to [Froncisz & Hyde, 1982]:

$$2\pi \cdot \nu = \frac{1}{(LC)^{\frac{1}{2}}} = 1/rn^{\frac{1}{2}} \left(\frac{T}{W}\right)^{\frac{1}{2}} \left(\frac{1}{\pi\epsilon\mu_0}\right)^{\frac{1}{2}} \quad , \tag{5.1}$$

where n is the number of gaps, T is the gap length, W is the trap gap width, ϵ is

the dielectric constant, μ_0 is the magnetic constant and r is the internal radius of the resonator. The expressions for the capacitance and inductance are

$$C = \frac{\epsilon W L}{T n} \tag{5.2}$$

$$L = \frac{\mu_0 \pi r^2}{L} \quad , \tag{5.3}$$

where L is the resonator length. The dimensions of the LGR should in general be smaller than $\lambda/4$, otherwise it will start to radiate. The radiation can be suppressed by an additional cylindrical shield of radius R, which should be smaller than the cutoff wavelength for the lowest propagation mode in a circular waveguide (see equation 3.44). A more accurate semi-empirical equation to predict the frequency of the LGR and include the effect of the shield and the fringing fields is given in [Froncisz & Hyde, 1982] and equals:

$$\nu = \frac{1}{2\pi}\left(1 + \frac{r^2}{R^2 - (r+W)^2}\right)^{\frac{1}{2}} \left(\frac{nT}{\pi W \epsilon \mu_0}\right)^{\frac{1}{2}} \frac{1}{r}\left(\frac{1}{1 + 2.5\,(T/W)}\right)^{\frac{1}{2}} \quad . \tag{5.4}$$

Equation 5.4 is claimed to be satisfactory in calculating the frequency within 10 % precision between 1−10 GHz. More discussion on the LGR can be also found in [Hyde & Froncisz, 1989; Rinard & Eaton, 2005].

The LGR we want to use for our experiment should have four gaps. In this way we also create four electrodes to connect the RF trapping potentials. Further we will use the name *resonator trap* for our LGR to emphasize that the resonator is also a trap. The dimensions of the resonator trap at which the resonance frequency equals 12.6 GHz are given in Table 5.1. Its picture is given in Figure 5.1 and we will call it Design I trap. A red line shows the path of the laser beams and they are at 60 ° with respect to the trap axis. An angle of 45 ° is not possible with the current trap length. End-cap electrodes are separated from each other by 5.71 mm and the excitation loop optimum position is at $H = 0.35$ mm from the RF electrode. It is also visible the conical hole for the fluorescence light. The simulations of the magnetic and electric fields in this structure has been performed by HFSS v.10 software by Ryszard Narkowicz of the university of Dortmund. As it is possible to see in Figure 5.2, the magnetic field in the trap center is about 160 - 180 A/m corresponding to a Rabi frequency of about $2\pi \cdot 2.8 - 2\pi \cdot 3.2$ MHz on π-transition. These values of the magnetic field were obtained with an input power of 1 W and

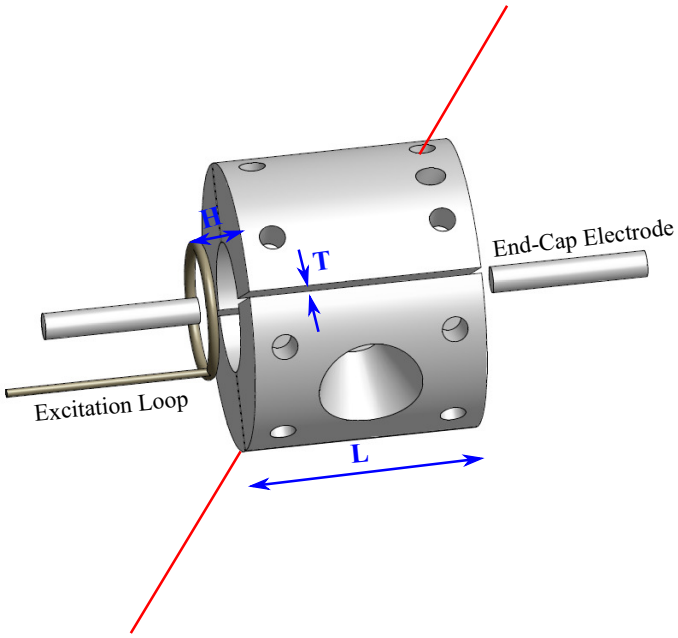

Figure 5.1: Basic design (Design I) of the resonator trap. The distance between the end-cap electrode and the resonator trap is 0.6 mm and the distance between the end-cap electrodes is therefore 5.71 mm. The distance between the excitation loop and the resonator trap is $H = 0.35$ mm. The red line shows the path of the laser beams and they are at 60° with the trap axis and the conical hole is used for the fluorescence light.

it is already three orders of magnitude higher than with the currently used linear trap setup. With a power of 2.5 W, currently available from the microwave setup, the Rabi frequencies can reach up to 5 MHz. According to simulations the return loss is also small and equals about -20 dB, indicating a VSWR of 1.21.

The material for the resonator trap should be chosen carefully. It must be suitable for UHV and, since the distances between the RF electrodes are negligible, it must have high breakdown voltages. The breakdown voltage V_b for the electrode separations (gap length) $T \leq 0.5$ mm has a linear dependence with T [Latham, 1981]:

$$V_b = \frac{E_c}{\beta} \cdot T, \tag{5.5}$$

where E_c is a critical (local) breakdown field that is constant with any variation of T and β is a local field enhancement factor. The last is caused by imperfections in

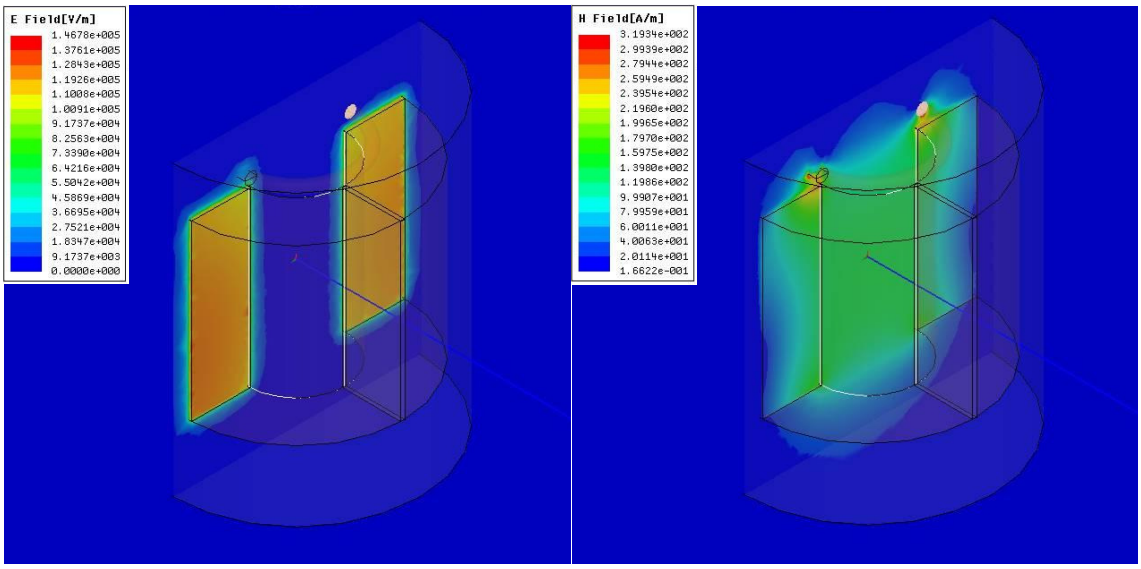

Figure 5.2: Simulation results of the resonator trap (Design I) as in Figure 5.1. Left: Electric field in $[\frac{V}{m}]$; Right: Magnetic field in $[\frac{A}{m}]$.

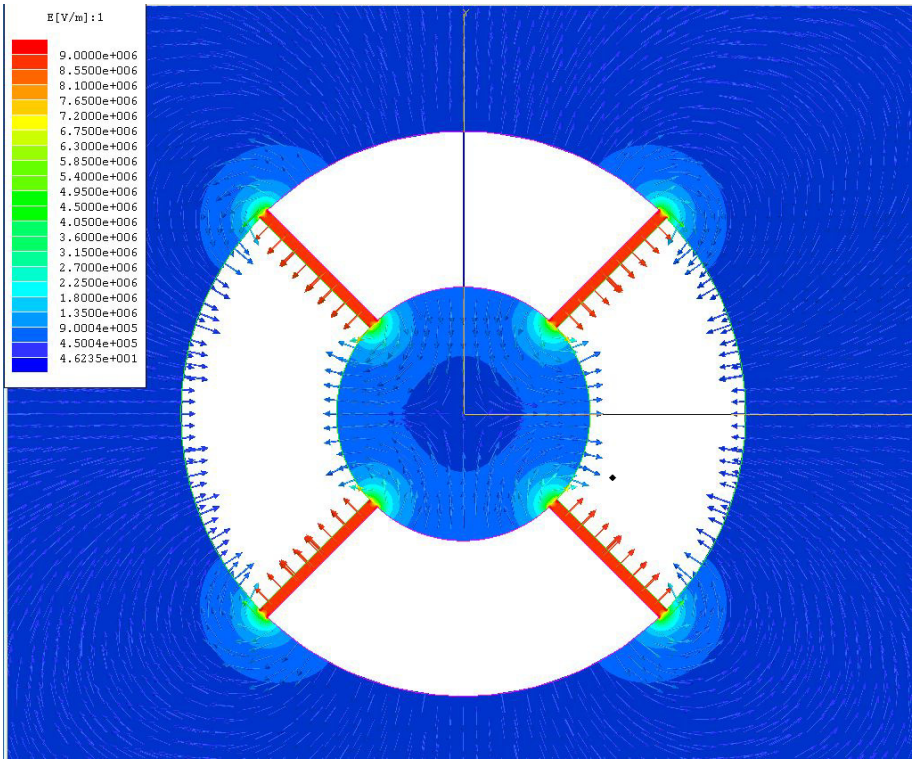

Figure 5.3: Maxwell 2D electric field simulation. The electric field in the gaps is about 8.8 MV/m at 1 kV potential applied to the opposite RF electrodes.

Dimensions	[mm]
D	2.5
L	4.51
W	1.52
T	0.11
H	0.35
D2	12
W2	1

Table 5.1: Dimensions of the resonator trap. D *is te inner diameter of the trap,* L *is its length,* W *is the trap wall width,* T *is the trap gap length, i.e. distance between the neighboring RF electrodes,* H *is the distance to the excitation loop,* D2 *is the inner diameter of the resonator trap holder and* W2 *is its width.*

the material as protrusions or whiskers. The higher is this factor, the lower is the V_b limit. For the current resonator trap the microwave electric field between electrodes that are separated by $T = 0.11\,\mathrm{mm}$ approaches $0.12\,\mathrm{MV/m}$ at $1\,\mathrm{W}$ power (see Figure 5.2 Left). The RF potential with amplitude of $1\,\mathrm{kV}$ produces between the electrodes an electric field of $8.8\,\mathrm{MV/m}$. This value is obtained from simulation using the free Maxwell 2D software and the results are depicted in Figure 5.3. In general there are no significant differences between the values of the breakdown voltage of the investigated materials in case of DC and low frequency AC potentials: AC breakdown voltages are slightly higher than DC in the UHV and both breakdown voltages regimes are insensitive to small pressure fluctuations. With increasing frequency of the AC potentials on the electrodes, though, the breakdown voltage increases [Karetnikov, 1997]. Therefore, the higher the frequency of the applied voltage waveform, the better it is. Based on a paper of Kildemo [Kildemo *et al.*, 2004] we used molybdenum (Mo) for the resonator trap since in RF experiments it has shown a breakdown voltage even higher than wolfram (W). Molybdenum has the breakdown electric field $E_b = \frac{E_c}{\beta}$ equal to $420\,\mathrm{MV/m}$ compared to $340\,\mathrm{MV/m}$ for Wolfram. Care should be taken if one wants to use copper (Cu) if the electric fields exceeds $100\,\mathrm{MV/m}$: the surface quality of the Cu electrodes is modified with each breakdown reducing each time the breakdown voltage limit. Even after one single breakdown short, Cu material surfaces has great damages. The average breakdown field for Cu equals $260\,\mathrm{MV/m}$ at RF voltages. The values for Mo, W and Cu are taken from [Kildemo *et al.*, 2004]. Therefore, for the Mo electrodes with the inter-electrode distance $T = 0.11\,\mathrm{mm}$ the breakdown voltage V_b equals about $29\,\mathrm{kV}$.

The resonator trap has to be supported inside the vacuum chamber. One of the

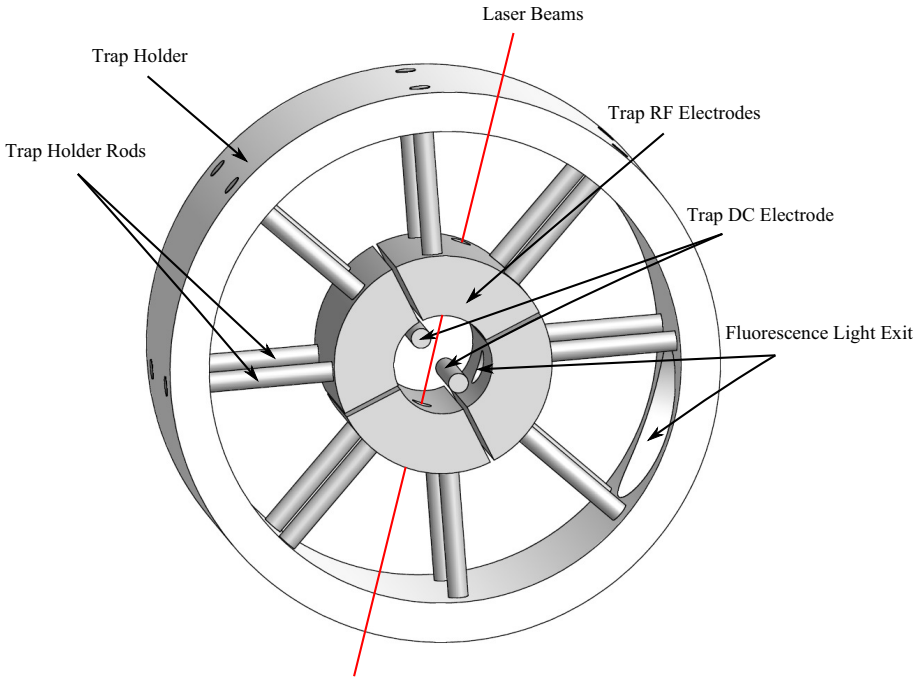

Figure 5.4: The resonator trap design with MACOR holder structure and Mo rods: Design II.

possible designs (Design II) is depicted in Figure 5.4. Here, a MACOR cylindrical structure with inner diameter of 12 mm was used to hold the resonator trap with *Mo* rods. The last are also needed to bring the RF signal to the trap electrodes. With the addition of the holders the performance of the resonator trap worsen immediately: the resonance frequency shifted to 13.34 GHz and the resonator trap structure started to radiate as it is possible to see from the simulation results presented in Figure 5.5. The resonance peak is also quite shallow with a return loss of -6.50 dB that corresponds to an VSWR of 2.8 (see Figure 5.6). Accordingly, the microwave magnetic field decreased down to 83 A/m, three times lower, and a Rabi frequencies of 1.4 MHz at 1 W and 2.2 MHz at 2.5 W are expected.

An alternative resonator trap design is depicted in Figure 5.7. The resonator can be machined from MACOR (or other vacuum compatible ceramic) and then metal-plated. The plating can be patterned later to form the structure in Figure 5.7. In this way the surface metal deposited on the outer cylinder creates also a shield that can solve the trap radiation problems. As it was already mentioned at the beginning of the section, the shield shifts the resonator resonance. Here we took the inner diameter of the shied equal to 12 mm. Therefore, the trap parameters presented in Table 5.1 needs to be slightly adjusted. For example, to increase the

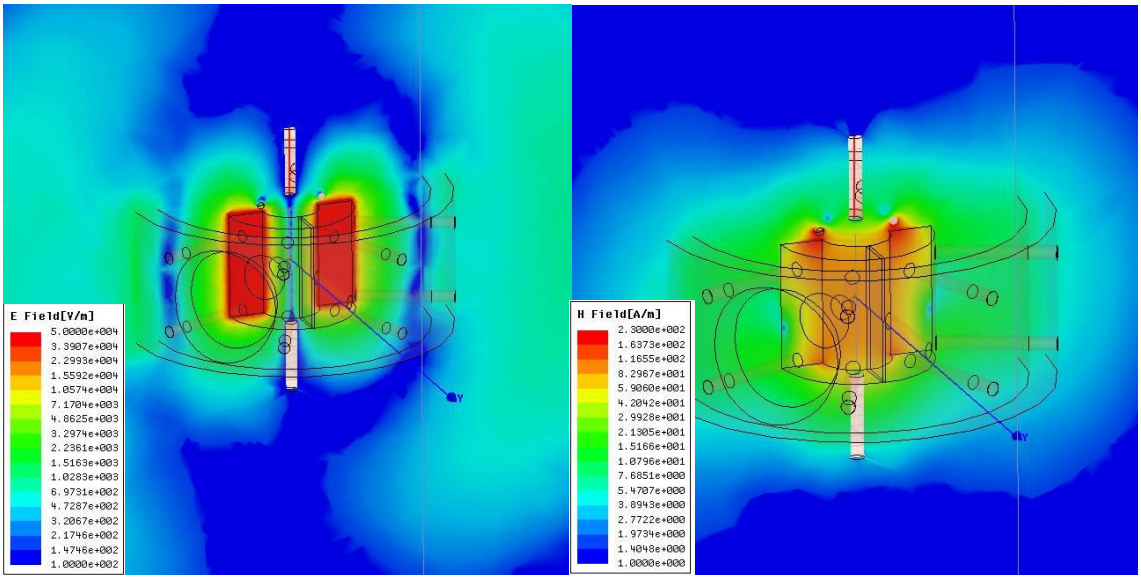

Figure 5.5: Simulation results of the resonator trap Design II. Left: Electric field in $[\frac{V}{m}]$; Right: Magnetic field in $[\frac{A}{m}]$

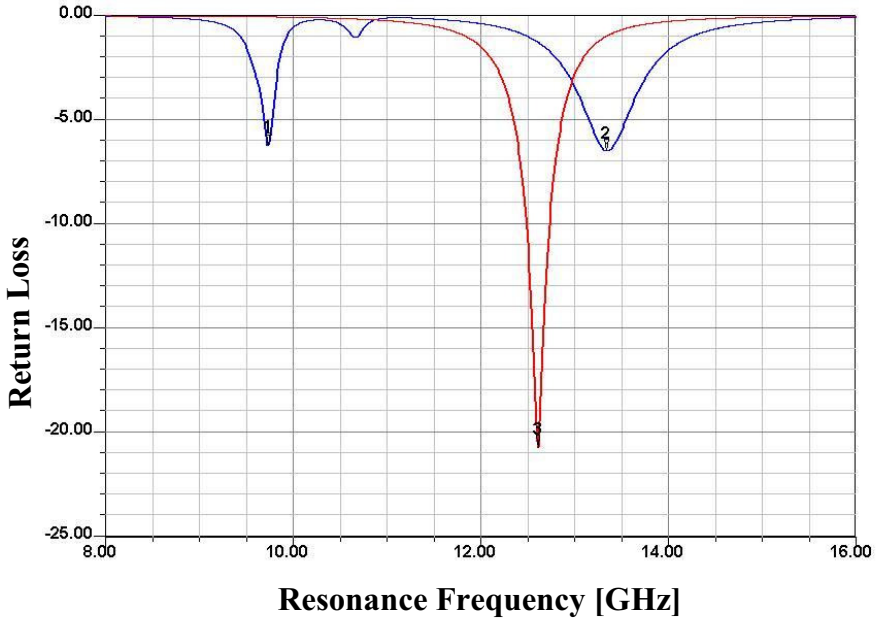

Figure 5.6: Return losses versus resonance frequency. Red curve is for the basic resonator trap, Design I, and the blue line is for the resonator trap with the holding structure, Design II.

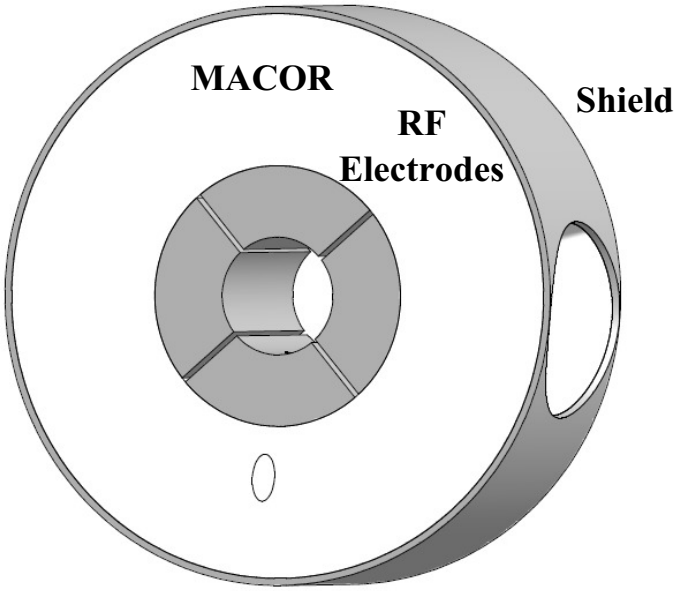

Figure 5.7: The resonator trap Design III. The trap is machined from MACOR and then metal-plated. The plating can be patterned later to form the structure similar to the basic resonator trap design (Design I). The metallic plating on the outer surface of the MACOR cylinder creates the shield to suppress radiation.

resonance frequency the trap gap length can be increased. Here, some new fields simulations will be advisable.

The resonator trap theoretical parameters can be summarized in the following. An RF source power of 15 W has been used in the experiment with the linear trap that results in a maximum peak voltage of 600 V. Considering the RF frequency of about 18.8 MHz, optimized for the linear trap, and the distance from the resonator trap center to the RF electrode of 1.25 mm, the expected radial trap frequency is about $2\pi \cdot 212$ kHz with q equal to 0.03. Considering a slightly higher voltage of 1000 V, the radial trap frequency is about $2\pi \cdot 350$ kHz with q equal to 0.05. When installing the resonator trap, that can have a different capacitance compared to the linear trap, the return losses must be measured and the capacitance of the RF resonator must be adjusted, as it was done with the linear trap. It is possible that the RF frequency as well as the maximum peak voltage produced will be different compared to the linear trap. The geometrical factor α must be estimated for the new trap as well. Hence, the axial trap frequencies can not be evaluated exactly. We can just presume that if the radial frequency is about $2\pi \cdot 350$ kHz and we want

10 ions in the ion chain, the axial frequency should be larger than $2\pi \cdot 66\,\mathrm{kHz}$, according to equation 3.34. For three ions in the chain with the same radial trap frequency the axial frequency should be larger than about $2\pi \cdot 186\,\mathrm{kHz}$.

6

Experimental Methods

This chapter explains the fundamental experimental techniques and procedures required for the experiments presented in the following chapters.

Initially, the steps of the complete measurement sequence, as it is used in the experiments, are briefly reviewed. Some of the experiments, such as the Rabi frequency measurements, are repeated routinely on a daily bases. The Rabi frequency is an important parameter for the experiments that include qubit manipulation. Some of the experiments, such as addressing and microwave scans, are used to characterize the new experimental setup. The problem of coherence is investigated more broadly: different microwave pulse sequences are investigated for a better compensation of the dephasing errors in the experiments.

6.1 Measurement Sequence

The coherent measurements performed in this thesis are based on the measurement sequence that consists of several consecutive steps: cooling of the ions (Doppler and sideband), preparation of the ions in the ground state $|\downarrow\rangle$, manipulation of the qubit state and the qubit state read-out.

1) Doppler cooling is performed by the 369 nm laser light that is 10−15 MHz red-detuned from the $^2S_{1/2}$ $(F = 1) \leftrightarrow {}^2P_{1/2}$ $(F = 0)$ *cooling transition* (light blue in Figure 3.7) and microwave radiation at resonance with the $|\downarrow\rangle \leftrightarrow {}^2S_{1/2}$ $(F = 1,\ m_F = 0)$ transition. In this way each experimental sequence starts with the similar phonon occupation number. Doppler cooling duration is about 9 ms for the measurements where the sideband cooling is not used and in the range of the 4−5 ms otherwise.

2) Sideband cooling (optional) is performed by microwave radiation tuned to the red sideband of the $^2S_{1/2}$ $|F = 0, m_F = 0\rangle \leftrightarrow {}^2S_{1/2}$ $|F = 1, m_F = 1\rangle$ carrier transition by the frequency of the axial COM mode ν_z and by the 369 nm laser light that is in resonance with the $^2S_{1/2}$ $(F = 1) \leftrightarrow {}^2P_{1/2}$ $(F = 1)$ *preparation transition* (blue in Figure 3.7). In this way the temperature of the ions and, respectively, the phonon number is further decreased. The duration of the sideband cooling is in the range of 4−5 ms.

3) The ions are prepared in the ground state $|\downarrow\rangle$ by shining for 2 ms the 369 nm laser light in resonance with the *preparation transition* [Baumgart, 2008].

4) Manipulation of the qubit state is performed by the microwave radiation using the VFG device that allows to set different amplitude, duration, frequency and phase of the microwave pulse. Besides, the manipulation can be performed coherently even during the swap between the different frequencies. The evolution time that was used in the experiments described in this work ranges 1.2−11 ms and the duration of the π-pulse is about 8 μs.

5) During the read-out the ion's fluorescence is collected. The 369 nm laser light is in resonance with the *cooling transition*. Read-out lasts 2 ms and the data are measured in *time bins*, the time increments in which the total readout time is subdivided. This allows to choose the best readout time after the data are measured (see section 6.3). Photo-multiplier counts are also collected during the cooling cycle and these data are used for preselection. It can happen that the ion becomes dark during cooling and its fluorescence level decreases to the level of the background counts after what it comes back to the previous level. The data points taken when the ion is dark are, therefore, discarded in the final analysis. The criterium for selection is a fluorescence level decrease for more than half the value of the average fluorescence level.

The total duration of the measurement sequence is about 20 ms since the experiment is triggered to the 50 Hz of the A/C power lines (see subsection 6.6.3). Each sequence is usually repeated about 50−70 times. Technical aspects of the different sequence steps are also described in section 3.3.

6.2 Laser Cooling

Trapped ions still have quite a big kinetic energy and they are usually not in the ground state of the trapping potential. The energy of the atomic beam is larger than 61 mV [Eiteneuer, 2009] corresponding to the temperature of the ions of about 708 K. The goal of any cooling is to reduce the kinetic energy of the ions so that the ions are crystalized, the Lamb-Dicke regime is achieved and, in the ideal case, the ions are in their ground motional state $|n = 0\rangle$ or close to it.

There are two different regimes for cooling: the weak and the strong binding limit, with the $\Gamma \gg \omega$ and $\Gamma \ll \omega$, respectively, where ω is the trap frequency and Γ is the transition width. In the weak binding limit the line-width is so wide that the sidebands are invisible. The ion behaves like a free particle and a velocity-dependent force from the incoming laser light decreases the kinetic energy of this particle providing cooling know as a Doppler cooling [Hänsch & Schavlow, 1975; Wineland & Dehmlet, 1975; Wineland & Itano, 1979]. In the strong binding limit, the sidebands are resolved and the incoming radiation can be tuned to a particular sideband. If the energy of the absorbed photons is smaller than the mean energy of spontaneously emitted photons, the kinetic energy of the ion decreases. In this regime the sideband cooling [Diedrich *et al.*, 1989] can be used.

6.2.1 Doppler Cooling

As the name suggests, this type of cooling uses the Doppler effect, i.e. the relative motion between the source and observer causes a change in the observed frequency of the electromagnetic wave. The ion will absorb or emit photons of different frequencies, depending on its motion relative to the light source: for the ion moving into the laser beam the laser frequency ω Doppler-shifted toward a higher frequency $\omega_+ = \omega(1 + v/c)$, while for the ion moving along the direction of propagation of the laser beam the frequency $\omega_- = \omega(1 - v/c)$. Here, v is the velocity of the ion and c is the speed of light. If the cooling laser is detuned below the ion's resonance ω_0 (red-detuning, $\omega < \omega_0$), the ion that moves toward this laser light will absorb the photon with the lower energy $E = \hbar\omega < \hbar\omega_0$ due the laser frequency Doppler shift. The ion has a greater probability to emit a photon with a higher energy than the absorbed photon. On average, more energy is emitted than absorbed, which leads to a cooling of the ion. The Doppler cooling limit (Doppler temperature) is

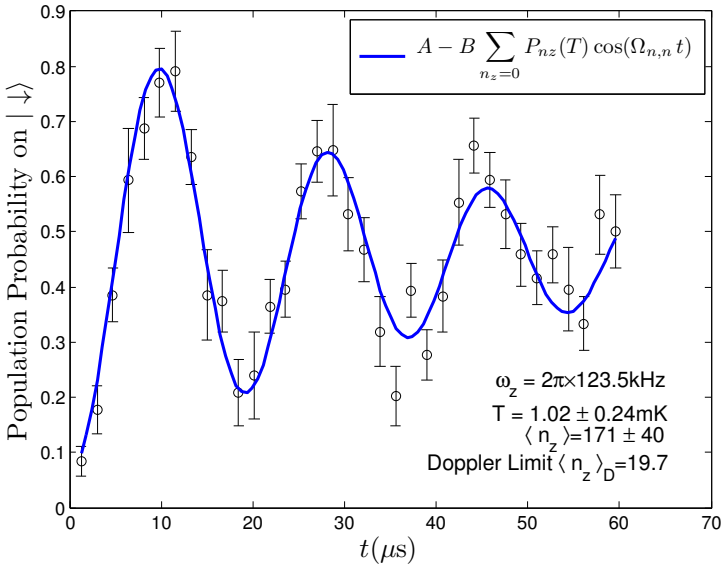

Figure 6.1: Damping of the Rabi oscillations performed on the carrier transition. From the fit (solid line) the ions' temperature T is extracted, which is above the Doppler cooling limit, as expected. In the fit Pn(T)(equation 6.3) is the thermal state distribution and $\Omega_{n,n} = \Omega(1 - \eta_{eff}^2 n)$ is the carrier Rabi frequency of the n_z-th motional mode.

[Stenholm, 1986]:

$$T_D = \frac{\hbar\Gamma}{2k_B} = \frac{\langle n_{min}\rangle \hbar\nu_z}{k_B}, \tag{6.1}$$

where k_B is the Boltzmann's constant, $\hbar$ is the reduced Planck's constant, $\langle n_{min}\rangle$ is the minimum achievable phonon number and ν_z is the angular axial trap frequency.

The temperature after the Doppler cooling was estimated using Rabi frequency measurements on both the carrier and the red-sideband transitions. The temperature measurement using the carrier transition is depicted in Figure 6.1. When excited on the carrier transition (n = n'), the excited state population as a function

of pulse duration t is given by [Walls & Milburn, 1994]:

$$P_{|\uparrow\rangle} = \sum_{n=0}^{\infty} P_n \sin^2\left(\frac{\Omega_{n,n}t}{2}\right) = \frac{1}{2}\left(1 - \sum_{n=0}^{\infty} P_n \cos(\Omega_{n,n}t)\right), \tag{6.2}$$

where the Rabi frequency is $\Omega_{n,n} = \Omega L_n(\eta_{eff}^2) = \Omega(1 - \eta_{eff}^2 n)$ (see equation 2.56) and a thermal state distribution P_n is given by [Loudon, 1983], Chapter 1:

$$P_n = \frac{1}{(1+\overline{n})}\left(\frac{\overline{n}}{(1+\overline{n})}\right)^n, \tag{6.3}$$

with the average occupation number $\overline{n} = \langle n \rangle$. From a fit (solid line in Figure 6.1), described by equation 6.2, the mean vibrational quantum number is $\overline{n} = 171(40)$, for an axial trap frequency of $\nu_z = 2\pi \cdot 123.5\,\mathrm{kHz}$. The Doppler temperature for the $^{171}\mathrm{Yb}^+$ ion ($\Gamma \approx 5\,\mathrm{MHz}$ for the $^2P_{1/2}\,|F=0\rangle \rightarrow ^2S_{1/2}\,|F=1\rangle$ transition [Balzer, 2003]) results from equation 6.1 in 0.12 mK, corresponding to an average phonon number $\overline{n} = 19.7$.

As one can notice, the measured temperature achieved after the Doppler cooling is substantially higher than the predicted Doppler limit. The Doppler cooling limit is imposed by the recoil energy which the ion experiences after the photon emission. This recoil energy corresponds to the heating rate of the ion and it counteracts any cooling effects. The Doppler cooling limit corresponds to the kinetic energy at which the cooling rate of the Doppler cooling equals the heating rate due to the ion's recoil. Therefore, in case that the heating is only due to recoil, the temperature of the ions equals the Doppler temperature and this is obtained for a maximum cooling rate that is achieved when the cooling laser frequency is red-detuned by $\Gamma/2$, where Γ is a natural linewidth of the cooling transition. Besides, the optimum power of the cooling laser should be found. For not properly provided cooling settings (different detuning and/or power) and additional heating sources (as you observe when the laser is switched off) the best temperature that can be obtained can be considerably higher. Bad settings are one reason, and a heating rate that by far exceeds the rate at the Doppler limit, due to technical problems, would be another common reason.

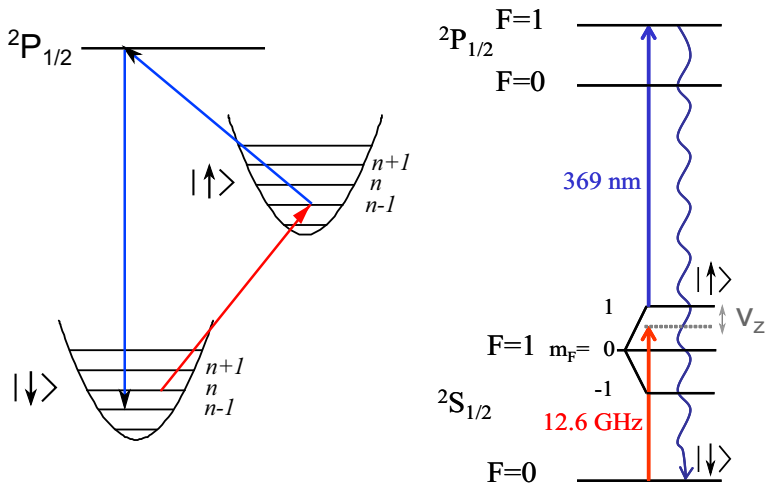

Figure 6.2: Sideband cooling. Left: The principle of sideband cooling. If a single ion is initially in state $|\downarrow\rangle|n\rangle$ and is illuminated by a radiation tuned to the red sideband, $\omega_0 - \nu_z$, where ω_0 is the resonance frequency of the carrier and ν_z is the resonance frequency of the harmonic oscillator, the state is excited to $|\uparrow\rangle|n-1\rangle$. The latter state will decay to $|\downarrow\rangle|n-2\rangle$, $|\downarrow\rangle|n-1\rangle$ (shown on the picture) or it will go back to $|\downarrow\rangle|n\rangle$. On average, the number of phonons in the mode decreases by 1 after each excitation/ emission cycle. Right: The $^{171}Yb^+$ ion partial energy-level diagram that shows the transition we use for sideband cooling in our experiment.

6.2.2 Sideband Cooling

We recall that the internal and motional states of an ion are coupled. The motional sideband are well resolvable, as was demonstrated before in Figure 6.9, hence sideband cooling is possible. The red and blue sidebands are at $\omega_0 - \nu_z$ and $\omega_0 + \nu_z$, respectively. The ion can absorb photons not only at the carrier frequency ω_0 but also at the upper and lower sidebands at the frequencies $\omega_0 \pm \nu_z$. If the ion is prepared in the state $|\downarrow\rangle|n\rangle$, the exciting radiation, tuned to the red sideband at $\omega_0 - \nu_z$, will excite the ion to the state $|\uparrow\rangle|n-1\rangle$ (see Figure 6.2, Left). The latter state will decay to $|\downarrow\rangle|n-2\rangle$, $|\downarrow\rangle|n-1\rangle$ (shown on the picture) or it will go back to $|\downarrow\rangle|n\rangle$. On average, the number of phonons in the mode decreases by 1 after each excitation/ emission cycle until the vibrational mode will reach its ground state, in case there are no competing effects that heat the ions. Investigation of heating effects is not the scope of this thesis.

To perform sideband cooling on the $^{171}Yb^+$ ion we use the hyperfine split transition $^2P_{1/2}|F=0, m_F=0\rangle \leftrightarrow ^2S_{1/2}|F=1, m_F=1\rangle$ detuned to the red by COM mode frequency ν_z (see Figure 6.2, Right). The cooling was always carried out on one ion

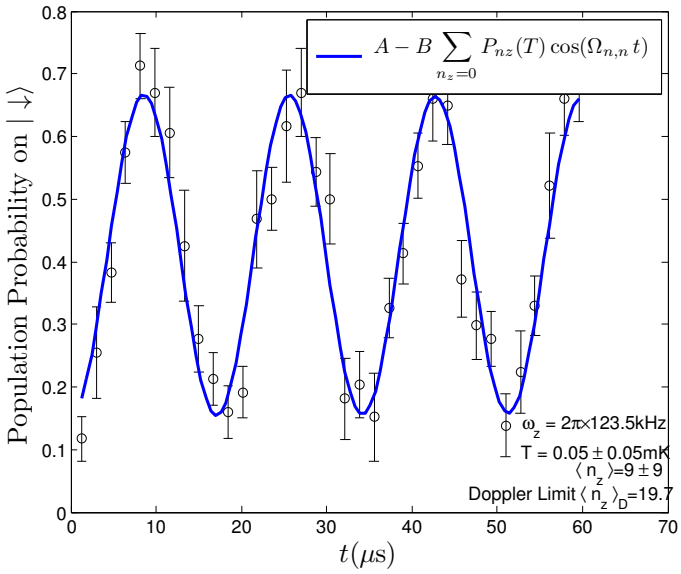

Figure 6.3: Carrier Rabi oscillation using sideband cooling. In the fit Pn(T)(equation 6.3) is the thermal state distribution and $\Omega_{n,n} = \Omega(1 - \eta_{eff}^2 n)$ *is the carrier Rabi frequency of the* n_z*-th motional mode. A minimum average phonon number of* $\overline{n} = 9(9)$ *is achieved.*

in the chain. The neighboring ions are then cooled due to the sympathetic cooling by the mutual Coulomb interaction. More details can be found in [Scharfenberger, 2012]. For two trapped ions the minimum average phonon number achieved is $\overline{n} = 9(9)$ (see Figure 6.3), for three trapped ions the minimum average phonon number currently achieved is $\overline{n} = 23(7)$. Cooling to the ground motional state becomes more complicated when the number of ions increases since the number of vibrational modes increases as well. Presumably, the radial vibrational modes are not cooled properly. Besides, different ions will be influenced by different patch potentials on the trap electrodes that can contribute to the heating of the ions.

6.3 Rabi Frequency Measurements

For Rabi frequency measurement the fourth step in the measurement sequence presented in section 6.1 is just a microwave pulse of defined duration T_{mw}. The

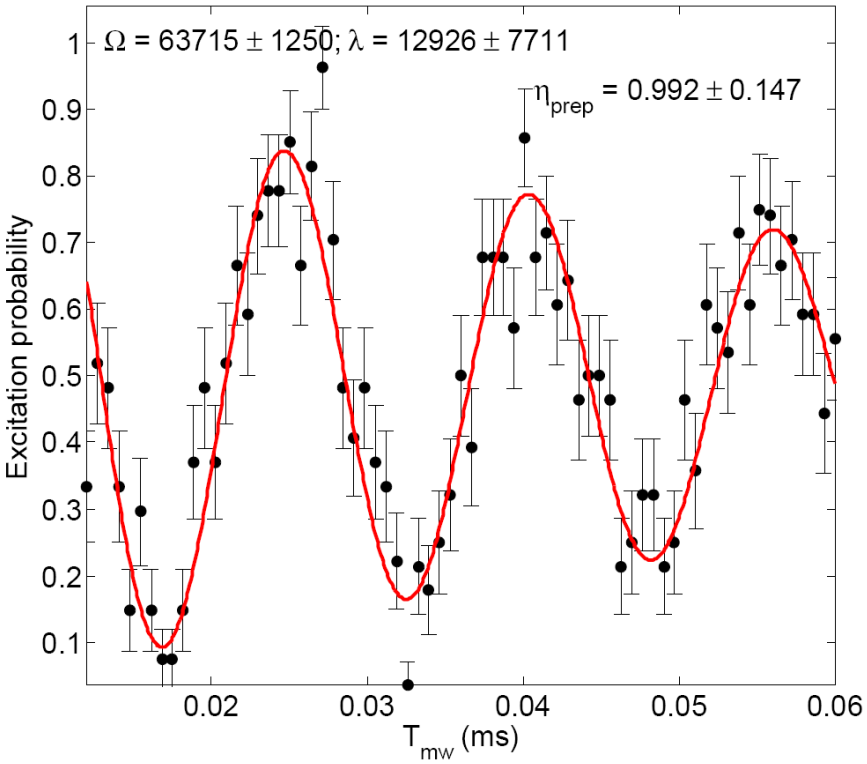

Figure 6.4: Rabi oscillations for ion one (two ions are trapped) on the σ^+ hyperfine transition of the $^{171}Yb^+$ ion at frequency of 12.645830 GHz. The probability to find the ion in the $^2S_{1/2}$ ($F = 1$, $m_F = 1$) state is plotted versus the microwave pulse duration T_{mw}. The fit is $B + A \cdot (1 - \exp(-\lambda \cdot T_{mw}) \cdot \cos(2\pi \cdot \Omega \cdot T_{mw} + \phi))$, where B is the background, A is the amplitude, Ω is the Rabi frequency, ϕ is the phase, λ is the decay constant and T_{mw} is the microwave pulse duration. η_{prep} is the preparation efficiency described by equation 6.8.

sequence is repeated for N different times T_{mw} plus there are M repetitions of the entire procedure to receive and averaged pattern. The probability to find the ion in the $^2S_{1/2}$ ($F = 1$, $m_F = 1$) state is plotted versus T_{mw} and an example of the Rabi fringes is shown in Figure 6.4. For this measurement the cooling, the preparation and the read-out cycles durations are 13 ms, 2 ms and 4 ms, respectively. The T_{mw} is varied in the range of 12−60 μs, $N = 71$ (i.e. there are 71 points in the Rabi fringes) and $M = 30$.

Two important prerequisites for the realization of a quantum computer are the preparation of the qubit in the desired state and the detection of the state with high accuracy. Considering the data from the simple Rabi experiment described here we give the definition of the detection and preparation efficiencies. The values

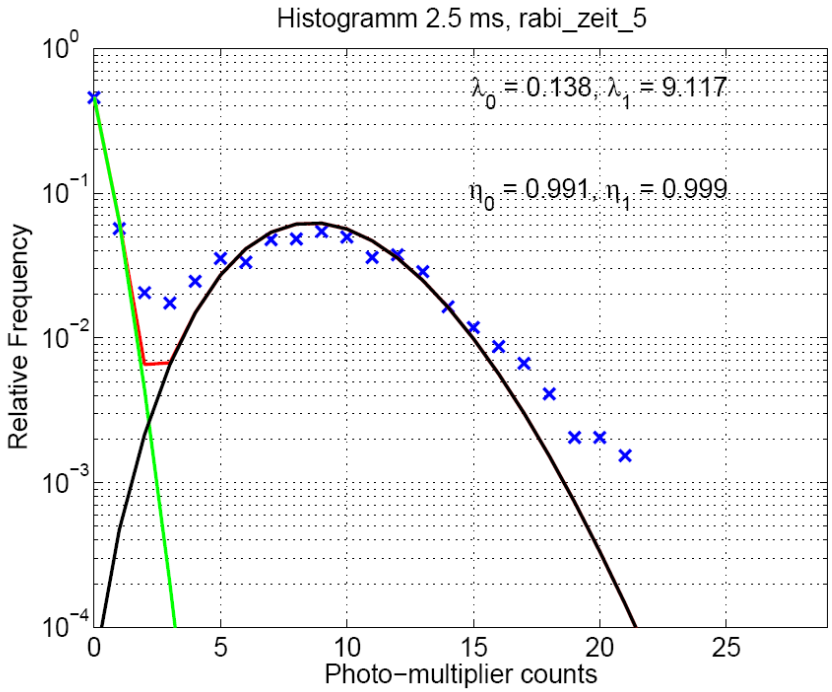

Figure 6.5: Distribution of the photo-multiplier photon counts in order to distinguish between the two states: dark state $^2S_{1/2}$, $(F = 0)$ and bright state $^2S_{1/2}$, $(F = 1)$. The threshold s *is one photon. The average photon counts for the dark state equals $\lambda_0 = 0.092$ and for bright state $\lambda_1 = 9.235$. η_0 and η_1 are detection efficiencies for the dark and bright states, respectively. Here, the reading time is 2.5 ms. The green and black solid lines are two Poissonian fits for the dark and bright state photon counts distribution, respectively. The red solid line is the fit for a sum of these two Poissonian distributions.*

for these efficiencies in the experiment are never exactly 100 % and that reduces the contrast of the measured fringes. Additionally, the detection and preparation efficiencies are used for error estimation of other parameters, i.e. parity and fidelity (see chapter 8).

Detection efficiency

The Rabi oscillation, as presented in Figure 6.4, shows how the population changes when interacting with the radiation for a certain time T_{mw}. To distinguish the states of the ion, a threshold s for the detected photon counts is set. If the photon counts number is below the threshold s, $n < s$, the ion is in the dark state $^2S_{1/2}$,

($F = 0$). On the contrary, if the photon counts number is above or equal the threshold s, $n \geq s$, the ion is in its bright state $^2S_{1/2}$, ($F = 1$). An example of readout data is shown in Figure 6.5. For each of the time bin there are two Poisson distributions for two different states of the ion in the form

$$p(n, \lambda) = \frac{\lambda^n e^{-\lambda}}{n!} \quad , \tag{6.4}$$

where n is the photo-multiplier counts and λ is the average of the photo-multiplier counts (center of the Poisson distribution). For the details of the data evaluation see [Hannemann, 2001; Timoney, 2010]. Summing over an entire Poissonian gives a result of 1, summing below and above the threshold s gives the detection efficiencies for the dark and bright states:

$$\eta_0 = \sum_{n=0}^{s-1} p(n, \lambda_0) \tag{6.5}$$

$$\eta_1 = \sum_{n=s}^{\infty} p(n, \lambda_1) \quad . \tag{6.6}$$

For too short readout time the results are all zeros, for a longer time two distinct peaks can be seen, as the time increases the second peak becomes indistinguishable. The best readout (integration) time is chosen based on the smallest detection error:

$$\epsilon = 1 - \frac{1}{2}(\eta_0 + \eta_1) \quad . \tag{6.7}$$

For the data in Figure 6.5, where the maximum readout time was set to 4 ms with the number of the readout time bins equal to 30, the best integration time is 2.5 ms.

Preparation efficiency

The preparation efficiency η_{prep} is described by the relation [Baumgart, 2008]:

$$\eta_{prep} = \frac{1}{2}\left(\frac{|\vec{\rho}|}{2\overline{\eta} - 1} + 1\right) \quad , \tag{6.8}$$

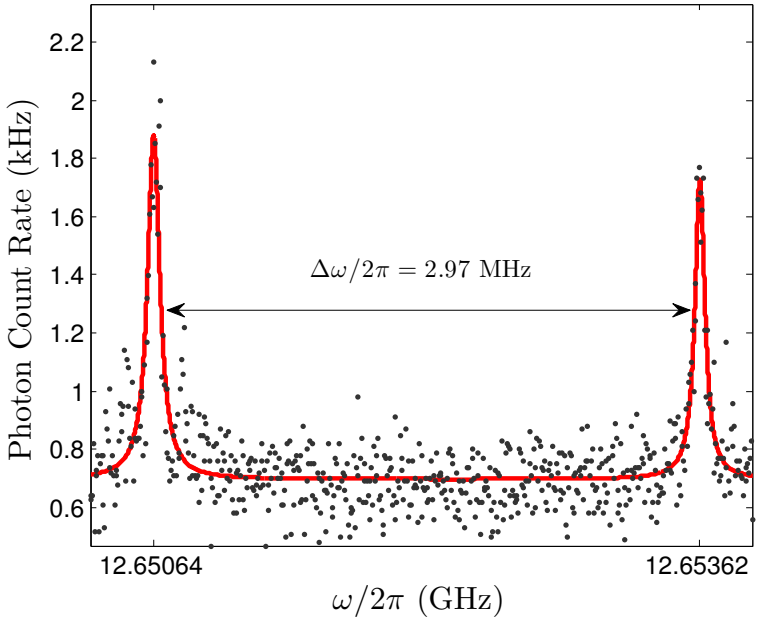

Figure 6.6: Individual addressing of two ions using microwaves. Every dot is an average of 50 repetitions. The solid line is a double Lorentzian fit giving 81(6) kHz and 65(6) kHz for the full widths at half maximum and 2.97(1) MHz frequency separation between the ions for $\nu_z = 2\pi \cdot 171.4(1)$ kHz axial trap frequency, corresponding to $\delta z = 11.2\ (1)$ μm ion separation.

where $|\vec{\rho}|$ is the length of the Bloch vector and it is determined by the contrast of the fitted Rabi oscillation fringes (maximum minus minimum value in the Rabi-spectrum), $\overline{\eta} = (\eta_0 + \eta_1)/2$ is the average detection efficiency. Here, η_0 and η_1 are the detection efficiencies of the dark and bright results, respectively.

6.4 Addressing of the Ions with Microwave

Individual addressing of ions in an inhomogeneous magnetic field has been already observed previously in our group [Johanning *et al.*, 2009a]. In the current experiment new permanent SmCo magnets have been installed directly on the trap

that are expected to deliver a gradient of about 20 T/m. Since this experiment has been build brand new, we would like to characterize the efficiency of the ions addressing in our new setup by measuring the effective gradient and by estimating the addressing error. As it was already explained in section 2.2.1, the frequency separation $\Delta\omega$ between two neighboring ions is proportional to the magnetic field gradient b and the spatial separation between the ions δz (see equation (2.34)). The spatial separation δz for two ions is easy to calculate analytically. The equilibrium position in case of trapped ions is determined by the trapping potential and the Coulomb repulsion of the ions. The potential energy for two ions is then

$$\begin{aligned} V &= V_{osc} + V_{Coulomb} \\ &= 2 \cdot \frac{1}{2} m \nu_z^2 z^2 + \frac{Q^2}{4\pi\varepsilon_0} \frac{1}{2z} \quad , \end{aligned} \tag{6.9}$$

where Q represents the electron charge, ε_0 is the vacuum permittivity, m is the atomic mass of the ion and z is half the distance between two ions. Taking the derivative of equation (6.9) and equating it to zero, we find the equilibrium position of the ion

$$z = \left(\frac{Q^2}{16\pi\varepsilon_0 m \nu_z^2} \right)^{1/3} \quad . \tag{6.10}$$

Hence, the distance between the two ions is

$$\delta z = 2 \cdot z = \left(\frac{Q^2}{2\pi\varepsilon_0 m \nu_z^2} \right)^{1/3} \quad . \tag{6.11}$$

For more than two ions the equilibrium positions can be found using the numerically calculated and scaled equilibrium positions of the ions given in [James, 1998]:

$$\delta z = \left(\frac{Q^2}{4\pi\varepsilon_0 m \nu_z^2} \right)^{1/3} \frac{2.018}{N^{0.559}} \quad , \tag{6.12}$$

where N is the number ions.

An example of the fluorescence spectrum of two $^{171}Yb^+$ ions confined in the linear ion trap is shown in Figure 6.6. After preparing the ions in the $|\downarrow\rangle$ ground state, an

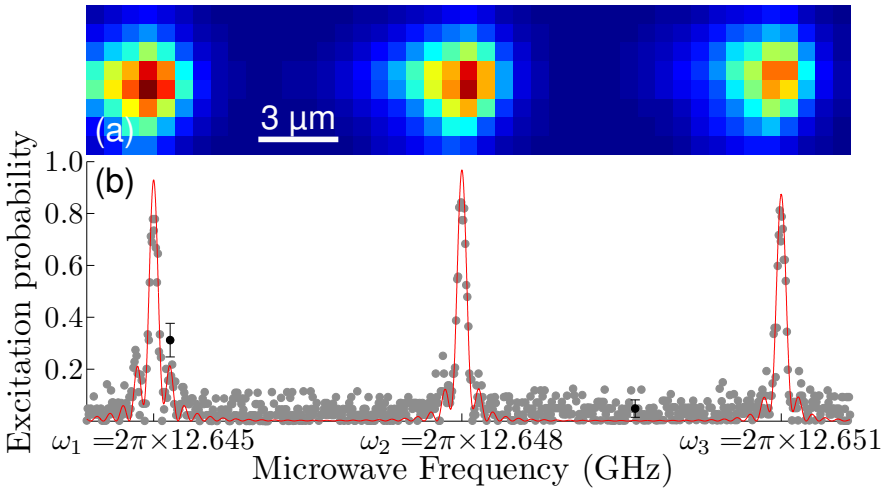

Figure 6.7: Individual addressing of three ions using microwaves. In (a) an image of three $^{171}Yb^{+}$ is shown recorded with an ICCD. Neighboring ions are separated by 11.9 μm at axial trap frequency of $\nu_z = 2\pi \cdot 123.5(2)$ kHz. (b) The microwave spectrum of the above ions. The separation between the ions in frequency space is 3.08(2) MHz. The solid line is a fit to the data. Every dot is an average of 50 repetitions. Two points with error bars are displayed representing the typical statistical standard deviations.

8 μs microwave pulse of frequency ω is applied, followed by the ion state detection. A higher count rate of resonance fluorescence near 369 nm indicates that one of the two ions is excited to the $|\uparrow\rangle$ state for $\omega \simeq \omega_1$ or $\omega \simeq \omega_2$. The axial trap frequency for this measurements equals $\nu_z = 2\pi \cdot 171.4(1)$ kHz. The frequency separation for this particular measurement equals $\Delta\omega = 2\pi \cdot 2.97(1)$ MHz. The heights and widths of two resonance peaks are slightly different due to the slightly different direction of the quantization axis. In this way one ion is driven strongly by the microwave radiation than the other.

In Figure 6.7 the individual addressing of three ions is presented. This microwave spectrum is taken in the same way described above. The inter-ion spacing equals 11.9 μm at the trap potential of $\nu_z = 2\pi \cdot 123.5(2)$ kHz. The resonance frequencies separation is $\Delta\omega = 3.08(2)$ MHz.

Ideally, one always wants to address only the desired ion and to minimize the influence of the addressing pulse on the neighboring, non addressed, ion. The non-resonant addressing probability of a neighboring ion, the addressing error ϵ_{err}, can

be defined as

$$\epsilon_{err} = \frac{\Omega^2}{\Omega^2 + \Delta\omega^2} \quad , \tag{6.13}$$

where Ω is the Rabi frequency on resonance of the addressed ion and $\Delta\omega$ is the detuning from resonance of the neighboring ion due to the magnetic field gradient. For the data presented in Figure 6.6, with $\Delta\omega = 2.97(1)$ MHz and the typical Rabi frequency of about $2\pi \cdot 60$ kHz, $\epsilon_{err} = 0.04\%$. This is the biggest addressing error observed in our experiment. For the axial trapping frequencies $2\pi \cdot 127.1(1)$ kHz, $2\pi \cdot 134.6(1)$ kHz, $2\pi \cdot 142.3(1)$ kHz and $2\pi \cdot 162.1(1)$ kHz the addressing error ϵ_{err} is less than 0.04%. The same is true for the data presented in Figure 6.7. Here an addressing error of 0.037 % is observed. Increasing the gradient or reducing the Rabi frequency will further reduce this error.

Individual ion microwave addressing has a substantially smaller error compared to laser light addressing. For the optical addressing scheme the addressing error is the ratio between the two Rabi-frequencies for the addressed and the neighboring ion [Benhelm, 2008; Gulde, 2000]. The individual laser addressing has errors on the order of few percent: $\epsilon_{err} < 5\,\%$ according to reference [Häffner *et al.*, 2005] and $\epsilon_{err} \simeq 7\,\%$ according to reference [Monz *et al.*, 2009]. In the first case the infidelity equals $P_\uparrow = \sin^2(0.05 \cdot \pi/2) < 0.615\%$ and in the second case $P_\uparrow = \sin^2(0.07 \cdot \pi/2) = 1.2\%$. The infidelities are given only for one π-pulse applied to the ion. Infidelity for our addressing error is less than $3.95 \cdot 10^{-5}\%$. Additionally, the probability to excite the neighboring ion increases after only few Rabi cycles in the individual laser addressing and can in principle reach 100% in a long sequence of gates. It can be compensated by additional pulse sequence. Microwave gradient addressing does not need any additional compensation. The residual excitation in the microwave scheme never exceeds the value stated above. The compensation is achieved by detuning. The generalized Rabi frequency might be large and the performance for very small time scales might be worse compared to optical schemes. The maximum unwanted excitation (spin precession), however, remains small for all times. By an appropriate choice of Rabi frequency and detuning, it can even be completely zero for any chosen time.

Magnetic Field Gradient Measurement

Varying the axial trapping potential (by varying the voltages on the end-cap electrodes) results in a variation of the separation δz between two ions. Measur-

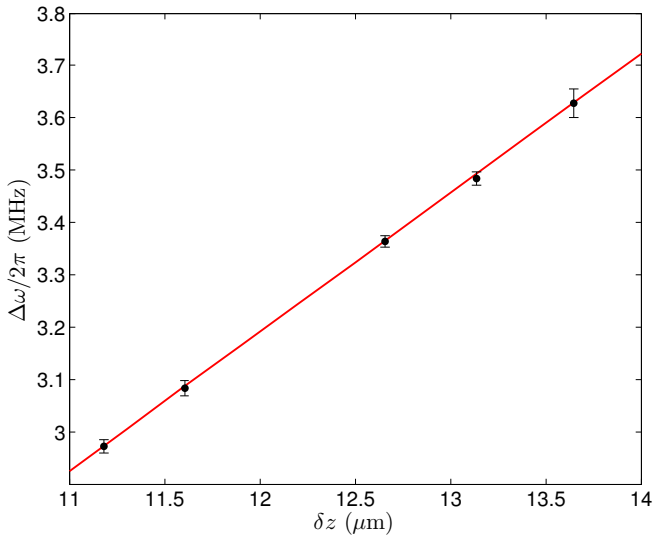

Figure 6.8: Determination of the magnetic field gradient. Two ions, separated by a distance δz, display microwave resonance frequencies differing by $\Delta\omega \equiv \omega_2 - \omega_1$. The difference in magnetic field ΔB experienced by the ions is deduced from $\Delta\omega$. The solid line results from a fit giving a gradient $b = 18.98(2)$ T/m.

ing the difference $\Delta\omega$ between their resonance frequencies as a function of δz ($\Delta\omega = \mu_B \cdot g_F \cdot b \cdot \delta z/h$, equation (2.34)) allows determination of the magnetic field gradient $b = 18.98(2)$ T/m experienced by the ions (Figure 6.8).

6.5 Coupling of the Internal and Motional States

In laser based experiments the coupling between the motional and the internal states is possible due to the sufficient momentum transferred from the photons to the ions. With microwaves this is no longer the case. But MAGIC (see section 2.2) allows to overcome this difficulty. In a magnetic field gradient, an ion's equilibrium position depends on the internal spin state. Therefore, motional and internal states can interact. The motional sidebands accompanying the qubit resonance frequency (see Figure 6.9) signifies the coupling between the motion of the trapped $^{171}Yb^+$ ion and its internal state [Johanning *et al.*, 2009a]. Experimentally determined magnetic field gradient and the axial trap frequency define the strength of the coupling equal to $\kappa_{11} = 0.0225$ (see Appendix M). The spectrum, taken as in Figure 6.6, is an average of 15 spectra each with different microwave pulse durations T_{mw}

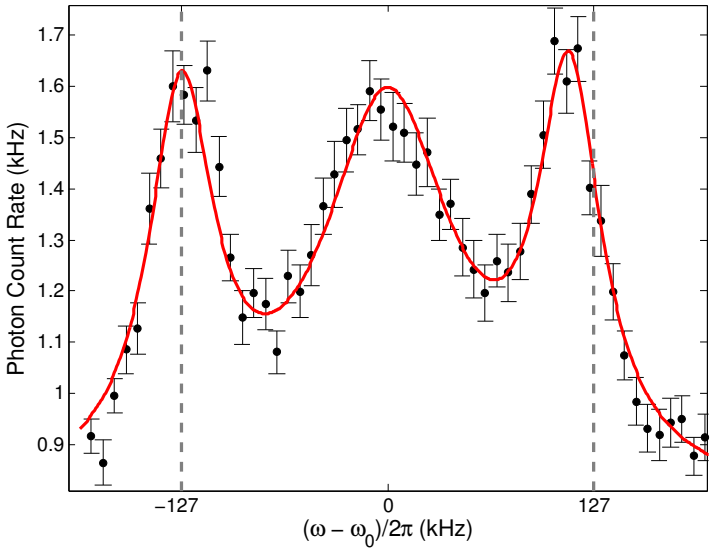

Figure 6.9: Detailed microwave spectrum of one ion (part of a two ion crystal). Motional sidebands are visible indicating the coupling between internal states and vibrational motion determined by $\kappa_{11} = 0.0225$. The spectrum is an average of spectra taken as in Figure 6.6, where each data point is in its turn an average of 50 repetitions, but with different microwave pulse durations T_{mw} ranging from 7 μs to 22 μs. The solid line indicates a fit with three Lorentzians with line-widths of the red and the blue sidebands equal to $2\pi \cdot 49(5)$ kHz and $2\pi \cdot 47(6)$ kHz, respectively. The carrier line-width is $2\pi \cdot 99(19)$ kHz. The trap frequency $\nu_z = 2\pi \cdot 127.1(1)$ kHz has been determined independently by parametric heating. Here, $\omega_0 = 12649886$ kHz is the σ^+ transition frequency of the ion and ω is the microwave frequency scan.

ranging from 7 μs to 22 μs. Each data point in each constituting spectrum is in its turn an average of 50 repeated measurements. The measured axial trap frequency is $\nu_z = 2\pi \cdot 127.1(1)$ kHz, π-pulse duration for a carrier is about 8 μs, for the sidebands about 22 μs, the full width at half maximum of the sidebands is about 47(6)−49(5) kHz.

The positions of the sidebands should correspond to the axial trap frequency. In Figure 6.9 the red sideband (left) is at 127(13) kHz and the blue sideband (right) is at 112(10) kHz relative to the carrier peak. These values are within 1σ to 2σ away from the axial trap frequency measured by the parametric heating. The discrepancy is due to the several factors that contribute to the broadening and the shifts

of the relative positions of the sideband peaks. The magnetic field fluctuations change the positions of the resonance sideband peaks in the microwave spectrum. Additionally, the magnetic field fluctuations and thermal excitations lead to the fluctuations of the Rabi frequency, broadening the resonance peaks. After the averaging over several microwave spectra is performed, the average sideband peaks' positions are shifted: each constituting spectrum, recorded for different microwave pulse durations, is taken at different times and, therefore, at slightly different experimental conditions with different resonance and Rabi frequencies. In further experiments, for example to investigate the sideband cooling [Scharfenberger, 2012], not averaged microwave spectra with a single pulse duration (for example $8\,\mu$s) have been used.

6.6 Coherence of the qubits

The time during which the the phase between the $|\downarrow\rangle$ and the $|\uparrow\rangle$ states remain well-defined is known as *coherence time*. It is a very important parameter in quantum computation since it defines for how long the quantum system can preserve the information that we want to transfer between the different qubits. For example, to perform an elementary unitary transformation, that involve at least two qubits, our coherence time should be at least equal to the time needed for that transformation.

The process of loosing the coherence is known as the *decoherence*. There are several sources of decoherence that can be divided into the following categories [Wineland *et al.*, 1998a]: decoherence of the ion motion; decoherence of the ion internal levels; and the decoherence caused by the non ideal applied fields which are responsible for the logic operations. The main source of decoherence in our experiment is noise on classical electro-magnetic fields: the fluctuations of the ambient magnetic field, i.e. noise from the alternating current (A/C) of the mains, and electric field noise from the trap electrodes. Magnetic field fluctuations result in fluctuating resonance frequencies of the qubits, and these are defined by the Zeeman effect. Electric noise of the electrodes can cause the heating of the ions and the correspondent increase in the vibrational phonon number, contributing in this way to the motional decoherence. These sources of noise cause fluctuations of the relative phase ϕ and as a consequence the dephasing of a qubit superposition $\alpha\,|\downarrow\rangle + e^{i\phi}\beta\,|\uparrow\rangle$.

In the following the measurement sequences applied in our experiments are described. They are used to characterize the coherence time of the experimental setup and to compensate, respectively, for the dephasing in the experiment. The

50 Hz trigger is used to compensate for the magnetic field fluctuations from the A/C mains at 50 Hz.

6.6.1 Ramsey Spectroscopy

The Ramsey-interference experiment [Ramsey, 1985] is the simplest method to investigate the coherence time of the experimental setup. It has the following sequence: 1) the qubit is prepared in the $|\downarrow\rangle$ state; 2) the first $\pi/2$-pulse is applied that creates a coherent superposition of $|\downarrow\rangle$ and $|\uparrow\rangle$ states; 3) after the evolution time τ the second $\pi/2$-pulse is applied; 4) the resulting state is detected. Ramsey fringes are recorded either in time domain, by keeping the phase of the second $\pi/2$-pulse constant and varying the evolution time τ, or in the frequency domain, by keeping τ fixed and varying the phase of the second $\pi/2$-pulse.

We usually measure the so called 'transverse coherence time', known also as 'spin-spin relaxation time' or 'phase coherence time' T_2. Dephasing affects the relative phase ϕ of the qubit superposition $\alpha|\downarrow\rangle + e^{i\phi}\beta|\uparrow\rangle$, randomizing it. Hence, after some finite evolution time τ the superposition decays into a mixed state and the probability to find the ion in the $|\uparrow\rangle$ state approaches 0.5. For the $^{171}Yb^{+}$ ion an hyperfine levels coherence time of > 10 min has been observed in case of magnetic field insensitive (to lowest order) clock states [Fisk *et al.*, 1995]. The coherence time in our experimental setup with the chosen qubit, that is magnetic field sensitive, is currently limited to 200 μs.

There is also another measure of decoherence called the 'longitudinal coherence time' or 'spontaneous emission time', T_1, i.e the lifetime of the $|\uparrow\rangle$ state. Typically T_1 is longer than the transverse relaxation time T_2. For the hyperfine split levels used as a qubit in the current experiment, T_1 can be extremely long since the natural decay times of hyperfine transitions are typically > 1 year [Advanced Research and Development Activity (ARDA), 2004]. The T_1 is usually measured by Rabi oscillation experiment, in our case on the π-transition of the $^{171}Yb^{+}$ ion hyperfine transition. The probability of spontaneous decay is very low and it will not be considered in this experiment.

6.6.2 Spin-Echo Technique

The spin-echo technique, originally invented in the nuclear magnetic resonance [Hahn, 1950], is extensively used also in quantum optics experiments because of

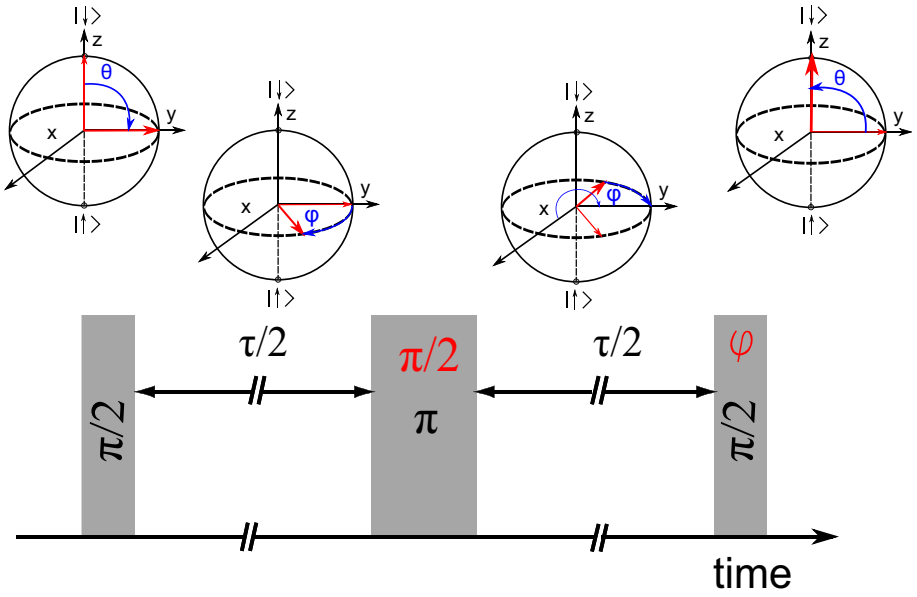

Figure 6.10: Spin-echo sequence performed on one ion.

its ability to compensate the detunings and fluctuations that are slow on the time scale of the evolution time τ. A spin-echo experiment is a Ramsey type experiment with an additional error correcting π-pulse after the half evolution time $\tau/2$ of the Ramsey sequence as it is possible to see in Figure 6.10. The Bloch vector is rotated by a $\pi/2$-pulse around the x-axis (see Figure 2.1) into the equatorial plane. The phase of the superposition state drifts and after a $\tau/2$ time the Bloch vector rotates by an angle φ on the equator. The spin-echo π-pulse with phase of $\pi/2$ rotates the Bloch vector by 180 ° around the y-axis. The Bloch vector continues to move in the same direction and after half evolution time $\tau/2$, rotating by an angle φ, it returns to its initial position. Applying the second $\pi/2$-pulse with phase $\varphi = \pi$ the state vector is projected into the initial state $|\downarrow\rangle$. Choosing the phase of the second $\pi/2$-pulse $\varphi = 0$ projects the state vector into an opposite state $|\uparrow\rangle$.

The coherence time measured with the spin-echo pulse sequence, that was applied to one ion in the chain of two trapped ions, is presented in Figure 6.11. The probability to find the ion in state $|\uparrow\rangle$, in case the phase of the second $\pi/2$-pulse equals $\varphi = 0$ (blue curve) or $\varphi = 180°$ (black curve), is plotted versus the evolution time τ, varied in the range of 0−4 ms. These measurements are performed at $\nu_z = 2\pi \cdot 171.4\,\text{kHz}$ and $T_{delay} = 5\,\text{ms}$ (see subsection 6.6.3). Using the spin-echo sequence the coherence time is increased by one order of magnitude and equals about 2 ms.

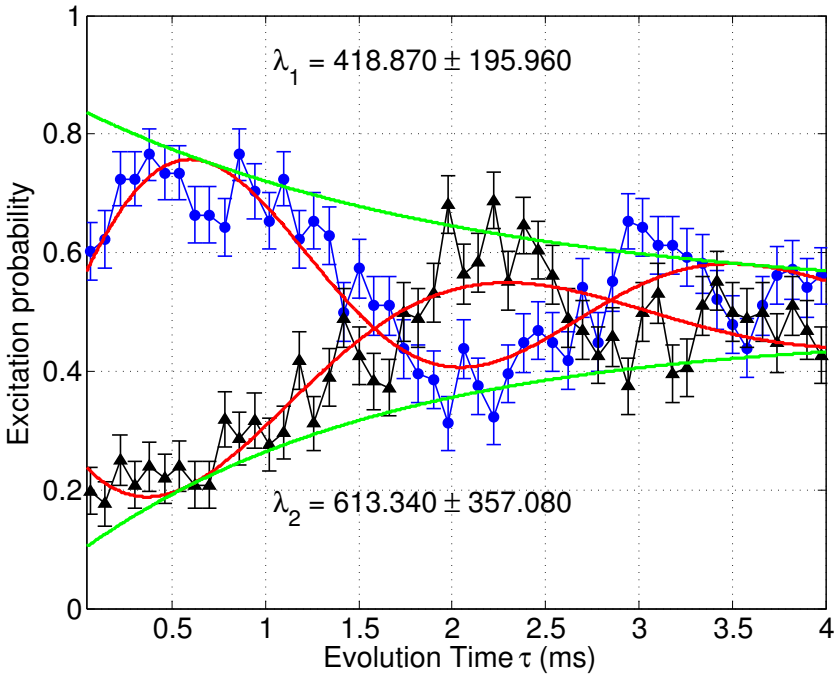

Figure 6.11: Coherence time measurements. The probability to find the ion in state $|\uparrow\rangle$, in case the phase of the second $\pi/2$-pulse equals $\varphi = 0$ (blue curve) or $\varphi = 180°$ (black curve), is plotted versus the evolution time τ, varied in the range of 0−4 ms. The red solid line is the fit $B + A \cdot (1 \mp \exp(-\lambda \cdot \tau) \cdot \cos(2\pi \cdot \Omega \cdot \tau + \phi))$, where B is the background, A is the amplitude, Ω is the Rabi frequency, ϕ is the phase, λ is the decay constant and τ is the evolution time. The green solid line corresponds to the $B + A \cdot (1 \mp \exp(-\lambda \cdot \tau))$. The measured coherence time is, therefore, $T_2 = 1/\lambda_1 = 2.4 \pm 1.1$ ms and $T_2 = 1/\lambda_2 = 1.6 \pm 1$ ms, respectively.

6.6.3 Noise components at 50 Hz

The main source of magnetic field noise arises from the alternating current (A/C) of the mains electricity supply i.e. field fluctuations at 50 Hz. In order to solve this problem the present experiment was triggered to the 50 Hz of the A/C power lines. A synchronization step is built into all sequences involving ADwin and VFG150. The ADwin system is waiting for a 50 Hz trigger and then outputs a TTL pulse, which is awaited by the VFG150. Hence, the total sequence duration should not exceed 20 ms, otherwise we have to wait longer for a next trigger. There is also a delay time, T_{delay}, between the 50 Hz trigger and the beginning of the experiment sequence itself. Varying the T_{delay} changes the magnitudes of the magnetic field

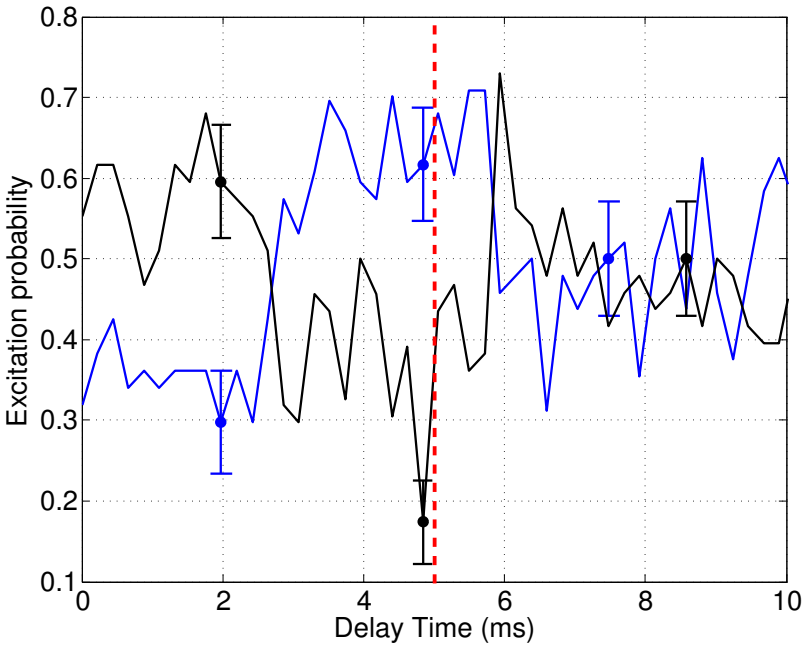

Figure 6.12: The probability to find the ion in the $|\uparrow\rangle$ state, in case the phase of the second $\pi/2$-pulse equals $\varphi = 0$ (blue curve) or $\varphi = 180°$ (black curve), is plotted versus the T_{delay}, varying in the range of 0−22 ms. The optimum time delay for the axial trap frequency of $\nu_z = 2\pi \cdot 171.4\,\mathrm{kHz}$ results in 5 ms, shown by the red line on the picture. The measurements are performed using the evolution time of $\tau = 2\,\mathrm{ms}$.

fluctuations. Hence, it is possible to choose the delay time where these fluctuations are minimum (see also reference [Riebe, 2005; Timoney, 2010]).

In our setup T_{delay} lies in the range of 3−5 ms. For each measurements that used the spin-echo sequence the best T_{delay} must be found. An example of such a measurement is presented in Figure 6.12, where the probability to find the ion in the $|\uparrow\rangle$ state, in case the phase of the second $\pi/2$-pulse equals $\varphi = 0$ (blue curve) or $\varphi = 180°$ (black curve), is plotted versus the T_{delay}, varying in the range of 0−22 ms. The data are taken at axial trap frequency of $\nu_z = 2\pi \cdot 171.4\,\mathrm{kHz}$ and with the evolution time equal to 2 ms. When the qubit superposition state looses its coherence, the probability goes to 0.5. For this particular measurement the best T_{delay} of about 5 ms is chosen indicated in Figure 6.12 by a red split line. The superposition state looses the coherence at about 6 ms.

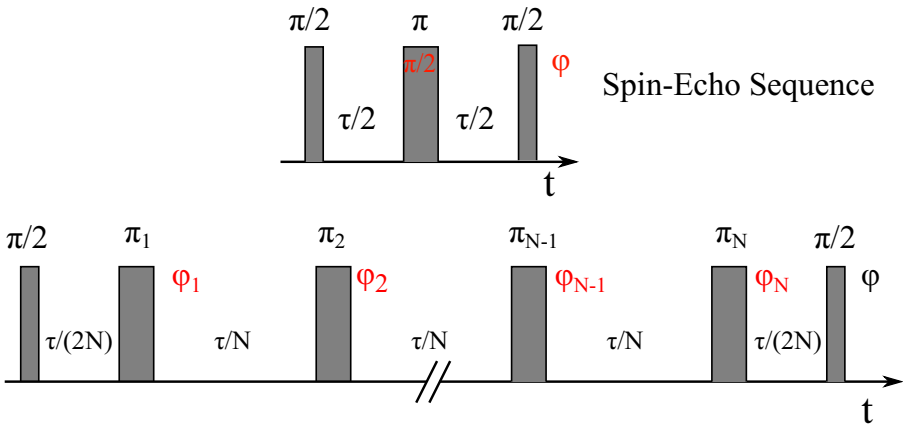

Figure 6.13: An example of the CPMG sequence with N π*-pulses compared to the spin-echo sequence. For the CMPG$_{YY}$ the phases* $\varphi_1 = \varphi_2 = ... = \varphi_{N-1} = \varphi_N = \pi/2$*, for the CMPG$_{XY}$* $\varphi_1 = \varphi_{N-1} = 0$ *(odd* π*-pulses) and* $\varphi_2 = \varphi_N = \pi/2$ *(even* π*-pulses).*

6.6.4 CPMG Technique

The Carr-Purcell-Meiboom-Gill (CPMG) technique [Gullion *et al.*, 1990; Haeberlen, 1976; Meiboom & Gill, 1958] consists of multiple, equally spaced π-pulses within the sequence instead of a single π-pulse used in the spin-echo sequence.

The phases φ of the π-pulses that are sandwiched between the two $\pi/2$-Ramsey pulses define around which axis in the $x - y$ plane the qubit will be rotated. In this work the same notations as in [Vandersypen & Chuang, 2004] are used. A π-pulse with phase $\varphi = 0$ rotates the qubit around the $-x$ axis, denoted also as a $\bar{x}$. The π-pulse with the phase $\varphi = \pi$ rotates the qubit around the x axis and the π-pulse with the phase $\varphi = -\pi/2$ rotates the qubit around the $-y$ axis, denoted also as a $\bar{y}$ axis. The axis are defined on the Bloch sphere in Figure 2.1.

Three different variants of the CPMG sequence have been used in the current experiment:

1) CPMG$_{YY}$: the π-pulses have the same uniform phases, i.e. $\varphi = \pi/2$;

2) CPMG$_{XY}$: the π-pulses are applied along the $\bar{x}$ axis, $\varphi = 0$, and along the y axis, $\varphi = \pi/2$, alternatingly;

3) CDD$_n$, concatenated dynamic decoupling pulse sequence: the π-pulses have a concatenated phase sequence engineered to reduce the dephasing errors.

The generalized CPMG sequence diagram is presented in Figure 6.13. For the CMPG_{YY} the phases $\varphi_1 = \varphi_2 = ... = \varphi_{N-1} = \varphi_N = \pi/2$ are identical. The π-pulses are equidistant and the distances between them equal to $\frac{\tau}{N}$, the ratio between the evolution time τ and the number of π-pulses N. The distances between the first $\pi/2$-pulse and the first π-pulse, the same as between the last π-pulse and the last $\pi/2$-pulse equal to $\frac{\tau}{2N}$, half of the time between the π-pulses. The sum of all the time intervals in the sequence must be equal to the evolution time τ.

The measurements were performed to investigate how the number of the applied π-pulses influences the coherence time. An example of these measurements for 32 and 256 π-pulses in the CPMG_{YY} sequence is shown in Figure 6.14 (a) and (b), respectively. Compared to the spin-echo sequence with coherence time equal to $T_2 = 2\,\text{ms}$, for the 32 π-pulses $T_2 \approx 17.2 \pm 0.5\,\text{ms}$ and for the 256 π-pulses $T_2 \approx 73.8 \pm 1.3\,\text{ms}$. The coherence time increases approximately by 1 ms by each four π-pulses added to the sequence [Piltz, 2013].

Nevertheless, during the experiments it has been revealed that increasing the number of π-pulses in the CPMG_{YY} sequence, produces a reduction of the measured effective coupling. The errors of the individual pulses accumulate during the sequence until there is no detectable phase shift anymore. Hence, the CNOT gate can not be performed with this pulse sequence.

The self-correcting sequence CPMG_{XY} was tried instead, where the π-pulses are applied along the $\bar{x}$ and y axis alternatingly. This sequence is less sensitive to the ions resonance frequency detunings and the pulse length errors, as came out during the measurements.

The concatenated dynamic decoupling pulse sequence (CDD_n) showed the best robustness compared to the previous two sequences. Dynamical decoupling (DD) term comes from [Viola *et al.*, 1999] who first introduced the idea to use the spin-echo effect and refocusing into quantum information processing. The CPMG pulse sequences are in fact the DD sequences. In concatenated DD pulse sequence the universal decoupling sequence is recursively embedded within itself [Khodjasteh & Lidar, 2005, 2007]. In our experiment, the universal decoupling sequence is:

$$\tau/2X\tau Y\tau/2 \quad . \tag{6.14}$$

The concatenated sequence CDD_n can be constructed as [Souza *et al.*, 2011]:

$$CDD_n = \left[\sqrt{CDD_{n-1}}\tau/2X\tau/2CDD_{n-1}\tau/2Y\tau/2\sqrt{CDD_{n-1}}\right]^2, \tag{6.15}$$

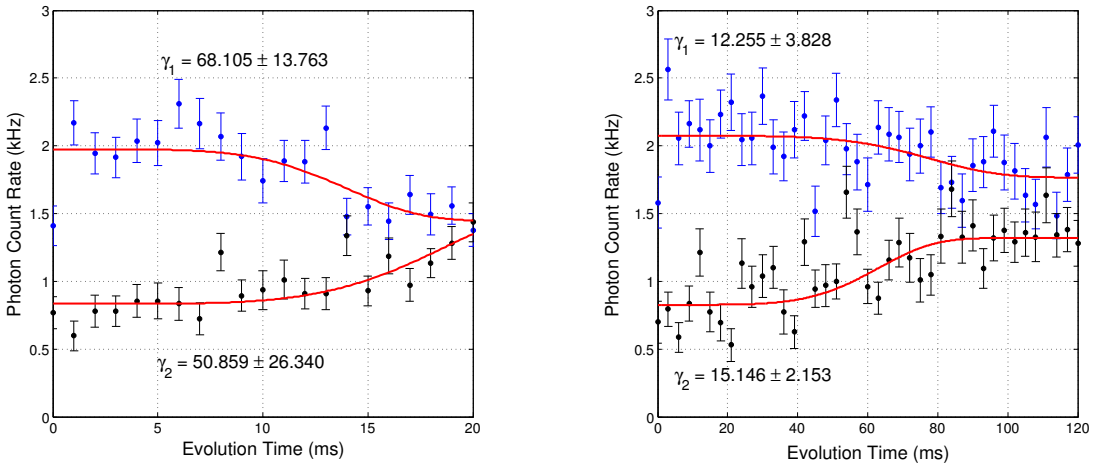

(a) (b)

Figure 6.14: Coherence time T_2 measurements for the CPMG$_{YY}$-sequence with (a) 32 and (b) 256 π-pulses. For the ion prepared in $|\uparrow\rangle$ and $|\downarrow\rangle$ states, the photon count rate is about 2 kHz and 0.7 kHz, respectively. The probability, proportional to the photon count rate, to find the ion in $|\uparrow\rangle$ state, when the phase on the last $\pi/2$-pulse is $\varphi = 0$ (blue dots) and $\varphi = 180°$, is plotted versus the evolution time τ varied in the range a) 0 - 20 ms and b) 0 - 120 ms . The T_2 was extracted from a fit of the form $y = p_0 + p_1 \cdot \exp(-(\frac{\tau}{T_2})^k)$, where $3 < k < 6$ [Ryan et al., 2010]. For the case (a) $T_2 \approx 17.2 \pm 0.5$ ms, for the case (b) $T_2 \approx 73.8 \pm 1.3$ ms. The fits are performed with a fit-parameter k = 5. Each data point was repeated 70 times and the error bars correspond to the mean standard deviations.

where $\mathrm{CDD}_1 = (\tau/2X\tau Y\tau/2)^2$. For example, the CDD_2 sequence is written as

$$CDD_2 = [(\tau/2X\tau Y\tau/2)\tau/2X\tau/2()()\tau/2Y\tau/2()]^2 \tag{6.16}$$

with 20 π-pulses in a total. The CDD_3 sequence is, respectively

$$CDD_3 = \{[(\tau/2X\tau Y\tau/2)\tau/2X\tau/2()()\tau/2Y\tau/2()]\tau/2X\tau/2[][]\tau/2Y\tau/2[]\}^2 \tag{6.17}$$

with in a total of 84 π-pulses. The content in the brackets of the same color and shape is identical.

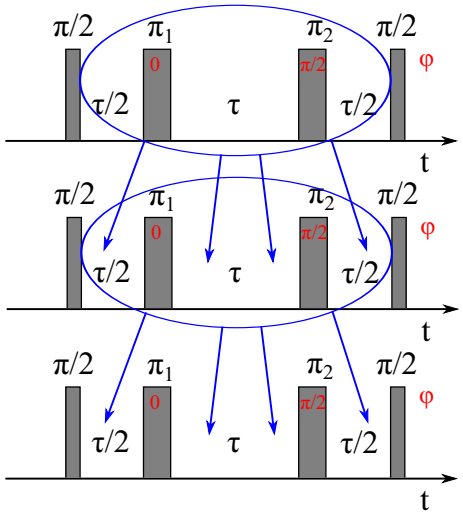

Figure 6.15: CDD_n sequence diagram. The universal decoupling sequence $\tau/2X\tau Y\tau/2$ is recursively embedded within itself.

The CDD_n sequence diagram is shown in Figure 6.15. Here, the $\tau/2 - X - \tau - Y - \tau/2$ sequence is inserted once after the first $\pi/2$-pulses, two times after the first π-pulse, and again once before the last $\pi/2$-pulse. The total sequence received in this way is inserted in the same way in the next $\tau/2 - X - \tau - Y - \tau/2$ sequence and so on.

The maximum coherence time achieved with the CDD_3 multiple π-pulse sequence equals about 11 ms measured at the axial trap frequency of 123.5 kHz. This is almost one order of magnitude bigger compared to the coherence time of 1.2 ms at the axial trap frequency of 127.1 kHz achieved using the simple spin-echo sequence with a single π-pulse.

7

Measurement of the Coupling Constant

Two hyperfine states of each trapped ion serve as an effective spin-1/2 system. Exposing a trapped ion Coulomb-crystal to a spatially varying magnetic field induces a spin-spin interaction mediated by the common vibrational motion of the ion crystal ([McHugh & Twamley, 2005; Wunderlich, 2002; Wunderlich & Balzer, 2003], see subsection 2.2.2). Such a Coulomb-crystal is called a 'pseudo-molecule' [Wineland *et al.*, 1987] and these Ising-like J-couplings between different ions are essential for conditional dynamics as a logical CNOT. After the presence of the coupling has been confirmed (see subsection 6.5), we would to assess quantitatively its strength and how it differs from the theoretical predictions. Besides, knowing of the coupling strength is required to have an idea about the possible available evolution time to perform the CNOT gates.

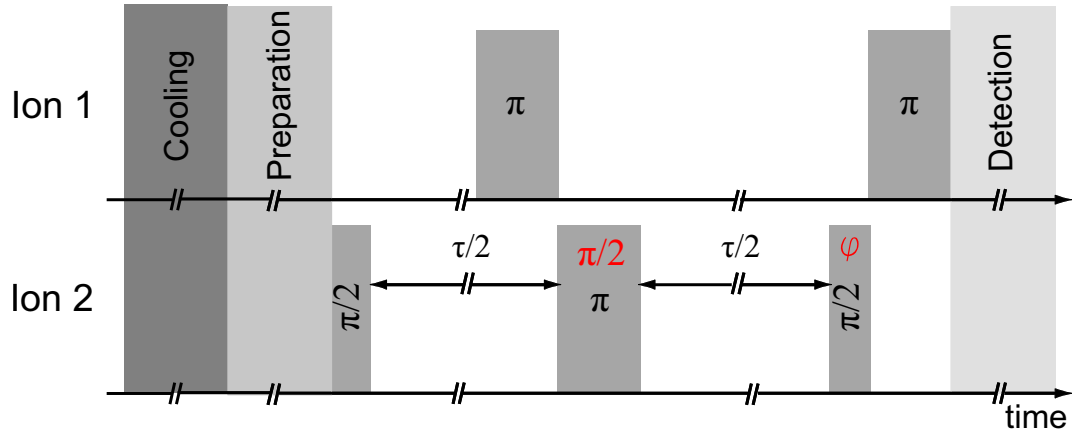

Figure 7.1: J-coupling constant measurements. Ion 2 is subjected to the spin-echo sequence. During such a sequence, ion 1 is prepared either in state $|\downarrow\rangle$ or in state $|\uparrow\rangle$. The probability to find ion 2 in $|\uparrow\rangle$ state is measured for different phase φ of the last $\pi/2$-pulse on ion 2.

7.1 Measurement of the Spin-Spin Coupling of two Ions

The Hamiltonian of the spin-spin coupling, according to equation 2.63, is:

$$H = -\frac{\hbar}{2}\sum_{i<j}^{N} J_{ij}\sigma_z^{(i)}\sigma_z^{(j)} \quad . \tag{7.1}$$

The free evolution operator of two coupled spins (in a rotating frame) is

$$U_J(t) = e^{i\frac{J_{12}t}{2}\sigma_z^{(1)}\sigma_z^{(2)}} \quad . \tag{7.2}$$

In order to measure the spin-spin coupling constant between ion 1 and ion 2, J_{12}, a Ramsey-type experiment (see subsection 6.6.1) is carried out that reveals a phase difference in the temporal evolution of one spin conditioned on the state of the other spin. The measurement sequence on two ions is shown in Figure 7.1. After the cooling is performed (here only Doppler cooling is used), both ions are prepared in the ground state $|\downarrow\rangle$. Ion 2 is subjected to a spin-echo sequence, described already in subsection 6.6.2. Due to the π-pulse in the middle of the sequence, the spin of the ion returns to its original position after the evolution time τ, i.e. it

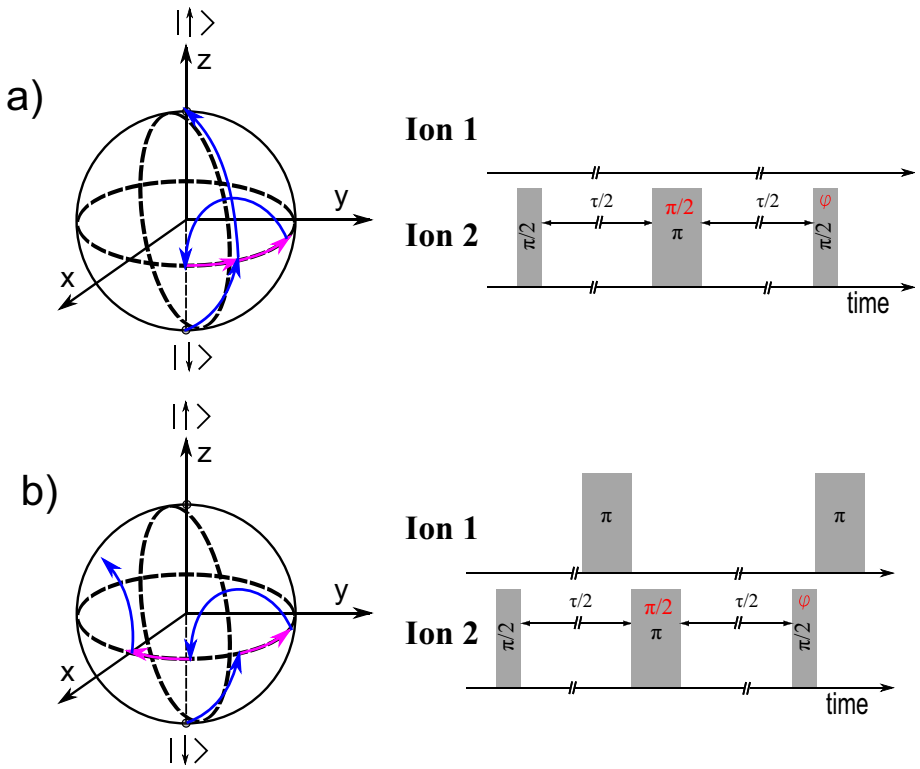

Figure 7.2: J-coupling constant measurements presented on the Bloch sphere. When the ion 1 is left in the $|\downarrow\rangle$ state, the spin-spin interaction is refocussed (magenta arrow on the Bloch sphere), as possible to see in picture a). In case ion 1 is prepared in $|\uparrow\rangle$ state, i.e. the spin has changed the sign, the evolution is in the opposite direction (magenta arrow on the Bloch sphere). Therefore, the coupling would not be removed, as it is possible to see in picture b).

is refocused. The phase of the second $\pi/2$-pulse is varying and we measure the probability of ion 2 to be in state $|\uparrow\rangle$. Microwave pulse durations T_{mw} are in the range of $4-10\,\mu$s while evolution time τ is about 2 ms. Only for the axial trapping potential of $2\pi \cdot 127.1$ kHz the evolution time is smaller and equal to 1.2 ms. In this case the harmonic oscillator energy levels separation is the smallest among the trapping potentials used in the experiment. Therefore, it is easier to excite the ion to the higher motional degrees of freedom. This heating of the ion can be provoked by the patch potentials or electric field noise from the trap electrodes.

During such a sequence on ion 2, ion 1 is either left in state $|\downarrow\rangle$ or it is excited to the state $|\uparrow\rangle$. In order to prepare ion 1 in the $|\uparrow\rangle$ state, a π-pulse is applied on it just before the middle π-pulse on ion 2. Since the measurements are performed on ion 2, ion 1 must be return to the $|\downarrow\rangle$ state. To do this a second π-pulse is applied

on ion 1 just after the second $\pi/2$-pulse on ion 2.

When ion 1 is left in the state $|\downarrow\rangle$, the effect of the spin-spin coupling is removed (see also [Vandersypen & Chuang, 2004]). In this case the spin precession of ion 2, after the π-pulse on ion 2 has been applied, continues in the same direction as before the π-pulse. This refocussing is demonstrated in Figure 7.2 a). The probability to find ion 2 in the excited state $|\uparrow\rangle$ when ion 1 is left in the ground state $|\downarrow\rangle$, in dependence on the phase φ of the last $\pi/2$-pulse on ion 2, is:

$$\begin{aligned} A_g &= R^{(2)}_{\frac{\pi}{2},\varphi} U_J\left(\frac{\tau}{2}\right) R^{(2)}_{\pi,\frac{\pi}{2}} U_J\left(\frac{\tau}{2}\right) R^{(2)}_{\frac{\pi}{2},0} \\ P_0(\varphi) &= |\langle 0_1,1_2|A_g|0_1,0_2\rangle|^2 = \cos^2\frac{\varphi}{2} \quad . \end{aligned} \tag{7.3}$$

When ion 1 is excited by a π-pulse simultaneously with ion 2, the ion 2 spin precession changes the direction after the π-pulse application and the coupling will not be refocussed anymore [Vandersypen & Chuang, 2004]. The corresponding demonstration on the Bloch sphere is shown in Figure 7.2 b). In that case the probability to find ion 2 in the excited state $|\uparrow\rangle$ when ion 1 is subjected to two consecutive π-pulses, in dependence on the phase φ of the last $\pi/2$-pulse on ion 2, is:

$$\begin{aligned} A_e &= R^{(1)}_{\pi,0} R^{(2)}_{\frac{\pi}{2},\varphi} U_J\left(\frac{\tau}{2}\right) R^{(2)}_{\pi,\frac{\pi}{2}} R^{(1)}_{\pi,0} U_J\left(\frac{\tau}{2}\right) R^{(2)}_{\frac{\pi}{2},0} \\ P_1(\varphi) &= |\langle 0_1,1_2|A_e|0_1,0_2\rangle|^2 = \cos^2\frac{\varphi - J\tau}{2} \quad . \end{aligned} \tag{7.4}$$

Here, $R^{(i)}_{\theta,\varphi}$, given in equation 2.61, indicates a single-spin rotation of spin i by an angle θ around an axis in the $x-y$ plane of the Bloch sphere that encloses an angle of φ with the x-axis. $U_J(t)$ is the free evolution operator described by equation 7.2. Equation 7.4 shows that during the excitation of ion 1 the signal receives an additional phase $J\tau$.

When the experiments were performed, it was possible to observe an additional phase shift, φ_0, in the measured Ramsey-fringes. We assume that this phase shift was produced by the stray electromagnetic fields present in our lab. Therefore, the phases in equations 7.3 and 7.4 are modified: in equation 7.3, $\frac{\varphi}{2}$ is replaced by $\varphi_g = \frac{\varphi}{2} + \varphi_0$, and in equation 7.4 one obtains $\varphi_e = \frac{\varphi}{2} - J\tau + \varphi_0$ instead of just $\frac{\varphi}{2} - J\tau$. For calculating the coupling constant this additional phase is not

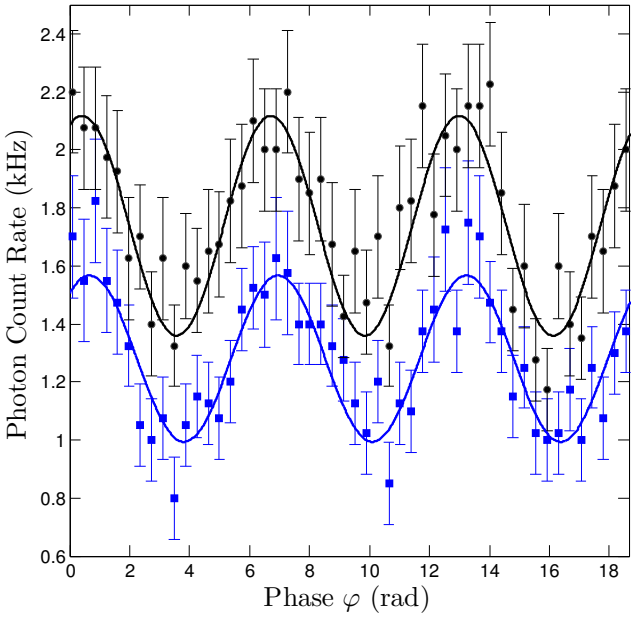

Figure 7.3: Spin-echo measurements of J-coupling between two ions. The Ramsey-fringes are measured with ion 2. Blue curve: the ion 1 is in the ground state $|\downarrow\rangle$ (coupling is turned effectively OFF). Black curve: the ion 1 is excited by the π-pulse after the time $\tau/2$ (coupling is turned effectively ON). Each data point represents 50 repetitions and it is 100 data points in each measurement. Here, the phase is varied in the range of $\varphi = 0 - 6\pi = 0 - 18.84\,\mathrm{rad}$, evolution time is $\tau = 2\,\mathrm{ms}$, $T_{delay} = 5\,\mathrm{ms}$, axial trapping frequency is $\nu_z = 2\pi \cdot 171.4(1)\,\mathrm{kHz}$ and the magnetic field gradient is $b = 18.98(2)\,T/m$.

important since we are interested in the relative phase shift. Hence, the coupling constant equals

$$J = (\varphi_g - \varphi_e)/\tau \quad . \tag{7.5}$$

7.2 Experimental Results

An example of the measured Ramsey fringes is shown in Figure 7.3 and in Figure 7.4. The data represents the probability to find ion 2 in the state where it scatters light and this probability is plotted versus the phase of the last $\pi/2$-pulse, applied

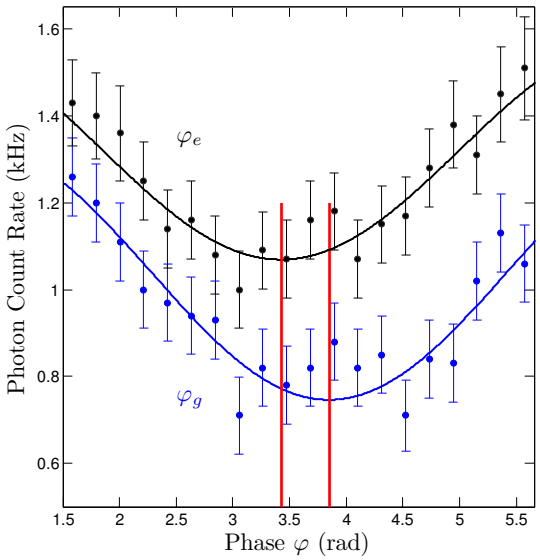

Figure 7.4: Spin-echo measurements of J-coupling constant between two ions. Blue square data points correspond to the case when ion 1 is left in the ground state $|\downarrow\rangle$ and the coupling is removed. Black circular data points correspond to the case when ion 1 is excited by a π-pulse after the evolution time $\tau/2$ such that the coupling is no longer refocused. Each data point represents 50 repetitions and, for clarity, an averaging over 5 data points has been additionally performed. Here, the phase is varied in a range of $\varphi = 1.5 - 5.7\,\mathrm{rad}$, evolution time is $\tau = 2\,\mathrm{ms}$, trigger delay time is $T_{delay} = 5\,\mathrm{ms}$, axial trapping frequency is $\nu_z = 2\pi \cdot 171.4(1)\,\mathrm{kHz}$ and the magnetic field gradient is $b = 18.98(2)\,T/m$. Vertical solid lines indicate the positions of the minima of the interference fringe. The corresponding coupling constant is $J_{12} = 2\pi \cdot (35 \pm 10)\,\mathrm{Hz}$.

on ion 2. In Figure 7.3 and in Figure 7.4 one set of data (blue squares) corresponds to the case when ion 1 is left in the ground state $|\downarrow\rangle$ and the effect of coupling is canceled. The other set of data (black circles) represents the case when the π-pulses act on ion 1, as it was described above. Both measurements were performed simultaneously: for each phase increment the data are collected when ion 1 is in the $|\downarrow\rangle$ state and immediately after that when ion 1 is in the $|\uparrow\rangle$ state. The solid line represents a fit yielding the phases φ_g and φ_e. Each data point represents 50 repetitions. In Figure 7.4, for clarity, an averaging over 5 data points has been additionally done. In Figure 7.3 the phase is varied in a range of $\varphi = 0 - 6\pi = 0 - 18.84\,\mathrm{rad}$. In the experiment we usually did not vary the phase for a so long period. In Figure 7.4 the phase is varied in a range of only 1.5−5.7 rad. The first period of Ramsey oscillation is chosen since here one expects less accumulation of

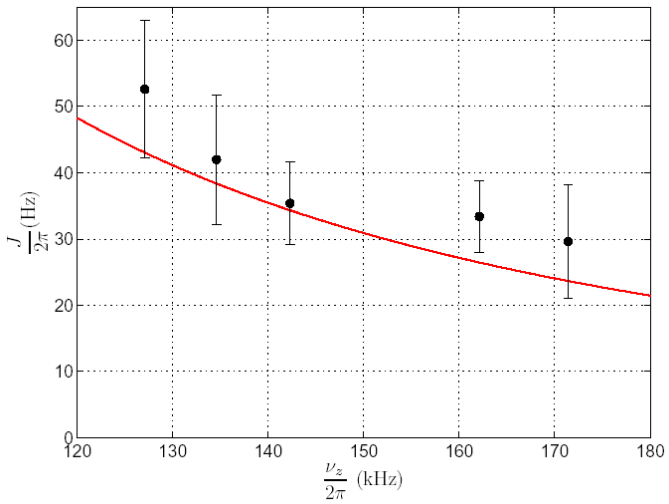

Figure 7.5: J-coupling for varying axial trap potential. The circles represent the measurement of the spin-spin interaction J_{12} between two ions for different axial trap potentials characterized by the angular trap frequency ν_z. The solid line represents the calculated values for the coupling constants at a magnetic field gradient of $b = 19\,T/m$.

the incremental phase error of the VFG itself. Besides, the simulations has shown that the most sensitive region for the phase measurements is the $4/3\pi$ region around the signal minimum [Gloger, 2011].

In Figure 7.4 it is possible clearly to see that the black curve minimum is shifted to the left compared to the blue curve minimum. The solid vertical lines demonstrate the positions of these minima. For this example the coupling constant $J_{12} = 2\pi \cdot (35 \pm 10)\,\text{Hz}$ is calculated, according to equation 7.5. Here, the evolution time is $\tau = 2\,\text{ms}$, the 50 Hz trigger delay is $T_{delay} = 5\,\text{ms}$ and the axial trapping frequency is $\nu_z = 2\pi \cdot 171.4(1)\,\text{kHz}$. One can also notice that the black curve is shifted up compared to the blue curve and this is due to the imperfect π-pulse on ion 1.

$\nu_z/(2\pi)$	127.1(1) kHz	134.6(1) kHz	142.3(1) kHz	162.1(1) kHz	171.4(1) kHz
# of measurements	10	21	21	17	14
$J_{12}^{exp}/(2\pi)$	53(10) Hz	42(10) Hz	35(6) Hz	33(5) Hz	30(9) Hz
$J_{12}^{th}/(2\pi)$	43.1 Hz	38.5 Hz	34.4 Hz	26.5 Hz	23.7 Hz

Table 7.1: Measured and theoretical J-coupling constants for different axial trapping potentials.

The coupling constants arising from the magnetic field gradient induced coupling (MAGIC) can be adjusted through variation of the trapping potential that determines the frequencies ν_n of the vibrational modes of the Coulomb ion crystal (see Appendix M). The coupling constant between two ions is proportional to the reverse of the squared ν_z (see equation 2.66). Therefore, to prove the variability of the coupling constants, they were measured at different axial confinements ν_z while keeping the magnetic field gradient b constant. The results are presented in Table 7.1 and in Figure 7.5, which shows the dependence of J-coupling constant between two ions on the strength of the axial trapping potential defined by the COM axial trap frequency ν_z.

Each data point in Figure 7.5 corresponds to the weighted average over several measurements (see Table 7.1) and the solid line represents the calculated coupling constants for a magnetic gradient of $b = 19.0\,\mathrm{T/m}$, where $J_{12} \propto \frac{b^2}{\nu_z^2}$ (see equation 2.66). All the coupling constant measurements were performed with Doppler cooling only and the minimum mean phonon number is about $\overline{n} \approx 150$ (see subsection 6.2.1).

As it is possible to see in Figure 7.5 and in Table 7.1, the measured and the theoretical values are in good agreement with each other and the measured results lie well within 1σ. As it is possible to see from Table 7.1, averaging over an increasing number, tending ideally to infinity, of experiments leads to a measured value closer to the predicted one. The biggest deviation of the coupling value from the theoretical one is for the trapping potentials at $2\pi \cdot 127.1(1)\,\mathrm{kHz}$, where only 10 measurements were used: it is quite difficult to perform the measurements at this or lower frequency since less energy is needed to excite the close upper motional mode. Since the measured data were taken using the spin-echo sequence with only one π-pulse, coherence time does not exceed 2 ms. This leads to the smaller possible phase shifts and, respectively, to a relatively large statistical error. These errors are reduced using more complicated sequences of pulses that increase the evolution time.

Later in the experiment, the coupling constant between the two trapped ions, J_{12}, at the axial trap frequency of $\nu_z = 2\pi \cdot 123.5(1)\,\mathrm{kHz}$ and in the presence of a magnetic field gradient of $b = 19\,\mathrm{T/m}$ was measured using the CDD_3 sequence with 84 π-pulses (see subsection 6.6.4). The principle of the measurement is the same as it was described above in this chapter. The only difference is that the spin-echo sequence with a single π-pulse was substituted with the multiple π-pulses sequence CDD_3. The concatenated pulse sequence allowed to use longer evolution time with a maximum $\tau = 8\,\mathrm{ms}$. As experiments demonstrated, the measured coupling gets smaller when the number of π-pulses increases. This is the reason why we will

J_{ij}	1	2	3
1	-	$2\pi \cdot 32(4)$ Hz	$2\pi \cdot 18(2)$ Hz
2	$2\pi \cdot 32(4)$ Hz	-	$2\pi \cdot 33(3)$ Hz
3	$2\pi \cdot 18(2)$ Hz	$2\pi \cdot 33(3)$ Hz	-

Table 7.2: Measured coupling constants for three ions. For the non-uniform magnetic gradient present in our setup and the axial tarp frequency of $\nu_z = 123.5\,\mathrm{kHz}$ *the calculated values of coupling are* $J_{12}^{th} = 2\pi \cdot 32.9\,\mathrm{Hz}$, $J_{23}^{th} = 2\pi \cdot 37\,\mathrm{Hz}$, $J_{13}^{th} = 2\pi \cdot 23.9\,\mathrm{Hz}$.

further call it the *effective* coupling.

An effective coupling constant between two trapped ions equals, therefore, $J_{12} = 2\pi \cdot 38(5)\,\mathrm{Hz}$. The theoretical value for the used axial trapping potential and magnetic field gradient of $b = 19\,\mathrm{T/m}$ is $J_{12}^{th} = 2\pi \cdot 45.5\,\mathrm{Hz}$ (see Appendix M).

The coupling constants between three trapped ions has been measured as well using the CDD_3 sequence with 84 π-pulses. The corresponding J_{ij} matrix is given in Table 7.2. For the non-uniform magnetic gradient present in our setup ($b_1 = 16.8\,\mathrm{T/m}$, $b_2 = 18.7\,\mathrm{T/m}$, $b_3 = 18.9\,\mathrm{T/m}$ where b_j is the gradient on the position of the ions) and the axial trap frequency of $\nu_z = 123.5\,\mathrm{kHz}$ the calculated values are $J_{12}^{th} = 2\pi \cdot 32.9\,\mathrm{Hz}$, $J_{23}^{th} = 2\pi \cdot 37\,\mathrm{Hz}$, $J_{13}^{th} = 2\pi \cdot 23.9\,\mathrm{Hz}$ (see Appendix M). The measured and theoretical values are in good agreement and the measured results lie within 1σ for J_{12} and J_{23} and within 3σ for J_{13}. The coupling constant J_{13} is more difficult to measure since the phase shift is relatively smaller compared to the coupling constants J_{12} and J_{23}. For each coupling constant the measurements of the phase shift, that is proportional to coupling constant (see equation 7.5), were performed for different evolution times varying in the range of $2 - 12\,\mathrm{ms}$. The averaged value of the phase shift were plotted versus the evolution time τ: about 6 measurements of phase shift were performed for 5 different evolution times τ resulting in the total of 30 measurements for each coupling constant. The coupling constants were found from the fit $\Delta\varphi = \varphi_0 + 4\pi J_{ij}\tau$. Larger number of measurements and larger phase shifts possible due to the more robust to the external noise CCD_3 sequence contribute to the decreasing of the statistical errors compared to the measured with the single π-pulse spin-echo sequence values presented in Table 7.1.

8

Two Ion CNOT Gate and Entanglement

A chain of trapped ions, forming a spin pseudo-molecule in an inhomogeneous magnetic field, is particularly suitable for carrying out multi-qubit gates because of the adjustable spin-spin coupling constants [Fisher *et al.*, 2010]. Here, the effective coupling between two spins was employed to implement a CNOT gate. Ion 2 represents the Target qubit and ion 1 is the Control qubit of the CNOT gate.

In order to execute a CNOT gate, the evolution time τ is chosen to achieve a phase shift of $\mid \pi/2 \mid = J\tau$ with respect to the reference (see equation 2.64). This phase shift depends on the initial state of the Control ion i.e. if the initial state of the Control qubit is up (down), the phase difference will be positive (negative). Therefore π is the maximum total phase difference.

One of the challenges of our setup was to increase the coherence time over the time necessary to perform the CNOT gate τ. In the experiments that used the spin-echo sequence the maximum achieved evolution time τ was about 2 ms. In order to receive a phase shift of $\mid \pi/2 \mid$ and considering the biggest measured coupling constant of 52.6 Hz at the axial trap frequency of $2\pi \cdot 127.1(1)$ kHz, τ must be of about 10 ms. We, on the contrary, had only something like 1.2 ms at the mentioned trap frequency.

Initially, in order to reduce the electric noise on the end-cap electrodes, we ex-

changed the end-cap power supply with a battery. Second, we reduced the trap frequency to $2\pi \cdot 123.5(1)\,\mathrm{kHz}$ in order to increase further the coupling constant J and thus to achieve a faster gate operation. Third, the coherence time was improved by a new variant of the CPMG multiple π-pulse sequence (see subsection 6.6.4). Instead of using the original proposal of identical π-pulses, their relative phases were varied in order to obtain a self-correcting sequence that is only sparsely susceptible to experimental imperfections. This sequence is applied to both ions participating in the CNOT gate. If these π-pulses were applied only to the Target ion, they would not only refocus unwanted dephasing, but also the interaction with the Control ion. Therefore, in order to preserve the J-type interaction between the ions and at the same time to compensate for errors due to the ambient fields the Control ion needs to be flipped each time the Target ion is flipped meaning that the same sequence must be applied on both ions.

This chapter reports, for the first time using a MAGIC-scheme, on the experimental realization of the CNOT gate and entanglement between two ions. The CNOT gate was executed exploiting the neighboring ions and the ions at the ends of the three-ion chain, demonstrating that entanglement between distinct ions is also possible. Finally, possible error sources, that reduce the fidelity of the measurements, are discussed. The results of this section are also published in reference [Khromova *et al.*, 2012].

8.1 Two Ion CNOT Gate

The CNOT measurement procedure starts by preparing ion 1 and ion 2 in the initial states according to the truth table given in equation 2.9. If ion 1 (ion 2) are needed in the excited state $|\uparrow_T\rangle$ ($|\uparrow_C\rangle$), a microwave π-pulse with $\varphi = 0$ is applied, corresponding to the rotation operator $R^{(T)}_{\pi,0}$ ($R^{(C)}_{\pi,0}$) described by equation 2.61. After this a spin-echo sequence with multiple π-pulses is applied. The first experiments to implement the CNOT gate were performed using the CPMG_{XY} multiple π-pulse sequence (see subsection 6.6.4). The complete procedure to obtain the CNOT logic operation can be summarized by the following expression:

$$R^{(T)}_{\frac{\pi}{2},\varphi}\left(U_J\left(\frac{\tau}{2N}\right)R^{(T)}_{\pi,\frac{\pi}{2}}R^{(C)}_{\pi,\frac{\pi}{2}}U_J\left(\frac{\tau}{N}\right)R^{(T)}_{\pi,0}R^{(C)}_{\pi,0}U_J\left(\frac{\tau}{2N}\right)\right)^{\frac{N}{2}}R^{(T)}_{\frac{\pi}{2},0} \quad , \tag{8.1}$$

where N is the number of π-pulses and τ is the evolution time. This expression is valid for an even number of π-pulses, as it was used in the current experiment.

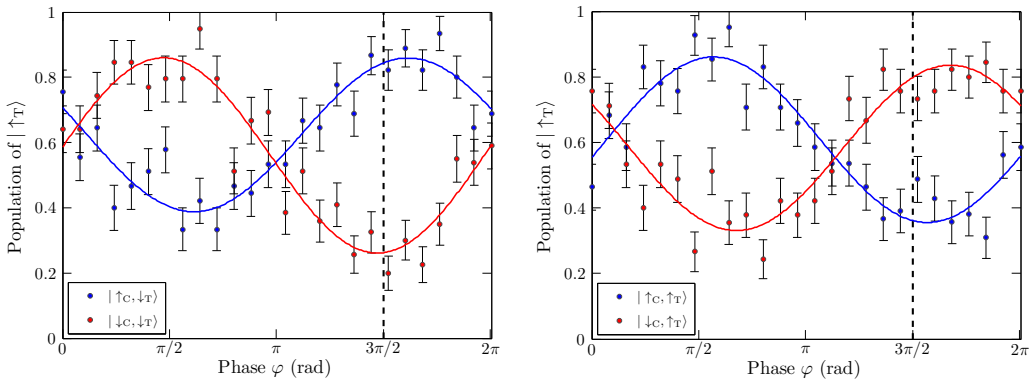

(a) (b)

Figure 8.1: Conditional quantum dynamics and a CNOT gate between the two neighboring ions. The coupling between ion 1 (Control) and ion 2 (Target) produces a phase shift on the target population as a function of the control qubit's state. A free evolution time of $\tau = 5\,\mathrm{ms}$ yields a phase shift of approximately π (3.1(2) radians) between the pairwise displayed curves. The target population varies sinusoidally as a function of the phase φ of the second Ramsey $\pi/2$-pulse applied to the target, and for $\varphi = 3\pi/2$, a CNOT gate results. Each data point represents 50 repetitions, the error bars correspond to the mean standard deviations and the solid lines are fits to the data. The $CPMG_{XY}$ spin-echo sequence with 24 π-pulses has been used for measurements.

The operation follows from right to left. The measurements are performed only on the Target qubit ion 2 and the Control qubit ion 1 must, therefore, be in the ground state $|\downarrow_C\rangle$ when the readout is performed. In case the Control qubit ion 1 was initially prepared in the $|\uparrow_C\rangle$ state, an additional π-pulse is applied to it after the gate operation sequence is finished and the Control qubit is flipped back to the $|\downarrow_C\rangle$ state. Thus, the detected fluorescence could only come from the Target qubit, where the phase shift acquired during the precession of Target qubit ion 2 is transferred into a population by a last $\pi/2$-pulse with varying phase φ, $R^{(T)}_{\frac{\pi}{2},\varphi}$. In case the Control qubit is prepared in the superposition state, as it will be used to produce an entangled state (see section 8.2), no additional pulse is applied to the Control qubit at the end of the CNOT sequence, when the readout on the Target qubit is performed. The time between the two $\pi/2$-Ramsey pulses equals the total evolution time τ.

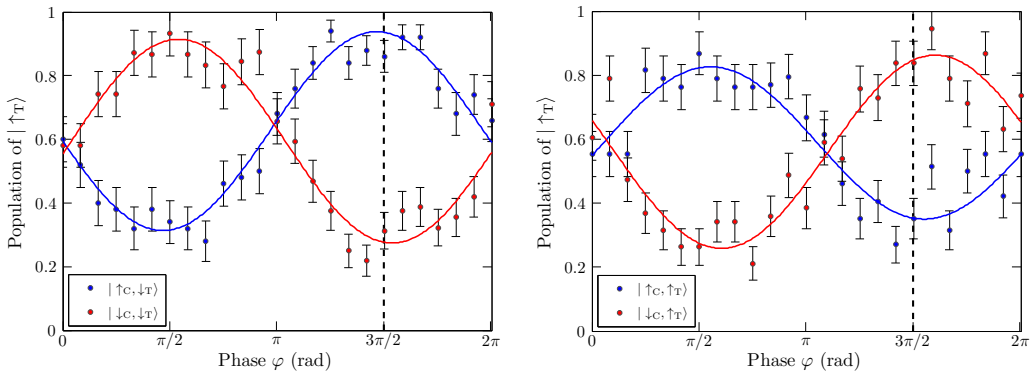

(a) (b)

Figure 8.2: Conditional quantum dynamics and a CNOT gate between the two neighboring ions. The coupling between ion 1 (Control) and ion 2 (Target) produces a phase shift on the target population as a function of the control qubit's state. A free evolution time of $\tau = 8\,\text{ms}$ yields a phase shift of approximately π (3.1(2) radians) between the pairwise displayed curves. The target population varies sinusoidally as a function of the phase φ of the second Ramsey $\pi/2$-pulse applied to the target, and for $\varphi = 3\pi/2$, a CNOT gate results. Each data point represents 50 repetitions, the error bars correspond to the mean standard deviations and the solid lines are fits to the data. The CDD_3 spin-echo sequence with 84 π-pulses has been used for measurements.

The population $P(\varphi)$ of $|\uparrow_T\rangle$ is measured for four different cases depending on the initial states of the Control and Target qubits. Figure 8.1 (a) and Figure 8.1 (b) demonstrates the corresponding resulting state population of the Target qubit as a function of φ of the last $\pi/2$-pulse, measured using the CPMG_{XY} multiple π-pulse spin-echo sequence with 24 π-pulses. The same measurements were performed with the CDD_3 sequence with 84 π-pulses that is more robust to the ambient magnetic field fluctuations. The results are presented in Figure 8.2 (a) and Figure 8.2 (b).

The CNOT operation is achieved when the phase $\varphi = 3\pi/2$ of the last $\pi/2$ pulse is selected. The four measured data sets are in agreement with the truth table of the CNOT gate, which induces a flip of the Target qubit if the Control qubit is in the initial state $|\uparrow\rangle$ or leaves it unchanged if the Control qubit is in the initial state $|\downarrow\rangle$. The fact that the population oscillates around 0.6 is connected to spurious detection of the Control qubit caused by the pulse errors. The evolution time to

achieve a phase shift $\Delta\varphi_{12} = \pi$ was chosen equal to $\tau = 5\,\text{ms}$ for the data in Figure 8.1 and $\tau = 8\,\text{ms}$ for the data in Figure 8.2.

8.2 Two-Ion Entangled State

In order to prove that our CNOT gate can indeed produce an entangled state according to equations 2.14 - 2.17, the Control qubit ion 1 is prepared in the superposition state

$$\frac{1}{\sqrt{2}}(|\downarrow\rangle_C - i\,|\uparrow\rangle_C) \tag{8.2}$$

by a microwave $\pi/2$-pulse with $\varphi = 0$. The Target qubit ion 2 is prepared in state $|\downarrow\rangle_T$ or $|\uparrow\rangle_T$. The excited state is prepared by the π-pulse with $\varphi = 0$ applied on the ground state $|\downarrow\rangle_T$. The resulting input state, in case the Target qubit ion 2 is prepared in the ground state $|\downarrow\rangle_T$,

$$\frac{1}{\sqrt{2}}(|\downarrow\rangle_C\,|\downarrow\rangle_T - i\,|\uparrow\rangle_C\,|\downarrow\rangle_T) \tag{8.3}$$

is subjected to the CNOT gate pulse sequence described by expression 8.1. The outcome state is

$$|\psi_B\rangle = \frac{1}{\sqrt{2}}(|\downarrow\rangle_C\,|\downarrow\rangle_T - i\,|\uparrow\rangle_C\,|\uparrow\rangle_T) \quad . \tag{8.4}$$

The generation of these nonclassical states was verified by means of a parity measurement. The parity indicates the amount of correlations between the two ions and is given by [Sackett *et al.*, 2000]:

$$\Pi = P_{\uparrow\uparrow} + P_{\downarrow\downarrow} - (P_{\uparrow\downarrow} + P_{\downarrow\uparrow}), \tag{8.5}$$

where P_{ij} with $i,j = \downarrow, \uparrow$ denotes the probability to find the Control and Target qubits in state $|i_C, j_T\rangle$. The population probabilities can be extracted from the photon-number distribution represented by a histogram of three Poissonians. There are two thresholds s_1 and s_2. The sum of the photon counts below the

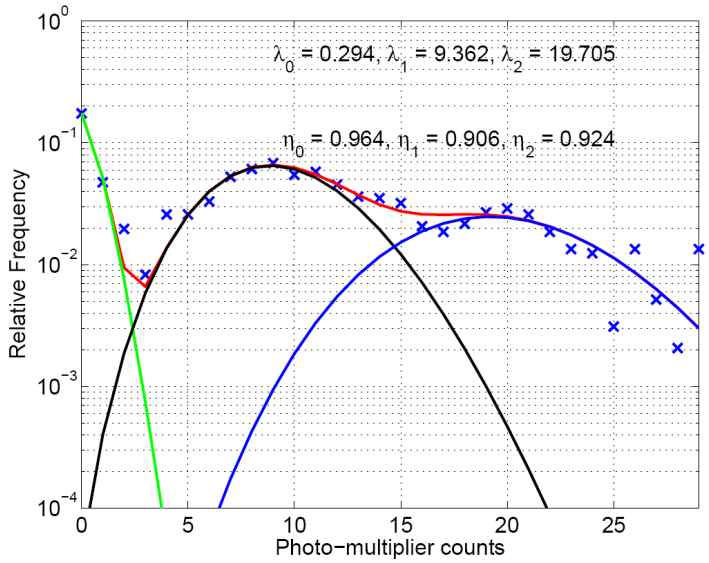

Figure 8.3: Histogram of three Poissonian distributions used to distinguish between the three populations of the measured parity of two ions. Here, λ's are the center of the Poisson distributions, η's are the detection efficiency: $\eta_0 = \sum_{n=0}^{n\leq s_1} p(n,\lambda_0)$, $\eta_1 = \sum_{n>s_1}^{n<s_2} p(n,\lambda_1)$, $\eta_2 = \sum_{n\geq s_2}^{n=\infty} p(n,\lambda_2)$, where s_1 and s_2 are the corresponding thresholds. The readout time for this histogram is 1.2 ms. The green, the black and the blue solid lines are three Poissonian fits for both ions in the $|\downarrow\rangle$ state, for both ions in the superposition $|\uparrow+\downarrow\rangle$ state and for both ions in the $|\uparrow\rangle$ state, respectively. The red solid line is the fit for a sum of these three Poissonian distributions.

threshold $\leq s_1$ gives the probability to find both ions in the $|\downarrow\downarrow\rangle$ states $P_{\downarrow\downarrow}$, the sum of the photon counts above the upper threshold $\geq s_2$ gives the probability to find both ions in the $|\uparrow\uparrow\rangle$ states $P_{\uparrow\uparrow}$, the sum of the photon-counts between both thresholds, $> s_1$ and $< s_2$ results in the probability $P_{\uparrow\downarrow} + P_{\downarrow\uparrow}$. An example of such a histogram is given in Figure 8.3. The correlations P_{ij} were measured along different bases by applying additional $\pi/2$-pulses (analysis pulse) of phase φ to both ions after the CNOT operation and in the z-basis, that is natural basis of our setup. An example of the population distributions measured after the additional $\pi/2$ analysis pulse is given in Figure 8.4 and the populations measured in the z-basis are shown in Figure 8.5. The resulting from this measurement values of the probabilities and density matrix element are given in Table 8.1.

Figure 8.6 shows the resulting parity signal $\Pi(\varphi)$ plotted versus the phase of the analyzing $\pi/2$ pulses. It oscillates with twice the phase variation $V \cdot \cos(2\varphi)$, as

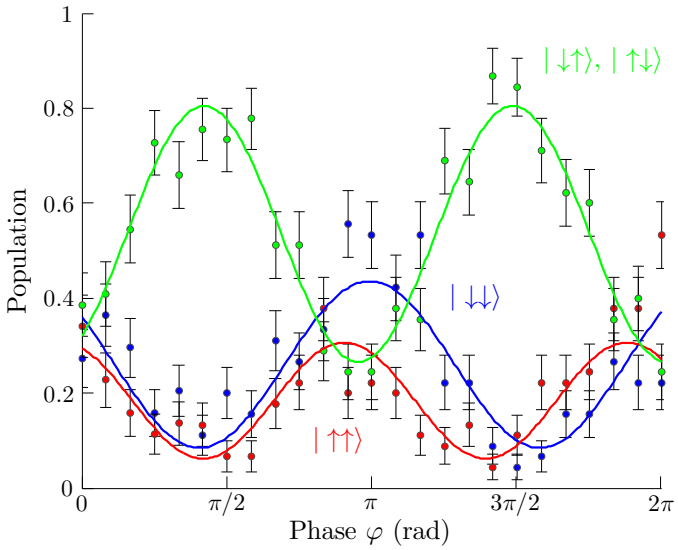

Figure 8.4: Populations of the bipartite entangled state: $P_{\downarrow\downarrow}$ (blue disks), $P_{\uparrow\uparrow}$ (red disks), $P_{\uparrow\downarrow} + P_{\downarrow\uparrow}$ (green disks), measured in different bases by applying the microwave $\pi/2$-pulses with varying phase φ to both ions.

one would expect for a bipartite entangled state. The parity of N entangled ions oscillates as $\cos(N\varphi)$. A non-entangled state yields just a $V \cdot \cos(\varphi)$ variation. The amplitude of the parity oscillations V is twice the magnitude of the density matrix element $\rho_{\uparrow\uparrow,\downarrow\downarrow}$ that characterizes the coherences, or off-diagonal elements, between the $|\uparrow\uparrow\rangle$ and $|\downarrow\downarrow\rangle$ components in the produced state. At the top of Figure 8.6 there is a resonance fluorescence image of two $^{171}Yb^{+}$ ions taken with an intensified CCD camera. Ions are separated by 13.9 μm at the axial trap frequency of $2\pi \cdot 123.5$ kHz.

The entangled state as in equation 8.4 is an ideal case. Due to the pulse imperfec-

$P_{\downarrow\downarrow}$	$P_{\downarrow\uparrow,\uparrow\downarrow}$	$P_{\uparrow\uparrow}$	$\rho_{\uparrow\downarrow}$
0.46 ± 0.01	0.27 ± 0.01	0.27 ± 0.01	0.27 ± 0.03

Table 8.1: The resulting values of the probabilities and density matrix element for the two ion parity measurements. N is the number of ions; P_{ij} denotes the probability that i *and* j *ions are in $|\downarrow\downarrow\rangle$, $|\uparrow\uparrow\rangle$ or $|\downarrow\uparrow, \uparrow\downarrow\rangle$; $\rho_{\uparrow\downarrow}$ denotes the amplitude of the density matrix element $\rho_{\uparrow\uparrow,\downarrow\downarrow}$.*

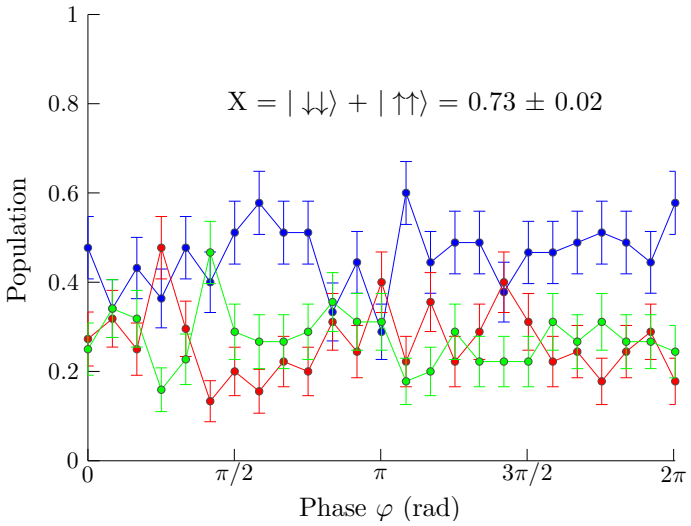

Figure 8.5: Populations of the bipartite entangled state: $P_{\downarrow\downarrow}$ (blue disks), $P_{\uparrow\uparrow}$ (red disks), $P_{\uparrow\downarrow} + P_{\downarrow\uparrow}$ (green disks), measured in z-basis.

tions and decoherence during the preparation of the entangled state, an entangled mixed state, described by the density matrix ρ, is produced, rather than a maximally entangled state $|\psi_B\rangle$. Hence, the fidelity, as a measure of an entangled state preparation efficiency, can be written as [Sackett *et al.*, 2000]:

$$F = \langle\psi_B|\rho|\psi_B\rangle = \frac{1}{2}(P_{\uparrow\uparrow} + P_{\downarrow\downarrow}) + |\rho_{\uparrow\uparrow,\downarrow\downarrow}| \quad . \tag{8.6}$$

Equation 8.6 can be also rewritten through the parity as

$$F = \frac{\Pi + 1}{4} + \frac{C}{4} = \frac{X}{2} + \frac{C}{4} \quad , \tag{8.7}$$

where $X = P_{\uparrow\uparrow} + P_{\downarrow\downarrow}$ and $C = 2 \cdot V$ is the contrast (maximum minus minimum value) of the parity oscillations.

For the measurements presented in Figure 8.6, the contrast is $C = 1.07 \pm 0.12$ and $X = 0.73 \pm 0.02$. The evaluated fidelity of a created Bell state is, therefore, $F = 0.63 \pm 0.03$ that exceeds the Bell limit of 0.5 and thus proves the existence of entanglement [Sackett *et al.*, 2000].

The parity measurements were performed using the CPMG_{XY} sequence with 24

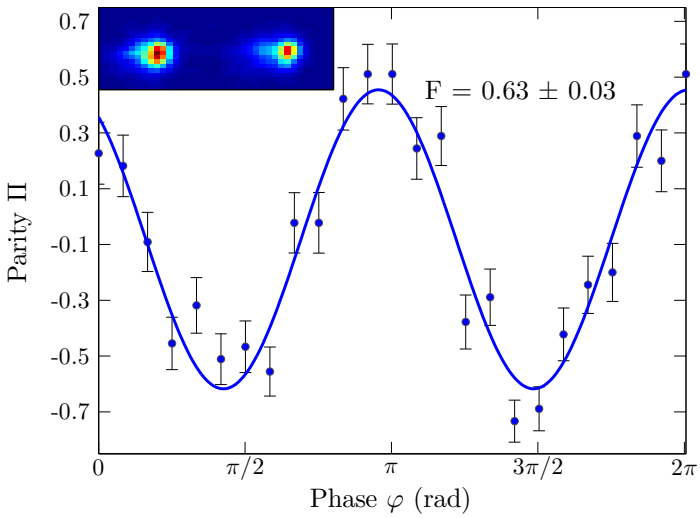

Figure 8.6: Parity Π *of a Bell state generated with a CNOT operation applied on the superposition state* $\frac{1}{\sqrt{2}}(|\downarrow_C\rangle + |\uparrow_C\rangle)\,|\downarrow_T\rangle$. *The parity is measured by first applying a* $\pi/2$ *pulse of phase* ϕ *on each of the two ions and then detecting if the two ions are in the same or in different states by measuring the fluorescence. The maxima of the parity indicates that the ions are most probably measured in correlated states* $|\uparrow_C, \uparrow_T\rangle$ *or* $|\downarrow_C, \downarrow_T\rangle$ *and the minima in anti-correlated states* $|\uparrow_C, \downarrow_T\rangle$ *or* $|\downarrow_C, \uparrow_T\rangle$. *Each data point represents 50 repetitions and error bars indicate one standard deviation. At the top of the picture there is a resonance fluorescence image of two* $^{171}Yb^+$ *ions taken with an intensified CCD camera. Ions are separated by* $13.9\,\mu$m *at the axial trap frequency of* $2\pi \cdot 123.5\,$kHz.

π-pulses and sideband cooling was used additionally to Doppler cooling to improve the parity contrast.

8.3 Entanglement in a Linear Ion Chain

8.3.1 Non-Neighboring Ions

One of the important requirements for the quantum computer is its scalability. For a complex calculations a quantum computer needs a large amount of entangled ions. As a simple example it will be demonstrated that using the MAGIC-scheme it is possible to entangled two ions that do not lie close to each other. The entanglement procedure shown here can be applied also to a longer linear chain.

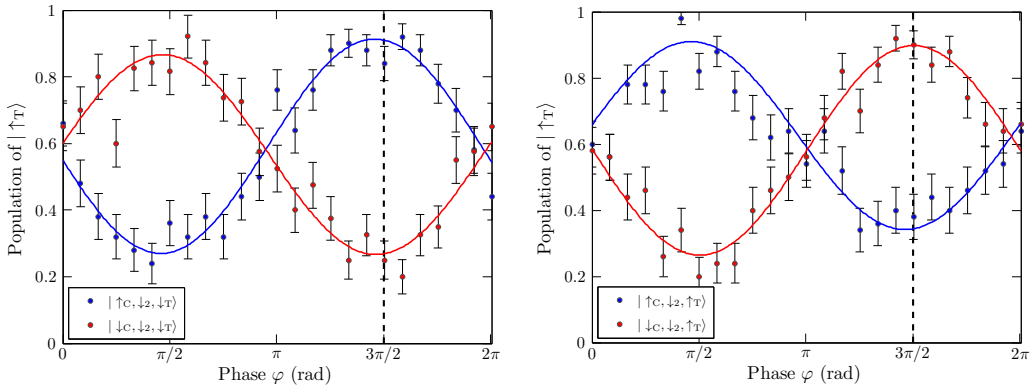

(a) (b)

Figure 8.7: Conditional quantum dynamics and CNOT gate between non-neighbouring ions. The coupling between ions number 1 (Control) and 3 (Target) produces a phase shift on the target population as a function of the control qubit's state. A free evolution time of $\tau = 11$ ms yields a phase shift of approximately π (3.1(2) radians) between the pairwise displayed curves. For $\varphi = 3\pi/2$, a CNOT gate results. Each data point represents 50 repetitions, the error bars correspond to the mean standard deviations and the solid lines are fits to the data.

The CNOT gate was performed between ion 1 (Control qubit) and ion 3 (Target qubit) in the same way described in section 8.1. First, all three ions are initialized in state $|\downarrow_C\downarrow_2\downarrow_T\rangle$. The first microwave $\pi/2$-pulse is applied on the Target qubit ion 3 after which the CDD_3 sequence is performed on both, the Control qubit ion 1 and the Target qubit ion 3. After the second microwave $\pi/2$-pulse with varying phase φ is applied on the Target qubit ion 3, population $P(\varphi)$ of $|\uparrow_T\rangle$ state is measured with the Control qubit ion 1 initially prepared in state $|\downarrow_C\rangle$ or $|\uparrow_C\rangle$. The last state is set by a π-pulse. Another pair of data is measured with the Target qubit ion 3 prepared in $|\uparrow_T\rangle$. The results of these measurements are demonstrated in Figure 8.7. The middle ion 2 is prepared in state $|\downarrow\rangle_2$ and left in this state during the whole measurement procedure. Thus, it does not interact with the other ions.

The evolution time of $\tau = 11$ ms is chosen to achieve a relative phase shift $\triangle\varphi_{13} = \pi$, where $\varphi_{13} = J_{13} \cdot \tau$ and J_{13} is the coupling constant between ion 1 and ion 3 in a chain of three ions. The CNOT operation is achieved when selecting $\varphi = 3\pi/2$ rad. The four measured sets of data are in agreement with the truth table of the CNOT gate (see equation 2.9).

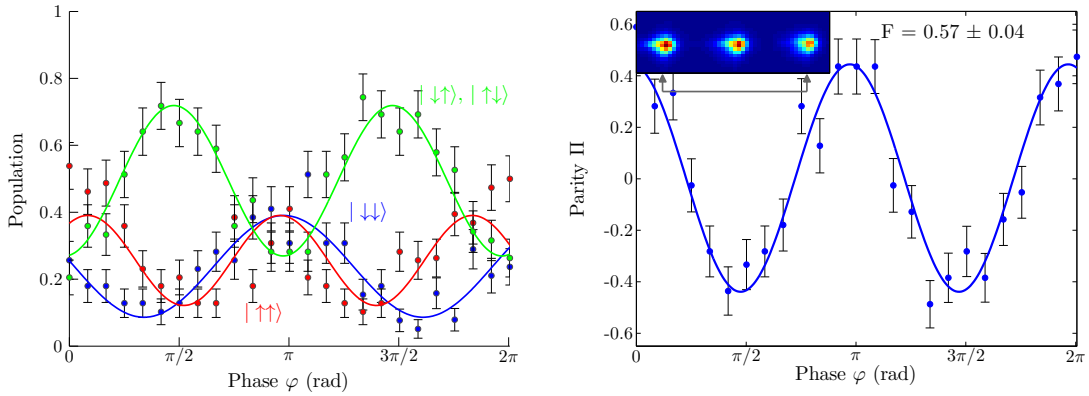

Figure 8.8: (a)Populations of the entangled state: $P_{\downarrow_C\downarrow_2\downarrow_T}$ (blue disks), $P_{\uparrow_C\downarrow_2\uparrow_T}$ (red disks), $P_{\uparrow_C\downarrow_2\downarrow_T} + P_{\downarrow_C\downarrow_2\uparrow_T}$ (green disks). (b) Parity signal $\Pi(\varphi)$ showing the quantum nature of the observed correlations of ion 1 and 3. Each data point represents 50 repetitions and the error bars indicate the standard deviation. At the top of this picture there is a resonance fluorescence image of three $^{171}Yb^+$ ions taken with an intensified CCD camera. Neighboring ions are separated by $11.9\,\mu$m *at the axial trap frequency of* $2\pi \cdot 123.5\,$kHz.

In order to entangle ion 1 and ion 3, the Control qubit ion 1 is prepared in the superposition state

$$\frac{1}{\sqrt{2}}(|\downarrow_C\downarrow_2\downarrow_T\rangle - i\,|\uparrow_C\downarrow_2\downarrow_T\rangle) \quad . \tag{8.8}$$

After the CNOT gate is applied the resulting bipartite entangled Bell state

$$|\psi_B\rangle = \frac{1}{\sqrt{2}}(|\downarrow_C\downarrow_2\downarrow_T\rangle + \mathrm{e}^{i\alpha}\,|\uparrow_C\downarrow_2\uparrow_T\rangle) \tag{8.9}$$

is obtained. The population distributions and the corresponding parity are presented in Figure 8.8. At the top of Figure 8.8 (b) there is a resonance fluorescence image of three $^{171}Yb^+$ ions taken with an intensified CCD camera. Neighboring ions are separated by $11.9\,\mu$m at the axial trap frequency of $2\pi \cdot 123.5\,$kHz. The population probabilities can be extracted from the photon-number distribution represented by an histogram of three Poissonians, as described in section 8.2.

$P_{\downarrow\downarrow}$	$P_{\downarrow\uparrow,\uparrow\downarrow}$	$P_{\uparrow\uparrow}$	$\rho_{\uparrow\downarrow}$
0.34 ± 0.01	0.32 ± 0.01	0.34 ± 0.01	0.22 ± 0.03

Table 8.2: The resulting values of the probabilities and density matrix element for the parity measurements of the two entangled **non-neighboring** *ions in a three-ions chain. N is the number of ions; P_{ij} denotes the probability that* i *and* j *ions are in $|\downarrow\downarrow\rangle$, $|\uparrow\uparrow\rangle$ or $|\downarrow\uparrow,\uparrow\downarrow\rangle$; $\rho_{\uparrow\downarrow}$ denotes the amplitude of the density matrix element $\rho_{\uparrow\uparrow,\downarrow\downarrow}$.*

$P_{\downarrow\downarrow}$	$P_{\downarrow\uparrow,\uparrow\downarrow}$	$P_{\uparrow\uparrow}$	$\rho_{\uparrow\downarrow}$
0.39 ± 0.01	0.24 ± 0.01	0.38 ± 0.01	0.26 ± 0.03

Table 8.3: The resulting values of the probabilities and density matrix element for the parity measurements of the two entangled **neighboring** *ions in a three-ions chain. N is the number of ions; P_{ij} denotes the probability that* i *and* j *ions are in $|\downarrow\downarrow\rangle$, $|\uparrow\uparrow\rangle$ or $|\downarrow\uparrow,\uparrow\downarrow\rangle$; $\rho_{\uparrow\downarrow}$ denotes the amplitude of the density matrix element $\rho_{\uparrow\uparrow,\downarrow\downarrow}$.*

The resulting values of the probabilities and the density matrix element for these measurements are given in Table 8.2.

For the measurements presented in Figure 8.8, the contrast is $C = 0.88 \pm 0.12$ and $X = 0.68 \pm 0.02$. The evaluated fidelity of a created Bell state is, therefore, $F = 0.56 \pm 0.03$, that exceeds the Bell limit of 0.5, as it was already mentioned in section 8.2.

8.3.2 Neighboring Ions

The CNOT gate between the ion 1 (Control qubit) and ion 2 (Target qubit) is performed in the same way described in subsection 8.3.1. Ion 3 was prepared in the ground state $|\downarrow\rangle_3$ and stayed in this state during the whole measurement. The Control qubit ion 1 is prepared in the superposition state

$$\frac{1}{\sqrt{2}}(|\downarrow_C\downarrow_T\downarrow_3\rangle - i\,|\uparrow_C\downarrow_T\downarrow_3\rangle) \quad . \tag{8.10}$$

The bipartite entangled Bell state

$$|\psi_B\rangle = \frac{1}{\sqrt{2}}(|\downarrow_C\downarrow_T\downarrow_3\rangle + \mathrm{e}^{i\alpha}\,|\uparrow_C\uparrow_T\downarrow_3\rangle) \tag{8.11}$$

is the result of a CNOT operation applied to the superposition input state described by equation 8.10. The resulting values of the probabilities and density matrix element for the corresponding measurements are given in Table 8.3.

The contrast is $C = 1.05 \pm 0.11$ and $X = 0.76 \pm 0.02$. The evaluated fidelity of a created Bell state is, therefore, $F = 0.64 \pm 0.03$ that also exceeds the Bell limit of 0.5.

8.4 Error Estimation

The sequence of pulses does not refocus the magnetic field fluctuations on a timescale faster than τ/N, where N is the number of π-pulses. Therefore, even for an increased free evolution time a reduction of the contrast of the measured signals is observed (compare Figure 8.1 and Figure 8.7). The coherence time measurements were performed on one ion, with three ions trapped, in analogy with the experiments described in subsection 6.6.4. The probability to find the ion in state $|\uparrow\rangle$, in case the phase of the last $\pi/2$-pulse is $\varphi = 0$ (upper plot of Figure 8.9) and $\varphi = 180°$ (lower plot of Figure 8.9), is plotted versus the evolution time τ, varied in the range of 0 - 24 ms.

The fidelity of the prepared entangled state, η, can be described by the expression

$$\eta = \eta_{pulse} \times \eta_{decoherence} \times \eta_{prep} = \frac{1}{2}\left(\frac{|\vec{\rho}|}{2\overline{\eta} - 1} + 1\right) \quad , \tag{8.12}$$

where η_{pulse} is the fidelity of the pulses in the sequence, $\eta_{decoherence}$ is the fidelity due to the decoherence processes and η_{prep} is the fidelity of ion's preparation in the initial state $|\downarrow\rangle$. The last fidelity is > 0.99 and will not be considered further in the calculations.

The average detection efficiency $\overline{\eta}$ is equal to 0.998 from the population distribution histograms corresponding to the measurements presented in Figure 8.9. The η_{pulse} (error due to the preparation pulse) is calculated using the excitation probability

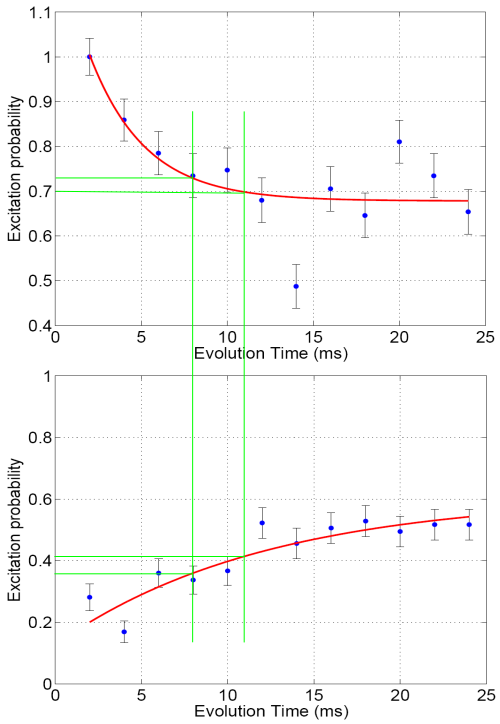

Figure 8.9: Coherence time measurement using the CDD_3 pulse sequence. The probability to find the ion in state $|\uparrow\rangle$, in case the phase of the last $\pi/2$-pulse is $\varphi = 0$ (upper plot) and $\varphi = 180°$ (lower plot), is plotted versus the evolution time τ, varied in the range of 0 - 24 ms. Each data point represent 100 repetitions, the error bars correspond to the mean standard deviations and the solid lines are fits to the data. Green solid lines show the excitation probability levels (horizontal lines) at 8 ms and 11 ms (vertical lines).

at the evolution time around zero in the following way. The highest excitation probability in the upper graph of Figure 8.9 equals 0.96 ± 0.04 (0.95 ± 0.04 for the second set of data not shown in Figure 8.9). The lowest excitation probability in the lower graph of Figure 8.9 is 0.05 ± 0.03 (0.13 ± 0.04 for the second set of data not shown in Figure 8.9). After averaging the highest (lowest) probabilities of two data sets, we subtract the lowest value from the highest value to determine the contrast of the data that in this case equals $|\vec{\rho}| = 0.87 \pm 0.06$. Considering $\eta_{decoherence} = 1$ at the zero evolution time

$$\eta \approx \eta_{pulse} = \frac{1}{2}\left(\frac{|\vec{\rho}|}{2\overline{\eta} - 1} + 1\right) = 0.95 \pm 0.03 \quad . \tag{8.13}$$

In a similar way as described above the contrast $|\vec{\rho}|$ is determined for an evolution times of 8 ms and 11 ms. The corresponding fidelities of the prepared entangled state are, thus, $\eta = 0.71 \pm 0.03$ for 8 ms and $\eta = 0.66 \pm 0.03$ for 11 ms. The fidelities due to the decoherence can be now calculated from equation 8.12:

$$\eta_{decoherence} = \frac{\eta}{\eta_{pulse}} \quad . \tag{8.14}$$

Therefore, for 8 ms the fidelity due to the decoherence equals $\eta_{decoherence} \approx 0.75 \pm 0.04$ and for 11 ms is $\eta_{decoherence} \approx 0.70 \pm 0.04$. Hence, due to the decoherence, the reduction of the final state fidelity is at least 30 % for the evolution time of 11 ms and 25 % for the evolution time of 8 ms. In future experiments microwave dressed states will be employed to extend the coherence time [Timoney *et al.*, 2011].

A photomultiplier is used to measure the parity signal as in Figure 8.8 (b) and Poissonian statistics is used to distinguish between the different ions' states. As one can see from the example of the histogram of three Poisonians in Figure 8.3, the distributions are overlapping and contributing to the errors in the detection. With the current detection efficiencies the maximum possible parity value is:

$$\Pi_{max} = \eta_0 + \eta_2 - 1 = 0.88 \quad , \tag{8.15}$$

the minimum possible parity value is

$$\Pi_{min} = 1 - 2\eta_1 = -0.80 \tag{8.16}$$

and the maximum visibility V_{max} is, therefore,

$$V_{max} = \frac{\Pi_{max} - \Pi_{min}}{2} = \frac{\eta_0 + \eta_2 - 2\eta_1}{2} = 0.84 \quad . \tag{8.17}$$

According to equation 8.7, the maximum fidelity that can be obtained with the current detection setup is

$$F_{max} = \frac{\Pi_{max} + 1}{4} + \frac{V_{max}}{2} = \frac{\eta_0 + \eta_1 + \eta_2}{2} - \frac{1}{2} = 0.89 \quad . \tag{8.18}$$

Hence, the overlap of the three Poissonian distributions reduces the fidelity by

11 %. In future experiments, detection will be improved by measuring the final state using a fast, spatially resolved detector.

9

Conclusion

The focus of this thesis was the realization of an experiment that enables quantum gates measurements to be performed using the MAGIC method. Due to the additional magnetic field gradient an effective Lamb-Dicke parameter κ arises that is proportional to the magnitude of the gradient and does not depend on the wavelength of the radiation used for qubit manipulation. Hence, microwave radiation, for which the standard Lamb-Dicke parameter is negligible, can be used in experiments instead of laser light. Not only it is much easier to generate and to control microwave radiation compared to a complicated laser systems with high quality, but also conditional quantum dynamics can be performed applying microwave radiation tuned to the frequency difference between the two hyperfine-split levels. Therefore, it is totally avoided the spontaneous emission, to which the optical qubits and the hyperfine qubits driven by Raman transitions are susceptible [Ozeri *et al.*, 2007]. Besides, for microwave radiation approach the sensitivity to the spectator modes of ion motion is reduced. Therefore, the requirement to cool the vibrational modes to the ground state is not strict in MAGIC-scheme, thus, giving an evident robustness against thermal excitation. In fact, quantum gates demonstrated in this thesis have been indeed carried out with thermally excited ions, with average phonon number of $\bar{n} = 23(7)$ for three trapped ions and $\bar{n} = 9(9)$ for two trapped ions. A limitation which remains is magnetic field fluctuations substantially limiting the available coherence time. Evidently, dealing with such a

complex experiment we are exposed to various sources of error, but a comprehensive quantitative assessment has still to be done.

The inhomogeneous magnetic field was created by two hollow cylindrical SmCo permanent magnets and mounted at each end-cap electrode of the trap with identical poles facing each other. They produce a gradient of about $b = 19\,\mathrm{T/m}$ at the center of the trap. Hyperfine levels of the $^2S_{1/2}$ ground state of $^{171}\mathrm{Yb}^+$ serve as a qubit in our experiments, namely $|\downarrow\rangle \equiv {}^2S_{1/2}$ ($F = 0$, $m_F = 0$) and $|\uparrow\rangle \equiv {}^2S_{1/2}$ ($F = 1$, $m_F = +1$). The state $|\uparrow\rangle$ is magnetically sensitive and undergoes an energy shift $\Delta E = g_F \mu_B B$ due to the linear Zeeman effect, while state $|\downarrow\rangle$ is insensitive to the magnetic field to the first order. Because of the gradient the ions with inter-ion spacing of δz have different energy shifts resulting in the frequency shifts $\Delta\omega \propto |b|/\nu_z^{2/3}$, where ν_z is the axial trap frequency of the common motional mode. This energy shift makes it possible to address the ions independently in frequency space by microwave radiation. In the current setup the non-resonant addressing error of a neighboring ion is less than 0.04%.

Efforts were also made to increase the microwave magnetic field at the position of the ions to achieve higher Rabi frequency and faster quantum gate operations. For this purpose a special circular waveguide was designed that allowed to increase the Rabi frequency, compared to the previous experiments, by a factor of 2.5 with a moderate power of 2.5 W. Besides, this waveguide allows to choose the microwave polarization directions in order to excite different transitions (π, $\sigma^{\pm}$) of the hyperfine qubit. The main reasons for the power losses in this antenna were due to the attenuation in the microwave cables, both vacuum and external, and the home-made SMA connectors. Therefore, the waveguide performance can be still improved in the future and the Rabi frequency can be further increased by at least an additional factor of 2.5 if a technical solution will be found to improve the vacuum connectors construction. The waveguide is placed inside the vacuum chamber at about 20 mm from the center of the trap. Moving the waveguide closer to the trap may also increase the Rabi frequency. Besides the circular waveguide used in the current experiment, a suggestion was made to build another Paul trap that combines the features of a loop-gap resonator and the linear ion trap. Such design could allow to obtain a Rabi frequencies in the range of several MHz.

The magnetic gradient induces a spin-spin interaction between the ions' internal states mediated by their common motional mode. All the ions in the Coulomb crystal interact with each other. The coupling constants were measured for two and three trapped ions. For two ions the coupling constants were measured for varying axial trapping potential. The measured data have shown a good agreement with the calculated dependence $J \propto \frac{b^2}{\nu_z^2}$. Therefore, it was demonstrated that the

coupling constants can be adjusted at will. In our experiment it was done by changing the axial trapping potential. In microstructured ion trap experiments one can considerably increase the coupling constants by increasing the magnetic field gradient (up to 100 T/m according to references [Kaufmann, 2011] and [Kaufmann, 2012]).

The main source of decoherence in our experiment is the noise superimposed to the classical electro-magnetic fields: the fluctuations of the ambient magnetic field, i.e. noise from the alternating current (A/C) of the mains, and electric field noise from the trap electrodes. Magnetic field fluctuations result in fluctuating resonance frequencies of the qubit due to the Zeeman effect. Electric field fluctuations affect the ions' position and, due to a magnetic field gradient presence, this leads to dephasing of Zeeman states. The coherence time in our experimental setup is currently limited to 200 μs. In order to be able to perform a CNOT gate between ions one needs a coherence time of about 10 ms considering the available coupling constants' strength. In order to compensate for the qubit superposition dephasing and to increase the coherence time, dynamical decoupling sequences have been used. The sequence with a single π-pulse between the two $\pi/2$-Ramsey pulses, know as a spin-echo sequence, prolonged the coherence time up to 2 ms. This sequence was used to measure the coupling constants between two trapped ions at different trapping potential. The other two sequences contain multiple π-pulses between the two $\pi/2$-Ramsey pulses. They are well known in the field of NMR, from where they originate, as CPMG sequences and in the field of quantum information as the dynamical decoupling sequences. The CPMG_{XY} sequence with 24 π-pulses and alternating phases prolonged the coherence time up to 5 ms and the concatenated dynamic decoupling sequence with 84 π-pulses and more complicated phase relation, named CDD_3, prolonged the coherence time further up to 11 ms. In order to keep the spin-spin coupling between the ions active, while compensating for errors caused by ambient fields, the multiple π-pulses sequence must be applied simultaneously on both coupled ions.

Finally, a CNOT gate was performed that employed the J-coupling created by the magnetic field gradient. The gate was performed between two neighboring and two non-neighboring ions in the three ion chain. The measured data are in agreement with the truth table of a CNOT gate that induces a flip of the target qubit or leaves it unchanged depending on the initial state of the control qubit. If the control qubit is prepared in the superposition state and the CNOT gate pulse sequence is applied to the Control and Target qubits, an entangled Bell state is created. The fidelity of this state lies above the Bell limit equal to 0.5 proving the non-classicality. Hence, the fidelity for the entangled state between two neighboring ions equals $F = 0.64(3)$ and between two non-neighboring ions

equals $F = 0.56(3)$. Not all the noise is corrected by the applied sequences. It was estimated that for a free evolution time of 11 ms the reduction of the entangled state fidelity due to the dephasing of Zeeman states is about 30 %. The detection efficiency reduces the fidelity by another 11 %. This can be definitely improved in future experiments.

In this work the fundamental principles of the MAGIC method were proved to work, for the first time, in an experimental setup and they worked consistently to perform quantum conditional dynamics between ions in an ion chain. Possible future application are also mentioned in a recently published article [Khromova *et al.*, 2012]. In the future, technical improvements to increase coherence time and fidelity are provisioned among which it is considered that magnetic field stabilization and improvement of the detection efficiency the most important. For the first case a magnetic field compensation system will be installed that will measure the magnetic field with sensors and will use feedback to compensate for the fluctuations by the external orthogonal coils. The final state measurement will be performed by a fast, spatially resolving detector. Another possibility to increase the coherence time is to use dressed-states for qubits to perform conditional quantum gates [Timoney *et al.*, 2011]. In the future the coupling constants matrix for longer ion strings will be measured. This will later allow to perform multiple qubit gates and to implement cluster states for one-way quantum computation. Besides, the dependence of coupling constants and gate fidelities on thermal excitation of ion strings will be investigated more systematically.

A

Glossary of Symbols

μ_B	Bohr magneton, $9.27400915(23) \times 10^{-24}$, $J \cdot T^{-1}$
h	Planck's constant, $6.62606957(29) \times 10^{-34}$, J/Hz
$\hbar$	Reduced Planck's constant, $1.054571726(47) \times 10^{-34}$, $J \cdot s$
g_F	Hyperfine Landé g-factor for an atom with total atomic angular momentum F = I+J. Since $g_I \ll g_J$ $g_F \approx g_J \frac{F(F+1)-I(I+1)+J(J+1)}{2F(F+1)}$
$g_F = 1$	For $^{171}\mathrm{Yb}^+$ $^2\mathrm{S}_{1/2}$, where $I = \frac{1}{2}$
Q	Elementary charge, $1.602176565(35) \times 10^{-19}$, C
$1u$	The unified atomic mass unit, $1.660538921(73) \times 10^{-27}$, kg
m	Mass of the ion, converted into the kg as $m(kg) = m(a.u.) \cdot u$
ε_0	Vacuum permittivity, $8.854187817620 \times 10^{-12}$, $F \cdot m^{-1}$

γ	Gyromagnetic ratio of electron, $\gamma = g_e \mu_B / \hbar$ with the g-factor $g_e = 2$
$I = \begin{pmatrix} 1 & 0 \\ 0 & 1 \end{pmatrix}$	Identity matrix
$\sigma_x = \begin{pmatrix} 0 & 1 \\ 1 & 0 \end{pmatrix}$	
$\sigma_y = \begin{pmatrix} 0 & -i \\ i & 0 \end{pmatrix}$	Pauli Matrices
$\sigma_z = \begin{pmatrix} 1 & 0 \\ 0 & -1 \end{pmatrix}$	
b	Magnetic field gradient
b_l	Magnetic field gradient at position of ion l

B

Ion in the External Magnetic Field

The Breit-Rabi formula

$$E_{J=1/2,m_J,I,m_I} = -\frac{\Delta E_{HFS}}{2(2I+1)} + g_I \mu_B m_F B + \pm \frac{\Delta E_{HFS}}{2}\left(1 + \frac{4m_F x}{2I+1} + x^2\right)^{1/2} \quad \text{(B.1)}$$

gives the energy levels of the hyperfine levels for electron total angular momentum $J = 1/2$ and arbitrary values of the nuclear spin I. In this formula, $\Delta E_{HFS} = h \cdot 12.642812\,\text{GHz}$ is the hyperfine splitting energy for the $^2S_{1/2}$ ground state of $^{171}\text{Yb}^+$, $m_F = m_I \pm m_J = m_I \pm 1/2$ (where the $\pm$ sign is taken to be the same as in equation B.1) is the total magntic quantum number, and

$$x = \frac{(g_I - g_J)\mu_B B}{\Delta E_{HFS}}, \quad \text{(B.2)}$$

where $g_I = 0.9837$, $g_I = 2.002540$, μ_B is the Bohr magneton and B is an external magnetic field.

The frequency shift of the *pi*-transition ($^2S_{1/2}$ ($F = 0$, $m_F = 0$) $\leftrightarrow$ $^2S_{1/2}$ ($F = 1$, $m_F = 0$)), $\Delta\nu_\pi$, and of the σ^+-transition ($^2S_{1/2}$ ($F = 0$, $m_F = 0$) $\leftrightarrow$ $^2S_{1/2}$ ($F = 1$,

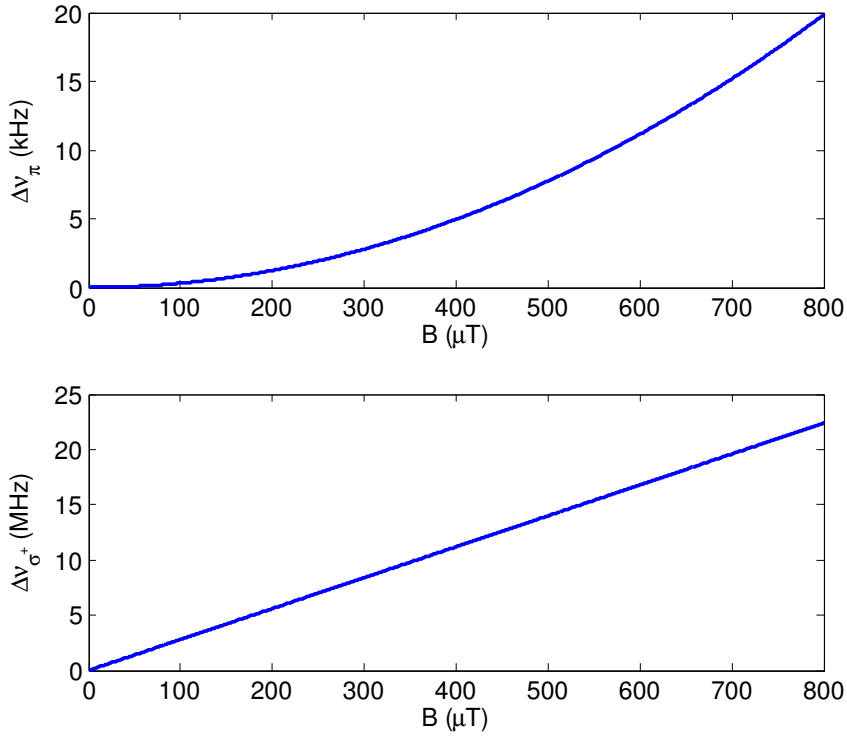

Figure B.1: Magnetic field induced frequency shift of the π (above) and σ (below) transitions in the ground state hyperfine-split levels of the $^{171}Yb^{+}$ ion.

$m_F = +1$)), $\Delta\nu_{\sigma^+}$, are plotted versus the changes of external magnetic field B in the range of $0 - 800\,\mu$T (see Figure B.1). The frequency shifts of the $\pi-$ and $\sigma^{\pm}-$ components are described by equations [Balzer, 2003]

$$\Delta\nu_{\pi} = \alpha_{\pi} \cdot B^2 \tag{B.3}$$

$$\Delta\nu_{\sigma^{\pm}} = \alpha_{\sigma} \cdot B, \tag{B.4}$$

where $\alpha_{\pi} = 0.0319\,\frac{\mathrm{Hz}}{\mu\mathrm{T}^2}$ and $\alpha_{\sigma} = 28\,\frac{\mathrm{kHz}}{\mu\mathrm{T}}$. The $\pi-$transition shows the dependence on the magnetic field B only in the second order. At the typical magnetic field in our experiment of about $600\,\mu$T the frequency shift of the $\sigma-$transition is almost 1500 times larger than the frequency shift of the $\pi-$transition.

C

RF Resonator

The external shield was made thinner in order to fit the structure inside the limited space of the vacuum system. The main box still needs to be thick enough to be able to carry the weight of the RF resonator body. This shielding box was designed to facilitate the access to the resonator. The legs of the shielding box are made of non-conductive plastic. The vacuum chamber itself is not directly placed on the table, but it has plastic pads under its aluminium supporting legs. This was done to avoid a common ground loop for the RF resonator and the vacuum chamber through the table.

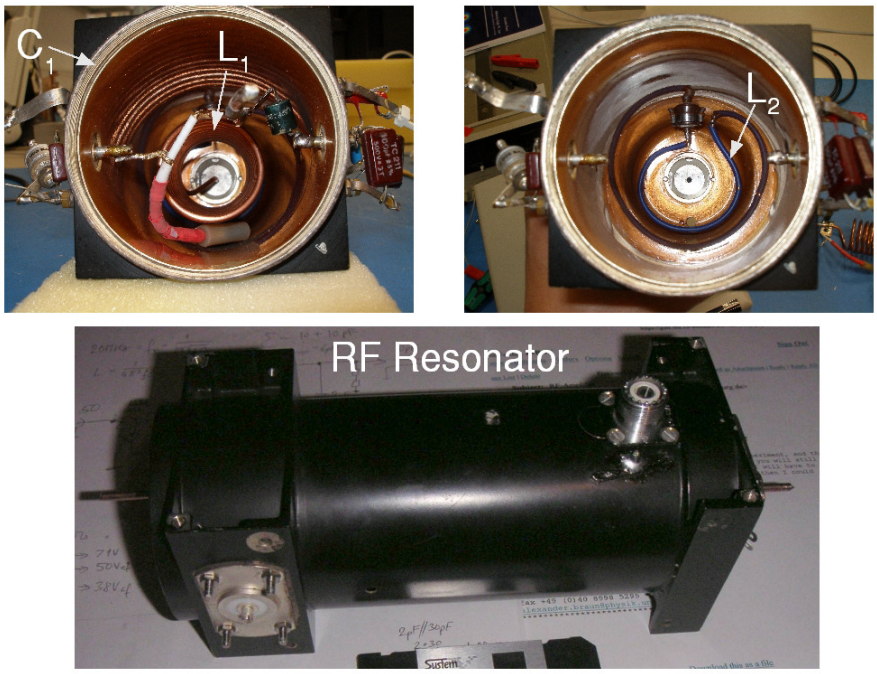

Figure C.1: Photo of the RF resonator used in the current experiment.

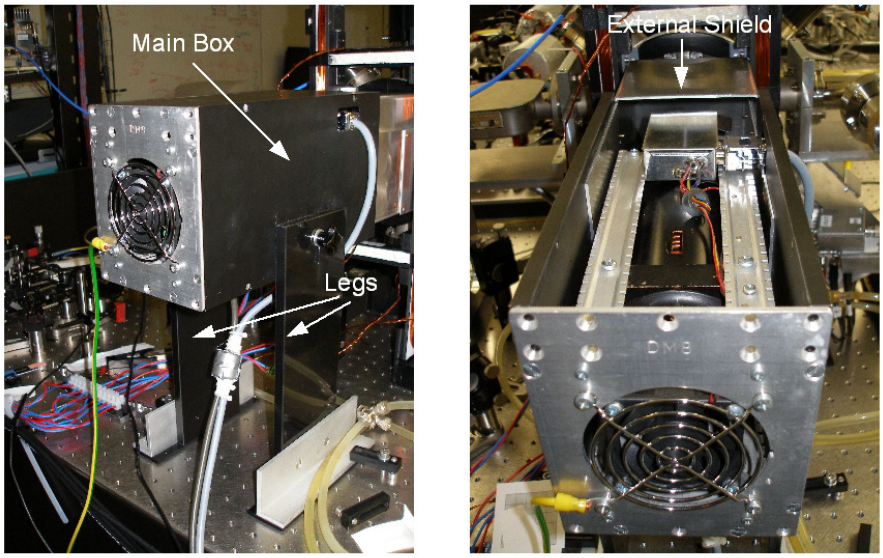

Figure C.2: RF resonator shielding box.

D

Two-AOM Double-Pass Systems

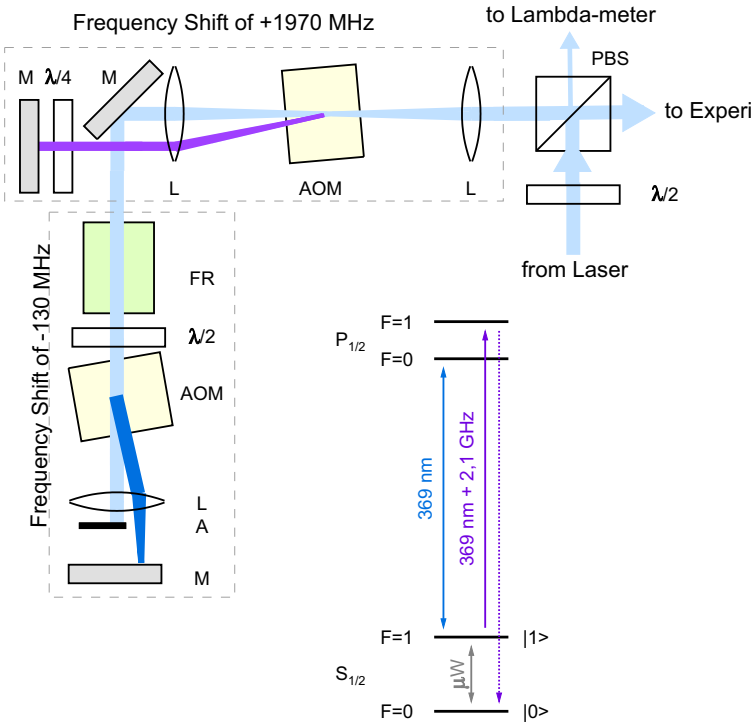

Figure D.1: Two-AOM double-pass system for 369.5 nm laser light. The image is taken from [Piltz, 2010] If the first AOM is switched off and the frequency of the second AOM is set to be > 65 MHz, the 369.5 nm laser light is red-detuned to the ${}^2S_{1/2}$ $(F = 1) \leftrightarrow {}^2P_{1/2}$ $(F = 0)$ transition and cooling is performed. If the frequency of the second AOM is set to 65 MHz, the UV laser is in resonance with the cooling transition and detection is performed. If the second AOM on the contrary is switched off and the first AOM is on, the UV laser light is 2.1 GHz blue-detuned and the preparation into the initial state $|0\rangle$ is possible.
Notations for the image: PBS - polarization beam splitter; L - lens; M - mirror; FR - Faraday rotator; A - absorber.

E

Vacuum System

E.1 Fluorescence Viewport.

The total length of the viewport is 47 mm. This is a so called recessed (inverted) viewport, where the window stainless steel support extrudes in the opposite way from standard models direction. The external tube diameter of this support is $\sim$ 96 mm and the clear view of the viewport window is 83 mm. The distance between the center of the trap and the viewport window is around 20 mm. The anti-reflection coating on both sides of the viewport window and for 369 nm was performed by the Institute For Laser Physics (Hamburg). First, UKAEA sent us the sub-assembly, as depicted in Figure E.1, then, after the coating was finished, this sub-assembly was sent back to the company: they fitted it into the tube and flange and sent us back the completed piece. The temperature for the coating procedure suggested by the company was 250 °C with a steady ramp rate of no more than 2 °C per minute.

Figure E.1: Viewport sub-assembly. This part was separately anti-reflection coated for the 369 nm UV light and later mounted onto the CF100 flange.

E.2 Laser Viewports.

The viewports are bakeable up to 400 °C, according to the specifications. After coating the bake-out temperature is limited to 250 °C. These viewports have additional screws that fix the window to the CF40 flange, as it is possible to see in Figure E.2. As it was shown in the experiment, this solution is not satisfactory. During the frequent heating and cooling cycles of the vacuum chamber on the initial stages of the experiment, when ultra-high vacuum was attempted to be achieved, these screws became loose and the windows can start to leak, making the vacuum quality unacceptable for our experiments. One needs to be very careful to tight these screws without demaging the windows. Anyway, better viewports are available, but they are also far more expensive.

Figure E.2: Laser viewport on the CF40 flange.

E.3 RF In-Vacuum Connection.

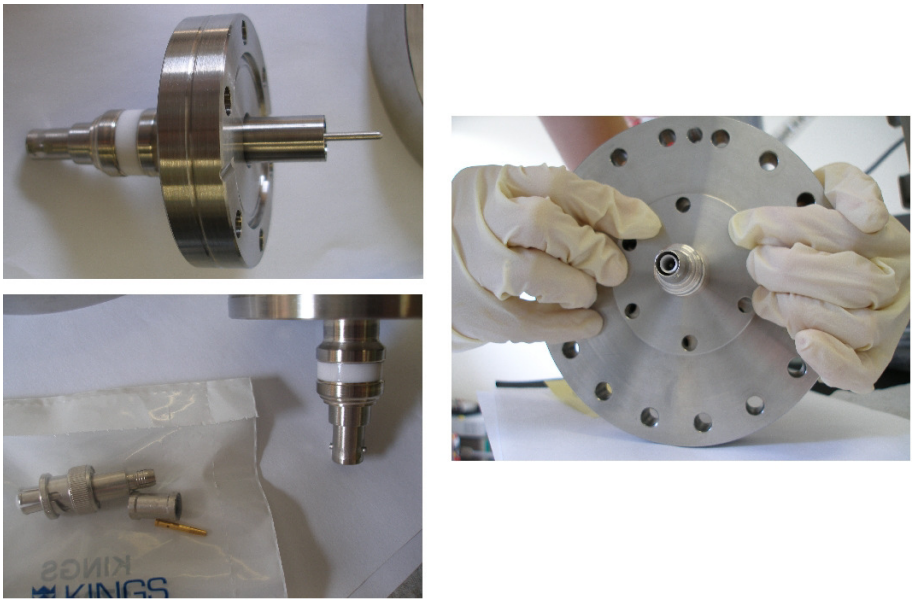

Figure E.3: The SVH-feedthrough on the CF40 flange used to connect the RF resonator. The Right picture demonstrates how this feedthrough is mounted on the CF100 to CF40 zero-length adapter.

F

SR850 Lock-In Amplifier

F.1 Theory of the Lock-In Amplifier

Lock-in amplifiers are used to detect very small signals in the presence of overwhelming noise. They use a technique known as phase- sensitive detection. Here, the input signal is multiplied by an additional reference signal by the special phase-sensitive detector (PSD), know also as a mixer. Therefore, the lock-in detects only the signals at the reference frequency. Noise signals at frequencies other than the reference frequency are rejected and will not affect the measurements. The reference signal can be supplied, for example, by the lock-in's internal oscillator and it has a fixed phase relationship to the signal.

The SR850 is a digital dual phase lock-in amplifier based on an DSP (Digital Signal Processing) architecture. The details can be found in the manual of the device [MODEL SR850 DSP Lock-In Amplifier Manual, January 2009]. The functions in the gray area are handled by the digital signal processor (DSP).

A lock-in amplifier is a device which is useful for measuring the amplitude and phase of even a small noisy signal. The device has two inputs: one is the measured input signal and the other is a reference. Lock-in amplifiers can generate their own internal reference signal, as used in our experiment, which can be described

as $V_{ref} = cos(\omega t + \theta_{ref})$, where ω is the reference signal frequency and θ_{ref} is the reference signal's phase. The input signal should have the same frequency as the reference signal in order the lock-in could perform its measurements. In our experiment, for example, this is achieved by modulating the current of the laser diode with the reference frequency. The input signal $V_s(t)$ (absorption spectrum) varies relatively slow and after modulation at frequency ω the measured signal is $V_{sig} = V_s(t) \cdot cos(\omega t + \theta_{sig})$ [1], where $V_s(t)$, ω and θ_{sig} are the input signal amplitude, frequency and phase, respectively. The phase-sensitive detector (PSD), which is also known as a demodulator or mixer, multiplies the modulated signal by the reference signal:

$$\begin{aligned} V_{sig}V_{ref} &= V_s(t) \cdot gain \cdot cos(\omega t + \theta_{sig}) \cdot cos(\omega t + \theta_{ref}) \\ &= \frac{1}{2} \cdot V_s(t) \cdot gain \cdot [cos(\theta_{sig} - \theta_{ref}) + cos(2\omega t + \theta_{sig} + \theta_{ref})] \end{aligned} \quad \text{(F.1)}$$

As can be seen in equation F.1, the result consists of two frequency components: one term at zero frequency (DC) and an other at the double frequency. The double frequency component will be removed by the low pass filter giving a final result equal to:

$$V_{out} = \frac{1}{2} \cdot V_s(t) \cdot gain \cdot cos(\theta_{sig} - \theta_{ref}). \quad \text{(F.2)}$$

The parameter 'gain' above is the amplifier overall gain (input to output) that is equal to $\frac{10\,\mathrm{V}\sqrt{2}}{sensitivity}$. The sensitivity of the lock-in is the RMS (root mean square) amplitude of an input signal, at the reference frequency, which results in a full scale DC output. Traditionally, full scale means $10\,V_{DC}$ at the X, Y or R BNC output. If the signal and the reference are in phase the output has the maximum voltage. Very often θ_{sig} and θ_{ref} are not equal. Most lock-in amplifiers have a phase-shifter to match the phases. Our lock-in has the phase-shifter and, additionally, a second PSD detector with another low pass filter. One of the detectors multiplies the reference and the input signal as before, and the other one multiplies the input signal with the reference phase shifted 90°. The two outputs become:

[1] Any DC component of the signal is removed by the AC coupling filter.

$$V_{outX} = \frac{1}{2} \cdot V_s(t) \cdot gain \cdot cos(\theta_{sig} - \theta_{ref}) \quad \text{(F.3)}$$

$$V_{outY} = \frac{1}{2} \cdot V_s(t) \cdot gain \cdot sin(\theta_{sig} - \theta_{ref}). \quad \text{(F.4)}$$

V_{outX} is the 'in phase' component of the output, while V_{outY} is the 'out of phase component'.These two quantities represent the signal as a vector relative to the lock-in reference oscillator. A new complex quantity is defined as :

$$V_{out} = V_{outX} + iV_{outY}. \quad \text{(F.5)}$$

No matter what the phase difference between the input and the reference is, the magnitude of V_{out} can now be used to find the amplitude of the input signal: $R = (X^2 + Y^2)^{1/2} = V_s(t)$. A dual-phase lock-in, such as the SR850, can measure X, Y, and R directly. Additionally, the phase θ between the signal and lock-in reference can be measured according to

$$\theta = tan^{-1}(Y/X). \quad \text{(F.6)}$$

In Table F.1 the current lock-in amplifier parameter settings are summarized. the Input and Filters menu sets the input signal source and configuration. The single-ended input amplifier (A) is selected (see also block diagram in Figure **??**). In Ground mode the shield of the input connector A is connected by 10 Ω to ground. The input signal is AC coupled, i.e. oscillates around a zero offset [2]. No line notch filters enabled: they usually remove signal inputs at 60(50) Hz and 120(100) Hz in case when the largest noise signals are at the power line frequencies. The Gain and Time Constant menu sets the full scale sensitivity, dynamic reserve, low pass filter time constant and slope. The sensitivity sets the maximum possible input signal amplitude (full scale) in order to avoid an overload of the PSD. The minimum reserve for the sensitivity of 200 mV is 4 dB. The dynamic reserve is the ratio of the largest tolerable noise signal (V_{noise}) to the full-scale signal (V_{fs}), expressed in dB. Hence, $V_{noise}/V_{fs} = 10^{\frac{4\,\mathrm{dB}}{20}} = 1.6$ and for the 200 mV full scale the noise as large as 320 mV can be tolerated. For the low-pass filter a 12 dB/octave roll-off is chosen. This means that for each successive doubling of frequencies above the cutoff frequency, the response falls 12 dB (amplitude decreases by four). A 12 dB/octave

[2]The AC coupling high pass filter passes signals above 160 mHz and attenuates signals at lower frequencies.

Menu Keys	Parameter	Parameter Setting
[REF/PHASE]	Ref Phase	−21.571
	Ref Source	Internal
	Ref Frequency	20 kHz
	Harmonic	#1
	Sine Output	0.016 V
[INPUT/FILTERS]	Source	A
	Grounding	Ground
	Coupling	AC
	Line Notches	Out
[GAIN/TC]	Sensitivity	200 mV
	Reserve	Min
	Time Constant	100 μs
	Filter db/oct.	12
	Synchronous	Off
[OUTPUT/OFFSET]	Front Panel	CH1
	Source	X
	Offset & Expand	X
	(a) Offset	0.00%
	(b) Expand	1

Table F.1: Parameter settings used in the SR850 Lock-In Amplifier.

slope corresponds to a second-order or two-pole (two reactive components meaning two capacitors) filter where two first order low pass filters are connected in series. Any gaussian noise at the filter input is filtered with an effective bandwidth equal to the ENBW (equivalent noise bandwidth). The ENBW depends upon the time constant and filter roll off. For the 100 μs time constant τ and 12 dB/octave roll off the ENBW equals $1.22 \times f_{3dB} = 1.22 \times 1/(2\pi \cdot \tau) = 1943$ Hz. The time constant is chosen to be bigger than the period of the reference signal (50 μs in our case) and it defines the window for the signal integration, i.e. how much periods of the signal would be averaged. Longer times effectively smooth the noise, but they should be chosen so that the output response is not too slow.

F.2 The Error Signal

The output of the lock-in amplifier (the error signal), as it is used in our experiment, has a particular shape (see Figure 3.15, (b)) that has to be explained. The photodiode delivers to the input of the lock-in a voltage signal, which is a function of some physical parameter that is controlled by us (i.e. current in our case). Modulating the laser-diode current results in a laser frequency modulation and, respectively, in the modulation of the photodiode output. If the laser frequency $\omega(t)$ is slowly varied, the signal of the photodiode can be written as:

$$V_s(\omega) = V_s(\omega_0 + m \cdot cos(\Omega t)), \tag{F.7}$$

where Ω is the modulation frequency and $\boldsymbol{m}$ is the modulation amplitude. We can expand V_s as a Taylor series

$$\begin{aligned} V_s(\omega_0 + m \cdot cos(\Omega t)) = V_s(\omega_0) + m \cdot cos(\Omega t) \cdot \frac{dV_s}{d\omega} + \\ \left(\frac{m^2 \cdot cos^2(\Omega t)}{2!}\right) \cdot \frac{d^2V_s}{d\omega^2} + \left(\frac{m^3 \cdot cos^3(\Omega t)}{3!}\right) \cdot \frac{d^3V_s}{d\omega^3} + ... \end{aligned} \tag{F.8}$$

and combining the terms we obtain:

$$\begin{aligned} V_s(\omega_0 + m \cdot cos(\Omega t)) = \left[V_s(\omega_0) + \frac{m^2}{4}\frac{d^2V_s}{d\omega^2} + ...\right] \\ cos(\Omega t)\left[m\frac{dV_s}{d\omega} + \frac{m^3}{8}\frac{d^3V_s}{d\omega^3} + ...\right] + \\ cos(2\Omega t)\left[\frac{m^2}{4}\frac{d^2V_s}{d\omega^2} + ...\right] + ... \end{aligned} \tag{F.9}$$

Hence, the intensity transmitted through the Rb cell contains a DC term, a term oscillating at Ω multiplied by the first derivative, one at 2Ω multiplied by the second derivative and so on. Running the signal described by F.9 through the lock-in amplifier gives an output, proportional to the modulation amplitude $\boldsymbol{m}$ and to the derivative (slope) of the spectrum:

$$V_{out} \approx \frac{1}{2} \cdot m \cdot \frac{dV_s}{d\omega} \cdot gain \cdot cos(\theta_{sig} - \theta_{ref}). \tag{F.10}$$

The output V_{out} depends not only on the input modulation $\boldsymbol{m}$, but also on the slope. Besides, the lock-in measures not only the magnitude of the derivative but also the phase, and so the sign of the derivative. In a situation when the laser has drifted below or above the resonance, the applied modulation causes the laser frequency to periodically shift closer and further from the resonance. This is reflected in the absorption intensity oscillations with the amplitude, that depends on the position on the slope: the steeper the slope - the higher the amplitude of the oscillation. The photodiode signal in this case has the same frequency as the modulation. Besides, below the resonance the photodiode signal is in phase and above the resonance the photodiode signal is 180 °C out of phase with respect to the modulation frequency. When the laser is on resonance, any change in the laser frequency due to the modulation takes the frequency away from the resonance and produces the decrease in the absorption signal. Hence, the photodiode signal will have a frequency twice the frequency of the modulation and the lock-in output averages to zero. To conclude, the lock-in output is positive below resonance and negative above with a zero crossing at the resonance frequency (dispersion-like curve).

F.3 The Reference Laser Lock-In Setup

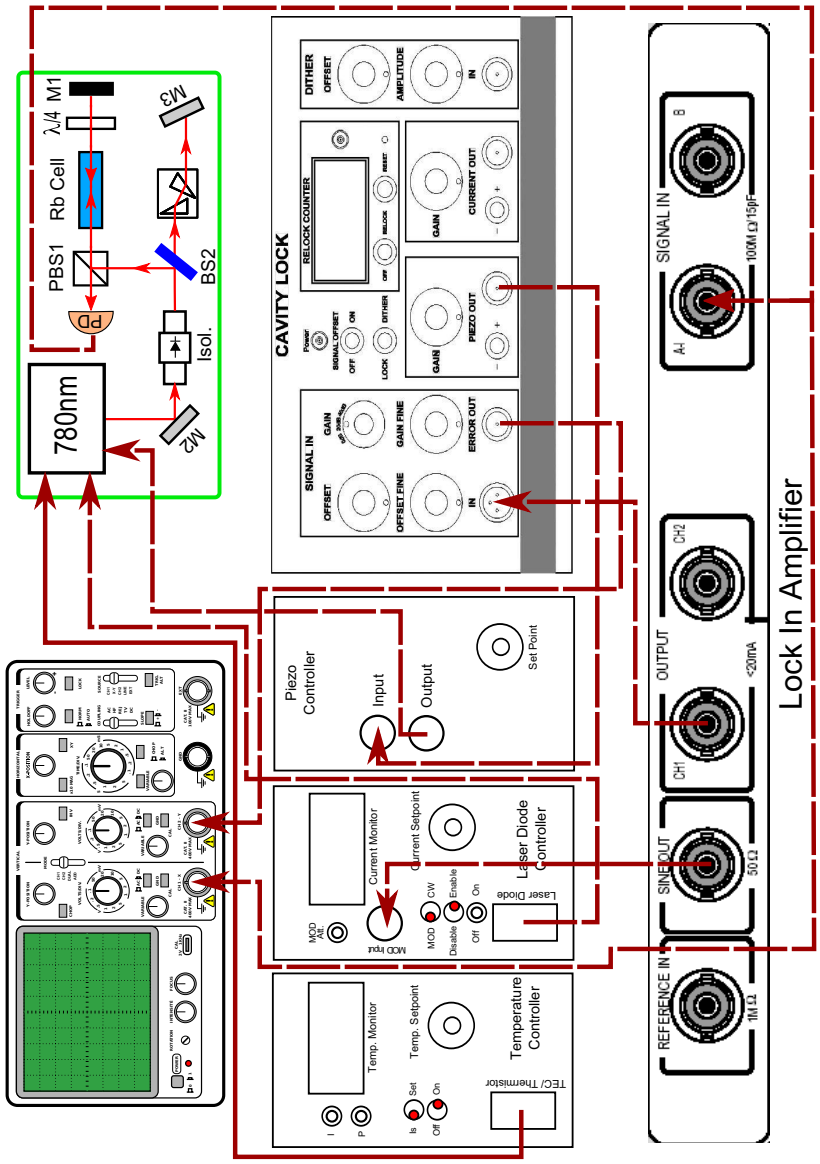

Figure F.1: Reference signal locking setup. The input to the Lock-In amplifier (SIGNAL IN) is a signal from a photodiode. The same photodiode signal is connected to the CH1 of the oscilloscope. The internal reference signal of the Lock-in Amplifier, equal to 20 kHz, is used to modulate the current of the diode laser at about 780 nm, used to excite the ^{87}Rb transition (SINE OUT of the Lock-in amplifier is connected to the MOD input of the laser diode controller). The error signal produced by the Lock-In amplifier is the input of the locking feedback circuit (OUTPUT CH1 of the Lock-In amplifier is connected to the SIGNAL IN, IN of the Cavity Lock). The feedback circuit output signal (ERROR OUT of the Cavity Lock) is connected to the oscilloscope CH2. The control voltage from the Piezo Out of the Cavity Lock is connected to the input of the diode laser piezo controller to adjust the frequency of the diode laser when the feedback loop is closed.

G

Heating of the static coils

Prior to the construction of the coils we must consider the amount of resistive dissipation during the operation of the coils. The instantaneous power dissipation in the coil is given by the product of the square of the current I and the coils resistance R_c:

$$P = I^2 \cdot R_c \tag{G.1}$$

and the total energy converted to heat is given by the integral of the power dissipation function:

$$E = R_c \cdot \int_{t_0}^{t_1} I^2 \cdot dt, \tag{G.2}$$

where t_0 and $t1$ are the start and stop times of the current flow. It can be simplified as:

$$E = R_c \cdot I^2 \cdot (t_1 - t_0). \tag{G.3}$$

The standard equation relating the change in thermal energy of a body to its change in temperature is:

$$\Delta E = M \cdot c \cdot \Delta T, \tag{G.4}$$

where M is the mass of the copper wire and c is the specific heat capacity that for copper equals $0.385\,\mathrm{J} \cdot \mathrm{g}^{-1} \cdot \mathrm{K}^{-1}$. The mass M of the copper wire is just the density of the copper ρ ($8940000\,\mathrm{g} \cdot \mathrm{m}^{-3}$) multiplied by the volume of copper wire V_C. The last value is easy found by multiplying the coil "filling factor" $F = \pi/4$

Thermal Conductivity ($\frac{W}{m \cdot K}$)	
Copper	401
Aluminium	237
POM plastic	0.31
Electrical Resistivity ($n\Omega \cdot m$)	
Copper	16.78

Table G.1: Properties of materials used for the coils.

[1] by the total volume V_T of the coil wire that in case of the rectangular coil equals $(b_{out} \cdot a_{out} - b_{in} \cdot a_{in}) \cdot L$. Here, b_{out} and a_{out} are the outer dimensions of the coil and b_{in} and a_{in} its inner dimensions. L is the length of the coil equal to $m \cdot d$, where m is the number of horizontal wires and d is the wire diameter. The resistance $R_c = \lambda \cdot \frac{L_w}{A_w}$, where *lambda* is the electrical resistivity of copper (see Table G.1), $L_w = \frac{V_C}{A_w}$ is the wire length and $A_w = \frac{\pi \cdot d^2}{4}$ is the cross-sectional area of the wire. Therefore, for our particular **main big coils** with the flowing current of 4.5 A the instantaneous power equals 170.13 W and the corresponding change of temperature is $\Delta T = \frac{P}{M \cdot c} = 0.16\,^{\circ}\mathrm{C/sec}$. This means that in 1 min the temperature of the copper wire will increase already by $9.6\,^{\circ}C$. The copper wires are polyimide isolated. Polyimide operational temperature reaches up to $232\,^{\circ}C$. With the current energy production of the coil this temperature can be reached in approximately 30 min. Two candidates for the coil frame material, aluminium and Polyoxymethylene (POM) thermoplastic, were investigated. The properties of the materials used in the coils are given in Table G.1.

The thermal energy produced by the copper wire is conducted away by the frame of the coil. The formula that describes the heat conduction is:

$$P = k \cdot A_{frame} \cdot \Delta T / L, \tag{G.5}$$

where P is power (instantaneous energy in Joules per second), A_{frame} is the area of the coil frame, k is the thermal conductivity of the frame, ΔT is the temperature difference between the faces of the frame and L is the thickness of the frame. Taking into account the instantaneous power of 170.13 W, the temperature difference between the copper wire and the frame equals $\Delta T = T_2 - T_1 = \frac{P \cdot L}{k \cdot A} = \frac{170.13\,\mathrm{W} \cdot 0.005\,\mathrm{m}}{k \cdot 0.039\,\mathrm{m}^2}$. For the aluminium frame $\Delta T = 0.09\,^{\circ}\mathrm{C}$ and for the POM plastic $\Delta T = 69.78\,^{\circ}\mathrm{C}$.

[1] The amount of space between the adjacent turns will depend on how neatly the coil is wounded. In ideal case each strand effectively occupies a total cross-sectional area of d^2 (d is wire diameter). Hence, the ratio between the effective occupied area d^2 and the actual cross-sectional area of the wire $\frac{\pi \cdot d^2}{4}$, F, equals $\frac{\pi}{4}$.

As it is possible to see, the POM plastic conducts the heat very bad. Besides, it has a melting point at 175 °C that can be reached very fast in the current conditions. Hence, for **the big main coils** with high current the aluminium frame was chosen. Additionally, this frame was constructed so to allow a water flow inside the frame to guarantee better cooling of the copper wire over the long operational times during the experiment. Besides, the aluminium frame helps avoiding the bending under the weight of the 290 loop of the copper wire as it is a possible case with the plastic frame. These frames were black anodized from outside in order to reduce the light reflections from their surfaces and lacquered with transparent lack from inside in order to avoid corrosion due to the contact with water.

The instantaneous power dissipation produced by the small rectangular coils with 1.5 A equals 3.36 W that results in a change of temperature of 0.018 °C/sec. For the circular coils with 1 A the instantaneous power dissipation is 1.11 W and the change of temperature equal to 0.008 °C/sec. The frames of these coils are made from POM since the production of energy by these coils is far smaller than by the big coils. To improve the heat transfer the copper wires of the small coils were covered with an epoxy characterized by high thermal conductivity. The temperature difference between the sides of the POM frame equals $\Delta T = 7.75\,^{\circ}\mathrm{C}$ for the small rectangular coils and $\Delta T = 3.45\,^{\circ}\mathrm{C}$ for the circular one.

The heat generated in the coil is dissipated via three main mechanism: conduction from the windings to the air, aluminium/POM frames and high thermal conductive epoxy ; convection to air and radiation. The measurements demonstrated that the circular coils has the temperature of 2.5 °C, at 1 A, higher than the room temperature after 8 hours and for the small rectangular coils the temperature increased by 7 °C, at 1.5 A, after about 9 hours of operation. The temperature of the big coils was not measured.

H

Microwave Antenna

H.1 Microwave Antenna Construction

Commercial SMA female connectors from ALLECTRA, used for the microwave circular waveguide probes (or antennas), are built from stainless steel and Cu-alloy, totally gold coated and there are two options for the connector insulator: glass ceramic and PTFE (Teflon). Glass ceramic has lower outgassing rate and, therefore, better adapted for vacuum than PTFE. Nevertheless, for us it is important to have 50 Ω impedance, therefore the PTFE connectors were chosen. ALLECTRA offers also already assembled SMA cables for UHV. These cables are Kapton coated, 50 Ω impedance, with an upper cut-off frequency of $\sim$ 17 GHz and attenuation of 1.9 dB/m at 1 GHz. At 12.6 GHz we expect something around 8 dB/m. Around 20 cm long cables were used inside the vacuum chamber to connect the antennas to the SMA-feedthrough. The expected attenuation is around 1.6 dB for each cable run.

The female commercial vacuum SMA connector consists of 7 parts, two of which are made out of PTFE [ALLECTRA, 2008]. The outer insulation was cut out at around 18 mm distance, the screen was cut out at 10 mm and the inner conductor was cut out at 12 mm. A crimp sleeve was put onto the cable and the

inner crimp sleeve was pushed under the screen. The latter has a fixing nut from the opposite side. Then the outer crimp sleeve was pushed over the inner crimp sleeve. The smallest PTFE ring (length 2 mm), a washer, was put over the inner conductor. See also Figure 3.32 for more information. The inner conductor part was then made thicker with solder to reach the preferred 1.27 mm outer diameter of a standard SMA connector pin. Another possible solution would have been to crimp a 12 mm long with 1.27 mm outer diameter stainless steel tube on the inner conductor. It would have an advantage over the soldering, since the soldering materials, with their high outgassing rates, are usually not suggested for use in UHV. Unfortunately, crimping did not work well while the inner conductor is too thin and easily breakable. After the inner conductor is ready, the outer crimp is crimped. The biggest PTFE part, the insulator, is cut to a length of ~ 6 mm from the original size and put over the inner conductor onto the PTFE washer. At the end around ~ 5.5 mm of the inner conductor is outside the PTFE insulator.

The ready microwave waveguide antenna is shown in Figure H.1. The antenna holder does not lie tightly on the waveguide body, as it is possible to see in Figure H.2. This facilitates the pumping out of the air from the region of the antenna holder.

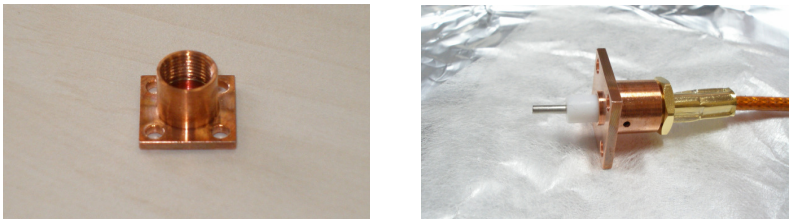

(a)

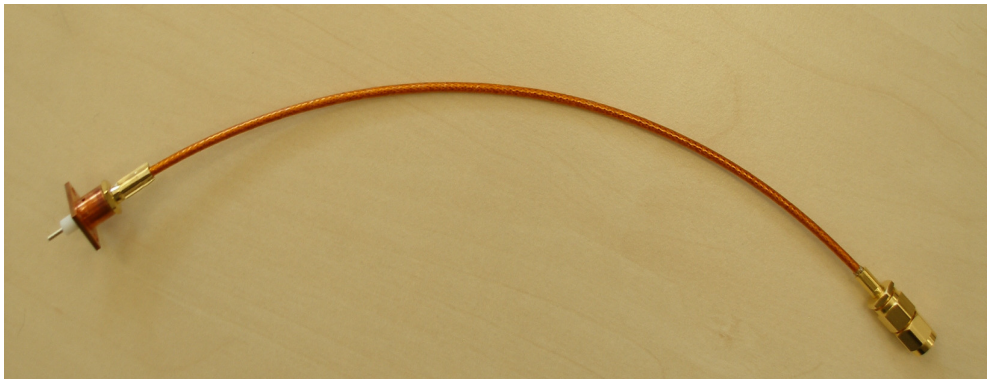

(b)

Figure H.1: (a) Photo of the antenna holder and the ready vacuum SMA connector; (b) Photo of the ready cable with antenna for the vacuum chamber;

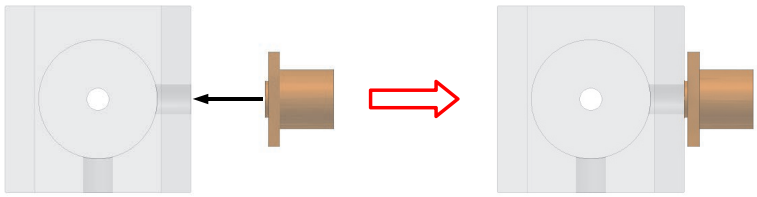

Figure H.2: Position of the antenna holder according to the circular waveguide.

I

Detection System

I.1 Objective

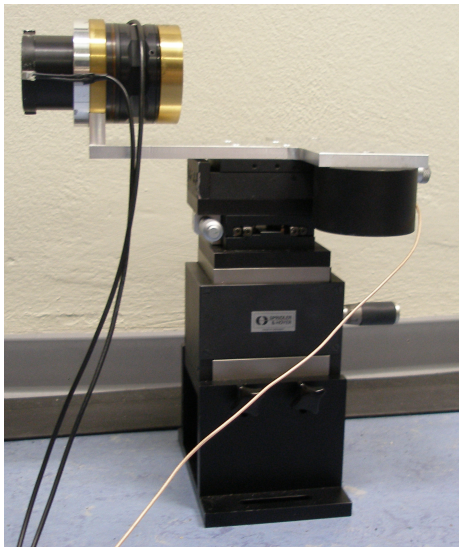

Figure I.1: The home-made objective on a translation stage with a piezo-actuator that helps to fine-adjust the focus of the objective in the sub-micrometer range. Two additional stages with micrometer-screws help to align the objective in the axial and the radial trap directions.

I.2 ICCD Camera

The intensifier of an ICCD camera consists of a photocathode, a micro-channel plate (MCP) electron multiplier, and a phosphor screen, all positioned in front of the CCD. It detects and amplifies the light, while the CCD is used for read-out. The incident photons striking the photocathode release electrons due to the photoelectric effect. Our image intensifier has an S20 type (sodium-potassium-antimonide-cesium: Na-K-Sb-Cs) photocathode and it is equipped with a quartz window, increasing the transmission of the UV light [PCO Computer Optics Manual, October 1993]. The absolute sensitivity S(λ) for this photocathode at 369 nm is 75 $\frac{mA}{W}$ that results in a photocathode quantum efficiency QE(λ)[1] of

$$QE(\lambda) = \frac{S(\lambda)}{\lambda} \cdot (1240 \cdot W \cdot \frac{nm}{A}) = \frac{75\,\frac{\mathrm{mA}}{\mathrm{W}}}{369\,\mathrm{nm}} \cdot (1240 \cdot W \cdot \frac{nm}{A}) \sim 0.25 = 25\%. \quad \text{(I.1)}$$

The QE of 25% means that each fourth photon ejects an electron. The photoelectrons released from the photocathode are accelerated toward the MCP due to the potential difference between the photocathode and MCP. The MCP consists of more than 10^6 individual miniature electron multipliers (parallel traversing channels). The electrons are multiplied inside the MCP and thereafter are accelerated towards the phosphor screen. The phosphor screen finally converts the multiplied electrons back to photons, which are guided to the CCD by a fiber optic or a lens. Our intensifier is coupled to the CCD via a lens. The image-intensifier inherently includes a shutter functionality: if the control voltage between the photocathode and the MCP is reversed, the emitted photoelectrons are not accelerated towards the MCP but return to the photocathode. Thus, no electrons are multiplied and emitted by the MCP, no electrons are going to the phosphor screen and no light is emitted from the image intensifier. In this case no light is detected by the CCD, which means that the shutter is closed. The process of reversing the control voltage at the photocathode is called **gating** and therefore ICCDs are also called gateable CCD cameras. The intensifier gain is varied by adjusting the voltage across the MCP.

[1] Quantum efficiency is the fraction of the photons that actually eject electrons from the photocathode.

Operation of the Camera

As soon as the mechanical shutter is completely opened and purging from accumulating charge in the pixels due to the dark current have been performed [2], $\overline{\textbf{READY}}$ signal goes low to indicate that the camera is ready to capture the first image (stage **1** in Figure 3.41). It remains low until the external trigger is applied to the **EXT SYNC** connector and the exposure begins, after that it goes high. Further, the $\overline{\textbf{READY}}$ signal goes low always when the camera exposure and read-out is finished and it is ready to take a new image. The negative edge of the $\overline{\textbf{READY}}$ pulse connected to the **TRIGGER** input of the SRS starts the burst (**BURST**) with one cycle at the **FUNCTION** output of the SRS generator (stage **2** in Figure 3.41), triggering the image intensifier and the CCD camera controller (stage **3** in Figure 3.41). This pulse is set to have a square form with a square wave frequency of $f = 1.4\,\text{Hz}$. The width of the pulse equals $\frac{1}{2 \cdot f} \sim 357\,\text{ms}$ for an exposure of 400 ms as used in the experiment . The camera exposure time is slightly longer than the time period that the photocathode is opened. This ensures that the action time of the image intensifier is completely within the exposure period of the camera so that no photons reach the CCD chip during the read-out. The SRS pulse repeats after the $\overline{\textbf{READY}}$ pulse negative edge reappears. This is the fastest way of taking images with the CCD camera. If the internal trigger of the SSR was used instead, the trigger rate had to be set to define the **FUNCTION** output pulse repetition frequency. For example, let's set the trigger rate for the internal trigger to 1 Hz, meaning that the burst repeats after 1/trigger rate=1 s. Taking into account the pulse width of 357 ms, when the photocathode is opened for exposure, it is available 643 ms before the next pulse occurs. Usually the CCD camera full frame reading takes around 500 ms. If the region-of-interest is chosen, this time is even shorter. All the rest of the time the camera has to wait for the next exposure trigger. This is an evident waste of time hence an external SRS triggering has been used to improve the readout.

[2] Actually, we did not set any Clear Mode for the camera in our experiment. Hence, the camera starts exposing immediately after the pl_exp_start_seq (see see Appendix O) is called that means the first exposure in our sequence may have a longer exposure time than the subsequent exposures. This is nevertheless not a problem for us.

J

Samarium Cobalt (Sintered) S2869 Properties

The Samarium Cobalt permanent magnets used in our experiment are situated inside the vacuum chamber. During the backing of the vacuum chamber to achieve UHV conditions, the magnets were subjected to a heating up to $145°C$ and relative cooling back to the room temperature of $20°C$. Heating/cooling rates are in the range of $\sim 8°C$ per hour. Samarium Cobalt permanent magnets are know to have a very high Curie Temperature T_c (see table J.1), that is the temperature at which the magnets are totally demagnetized. The magnet can not restore its magnetic force even after the temperature is reduced to standard. Besides, heating a Samarium Cobalt permanent magnets to T_c can cause structural damage. Therefore, it is strongly recommended not to reach these temperatures. There is also another temperature limit, the maximum operation temperature, to which the magnet may be exposed for continuous time without significant structural changes or losses of the magnetic properties (see table J.1). This temperature is different for different materials and the different designs of the magnets.

One can classify the losses of the magnetic strength due to the change in temperature in reversible and irreversible. Each magnet is characterized by its particular temperature coefficient T_{kB_r} (in $\%/°C$) that describes the reversible change of the residual magnetic flux density B_r, when the temperature is changed. This means

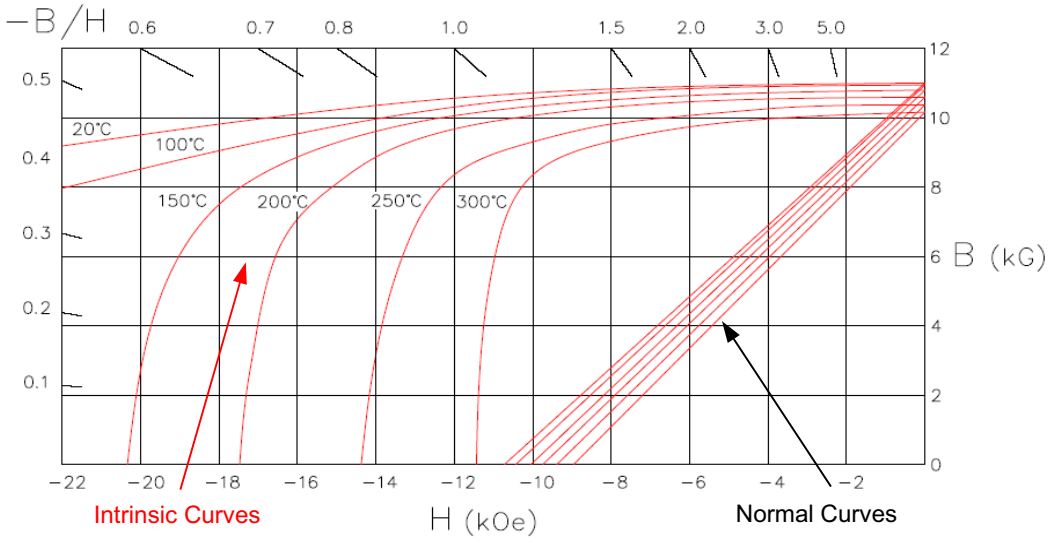

Figure J.1: Demagnetization Curve of SmCo28 Samarium Cobalt (Sintered) Magnets [Magnetic Component Engineering Inc, 2009b].

that if the magnet is heated up to $145°C$, assuming room temperature is $20°$ and considering the temperature coefficient for SmCo S2869 $T_{kB_r} = -0.03\,\%/°\mathrm{C}$ (see table J.1), its reversible loss is $(145 - 20) \times (-0.03) = -3.75\%$. When the temperature is returned to the original level, the magnet also recovers its original characteristic. Usually, this coefficient is negative for all materials that means B_r decreases when the temperature increases. B_r is the magnetic flux density that remains in a material when the magnetizing force H is zero, after saturation has occurred, and it does not depend on the shape of the magnets.

Irreversible losses of the magnetic properties at elevated temperatures are due to magnet design: these losses occur when the operating point of the magnet falls below the knee of the demagnetization curve and the operating point is defined by the permeance coefficient, which depends on the geometry of the magnet, as will be explained below. This explains why magnets demagnetize even though the magnet's maximum operating temperature was not reached. Let's look at the B-H curves of the Samarium Cobalt magnet type, that is used in our experiment (see Figure J.1). A magnet can be partially demagnetized in the presence of an additional magnetic field. Figure J.1 demonstrates the second quadrant of the hysteresis curve of the magnet, also called demagnetization curve. This curve

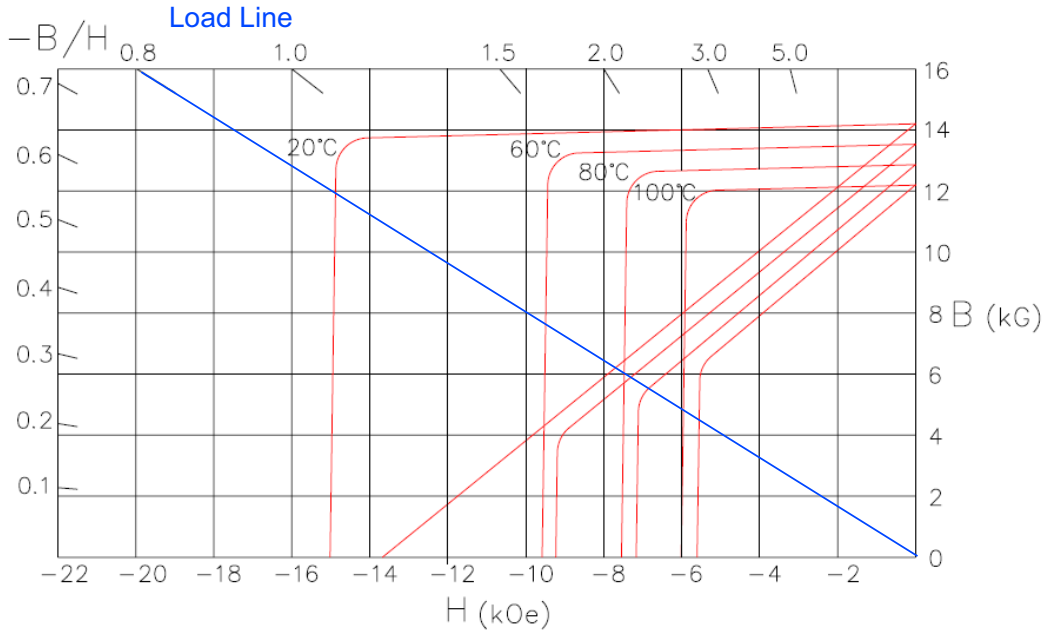

Figure J.2: Demagnetization Curve of N5064 Neodymium Iron Boron (Sintered) Magnets [Magnetic Component Engineering Inc, 2009a].

shows how the magnetic flux density (B, *normal curve*) and magnetization (J, *intrinsic curve*) respond to the changes in the demagnetizing force (-H) [1]. The magnetic flux density is a total value consisting of the magnetization of a magnet and any external magnetic field i.e. $B = J + \mu_0 \cdot H$. The numbers on the left and top of the graph are the permeance coefficient also referred as the 'operating slope', load line or B/H of the magnet (blue line in Figure J.2). Usually, this parameter refers to an 'open circuit' condition (i.e there is no any other source of the magnetic field around our permanent magnet). This parameter depends on the design of the magnet and the smaller it is the bigger the influence of the temperature on the magnetic properties. One needs to know the permeance coefficient for certain magnet in order to determine the operation point on the demagnetization curve. For example, in Figure J.2 this parameter equals 0.8 and the load (operation) line is drawn from this point to the origin of the graph ($B = 0$, $H = 0$). The normal curves for a $N5064$ permanent magnets at $60°C$, $80°C$ and $100°C$ have the 'knee' in the curve. If the load line crosses above this 'knee' in the curve, then the magnet is operating in its safe linear region and would perform as expected. If the load

[1] Usually, the intrinsic curve is interesting when one wants to investigate the reacion of the permanent magnet to the external magnetic field.

line is below the 'knee on the curve', the magnet will demagnetize (at $100°C$ in the following example). It is possible to notice that the 'knee' gets higher with an increased temperature making the magnets more vulnerable to demagnetization. The permeance coefficient for hollow cylindrical permanent magnets with axial magnetization can be calculated by the formula

$$P_C \equiv B/H = \frac{4 \cdot L_e}{(D_o^2 - D_i^2)} \cdot \sqrt{\frac{L \cdot (D_o + D_i)}{2} + \frac{(D_o^2 + D_i^2)}{4}}, \tag{J.1}$$

where L_e is the effective magnetic length equal to the true geometrical length L for the high coercivity SmCo magnets; D_o and D_i are the outer and inner diameters of the magnets. For a detailed calculation see [Parker, 1990]. Hence, for our magnets $P_C = 8.15$ and our load line is very steep. Our magnets are rated to have a maximum operating temperature of $350°C$, that is actually fairly higher if compared to the temperature used to achieve UHV conditions. The normal lines measured up to $300°C$ do not have the 'knees' and if there would be a 'knee' for higher temperature it would definitely lies below our steep load line.

The value of the demagnetization force at which the resultant residual magnetic flux density B_r is reduced to zero is called coercive force (H_c). The point, where the intrinsic curve (J curve) crosses the -H axis, is called H_{ci}, intrinsic coercive force. The intrinsic curve describes the magnetic flux density produced by the magnet alone, without additional magnetic flux density produced by an external field strength H. H_{ci} is always greater than H_c in the second quadrant of the hysteresis due to the relation $J = B - (-\mu_0 \cdot H) = B + \mu_0 \cdot H$. The value of H_{ci} is very close to the amount of H required to completely demagnetize the magnetic material as compared to H_c that causes the magnet's net effect to be zero. An infinite H_{ci} would mean that the magnet is truly 'permanent' and high H_{ci} not only allows the magnet to withstand a demagnetization field, but also provides less susceptibility to demagnetization at elevated temperatures or other adverse conditions.

Other parameters that are usually mentioned in the specification sheets of the permanent magnets are the H_k coercive force, the maximum energy product BH_{max} and the recoil permeability μ_{rec}. The H_k coercive force is the value of the H_{ci} at $0.9 \cdot B_r$. H_k values that approach the H_{ci} values are considered peculiar sign of an extremely good magnetic material. The recoil permeability $\mu_{rec} \cong \frac{B_r}{H_c}$ is the slope of the demagnetization curve and it is approximately equal to the slope of the major loop at $H = 0$ and at B_r. Hence, $BH_{max} = \frac{B_r^2}{(4\mu_{rec})}$ ant it represents the maximum product $B \times H$ on the demagnetization curve. The smaller the recoil permeability, the more square is the intrinsic curve, the bigger is the coercive force ($H_c \cong \frac{B_r}{\mu_{rec}}$) and, respectively, the harder it is to demagnetize the magnet. The

Magnetic Properties of SmCo S2869		
	Nom.	**Min.**
B_r (Gauss)	11000	10800
H_c (Oesterd)	10300	9000
H_k (Oesterd)	15000	12000
H_{ci} (Oesterd)	20000	19000
BH_{max} (MGOe)	28.0	27.0
Temperature Coefficient of B_r, T_{kBr} $(\%/^\circ C)$	-0.03	N/A
Recoil Permeability (μ_{rec})	1.05	N/A
T_c, Curie Temperature $(^\circ C)$	800	N/A
Maximum Operating Temperature $(^\circ C)$	350	N/A

Table J.1: Magnetic properties of SmCo permanent magnets of type S2869 [Magnetic Component Engineering Inc, 2009b].

magnetic and physical properties of the SmCo permanent magnets of type S2869, identical to that we used, are summarized in Tables J.1 and J.2.

Physical Properties of SmCo S2869	
Density (Ibs/in^3)	0.3
Coeff. of Linear Expan. $\perp$ to <M> ($10^{-7}/^\circ C$ approx.)	110
Coeff. of Linear Expan. $\parallel$ to <M> ($10^{-7}/^\circ C$ approx.)	90
Compressive Strength (psi $\times$ 10^3)	29
Young's Modulus (psi $\times$ 10^6)	29
Vicker's Hardness (HV)	600
Common Industry Name	SmCo28, Sam28
Electrical Resistivity ($\mu\Omega \cdot cm$)	90
Typical Appearance	Silver
Type	Sm2Co17

Table J.2: Physical properties of SmCo permanent magnets of type S2869.

K

Micro-motion compensation

K.1 RF-Photon correlation software

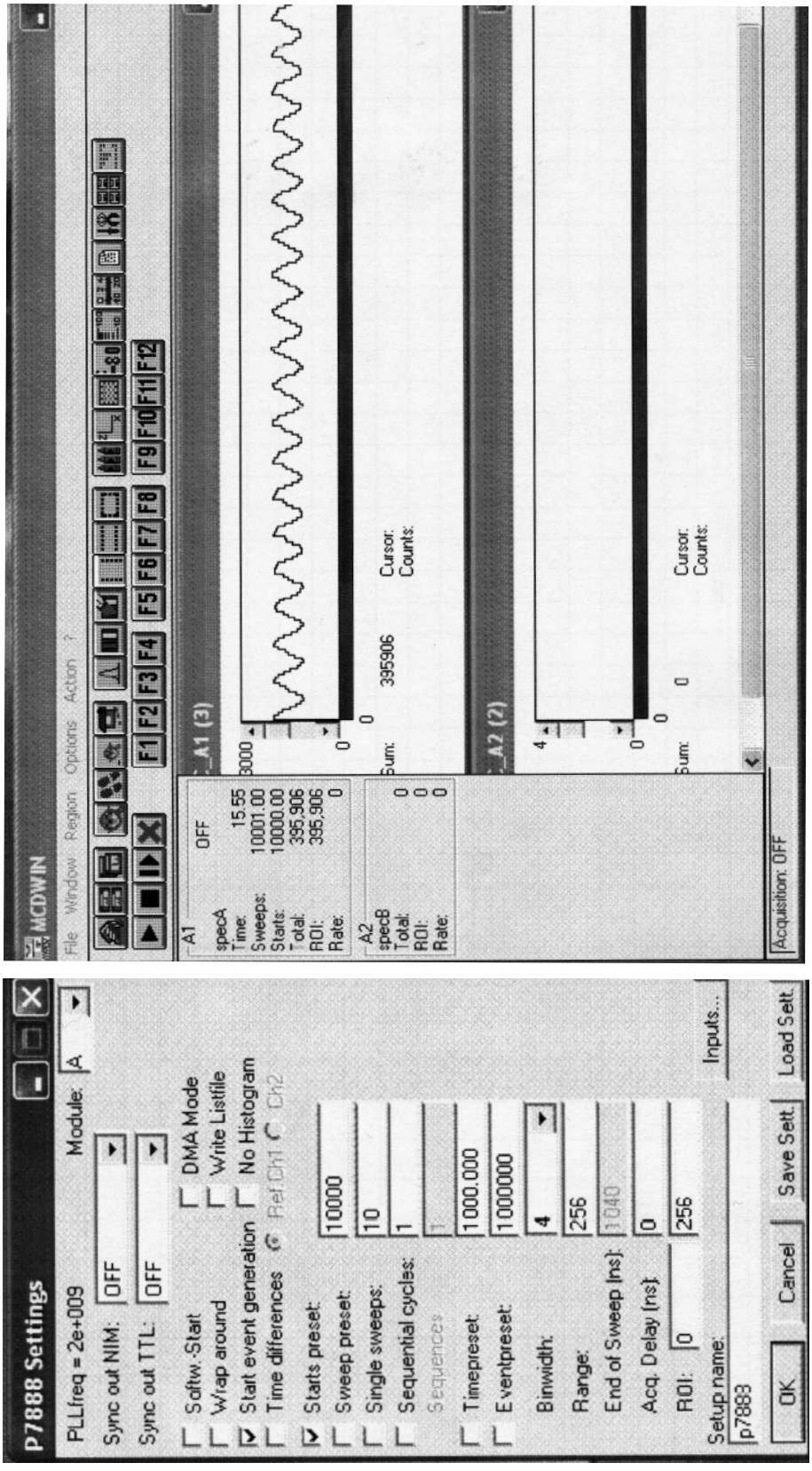

Figure K.1: Time-to-digital converter (TDC) software settings.

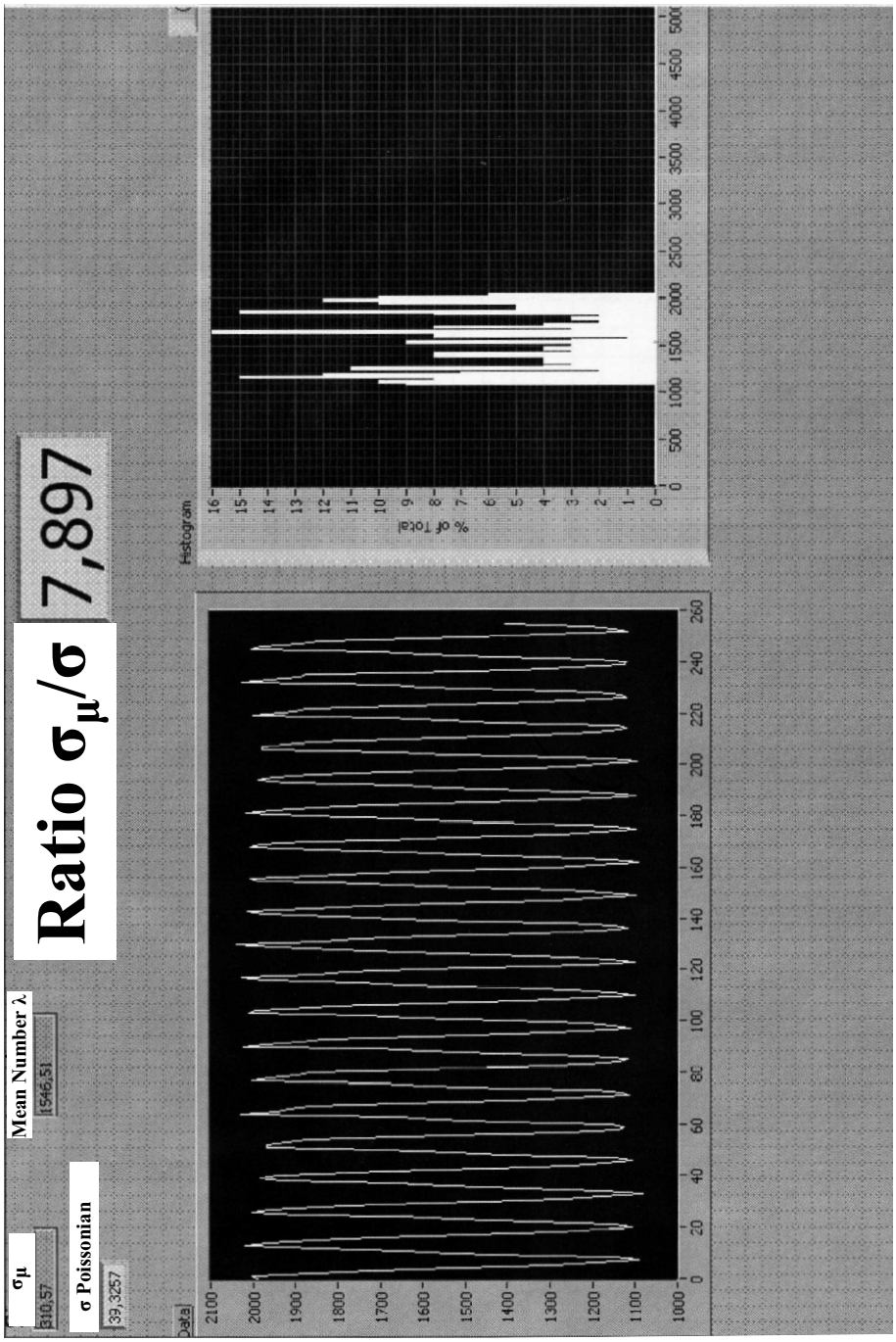

Figure K.2: Left: The number of photon counts versus the time delay. The range of 256 corresponds to $1\,\mu$s *and there are 20 periods of* 20 MHz *signal. Right: The data collected by TDC are plotted as histograms with the bins representing the photon counts. In case of negligible micro-motion this histogram is described by a purely Poissonian distribution where the standard deviation* $\sigma = \sqrt{\lambda}$*, with* λ *the mean number of occurrences. With increased micro-motion the distribution deviates from the Poissonian, the standard deviation increases and it will be notated as* σ_μ*. A good compensation is achieved when the ratio between these two standard deviations,* $\frac{\sigma_\mu}{\sigma}$*, is close to one.*

L

The matrix S_{nl}

The matrix element S_{nl} describes the scaled deviation of ion l from its equilibrium position when a vibrational mode n is excited. These values can be found in literature [James, 1998]. Here are given the S_{nl}, n - number of row and l - number of column, values for two ions:

S	1	2
1	0.7071	0.7071
2	-0.7071	0.7071

and for three ions:

S	1	2	3
1	0.5774	0.5774	0.5774
2	-0.7071	0	0.7071
3	0.4082	-0.8165	0.4082

M

The κ-parameter calculations

An effective Lamb-Dicke parameter created due to the magnetic field gradient equals (see equation 2.65):

$$\eta_{eff} \approx \kappa_{nl} = \frac{\Delta z \partial_z \omega_l}{\nu_n} S_{nl} = \frac{\Delta z_n g_F \mu_B b_l}{\hbar \nu_n} S_{nl}, \tag{M.1}$$

where $\Delta z_= \sqrt{\hbar / 2m\nu_n}$ is the extension of the ground state wave function of vibrational mode n, $\Delta z_n \partial_z \omega_l$ gives the internal frequency change that ion l undergoes when its position is shifted by Δz_n, ν_n is the frequency of the phonon of mode n and S_{nl} is the matrix element explained in appendix L, b_l is the magnetic field gradient at the position of ion l.

For N ions in a trap, there are N axial vibrational modes and additional $2N$ modes for motions transverse to the axis. For two ions there are two modes, ν_z and $\nu_2 = \sqrt{3}\nu_z$ (breathing mode); for three ions there are three modes: ν_z, $\nu_2 = \sqrt{3}\nu_z$ and $\nu_3 = \sqrt{5.8}\nu_z$, as it is possible to find in [James, 1998].

The calculations for the κ-parameter will be presented for two axial common mode (COM) frequencies: $\nu_1 \equiv \nu_z = 2\pi \cdot 127.1\,\mathrm{kHz}$ and $\nu_1 \equiv \nu_z = 2\pi \cdot 123.5\,\mathrm{kHz}$. For the rest of the trap frequencies the calculations can be done in a similar way.

The extension of the ground state wave-function for the COM mode ($n = 1$) and the axial trap frequency $\nu_1 = 2\pi \cdot 127.1\,\mathrm{kHz}$ is $\Delta z = 15.25\,\mathrm{nm}$, for the breathing mode ($n = 2$) is $\Delta z = 11.59\,\mathrm{nm}$ and for the $n = 3$ is $\Delta z = 9.83\,\mathrm{nm}$. The extension of the ground state wave-function for the COM mode ($n = 1$) and the axial trap frequency $\nu_1 = 2\pi \cdot 123.5\,\mathrm{kHz}$ is $\Delta z = 15.47\,\mathrm{nm}$, for the breathing mode ($n = 2$) is $\Delta z = 11.75\,\mathrm{nm}$ and for the $n = 3$ is $\Delta z = 9.97\,\mathrm{nm}$.

Two Ions

The magnetic field gradient for two ions was measured to be $b_1 = b_2 = 18.98(2)\,\mathrm{T/m}$. This discussion can be found in section 6.4. Using equation M.1, $\partial_z\omega_1 = \partial_z\omega_2 = 1.67 \cdot 10^{12}\,\mathrm{Hz/m}$. Hence, for the axial trap frequency $2\pi \cdot 127.1\,\mathrm{kHz}$, $\kappa_{11} = \kappa_{12} = 0.0225$, $\kappa_{21} = -0.0099$ and $\kappa_{22} = 0.0099$. The values for the S_{11}, S_{12}, S_{21} and S_{22} are given in appendix L.

For the axial trap frequency $2\pi \cdot 123.5\,\mathrm{kHz}$, $\kappa_{11} = \kappa_{12} = 0.0235$, $\kappa_{21} = -0.0103$ and $\kappa_{22} = 0.0103$. The theoretical values of the coupling constants for $2\pi \cdot 127.1\,\mathrm{kHz}$ and $2\pi \cdot 123.5\,\mathrm{kHz}$ trap axial frequency can be calculated using equation 2.64, $J_{i,j} = \sum_{n=1}^{N} \nu_n \kappa_{ni} \kappa_{nj}$. Hence,

$$J_{12}^{127.1}/2\pi = \nu_1\kappa_{11}\kappa_{12} + \nu_2\kappa_{21}\kappa_{22} = 42.8\,\mathrm{Hz}$$

$$J_{12}^{123.5}/2\pi = \nu_1\kappa_{11}\kappa_{12} + \nu_2\kappa_{21}\kappa_{22} = 45.5\,\mathrm{Hz}.$$

Three Ions

The magnetic field gradient at position of ion 1, ion 2 and ion 3 is $b_1 = 16.8\,\mathrm{T/m}$, $b_2 = 18.7\,\mathrm{T/m}$ and $b_3 = 18.9\,\mathrm{T/m}$, respectively. Therefore,

$$\begin{aligned} \partial_z\omega_1 &= 1.477 \cdot 10^{12}\,\mathrm{Hz/m} \\ \partial_z\omega_2 &= 1.645 \cdot 10^{12}\,\mathrm{Hz/m} \\ \partial_z\omega_3 &= 1.662 \cdot 10^{12}\,\mathrm{Hz/m}. \end{aligned}$$

The κ-parameters values for three ions and the axial trap frequency of the COM

κ	1	2	3
1	0.0170	0.0189	0.0191
2	-0.0091	0.0000	0.0102
3	0.0032	-0.0072	0.0036

Table M.1: κ-parameters calculated for three ions and the axial trap frequency of $2\pi \cdot 123.5\,\mathrm{kHz}$.

mode ($n = 1$) of $2\pi \cdot 123.5\,\mathrm{kHz}$ are summarized in Table M.1. The coupling constants J_{ij} are, therefore,

$$\begin{aligned} J_{12}/2\pi &= \nu_1\kappa_{11}\kappa_{12} + \nu_2\kappa_{21}\kappa_{22} + \nu_3\kappa_{31}\kappa_{32} &&= 32.9\,\mathrm{Hz} \\ J_{23}/2\pi &= \nu_1\kappa_{12}\kappa_{13} + \nu_2\kappa_{22}\kappa_{23} + \nu_3\kappa_{32}\kappa_{33} &&= 37.0\,\mathrm{Hz} \\ J_{13}/2\pi &= \nu_1\kappa_{11}\kappa_{13} + \nu_2\kappa_{21}\kappa_{23} + \nu_3\kappa_{31}\kappa_{33} &&= 23.9\,\mathrm{Hz}. \end{aligned}$$

N

Rabi Frequencies

The total angular momentum is given by

$$\vec{F} = \vec{I} + \vec{J}, \tag{N.1}$$

where $\vec{I}$ is the nuclear spin and $\vec{J}$ is the total electronic angular momentum, $\vec{J} = \vec{L} + \vec{S}$ with angular momentum $\vec{L}$ and spin $\vec{S}$.

For $^{171}Yb^{+}$, the nuclear spin is $I = 1/2$ and for the hyperfine splitting of the ground state $^{2}\mathrm{S}_{1/2}$ [1] $J = 1/2$, $S = 1/2$ and $L = 0$.

The Rabi frequency is defined as

$$\Omega = \frac{\vec{\mu} \cdot \vec{B}_{mw}}{\hbar}. \tag{N.2}$$

[1] $^{2S+1}L_J$

The magnetic dipole momentum $\vec{\mu}$ can be rewritten as

$$\vec{\mu} = \frac{2\mu_B}{\hbar}\vec{J}, \tag{N.3}$$

where μ_B is the Bohr magneton. The magnetic dipole momentum for the $|\downarrow\rangle \longrightarrow |\uparrow\rangle$ hyperfine split transition of the ion, $\vec{\mu}_{\downarrow\uparrow}$, excited by the microwave magnetic field $\vec{B}_{mw}$ can be written in general form as

$$\vec{\mu}_{\downarrow\uparrow} = \langle\uparrow|\vec{\mu}|\downarrow\rangle \tag{N.4}$$

The eigenvectors of J^2 and J_z are

$$\begin{aligned} J^2\,|j,m\rangle &= \hbar^2 j(j+1)\,|j,m\rangle & \text{(N.5)}\\ J_z\,|j,m\rangle &= \hbar m\,|j,m\rangle\,. & \text{(N.6)} \end{aligned}$$

The spin raising and lowering operators acting on these eigenvectors give:

$$J_\pm|j,m\rangle = \hbar\sqrt{j(j+1)-m(m\pm1)}|j,m\pm1\rangle, \tag{N.7}$$

where

$$J_\pm = J_x \pm iJ_y. \tag{N.8}$$

The microwave magnetic field can be written as

$$\begin{aligned} \vec{B}_{mw} \equiv \vec{B}_{mw}(\vec{r},t) &= \vec{B}(r)\cos(\omega_{mw}t) = & \text{(N.9)}\\ &= \frac{1}{2}\left[\vec{B}(r)e^{-i(\omega_{mw}t)} + \vec{B}(r)^* e^{i(\omega_{mw}t)}\right], \end{aligned}$$

or, using the complex phasor as in [Böhi *et al.*, 2010],

$$B_{mw} \equiv \begin{pmatrix} B_x e^{-i\phi_x} \\ B_y e^{-i\phi_y} \\ B_z e^{-i\phi_z} \end{pmatrix}. \tag{N.10}$$

The quantization axis is pointing along the z-axis. The microwave magnetic field couples to the magnetic momentum of the electron spin of the ion. The Rabi frequency on the $^{171}Yb^{+}$ hyperfine transition $|F=0,m_F=0\rangle \leftrightarrow |F'=1,m'_F\rangle$, where $m'_F=-1,0,1$ is

$$\Omega_{0,0}^{1,m'_F} = \frac{2\mu_B}{\hbar}\langle 1,m'_F|J\cdot B_{mw}|0,0\rangle \tag{N.11}$$

with $J=(J_x,J_y,J_z)$. Using equation N.8, the scalar product $J\cdot B_{mw}$ can be written as

$$\begin{aligned} J\cdot B_{mw} &= B_x e^{-i\phi_x}J_x + B_y e^{-i\phi_y}J_y + B_z e^{-i\phi_z}J_z \qquad \text{(N.12)}\\ &= \frac{1}{2}(B_x e^{-i\phi_x} - iB_y e^{-i\phi_y})J_+ + \frac{1}{2}(B_x e^{-i\phi_x} + iB_y e^{-i\phi_y})J_- + B_z e^{-i\phi_z}J_z, \end{aligned}$$

according to [Böhi *et al.*, 2010]. The Rabi frequencies are:

$$\Omega_- \equiv \Omega_{0,0}^{1,-1} = \frac{2\mu_B}{\hbar}\langle 1,-1|\frac{1}{2}(B_x e^{-i\phi_x} + iB_y e^{-i\phi_y})J_-|0,0\rangle \tag{N.13}$$

$$\Omega_\pi \equiv \Omega_{0,0}^{1,0} = \frac{2\mu_B}{\hbar}\langle 1,0|B_z e^{-i\phi_z}J_z|0,0\rangle \tag{N.14}$$

$$\Omega_+ \equiv = \Omega_{0,0}^{1,1} = \frac{2\mu_B}{\hbar}\langle 1,1|\frac{1}{2}(B_x e^{-i\phi_x} - iB_y e^{-i\phi_y})J_+|0,0\rangle \tag{N.15}$$

In order to make use of equation N.7, the eigenstates of the ion $|JIFm_F\rangle$ should be rewritten as a superposition of the uncoupled states $|JIm_Jm_I\rangle$ as

$$|JIFm_F\rangle = \sum_{m_J,m_I} C(J,I,m_J,m_I;F,m_F)\,|JIm_Jm_I\rangle\,, \tag{N.16}$$

where coefficients C are known as the Clebsch-Gordon coefficients and they are defined as [Cowan, 1981]

$$C(J,I,m_J,m_I;F,m_F) = (-1)^{J-I+m_F}\sqrt{2F+1}\begin{pmatrix} J & I & F \\ m_J & m_I & -m_F \end{pmatrix}, \tag{N.17}$$

where the matrix term denotes a Wigner 3-j symbol. Since, $m_F = m_J + m_I$, the double sum in equation N.16 can be replaced by a single sum over m_J. Hence,

$$|JIFm_F\rangle = \sum_{m_J=-J}^{m_J=+J} (-1)^{J-I+m_F} \sqrt{2F+1} \begin{pmatrix} J & I & F \\ m_J & m_I & -m_F \end{pmatrix} |JIm_J(m_F - m_J)\rangle \,. \tag{N.18}$$

For simplicity J and I in equation N.18 are omitted in the following discussions. For $J = 1/2$ there are two possible values of m_J: -1/2 and 1/2. For $I = 1/2$ there are two possible values of m_I: -1/2 and 1/2. Hence, there are four possible uncoupled angular momentum basis states $|m_J m_I\rangle$. Therefore,

$$|F=0, m_F=0\rangle = -\sqrt{\frac{1}{2}} \left|-\frac{1}{2}, \frac{1}{2}\right\rangle + \sqrt{\frac{1}{2}} \left|\frac{1}{2}, -\frac{1}{2}\right\rangle \tag{N.19}$$

$$|F=1, m_F=-1\rangle = \left|-\frac{1}{2}, -\frac{1}{2}\right\rangle \tag{N.20}$$

$$|F=1, m_F=0\rangle = \sqrt{\frac{1}{2}} \left|-\frac{1}{2}, \frac{1}{2}\right\rangle + \sqrt{\frac{1}{2}} \left|\frac{1}{2}, -\frac{1}{2}\right\rangle \tag{N.21}$$

$$|F=1, m_F=1\rangle = \left|\frac{1}{2}, \frac{1}{2}\right\rangle . \tag{N.22}$$

The recurrence equation N.7 in the basis $|JIm_J m_I\rangle$ is:

$$J_\pm \,|JIm_J m_I\rangle = \hbar\sqrt{J(J+1) - m_J(m_J \pm 1)}\,|JI(m_J \pm 1)m_I\rangle \,. \tag{N.23}$$

Hence, combining relations in equation N.19 - N.23,

$$J_- \,|F=0, m_F=0\rangle = \sqrt{\frac{1}{2}}\hbar \left|-\frac{1}{2}, -\frac{1}{2}\right\rangle \tag{N.24}$$

$$J_+ \,|F=0, m_F=0\rangle = -\sqrt{\frac{1}{2}}\hbar \left|\frac{1}{2}, \frac{1}{2}\right\rangle \tag{N.25}$$

$$J_z \,|F=0, m_F=0\rangle = \frac{1}{2}\sqrt{\frac{1}{2}}\hbar \left|-\frac{1}{2}, \frac{1}{2}\right\rangle + \frac{1}{2}\sqrt{\frac{1}{2}}\hbar \left|\frac{1}{2}, -\frac{1}{2}\right\rangle \tag{N.26}$$

Taking into account that

$$\delta_{ij} = \begin{Bmatrix} 1, & \text{if } i = j \\ 0, & \text{if } i \neq j \end{Bmatrix}, \tag{N.27}$$

$$\langle 1, -1|J_-|0, 0\rangle = \sqrt{\frac{1}{2}}\hbar \tag{N.28}$$

$$\langle 1, 0|J_z|0, 0\rangle = \frac{\hbar}{2} \tag{N.29}$$

$$\langle 1, 1|J_+|0, 0\rangle = -\sqrt{\frac{1}{2}}\hbar. \tag{N.30}$$

$$\Omega_- = -\sqrt{2}\frac{\mu_B}{\hbar}B_- e^{-i\phi_-} \tag{N.31}$$

$$\Omega_\pi = \frac{\mu_B}{\hbar}B_\pi e^{-i\phi_\pi} \tag{N.32}$$

$$\Omega_+ = \sqrt{2}\frac{\mu_B}{\hbar}B_+ e^{-i\phi_+}, \tag{N.33}$$

where

$$B_- e^{-i\phi_-} = \frac{1}{2}(B_x e^{-i\phi_x} + iB_y e^{-i\phi_y}) \tag{N.34}$$

$$B_\pi e^{-i\phi_\pi} = B_z e^{-i\phi_z} \tag{N.35}$$

$$B_+ e^{-i\phi_+} = \frac{1}{2}(B_x e^{-i\phi_x} - iB_y e^{-i\phi_y}), \tag{N.36}$$

where B_π, B_- and B_+ are the real-valued amplitudes of the magnetic field components parallel to the static magnetic field, that defines the quantization axis, and perpendicular, respectively. ϕ_π, ϕ_- and ϕ_+ are the correspondent phases of these components.

The Ω_-, Ω_π and Ω_+ are measured in the experiment: $\Omega_- = 77.1 \pm 0.3\,\text{kHz}$, $\Omega_+ = 52.0 \pm 0.4\,\text{kHz}$ and $\Omega_\pi = 65.5 \pm 0.3\,\text{kHz}$. The microwave magnetic field components in x-, y- and z-directions can be, therefore evaluated using equations (N.32 — N.33) and (N.35 — N.36):

$$B_x = B_+ + B_- \tag{N.37}$$
$$B_y = i(B_+ - B_-), \tag{N.38}$$

where the phases were omitted for clarity.

O

CCD Camera Labview Interface

It was not trivial to control the commercial ICCD camera from Roper Scientific Inc. using Labview, since the necessary drivers were not initially available and later they were not free. Theoretically, Labview can automatically create a set of VIs from a DLL using the Import Shared Library Wizard, where each VI will contain a Call Library Function Node (CLFN) corresponding to one function in the DLL and with the relevant inputs and outputs. However, this automatical import is not without problems since Labview not always interprets the type of data correctly. There is a vast amount of possibilities on how to use the PVCAM DLL library without the Labview Wizard. Some of them require professional programming skills. We found convenient to create a wrapped DLL using Visual C++ (VC) 2008 Express Edition that is a free software. In this way it is possible to use the functions of the existing PVCAM library and directly convert the C code types of data of this library into the Labview types of data. Then it is quite straightforward to integrate the created new functions of a new library into Labview with the help of the CLFN. Some nice tutorials about how to build DLL using Visual C++ can be found on the National Instruments site, for example here [National Instuments Inc., 2008]. VC creates a DLL project with one *source* file (.cpp) with the same name as the project. It also generates automatically a stdafx.cpp file that together with the header file stdsfx.h build a pre-compiled header (PCH) file named project_name.pch and a pre-compiled types file named stdafx.obj. The

source file for our DLL is given and explained below (O.1). It contains a DLLMain function, as it must, and the declarations and definitions of different functions to be exported. To access these functions within the DLL, one needs to use extern "C" _declspec (dllexport) tag with any function declaration and _declspec (dllexport) with any function definition to be exported, as it is demonstrated in the source file given below. In this code one also finds functions as DSSetHandleSize and MoveBlock. They are Labview manager functions. To use them one must include extcode.h in the DLL and link the project to the labview.lib (for Visual C++) that is situated in the *cintools* directory of the Labview. DSSetHandleSize resizes the block of memory referenced by the specified handle. For example in the part of our C code:

```
if (!pl_pvcam_init()){
    pl_error_message(pl_error_code(),msg);
    templength = strlen(msg);
    err = DSSetHandleSize(output, sizeof(char) * templength + 4);
    if(err != noErr)
    {
    return -1; /* Memory issue */
    }
    (*output)->cnt = templength; /* cnt - number of bytes that follow */
    MoveBlock((&msg),(*output)->str, (*output)->cnt); /* str - array [0..Maxcnt]↩
        of Char */
}
```

If the camera library is not initialized, the error is received and the message (*msg*) that explains the error is provided. Here pl_pvcam_init(), pl_error_message() and pl_error_code() are the PVCAM library functions. The error message has a C string type but we want it to be visualized in Labview, where the string has first four additional bytes that indicate the length of the string. Therefore, we use DSSetHandleSize to resize handle to the *output*, the variable we will read by Labview and that satisfies the Labview requirements. The output of this operation, *err*, has MgErr data type that is a Labview data type corresponding to a set of error codes the Labview manager routines returns. If there are errors, the C program returns -1 and the program stops. Otherwise, the program returns 0 and another LabVIEW Manager Function MoveBlock finally copies the string data from the C string *msg* into the LStrHandle (Labview string handle) variable *output*, where *str* and *cnt* are the structure members of LStrHandle:

```
typedef struct { int32 cnt;
/* number of bytes that follow */
 uChar str[1];
 /* cnt bytes */ }
LStr, *LStrPtr,**LStrHandle;
```

Hence, *cnt* defines the length of the string and *str* is the array that contains the specified characters order.

Few short explanations of the PVCAM library functions, that are necessary to control the CCD camera, are given in the source code itself (see O.1). For more details please consult the Roper Scientific manual [Roper Scientific Inc., April 2003].

Considering the Labview software written to control the camera in the current experiment 6 functions were created:

1. initCam(), for camera library and hardware initialization.

2. getTemperature(), to get the temperature of the camera.

3. setTemperature(), to set the camera temperature. In our experiments a fixed temperature of $-30°$C has been used.

4. setParam(), to set the gain of the camera and the shutter mode. We usually use a gain of 2 (medium) and shutter mode 2 (OPEN_PRE_SEQUENCE), where the shutter is opened before the first exposure of the sequence and it is closed after the sequence is finished.

5. AcquireStandard(), the function responsible for the CCD camera image acquisition. We set from Labview the exposure time, exposure mode, region of interest (ROI) coordinates and the preferred binning. The default ROI is the full frame of the camera chip equal to [0, 512; 0, 512] pixels. During our measurements we use binning 1 (no binning). The time mode was set to 1, STROBED_MODE, in which the camera waits for an external trigger to begin each exposure in the acquisition sequence. The results of each exposure are copied from the buffer into the Labview ARRAY[]. After each exposure in the sequence and when readout is finished the CCD charges are cleared and the buffer containing the data is emptied.

6. closeCam(), frees the used camera and prepares it for power-down, closes the PVCAM library.

These functions are called by the Labview Call Library Function Node (CLFN) of Labview, placed in the *block diagram*. An example of the AcquireStandard() function called by Labview is shown in Figure O.1. In the Function panel of the CLFN the path of the new wrapped DLL library is given. One can find than the name of the desired function under the Function name drop-down menu (Figure O.1, a). The types of the parameters are set in the menu Parameter of the CLFN (Figure O.1, b) in correspondence with the data types used in the source code.

A data type is chosen from the drop-down menu with the same name. Then the appropriate controls and indicators are connected. Attention should be paid in case of AcquireStandard() function since here the memory for the output ARRAY[] must be pre-allocated. In case of 1d array, as in our case, the input array with the size equal to $n \times m$ is required, where n and m are sizes of the ROI region in horizontal and vertical directions.

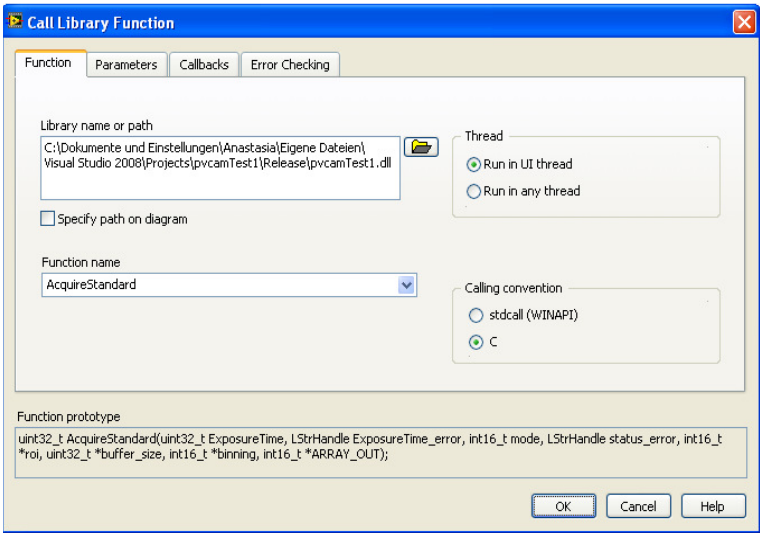

(a)

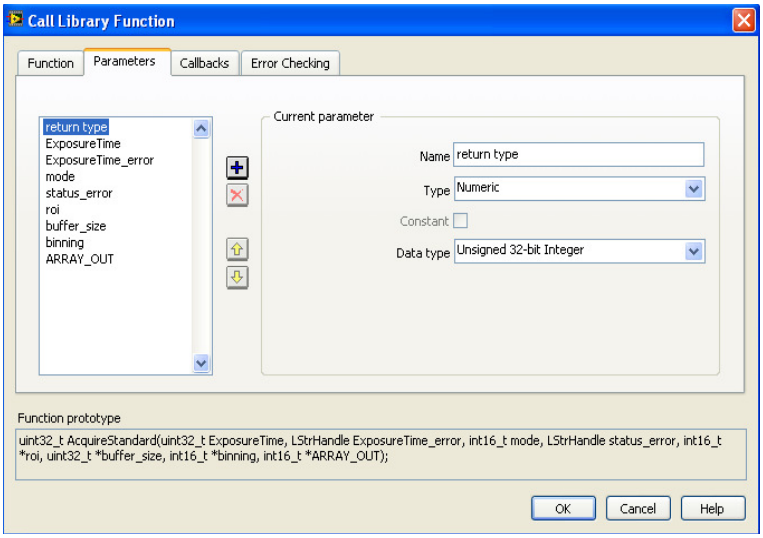

(b)

Figure O.1: Call Library Function Node (a) Function Tab; (b) Parameters Tab

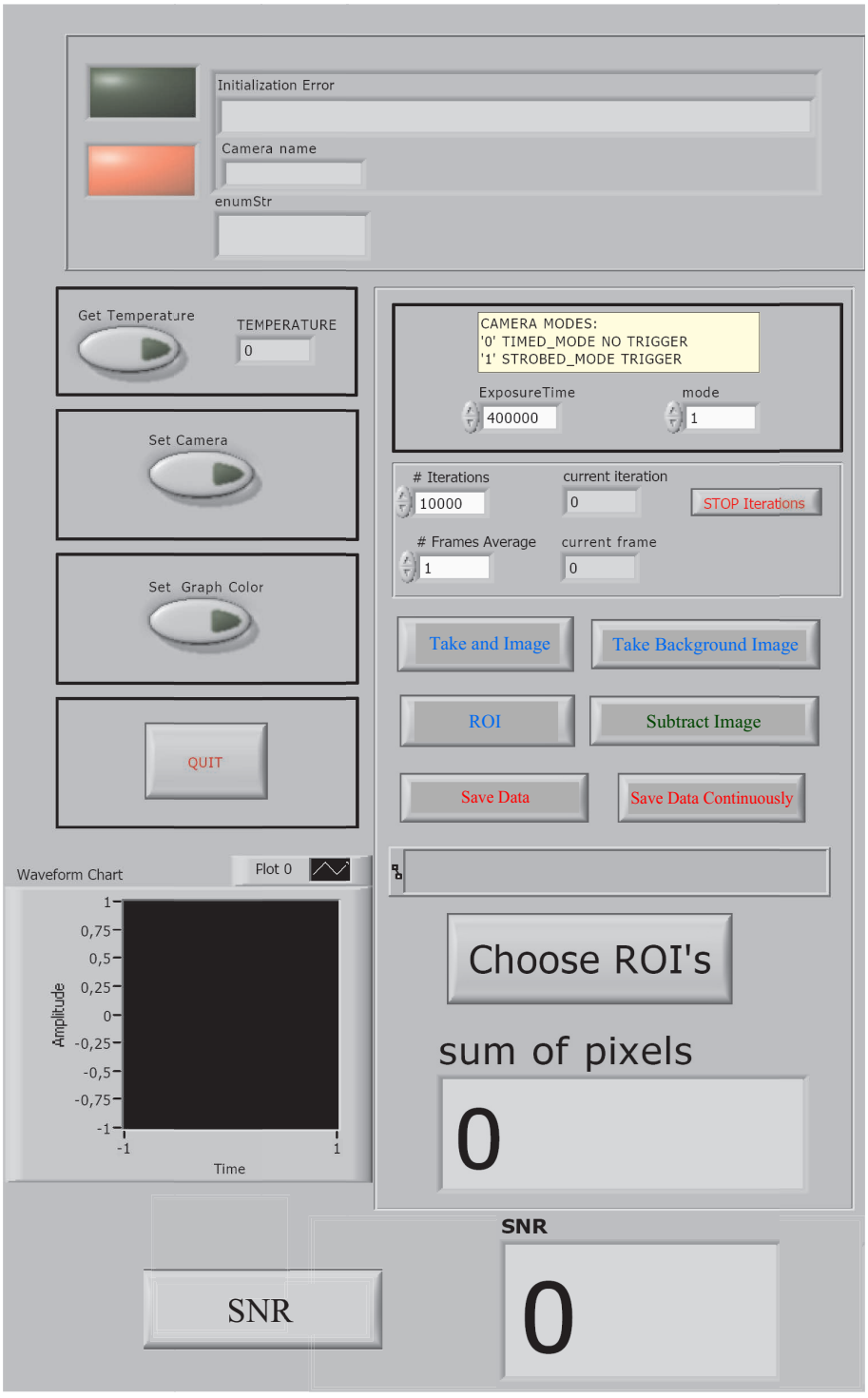

Figure O.2: Front panel of the CCD camera main program Labview interface

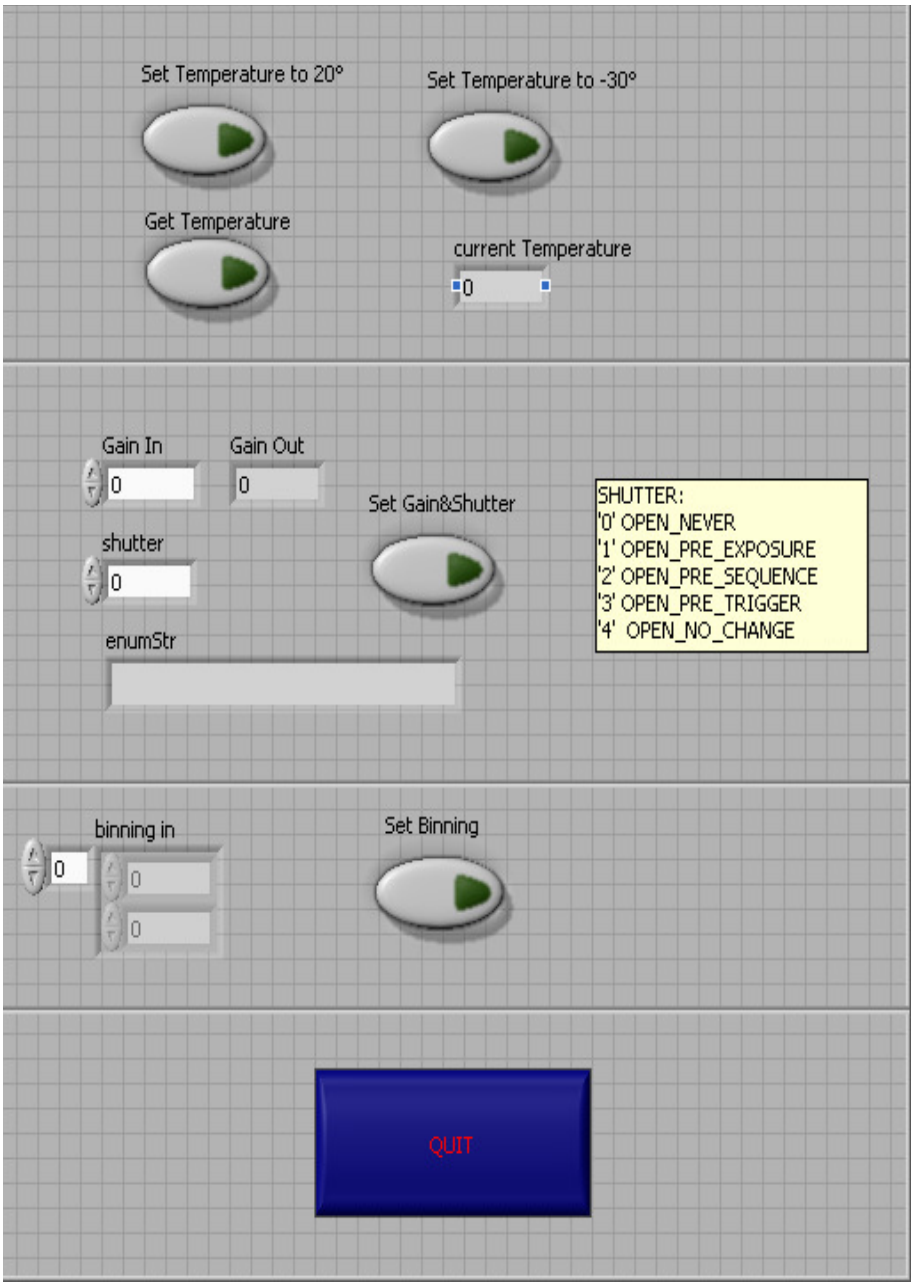

Figure O.3: Front panel of the CCD camera subprogram that sets the parameters of the camera before the acquisition.

A part of the graphical CCD camera Labview interface is shown in Figure O.2. In case the camera is found and the initialization of both the camera library and hardware is successful, the GREEN button is ON. Otherwise, the RED button is activated and the program stops running. If there is no errors in the initialization, one can check the current CCD camera temperature pressing on the *Get Temperature* button. The small window on the right will show the result. Prior starting to take images with the camera, several setting should be performed. Pressing on the button *Set Camera*, an additional window will appear (see Figure O.3). Here, one sets the temperature to $-30°$C, camera gain, shutter mode and binning, if necessary. After the settings are done it is needed to press *QUIT* in order to come back to the main program. One needs to set also the exposure time, acquisition mode and number of frames to take (*# iterations*). *# Frames Average* defines how many images (frames) are averaged for final image visualization. *Take an Image* starts an acquisition. If you want to stop it before the defined number of iterations are performed — press the *STOP* iterations button. The camera will perform the last exposure and will stop taking images. *Set Graph color* button allows the user to set its own color table, otherwise the *Intensity Graph* uses the default color map. *SAVE Data* saves the last frame into the ascii file and *SAVE Data Continuously*, as the name suggests, continues saving the images into different files, that are automatically progressively numerated, until the button remains pressed. If a background image is needed, the laser beams are blocked and after that the *Take Background Image* button is pressed. Later, if the *Subtract Background* button is pressed before the *Take an Image* button, the background image is subtracted from each frame image that follows. It is more convenient to use smaller frames for this operation since with a full frame the procedure is quite slow. The full frame images are usually used when the CCD camera alignment is performed and the position of the ions is not known. Later, one can choose a specific region of interest (ROI) that contains the ions. In this way the acquisition times are significantly reduced accordingly. To chose the ROI one needs to make just one full frame acquisition, then press *Choose ROI's* button. This button opens another subprogram (subvi), where one can choose three ROIs: one region is around the ions, and two regions are taken somewhere in the background. The last two regions are only needed if one wants to estimate the Signal-to-Noise ratio (SNR) that is convenient for improving the contrast of the ions image. Signal in this case is a mean pixel value in the region of ions divided by the noise that was calculated as a mean pixel value in the two background images. If one wants to use the small ROI containing the ions, the button ROI has to be pressed before the *Take an Image* button is pressed. *Sum of pixels* gives the average pixel value in the chosen region of frame and the *Wavefront* to the left indicates how these values change with each new frame.

Listing O.1: Source code for DLL creation

```
================================================================================
       DYNAMIC LINK LIBRARY : pvcamTest1.dll
...\Visual Studio 2008\Projects\pvcamTest1\Release
================================================================================

#include "extcode.h"      /* Labview header file */
#include "platdefines.h"  /* Labview header file */
#include "fundtypes.h"    /* Labview header file */
#include "stdafx.h"
#include <stdio.h>
#include <stdlib.h>
#include <windows.h>
#include <iostream>
#include <fstream>
#include <string.h>
#include <ctype.h>
#include <malloc.h>

#include "master.h"   /* PVCAM library header file */
#include "pvcam.h"    /* PVCAM library header file */

int16 hCam;     /* camera handle */
uns32 size;     /* size of one frame in bytes */
uns16 *frame;     /* pointer to the image */
int16 status;
uns32 not_needed;
uns32 index;/* enum value returned for index & param_id*/
int32 enumValue;
char enumStr[100];
int16 Temperature;
int16 TemperatureSet;
int16 Gain;
uns32 ExposureTime;
char msg[ERROR_MSG_LEN];
char cam_name[CAM_NAME_LEN];    /* camera name */
uns16 TimeRes=1; /* Time resolution: 1 equivalent to micros, 0 to ms */
int templength = 0;
int templength2 = 0;
MgErr err;
MgErr err2;

/* To access the functions within the DLL it is necessary to tell the compiler ↩
    to export the desired symbols.
   To do so one needs to use extern "C" _declspec(dllexport) tag with any ↩
       function declaration and _declspec(dllexport)
   with any function definition to be exported. */

/* Function declarations */

extern "C" _declspec(dllexport) int initCam(LStrHandle output, LStrHandle ↩
    output2);
extern "C" _declspec(dllexport) int getTemperature();
extern "C" _declspec(dllexport) int setTemperature(int16_t TemperatureSet);
extern "C" _declspec(dllexport) int setParam(int16_t Gain, char enumStr[100],↩
    LStrHandle Gain_err_message, uns32 shutter);
extern "C" _declspec(dllexport) int AcquireStandard(uns32 ExposureTime,↩
    LStrHandle ExposureTime_error,int16_t exp_mode, LStrHandle status_error, ↩
    int16 roi[],uns32 *buffer_size, int16 bin[],int16 ARRAY[]);
extern "C" _declspec(dllexport) int finishAcquireStandard();
extern "C" _declspec(dllexport) int closeCam();
```

```
/* DllMain fuction, which is the entry point for the library.  */

BOOL APIENTRY DllMain( HANDLE hModule,
                       DWORD  ul_reason_for_call,
                       LPVOID lpReserved
                     )
{
    return TRUE;
}


/* Function definitions */

/* 1. The function initCam initiates camera library and camera hardware. */

_declspec(dllexport) int initCam(LStrHandle output,LStrHandle output2)
/* LStrHandle - Labview string handle*/
{

frame=NULL;
size=0;

if (!pl_pvcam_init()){   /* Opens and initializes the camera library*/

    pl_error_message(pl_error_code(),msg);
    /* pl_error_message() - returns a string explaining input error code */
    /* pl_error_code() - returns the most recent error condition */
    templength = strlen(msg);
    err = DSSetHandleSize(output, sizeof(char) * templength + 4);
    if(err != noErr)
    {
    return -1; /* Memory issue */
    }
    (*output)->cnt = templength;

/*  MoveBlock (LabVIEW Manager Function): Moves size bytes from one address to ↩
    another. The source and destination memory blocks can overlap.
    MoveBlock (pointer to source, pointer to destination, # bytes you want to ↩
        move)
    MoveBlock function copies the string data from the C++ string into the ↩
        LStrHandle variable. */
    MoveBlock((&msg),(*output)->str, (*output)->cnt);
    }

pl_cam_get_name(0, cam_name); /* Returns the name of the camera*/
    templength2 = strlen(cam_name);
    err2 = DSSetHandleSize(output2, sizeof(char) * templength2 + 4);
    if(err2 != noErr)
    {
    return -1; /* Memory issue */
    }
    (*output2)->cnt = templength2;
    MoveBlock((&cam_name),(*output2)->str, (*output2)->cnt);

if (!pl_cam_open(cam_name, &hCam, OPEN_EXCLUSIVE)){ /* Reserves and initializes ↩
    the camera hardware */
    pl_error_message(pl_error_code(),msg);
    templength = strlen(msg);
    err = DSSetHandleSize(output, sizeof(char) * templength + 4);
```

```
    if(err != noErr)
    {
    return -1; /* Memory issue */
    }
    (*output)->cnt = templength;
    MoveBlock((&msg),(*output)->str, (*output)->cnt);/* cnt - number of bytes ↩
        that follow*//* str - cnt bytes */
    return 0;
    }

if (!pl_cam_check(hCam)){ /* Fails if hcam is not the handle of an open camera ↩
    */
    pl_error_message(pl_error_code(),msg);
    templength = strlen(msg);
    err = DSSetHandleSize(output, sizeof(char) * templength + 4);
    if(err != noErr)
    {
    return -1; /* Memory issue */
    }
    (*output)->cnt = templength;
    MoveBlock((&msg),(*output)->str, (*output)->cnt);/* cnt - number of bytes ↩
        that follow*//* str - cnt bytes */
    }

return 1;
}


/* 2. The function getTemperature returns the current measured temperature of ↩
    the CCD in °C */

_declspec(dllexport) int getTemperature()
{
pl_get_param(hCam,PARAM_TEMP, ATTR_CURRENT, &Temperature); /* Returns the ↩
    requested attribute for a PVCAM parameter*/
return Temperature/100;
}


/* 3. The function setTemperature sets the temperature of the CCD camera */

 _declspec(dllexport) int setTemperature(int16_t TemperatureSet)
{
pl_set_param(hCam, PARAM_TEMP_SETPOINT,&TemperatureSet); /* sets the current ↩
    value for a PVCAM parameter*/
pl_get_param(hCam,PARAM_TEMP, ATTR_CURRENT, &Temperature);

return Temperature/100;
}


/* 4. The function setParam sets camera Gain and Shutter Mode (see the beginning↩
     of the code)*/

_declspec(dllexport) int setParam(int16_t Gain, char enumStr[100], LStrHandle ↩
    Gain_err_message, uns32 shutter)
{
if ((Gain != 1) && (Gain !=2) && (Gain !=3)){
    char err_message[54]="Gain should be 1 for LOW, 2 for Medium and 3 for HIGH"↩
        ;
    int length = 0;
    MgErr err;
```

```
    length = strlen(err_message);
    err = DSSetHandleSize(Gain_err_message, sizeof(char) * length + 4);
      if(err != noErr)
          {
         return -1; /* Memory issue */
            }
    (*Gain_err_message)->cnt = length;
    MoveBlock((&err_message),(*Gain_err_message)->str, (*Gain_err_message)->cnt)↩
        ;
    return 0;
      }

pl_set_param(hCam, PARAM_GAIN_INDEX, &Gain);

if (pl_set_param(hCam, PARAM_EXP_RES_INDEX,&TimeRes)){
    pl_get_param(hCam, PARAM_EXP_RES, ATTR_CURRENT,&index);
    pl_get_enum_param(hCam, PARAM_SHTR_OPEN_MODE, index, &enumValue, enumStr, ↩
        100); */ Returns the enumerated values of the parameter. */
      };

/* SHUTTER modes:
'0' OPEN_NEVER
'1' OPEN_PRE_EXPOSURE
'2' OPEN_PRE_SEQUENCE
'3' OPEN_PRE_TRIGGER
'4' OPEN_NO_CHANGE */

if(pl_set_param(hCam, PARAM_SHTR_OPEN_MODE, &shutter)){
    pl_get_param(hCam, PARAM_SHTR_OPEN_MODE, ATTR_CURRENT, &index);
    pl_get_enum_param(hCam, PARAM_SHTR_OPEN_MODE, index, &enumValue, enumStr, ↩
        100);
      };

return 1;
}


/* 5. The function AcquireStandard starts the standard acquisition mode of the ↩
    camera. */

_declspec(dllexport)int AcquireStandard(uns32 ExposureTime, LStrHandle ↩
    ExposureTime_error, int16_t exp_mode, LStrHandle status_error, int16 roi[],↩
    uns32 *buffer_size, int16 bin[], int16 ARRAY[] )
{

/* Init a sequence set the region, exposure mode and exposure time*/

if (!pl_exp_init_seq()){ /* Initialize the sequence: prepares the portion of ↩
    library assiciated with the exposure control */
      return 0;
    };


if ((ExposureTime<1) || (ExposureTime>10000000)){
    char err_message[65]="Exposure Time should be in the (1..10000000) range (in↩
         microsec)";
    int length = 0;
    MgErr err;
    length = strlen(err_message);
    err = DSSetHandleSize(ExposureTime_error, sizeof(char) * length + 4);
    if(err != noErr)
```

```
    {
    return 0; /* Memory issue */
    }
    (*ExposureTime_error)->cnt = length;
    MoveBlock((&err_message),(*ExposureTime_error)->str, (*ExposureTime_error)->↩
        cnt);
    return 0;
    }

/* Define region of interest for the CCD image*/

//bin[0]->sbin, bin[1]->pbin
rgn_type region ={roi[0], roi[1]-1, bin[0], roi[2], roi[3]-1, bin[1]};
//rgn_type region ={roi[0], roi[1]-1, 1, roi[2], roi[3]-1, 1};

/* CAMERA MODES:
'0' TIMED_MODE (no trigger): begins a single exposure or the first exposure of a↩
     sequence.
'1' STROBED_MODE (trigger): waits for a trigger to begin each exposure in a ↩
    sequence */

pl_exp_setup_seq(hCam, 1, 1, &region, exp_mode, ExposureTime, &size); /* ↩
    Prepares the camera to perform a readout. */

*buffer_size=size;

frame=(uns16*)malloc(size); /* malloc function allocates space for an object of ↩
    specified size.*/


/* Start the acquisition*/

pl_exp_start_seq(hCam, frame); /* Begins exposing, returns immediately */

/* Wait for data or error*/
/* Checks the status of the current exposure*/

while (pl_exp_check_status(hCam, &status, &not_needed) && (status != ↩
    READOUT_COMPLETE && status != READOUT_FAILED) );

    /* Check Error Codes */

    if (status == READOUT_FAILED){
    pl_error_message(pl_error_code(),msg);
    int length = 0;
    MgErr err;
    length = strlen(msg);
    err = DSSetHandleSize(status_error, sizeof(char) * length + 4);
    if(err != noErr)
    {
    return 0; /* Memory issue */
    }
    (*status_error)->cnt = length;
    MoveBlock((&msg),(*status_error)->str, (*status_error)->cnt);
    }

    char msg2[12]="Image Taken";
    int length = 0;
    MgErr err;
    length = strlen(msg2);
    err = DSSetHandleSize(status_error, sizeof(char) * length + 4);
    if(err != noErr)
```

```
    {
    return 0; /* Memory issue */
    }
    (*status_error)->cnt = length;
    MoveBlock((&msg2),(*status_error)->str, (*status_error)->cnt);


/* Copies the data from the buffer to the Labview ARRAY */

     MoveBlock(frame, ARRAY, (size_t)size);
     //memcpy(ARRAY,frame,(size_t)size);

/* Finish the sequence*/
pl_exp_finish_seq(hCam, frame, 0);

/* Uninit sequence*/
pl_exp_uninit_seq();

free(frame);

return 1;
}


/* 6. The function closeCam frees the current camera, prepares it for power-down↩
    ; closes the PVCAM library, frees memory. */

_declspec(dllexport) int closeCam()
{
pl_cam_close(hCam);
pl_pvcam_uninit();

return 1;
}
```

P

Devices

Trap Drive

Synthesized Function Generator	Stanford Research Systems	DS345
Amplifier	Kalmus	Model 714FC-CE
RF Resonator	Prague University	Ivo Polak design
Capacitance Meter	Rohde & Schwarz	$1\,\mathrm{pF} - 100\,\mu\mathrm{F}$
Antenna Analyzer	MFJ	Model MFJ 259B

369 nm Laser System

Laser diode	Nichia	NDU1113E
AOM at 65 MHz	IntraAction	ASM-702B8M
AOM at 985 MHz	Brimrose	TEF-1050-50-369

Experiment Control

DSP	Jäger GmbH	ADwin-Pro (USB)
LabVIEW	National Instruments	Version 9.0
VFG150 (USB)		In-house

Vacuum

Vacuum Chamber	Hositrad	in-house design
Ion Getter Pump	StarCell® VacIon® Varian	Model 919-0110, 20 l/s
F100 View-port	UKAEA	in-house design
CF40 View-ports	Laseroptex	
AR Coating	Tafelmaier Dünnschiht Technik GmbH	
SHV Feed-through	LewVac	5 kV DC, I = 5 A
CF100 to CF40 Adapter	Allectra	
Capton Coaxial Cable	Allectra	311-KAP50
Capton Cable 'Caburn UHV'	Allectra	311-KAP2
Power Feed-through	Allectra	264-030CU5K-12-C40
SMA Feed-through	Allectra	242SMADF50-C40-2
SMA Coaxial Cable	Allectra	380-SMA-MM-1000

Lambda-meter

Lock-in-Amplifier	Stanford Research Systems	SR850 DSP
Photodiodes	Hamamatsu	S4707-01
Counter	Hewlett Packard	HP5334B

Microwave

Dual-Loop PLL-Oscillator	MITEQ	DLCRO-010-12568-3-15P
Mixer	MACOM	M79
Preamplifier +10 dB	Minicircuits	ZX60-14012L
Power Amplifier +35 dB	Globes	10 W PA Elsira
Attenuator	Minicircuits	VAT-10+ VAT-20+
Isolators	TKI	Ferrit IC 12.5-10W
Power Supply (±48 V)	Mean Well	SP-200-48
Power Supply (±15 V)	Traco Power	ESP 36-15SN
Rubidium Atomic Clock	Stanford Research Systems	FS725
Crystal Detector, 0.01-18 GHz	Narda	Model 4503

SMA Female Connector	Allectra	245-CON-SMA-F, 50Ω
SMA Cables	Allectra	311-KAP50
Directional Coupler, UMCC 2-18 GHz		DC-S000-16S

Detection System

Image Intensifier	PCO Computer Optics GmbH	Intensified Relay Optics (IRO)
CCD Detector	Princeton Instruments Inc.	Model TE/CCD-512-TKB
CCD Controller	Roper Scientific Inc.	ST-133 5 MHz
Photomultiplier	Hamamatsu	R5600P
Photomultiplier	Hamamatsu	R7518P
Photon Counting Unit	Hamamatsu	C6465

Micro-motion Compensation

Time-to-Digital Converter	Fast Com Tec GmbH	P7888

Magnetic Field Measurements

Hall Sensor	Toyo Corporation	STF99-0404
Gauss/Teslameter	F. W. Bell	9550

Technical Information

Q.1 Hositrad custom Vacuum Chamber Sketch

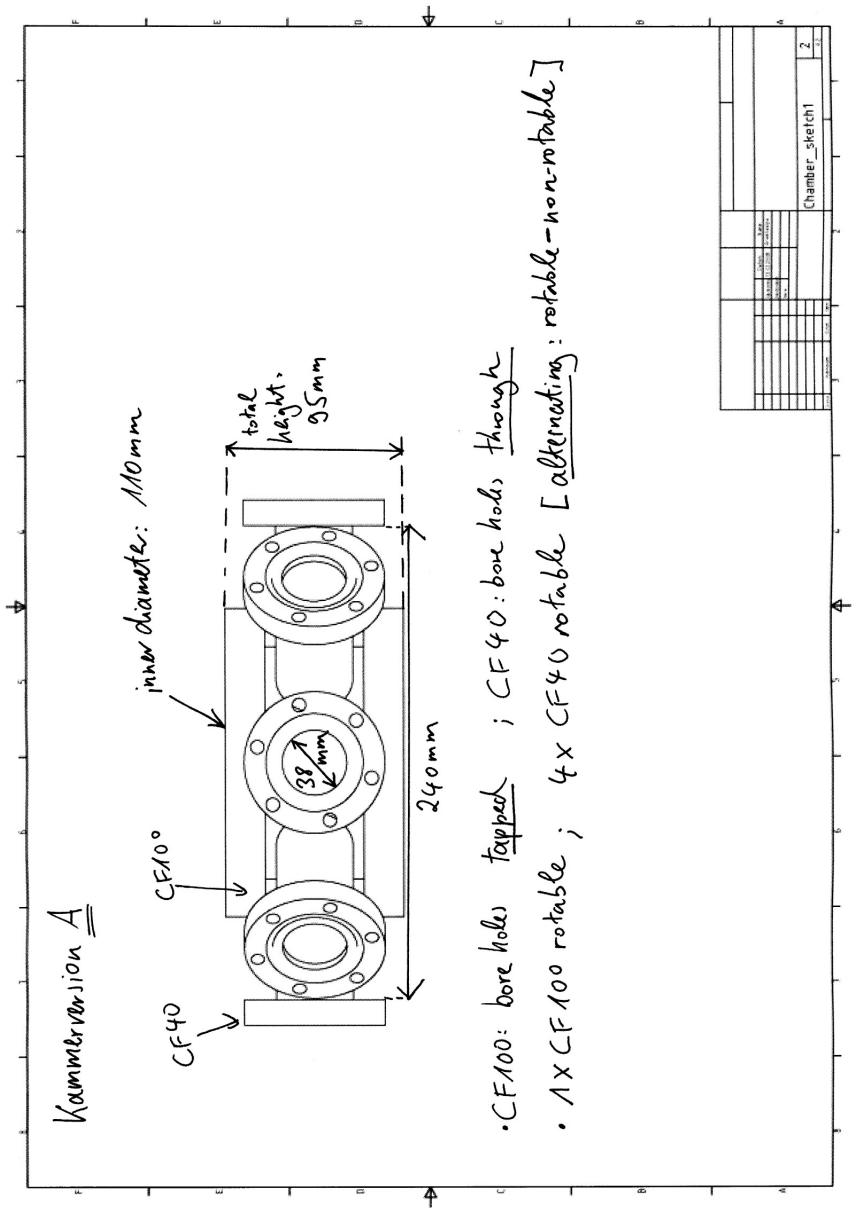

Figure Q.1: Vacuum Chamber (Hositrad).

Q.2 Allectra SMA Feedthrough Losses at different Frequencies

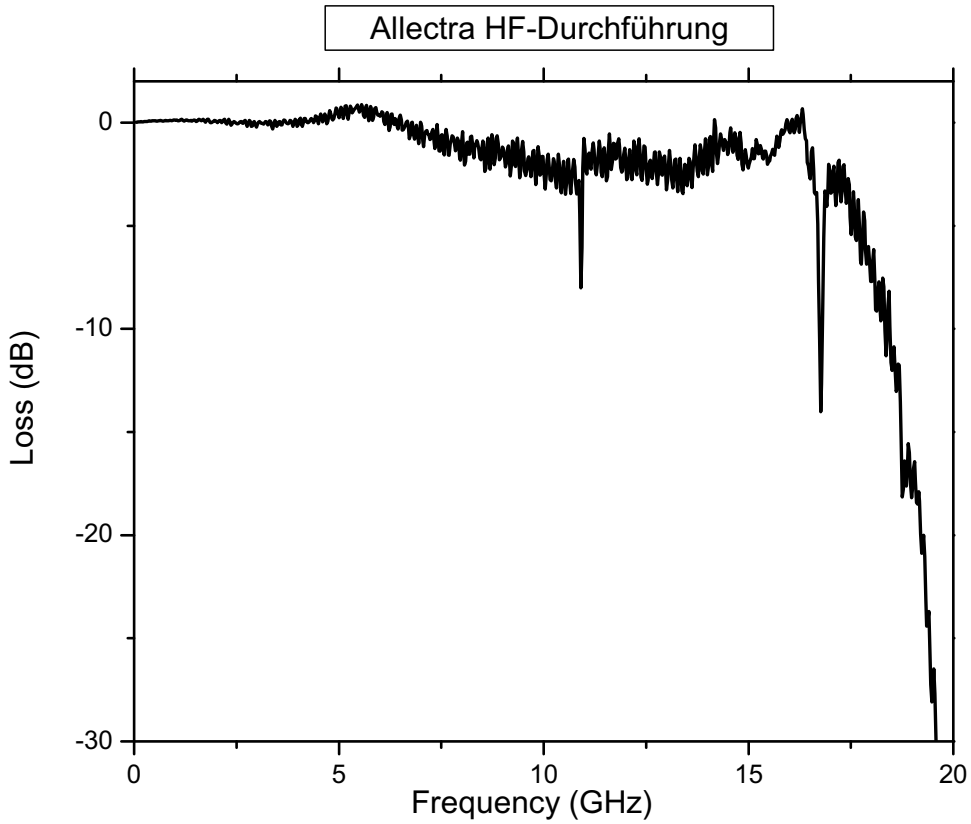

Figure Q.2: Losses at different frequencies for the SMA-feedthrough (ALLECTRA).

Q.3 Laser Settings

Wavelength, (nm)	Current, (mA)	Temperature, (a.u.)	Piezo, (a.u.)	Power, (μW)
369	61.8	540	4/0	63
399	39.8	795		115
935	117.8	1068	0/9	490
638	126.0	990	3/0	7900
780	53.2	1148	0/7	

Table Q.1: The actual settings of the current, temperature and piezo controllers used in the experiment to achieve the required wavelengthes of the laser diodes. The 780 nm laser diode is used in the lambda-meter for the ^{87}Rb reference.

Q.4 Helmholtz Coils Settings

The fields used in our experiment are summarized in Table Q.2.

	I[A]	B[Gauss]
Big1	short	0
Big2	-0.598	5.33
SmallDown	-3.411	5.22
SmallUp	0	0
RoundC	-0.040	0.12
RoundW	-0.040	0.12

Table Q.2: The actual settings of the currents for the Helmholtz coils pair.

For the coils connected in series the components of the magnetic field can be described by relations

$$\boxed{\begin{aligned} B_x &= 17.88(6) \cdot I \\ B_y &= 3.00(2) \cdot I \\ B_z &= 5.96(9) \cdot I \end{aligned}} \qquad \text{(Q.1)}$$

In order to find the magnetic field by a single coils the corresponding relations in Q.1 have to be divided by two.

Bibliography

Advanced Research and Development Activity (ARDA). 2004. *A Quantum Information Science and Technology Roadmap.* `http://qist.lanl.gov/qcomp_map.shtml`.

ALLECTRA. 2008. *Assemly Instruction for SMA Female Connector.*

Balzer, Christoph H. 2003. *Zur Dynamik eines beobachteten einzelnen Quantensystems: Das Quanten-Zeno-Paradox.* Ph.D. thesis, Universität Hamburg.

Barenco, A., Bennett, C. H., Cleve, R., DiVincenzo, P., Margolus, N., Shor, P., Sleator, T., Smolin, A., & Weinfurter, H. 1995. Elementary gates for quantum computation. *Phys. Rev. A*, **52**, 3457–3467.

Barrett, M. D., Chiaverini, J., Schaetz, T., Britton, J., Itano, W. M., Jost, J. D., Knill, E., Langer, C., Leibfried, D., Ozeri, R., & Wineland, D. J. 2004. Deterministic Quantum Telepoltation of Atomic Qubits. *Nature*, **429**, 737–739.

Bauch, A., Schnier, D., & Tamm, C. 1992. Collisional population trapping and optical deexcitation of ytterbium ions in a radiofrequency trap. *J. Mod. Opt.*, **39**, 389–401.

Baumgart, Ingo. 2008. *Optimierte Präparation eines $^{171}Yb^{+}$-Ions in den Zustand $^{2}S_{1/2}$, $(F = 0)$.* Diplomarbeit, Universität Siegen.

Benhelm, J., Kirchmair, G., Roos, C. F., & Blatt, R. 2008. Towards fault-tolerant quantum computing with trapped ions. *Nature*, **4**, 463–466.

Benhelm, Jan. 2008. *Precition Spectroscopy and Quantum Information Processing with Trapped Calcium Ions.* Ph.D. thesis, Universität Innsbruck.

Bennett, C. H., Brassard, G., Crépeau, C., Jozsa, R., Peres, A., & Wootters, W. K. 1993. Teleporting an Unknown Qauntum State via Dual

Classical and Einstein-Podolsky-Rosen Channels. *Phys. Rev. Lett.*, **70**, 1895–1899.

Böhi, P., Riedel, M. F., Hänsch, T. W., & Treutlein, P. 2010. Imaging of microwave fields using ultracold atoms. *Appl. Phys. Lett.*, **97**, 051101.

Bouwmeester, D., Pan, J.-W., Mattle, K., Einble, M., Weinfurter, H., & A., Zeilinger. 1997. Experimental quantum teleportation. *Nature*, **390**, 575–579.

Braun, Alexander. 2007. *Addressing Single Yb^+ Ions.* Ph.D. thesis, Universität Siegen.

Burgarth, Volker. 1998. *Ein Michelson-Lambdameter und eine Frequenzmarke für hoch-präzise Wellenlängenmessungen.* Masterarbeit, Universität Hamburg.

Castell, R., Demtröder, W., Fisher, A., Kullmer, R., Weickenmeier, H., & Wickert, K. 1985. The Accuracy of Laser Wavelength Meters. *Appl. Phys. B*, **38**, 1–10.

Cirac, J.I., & Zoller, P. 1995. Quantum Computations with Cold Trapped Ions. *Phys. Rev. Lett.*, **74**, 4091–4094.

Cowan, R.D. 1981. *The Theory of Atomic Structure and Spectra.* University of California Press.

Demtröder, W. 2008. *Laser Spectroscopy.* Springer.

Diedrich, F., Berquist, J. C., Itano, W. M., & Wineland, D. J. 1989. Laser cooling to the zero-point energy of motion. *Phys. Rev. Lett.*, **62**, 403–406.

DiVincenzo, D. P. 1995. Two-bit gates are universal for quantum computation. *Phys. Rev. A*, **51**, 1015–1022.

DiVincenzo, D. P. 2000. The Physical Implementation of Quantum Computation. *Fortschr. Phys.*, **48**, 771–783.

Eiteneuer, Daniel. 2009. *Bau und Charakterisierung einer Ytterbium-Quelle für mikrostruktierte Ionenfallen.* Masterarbeit, Universität Siegen.

Feynman, R. P. 1982a. Quantum mechanical computers. *Foundantions of physics*, **16**, 507–531.

Feynman, R. P. 1982b. Simulating physics with computers. *Int. J. Theor. Phys.*, **21**, 467–488.

Fisher, R., Helmer, F., Glaser, S. J., Marquardt, F., & Schulte-Herbrüggen, T. 2010. Optimal control of circuit quantum electrodynamics in one and two dimensions. *Phys. Rev. B*, **81**, 085328.

Fisk, P. T. H., Sellars, M. J., Lawn, M. A., Coles, C., Mann, A. G., & Blair, D. G. 1995. Very High Q Microwave Spectroscopy on Trapped $^{171}Yb^{+}$ Ions: Application as a Frequency Standard. *IEEE Trans. Instr. Meas.*, **44**, 113–116.

Fridenauer, H., Schmitz, H., Glueckert, J., Porras, D., & Schaetz, T. 2008. Simulating a quantum magnet with trapped ions. *Nature Phys.*, **4**, 757–761.

Froncisz, W., & Hyde, J. S. 1982. The Loop-Gap Resonator: A New Microwave Lumped Circuit ESR Sample Structure. *J. of Mag. Res.*, **47**, 515–521.

Gerritsma, R., Kirchmair, G., Zähringer, F., Solano, E., Blatt, R., & Roos, C. F. 2010. Quantum simulation of the Dirac equation. *Nature Lett.*, **463**, 68–71.

Ghosh, P. 1995, reprinted 2007. *Ion Traps*. Oxford University Press.

Gloger, Timm Florian. 2011. *Mikrowellenquelle mit phasenkohärenter Frequenzumschaltung zur Quantenzustandsmanipulation*. Masterarbeit, Universität Siegen.

Grover, L. K. 1996. A fast quantum mechanical algorithm for database search. *Proc. 28th Annual ACM Symposium on the Theory of Computing (STOC)*, 212–219.

Gulde, Stephan Tilo. 2000. *Experimental Realization of Quantum Gated and the Deutsch-Jozsa Algorithm with Trapped $^{40}Ca+$ Ions*. Ph.D. thesis, Universität Innsbruck.

Gullion, T., Baker, D. B., & Conradi, M. S. 1990. New, Compensated Carr-Purcell Sequences. *J. Magn. Reson.*, **89**, 479–484.

Haeberlen, U. 1976. *High Resolution NMR in Solids: Selective Averaging*. Academic, New York.

Häffner, H., Hänsel, W., Roos, C. F., Benhelm, J., Chek-al kar, D., Chwalla, M., Körber, T., Rapol, U. D., Riebe, M., Schmidt, P. O., Becher, C., Gühne, O., Dür, W., & Blatt, R. 2005. Scalable multiparticle entanglement of trapped ions. *Nature*, **438**, 643–646.

Hahn, E. L. 1950. Spin Echoes. *Phys. Rev.*, **80**, 580–594.

Haljan, P. C., Brickman, K.-A., Deslauriers, L., Lee, P. J., & Monroe, C. 2005. Spin-Dependent Forces on Trapped Ions for Phase-Stable Quantum Gates and Entangled States of Spin and Motion. *Phys. Rev. Lett.*, **94**, 153602.

Hannemann, Thilo. 2001. *Schätzung von Quantenzuständen und Charakterisierung von Quantenkanälen*. Ph.D. thesis, Universität Hamburg.

Hänsch, T. W., & Schavlow, A. L. 1975. Cooling of gasses by laser radiation. *Opt. Commun.*, **13**, 68–69.

Hardy, W. N., & Whitehead, L. A. 1981. Split-ring resonator for use in magnetic resonance from 200 - 2000 MHz. *Rev. Sci. Instrum.*, **52**, 213–216.

Hosaka, K., Webster, S. A., Blythe, P. J., Stannard, A., Beaton, D., Margolis, H. S., Lea, S. N., & Gill, P. 2005. An optical frequency standard based on the electric octupole transition in $^{171}Yb^{+}$. *IEEE Trans. Instr. Meas.*, **54**, 759–762.

Hyde, J. S., & Froncisz, W. 1989. *Advanced EPR: applications in biology and biochemistry*. Elsevier Science Publishers.

Inoué, S., & Spring, K. R. 1997. *Video microscopy: the fundamentals*. Plenum Press.

Islam, R., Edwards, E.E., Kim, K., Korenblit, S., Noh, C., Carmichael, H., Lin, G.-D., Duan, L.-M., Wang, C. C., Freericks, J. K., & Monroe, C. 2011. Onset of a quantum phase transition with a trapped ion quantum simulator. *Nature Commun.*, 377–384.

James, D. F. V. 1998. Quantum dynamics of cold trapped ions with application to quantum computation. *Applied Physics B*, **66**, 181–190.

Johanning, M., Braun, A., Timoney, N., Elman, V., Neuhauser, W., & Wunderlich, C. 2009a. Individual Addressing of Trapped Ions and Coupling of Motional and Spin States Using rf Radiation. *Phys. Rev. Lett.*, **102**, 073004.

Johanning, M., Varón, A. F., & Wunderlich, Chr. 2009b. Quantum Simulations with Cold Trapped Ions. *Journal of Physics B: At. Mol. Opt. Phys.*, **42**, 154009.

Johanning, M., Braun, A., Eiteneuer, D., Paape, C., Balzer, C., Neuhauser, W., & Wunderlich, C. 2011. Resonance-enhanced isotope-selective photoionization of YbI for ion trap loading. *Appl. Phys. B*, **103**, 327–338.

Karetnikov, M. D. 1997. AN ORIGIN OF RF BREAKDOWN IN VACUUM. *Particle Accelerators*, **57**, 189–214.

Kaufmann, Delia. 2011. *Mikrostrukturierte segmentierte Paul-Falle mit einstellbarem Magnetfeldgradienten.* Ph.D. thesis, Universität Siegen.

Kaufmann, Peter. 2012. *Präzise Wellenlängenmessung und Computer-Steuerung für Experimente mit gespeicherten Yb^+-Ionen.* Masterarbeit, Universität Siegen.

Khodjasteh, K., & Lidar, D. A. 2005. Fault-Tolerant Quantum Dynamical Decoupling. *Phys. Rev. Lett.*, **95**, 180501.

Khodjasteh, K., & Lidar, D. A. 2007. Performance of deterministic dynamical decoupling schemes: Concatenated and periodic pulse sequences. *Phys. Rev. A.*, **75**, 062310.

Khromova, A., Piltz, Ch., Scharfenberger, B., Gloger, T. F., Johanning, M., Varón, A. F., & Wunderlich, Ch. 2012. Designer Spin Pseudomolecule Implemented with Trapped Ions in a Magnetic Gradient. *Phys. Rev. Lett.*, **108**, 220502.

Kielpinski, D., Cetina, M., Cox, J. A., & KÃ¤rtner, F. X. 2006. Laser cooling of trapped ytterbium ions with an ultraviolet diode laser. *Opt. Lett.*, **31**, 757–759.

Kildemo, M., Calatroni, S., & Taborelli, M. 2004. Breakdown and field emission conditioning of Cu, Mo, and W. *Phys. Rev. Special Topics - Accelerators and Beams*, **7**, 092003.

Kraft, S., Deninger, A., Trück, Ch., Fortágh, J., Lison, F., & Claus, Zimmermann. 2005. Rubidium Spectroscopy at 778-780 nm with a Distributed Feedback Laser Diode. *Laser Phys. Lett.*, **2**, 71–76.

Lanyon, B. P., Hempel, C., Nigg, D., Müller, M., Gerritsma, R., Zähringer, F., Schindler, P., Barreiro, J. T. amd Rambach, M., Kirchmair, G., Hennrich, M., Zoller, P., Blatt, R., & Roos, C. F. Universal Digital Quantum Simulation with Trapped Ions. *Science*, **334**, 57–61.

Latham, R. V. 1981. *High Voltage Vacuum Insulation: The Physical Basis.* Academic Press Inc. (London) LTD.

Leibfried, D., DeMarco, B., V., Meyer, Lucas, D., Barrett, M., Britton, J., Itano, W. M., Jelenkovic, B., Langer, C., Rosenband, T., & Wineland, D. J. 2003. Experimental demonstration of a robust, high-fidelity geometric two ion-qubit phase gate. *Nature*, **422**, 412–415.

Loudon, R. 1983. *The quantum theory of light.* Oxford University Press, second edition.

Magnetic Component Engineering Inc. 2009a. *Materials: Neodymium Iron Boron Sintered, N5064.* `http://www.mceproducts.com/materials/material-details.asp?id=1079&MaterialTypeCode=1003`.

Magnetic Component Engineering Inc. 2009b. *Materials: Samarium Cobalt Sintered, S2869.* `http://www.mceproducts.com/materials/material-details.asp?id=1039&MaterialTypeCode=1005`.

McHugh, D., & Twamley, J. 2005. Quantum computer using a trapped-ion spin molecule and microwave radiation. *Phys. Rev. A*, **71**, 012315.

McLoughlin, J., Nizamani, A., Siverns, J., Sterling, R., Hughes, M. Bjoern, Lekitsch, B., Stein, B., Weidt, S., & Hensinger, W. 2011. Versatile ytterbium ion trap experiment for operation of scalable ion-trap chips with motional heating and transition-frequency measurements. *Phys. Rev. A*, **83**, 013406.

Mehdizadeh, M., Ishii, T. K., Hyde, J. S., & Froncisz, W. 1983. Loop-Gap Resonator: A Lumped Mode Microwave Resonant Structure. *IEEE Trans. on Microwave Theory and Techniques*, **MTT-31**, 1059–1064.

Meiboom, S., & Gill, D. 1958. Modified Spin-Echo Method for Measuring Nuclear Relaxation Times. *Rev. Sci. Instr.*, **29**, 688–691.

Milburn, G. J., Schneider, S., & James, D. F. 2000. Ion trap quantum computing with warm ions. *Fortschr. Physik*, **48**, 801–810.

Mintert, F., & Wunderlich, Chr. 2001. Ion-Trap Quantum Logic Using Long-Wavelength Radiation. *Phys.Rev.Lett.*, **87**, 257904–1.

Mizel, A., Lidar, D. A., & Mitchell, M. 2007. Simple proof of equivalence between adiabatic quantum computation and the circuit model. *Phys. Rev. Lett.*, **99**, 070502.

MODEL DS345 Synthesized Function Generator. March 2005. *Stanford Research Systems Inc.*

MODEL SR850 DSP Lock-In Amplifier Manual. January 2009. *Stanford Research Systems Inc.*

Mølmer, K., & Sørensen, A. 1999. Multiparticle Entanglement of Hot Trapped Ions. *Phys. Rev. Lett.*, **82**, 1835–1838.

Monroe, C., Meekhof, D. M., King, B. E., Itano, W. M., & Wineland, D.J. 1995. Demonstration of a Fundamental Quantum Logic Gate. *Phys. Rev. Lett.*, **75**, 4714–4717.

Monz, T., Kim, K., Hänsel, W., Riebe, M., Villar, A. S., Schindler, P., Chwalla, M., Hennrich, M., & Blatt, R. 2009. Realization of the Quantum Toffoli Gate with Trapped Ions. *Phys. Rev. Let.*, **102**, 040501.

Monz, T., Schindler, P., Barreiro, J. T., Chwalla, M., Nigg, D., Coish, W. A., Harlander, M., Hänsel, W., Hennrich, M., & Blatt, R. 2011. 14-Qubit Entanglement: Creation and Coherence. *Phys. Rev. Let.*, **106**, 130506.

National Instuments Inc. 2008. *Building a DLL with Visual C++.* `http://zone.ni.com/devzone/cda/tut/p/id/3056`.

Nielsen, M., & Chuang, I. 2000. *Quantum Computation and Quantum Information.* Cambridge University, Cambridge, England.

NTE/CCD Detector Manual. September 2001. *Princeton Instruments Inc., Roper Scientific Inc.*

Olmschenk, S., Younge, K. C., Moehring, D. L., Matsukevich, D. N., Maunz, P., & Monroe, C. 2007. QManipulation and detection of a trapped Yb^+ hyperfine qubit. *Phys. Rev. A*, **76**, 052314.

Olmschenk, S., Matsukevich, D. N., Maunz, P., Hayes, D., Duan, L.-M., & Monroe, C. 2009. Quantum Teleportation between Distant Matter Qubits. *Science*, **323**, 486–489.

Ospelkaus, C., Warring, U., Colombe, Y., Brown, K. R., Amini, J. M., Leibfried, D., & Wineland, D. J. 2011. Microwave quantum logic gates for trapped ions. *Nature*, **476**, 181–185.

Owens, J. C. 1967. Optical Refractive Index of Air: Dependence on Pressure, Temperature and Composition. *Appl. Optics*, **6**, 51–59.

Ozeri, R., Itano, W. M., Blakestad, R. B., Britton, J., Chiaverini, J., Jost, J. D., Langer, C., Leibfried, D., Reichle, R., Seidelin, S., Wesenberg, J. H., & Wineland, D. J. 2007. Errors in trapped-ion quantum gates due to spontaneous photon scattering. *Phys. Rev. A.*, **75**, 042329.

Parker, R. J. 1990. *Advances in permanent magnetism.* John Wiley & Sons.

Paul, W. 1990. Electromagnetic Traps for Charged and Neutral Particles. *Rev. Mod. Phys.*, **62**, 531–540.

PCO Computer Optics Manual. October 1993. *IRO Intensified Relay Optics. Operating Instructions.*

Piltz, Christian. 2010. *Aufbau von Laserlichtquellen und Optik zur Speicherung und Kühlung von Ytterbium+-Ionen.* Masterarbeit, Universität Siegen.

Piltz, Christian. 2013. Ph.D. thesis, Universität Siegen.

Piston, D. W. 1998. Choosing Objective Lenses: The Importance of Numerical Aperture and Magnification in Digital Optical Microscopy. *Biol.Bull.*, **195**, 1–4.

Pulinets, S.A., Ouzounov, D., Ciraolo, L., Singh, R., Cervone, G., Leyva, A., Dunajecka, M., Karelin, A. V., Boyarchuk, K. A., & Kotsarenko, A. 2006. Thermal, atmospheric and ionospheric anomalies around the time of the Colima M7.8 earthquake of 21 January 2003. *Ann. Geophys.*, **24**, 835–849.

Raizen, M. G., Gilligan, J. M., Bergquist, J. C., Itano, W. M., & Wineland, D. J. 1992. Ionic Crystals in a linear Paul trap. *Phys. Rev. A*, **45**, 6493–6501.

Ramsey, N. F. 1985. *Molecular Beams.* Oxford University Press, New York.

Raussendorf, R., & Briegel, H. J. 2001. A one-way quantum computer. *Phys. Rev. Let.*, **86**, 5188–5191.

Reuner, Jörg. 2007. *Aufbau frequenzstabilisierter Diodenlasersysteme mit Emissionswellenlängen bei 399 nm, 638 nm und 935 nm.* Masterarbeit, Universität Siegen.

Riebe, M., Häffner, H., Roos, C. F., Hänsel, W., Ruth, M., Benhelm, J., Lancaster, G. P. T., Körber, T. W., Bechner, C., Schmidt-Kaller, F., James, D. F. V., & Blatt, R. 2004. Deterministic Quantum Telepoltation of Atomic Qubits. *Nature*, **429**, 734–737.

Riebe, Mark. 2005. *Preparation of Entangled States and Quantum Teleportation with Atomic Qubits.* Ph.D. thesis, Universität Innsbruck.

Rieder, C. L. 1999. *Methods in cell biology.* Academic Press.

Rinard, G. A., & Eaton, G. R. 2005. *Biomedical EPR, Part B: Methodology, Instrumentation, and Dynamics.* Kluwer Academic Publishers.

Roberts, M., Taylor, P., Barwood, G. P., Gill, P., Klein, H. A., & Rowley, W. R. C. 1997. Observation of an Electric Octupole Transition in a Single Ion. *Phys. Rev. Lett.*, **78**, 1876–1879.

Roberts, M., Taylor, P., Gateva-Kostova, S.V., Clarke, R., Rowley, W., & Gill, P. 1999. Measurement of the $^2S_{1/2}$-$^2D_{5/2}$ clock transition in a single $^{171}Yb^+$ ion. *Phys. Rev. A*, **60**, 2867–2872.

Roberts, Matthew. 1996. *Spectroscopy of a Single Ytterbium Ion.* Ph.D. thesis, Imperial College, University of London.

Roper Scientific Inc. April 2003. *PVCAM 2.6.*

Ryan, C. A., Hodges, J. S., & Cory, D. G. 2010. Robust Decoupling Techniques to Extend Quantum Coherence in Diamond. *Phys. Rev. Lett.*, **105**, 200402.

Sackett, C. A., Kielpinski, D., King, B. E., Langer, C., Meyer, V., Myatt, C. J., Rowe, M., Turchette, Q. A., Itano, W. M., Wineland, D. J., & Monroe, C. 2000. Experimental entamglement of four particles. *Nature*, **404**, 256–259.

Scharfenberger, Benedikt. 2012. Ph.D. thesis, Universität Siegen.

Schmidt-Kaler, F., Häffner, H., Riebe, M., Gulde, S., Lancaster, G. P. T., Deutschle, T., Becher, C., Roos, C. F., Eschner, J., & Blatt, R. 2003. Realization of the Cirac-Zoller controlled-NOT quantum gate. *Nature*, **422**, 408–411.

Schneider, Christian. 2007. *Entwicklung eines Objektivs hoher numerischer Apertur zum Nachweis der Resonanzfluoreszenz einzelner gespeicherter Ionen.* Masterarbeit, Universität Siegen.

Schützhold, R. 2007. Analogue of cosmological particle creation in an ion trap. *Phys. Ref. Lett.*, **99**, 201301.

Shor, P. W. 1994. Algorithms for Quantum Computation: discrete logarithms and factoring. *In Proc. 35th Annual Symposium on Foundations of Computer Science*, 124–134. IEEE Computer Society Press.

Shor, P. W. 1995. Scheme for reducing decoherence in quantum computer memory. *Phys. Rev. A.*, **52**, 2493–2496.

Silver, S. 1997. *Microwave Antenna Theory and Design.* Peter Peregrinus Ltd.

Solano, E., de Matos Filho, R. L., & Zagury, N. 1999. Deterministic Bell states and measurement of the motional state of two trapped ions. *Phys. Rev. A.*, **59**, R2539–R2543.

Sørensen, A., & Mølmer, K. 1999. Quantum Computation with Ions in Thermal Motion. *Phys. Rev. Let.*, **82**, 1971–1974.

Sørensen, A., & Mølmer, K. 2000. Entanglement and Quantum Computation with Ions in Thermal Motion. *Phys. Rev. A.*, **62**, 02231.

Souza, A. M., Álvarez, G. A., & Suter, D. 2011. Robust Dynamical Decoupling for Quantum Computing and Quantum Memory. *Phys. Rev. Let.*, **106**, 240501.

ST-133 5 MHz Controller Manual. April 1999. *Princeton Instruments Inc., Roper Scientific Inc.*

Steane, A. 1997. The ion trap quantum information processor. *Applied Physics B*, **64**, 623–642.

Steck, D.A. 2010. *Rubidium 87 D line Data.* `http://steck.us/alkalidata`. Revision 2.1.4.

Stenholm, S. 1986. The semiclassical theory of laser cooling. *Rev. Mod. Phys.*, **58**, 699–739.

Stone, J.A., & Zemmerman, J. H. 2010. *Index of Refraction of Air.* `http://emtoolbox.nist.gov/Wavelength/Documentation.asp`. NIST.

Taylor, P., Roberts, M., Gateva-Kostova, S. V., Clarke, R. B. M., Barwood, G. P., Rowley, W. R. C., & Gill, P. 1997. Investigation of the $^2S_{1/2} - {}^2D_{5/2}$ clock transition in a single ytterbium ion. *Phys. Rev. A*, **56**, 2699–2704.

Timoney, N., Baumgart, I., Johanning, M., Varón, A. F., Plenio, M. B., Retzker, A., & Wunderlich, Ch. 2011. Quantum gates and memory using microwave-dressed states. *Nature*, **476**, 185–188.

Timoney, Nuala. 2010. *Robust rotations and coherent quantum states with a single trapped ion.* Ph.D. thesis, Universität Siegen.

Toyo Corporation. August 2010. *Hall Sensor STF99-0404.* `http://www.toyo.co.jp/bell/probe/bell02.html`.

Ursin, R., Jennewein, T., Aspelmeyer, M., Kaltenbaek, R., Lindenthal, M., & Zeilinger, A. 2004. Quantum Teleportation Link across the Danube. *Nature*, **430**, 849–849.

Vandersypen, L. M. K., & Chuang, I. L. 2004. NMR Techniques for Quantum Control and Computation. *Rev. Mod. Phys.*, **76**, 1037–1069.

Viola, L., Knill, E., & Lloyd, S. 1999. Dynamical Decoupling of Open Quantum Systems. *Phys. Rev. Lett.*, **82**, 2417–2421.

Walde, P. 2001. Understanding Circular Waveguide - Experimentally. *QEX*, 37–48.

Walls, D. F., & Milburn, G. J. 1994. *Quantum Optics.* Springer-Verlag Berlin.

Walther, P., Resch, K. J., Rudolph, T., Schenk, E., Weinfurter, H., Vedral, V., Aspelmeyer, M., & Zeilinger, A. 2005. Experimental One-Way Quantum Computing. *Nature*, **434**, 169–176.

Weel, M., & Kumarakrishnan, A. 2002. Laser-frequency stabilization using a lock-in amplifier. *Can. J. Phys.*, **80**, 1449–1458.

Wineland, D. J., & Dehmlet, H. G. 1975. Proposed 10^{14} $\delta\nu < \nu$ laser fluorescence fpectroscopy on Tl^{+} mono-ion oscillator. *Bull. Am. Phys. Soc.*, **20**, 637.

Wineland, D. J., & Itano, W. M. 1979. Laser cooling of atoms. *Phys. Rev. A*, **20**, 1571–1540.

Wineland, D. J., Bergquist, J. C., Itano, W. M., Bollinger, J. J., & Manney, C. H. 1987. Atomic-Ion Coulomb Clusters in an Ion Trap. *Phys. Rev. Lett.*, **59**, 2935–2938.

Wineland, D.J., Monroe, C., Itano, W.M., Leibfried, D., King, B.E., & Meekhof, D.M. 1998a. Experimental Issues in Coherent Quantum-State Manipulation of Trapped Atomic Ions. *J. Res. Natl. Inst. Stand. Technol.*, **103**, 259–328.

Wineland, D.J., Monroe, C., Itano, W.M., King, B.E., Leibfried, D., Meekhof, D.M., Myatt, C., & Wood, C. 1998b. Experimental Primer on the Trapped Ion Quantum Computer. *Fortschr. Phys.*, **46**, 363–390.

Wood, R. L., Froncisz, W., & Hyde, J. S. 1984. The loop-gap resonator. II. Controlled return flux three-loop, two-gap microwave resonators for ENDOR and ESR spectroscopy. *J. of Mag. Res.*, **58**, 243–253.

Wunderlich, C. 2002. *Laser Physics at the Limits.* Springer-Verlag Berlin Heidelberg.

Wunderlich, C., & Balzer, C. 2003. Quantum measurements and new concepts for experiments with trapped ions. *Advances in Atomic Molecular, and Optical Physics*, **49**, 293–372.

Yu, N., & Maleki, L. 2000. Lifetime measurements of the $4f^{14}5d$ metastable states in single ytterbium ions. *Phys. Rev. A*, **61**, 022507.

Acknowledgements

First, I would like to thank Prof. Dr. Christof Wunderlich for giving me the possibility to make an interesting research full of challenges.

Of course I was not fighting alone with the milestones of this research. I would like to thank the collegues with whom I closely worked over the past years: Benedikt Scharfenberger, Christian Piltz and Andrés Varón, for the nice and fruitful collaboration. Thanks to Benedikt, who always reminded me at the beginning of the week that once upon a time will come again Friday and thanks to Christian who was always ready to provide support in critical situations when everything was damn wrong. I wish good luck to Benedikt with completing his Thesis and to Christian with the successful implementation of further milestones.

I would like to thank also our postdocs, Andrés Varón and Michael Johanning, for having patience with me and my millions of questions.

Special thanks goes also to the people who helped me a lot to materialize this thesis: Delia Kaufmann, Christian Piltz, Andrés Varón, Michael Johanning and my husband Francesco Voltolina. Thank you guys for your corrections and your suggestions.

There is of course a very important person in my life during the PhD time - Gudrun Bingener. Without her I would be totally lost in the bureaucracy. Thank you, Gudrun, for helping me with everything beyond the research and not letting me down. In the same category is the special gratitude also to dear Delia who systematically reminded me about the happenings around. Thanks to you I attended most of the seminars and meetings. Thank you also for cheering me up on the dark-dark days.

Actually, the experiment started from absolute zero. We did not have even the optical tables when I started the PhD. A lot of work and help came from our mechanical workshop. At this point I would like really to thank the head of the mechanical workshop Guido Schmidt. He always perfectly understood what I want and what I need, even better than myself. Thank you for always helping.

The lab means work, the office - fun, and there is no fun without Delia Kaufmann, Tomas Collath, Nuala Timoney (already two years away), Tanveer Baig and Eman Asenwar (already half year away). Thank you guys for the nice atmosphere.

I would like to say a very huge thank also to my big dear family. It is not easy to be so far away and not to have the possibility to come easily home whenever it

hurts. Thank you for being still close and believing in me. Without your support I would achieve nothing.

Finally, I would like to thank my husband Francesco for his always present support, understanding and his iron patience. I do not know what I was doing without you. Thank you for being critical, also during the corrections of this thesis. Thank you so much for your love. It helps me always.